Fundamental insights into dynamic ionic exchange in vertically-oriented nanostructured materials via fast electrogravimetric methods. Applications to energy storage mechanisms.

Tao Lé

Sorbonne Université

École Doctorale 388 – Chimie Physique et Chimie Analytique de Paris Centre

Laboratoire Interfaces et Systèmes Électrochimiques, LISE – UMR 8235

Institut Nanosciences et Cryogénie, INAC– CEA de Grenoble

Fundamental insights into dynamic ionic exchange in vertically-oriented nanostructured materials via fast electrogravimetric methods. Applications to energy storage mechanisms.

Presented by Tao LÉ

Ph.D. Thesis

Under the supervision of Dr. Hubert PERROT

Presented and defended on October 31, 2018

Before a jury composed of:

Mme. Fannie ALLOIN	Directeur de Recherche CNRS	Rapporteur
M. Pierre-Louis TABERNA	Chargé de Recherche CNRS	Rapporteur
M. Mathieu SALANNE	Professeur Sorbonne Universités/PHENIX	Examinateur
M. François TRAN VAN	Professeur Université François Rabelais/PCM2E	Examinateur
M. Hubert PERROT	Directeur de Recherche CNRS	Directeur de thèse
Mme. Ozlem SEL	Chargée de Recherche CNRS	Co-encadrante de thèse
M. Gérard BIDAN	Conseiller Scientifique CEA	Co-Directeur de thèse
M. David ARADILLA	Chercheur CEA	Co-encadrant de thèse

Whatever the mind can conceive and believe, it can achieve.

Napoleon Hill

Remerciements

L'achèvement du travail qui va suivre n'aurait pu voir le jour sans l'aide et le soutien précieux que m'ont apporté de nombreuses personnes dont une partie figure sur cette page, et à qui je vais tenter d'exprimer toute ma gratitude sans toutefois parvenir à la moitié de ce qu'elles méritent.

Mes remerciements vont en premier lieu à mon directeur de thèse, Hubert Perrot, pour sa disponibilité et son aide très précieuse tout au long de la thèse, même lorsque cela devait se faire à distance. Je souhaite également remercier chaleureusement mon co-directeur, Gérard Bidan, pour ses conseils avisés et le temps précieux qu'il m'a accordé. Par le biais de nos discussions, Gérard et Hubert ont tous deux su m'apporter soutien, savoir-faire et rigueur scientifique.

Mes remerciements vont également au labex MATISSE et au CEA pour avoir financé ces travaux, ainsi qu'à Frédéric Chandezon et Sandrine Lyonnard pour m'avoir si bien accueilli au sein du SyMMEs/STEP.

J'aimerais exprimer ma profonde gratitude à David Aradilla pour m'avoir épaulé et encouragé avec tant d'intensité pendant ces trois dernières années. Merci pour toutes les connaissances que tu m'as apportées et pour ton adaptabilité avec ma façon de faire. C'était un honneur d'être ton premier doctorant. Un immense merci également à Ozlem Sel pour ton engouement, ta disponibilité et ton aide lors de chacune de mes venues au LISE.

Pour leurs apprentissages et l'immense aide qu'ils m'ont apporté dans la synthèse des électrodes, je remercie profondément Pascal Gentile, Marc Delauney, Catherine Debiemme-Chouvy et Florence Billon. Je tiens également à remercier Stefano Mossa, Laurent Gonon et Vincent Mareau pour nos discussions très enrichissantes.

Merci infiniment Natacha, Laurent et Joao, les doctorants sur qui la France compte, pour tous ces moments incroyables qui ont rendu l'environnement de cette thèse tellement plus vivant. Et à tous mes amis et collègues de Grenoble, Nicolas, Adrien, Christopher, Anthony, Rémi, Émilie, Clément, Hakima, Lucille, Jérôme, Dominic et Gontran, ainsi que Élise et Wanli à Paris, mille merci pour tous ces superbes moments passés, ces repas enjoués, ces sorties sportives et ces moments plus décontractés qui ont tous joué un rôle essentiel dans ma thèse. Un grand merci à Martine Chaduc, Charles Picot, Joëlle Paparella et Sarah Mauduit pour leur aide lors de mes nombreuses missions.

Au-delà de l'aventure de ces trois dernières années, j'emprunte ces quelques lignes pour transmettre à tous mes amis qui m'ont soutenu, à tous ceux avec qui nous avons partagé des moments inoubliables, à ma famille, et à toi Jade, que mon cœur est à vous et vous sera pour toujours reconnaissant.

General table of contents

Abbreviation list

AC: Areal Capacitance

***ac*:** Alternating Current

ACN: Acetonitrile

ATP: Adenosine Triphosphate

BET: Brunauer-Emmett-Teller

CA: Activated Carbon

CAES: Compressed Air Energy Storage

CDC: Carbide Derived Carbon

CEA: Commissariat à l'Energie Atomique et aux Energies Alternatives

CNT: Carbon Nano-Tube

CV: Cyclic Voltammetry

CVD: Chemical Vapor Deposition

ECR-CVD: Electron Cyclotron Resonance-Plasma Enhanced Chemical Vapor Deposition

ECW: Electrochemical Window

EDL: Electrochemical Double Layer

EDLC: Electrochemical Double Layer Capacitor

EDOT: 3,4-Ethylenedioxythiophene

EIS: Electrochemical Impedance Spectroscopy

EMI-TFSI: 1-Ethyl-3-methylimidazolium bis(trifluoromethylsulfonyl)imide

EQCM: Electrochemical Quartz Crystal Microbalance

EQCM-D: Electrochemical Quartz Crystal Microbalance with Dissipation monitoring

ERGO: Electrochemically Reduced Graphene Oxide

ESR: Equivalent Series Resistance

FEG: Field Emission Gun

FEGSEM: Field Emission Gun Scanning Electron Microscopy

FRA: Frequency Response Analyzer

FTIR: Fourier Transform Infrared Spectroscopy

GCD: Galvanostatic Charge-Discharge

GF: Graphene Foam

IHP: Inner Helmholtz Plane

LAES: Liquid Air Energy Storage

LISE: Laboratoire Interfaces et Systèmes Electrochimiques

LPCVD: Low Pressure Chemical Vapor Deposition

MEMS: Micro Electro-Mechanical Systems

MPE: Mass Per mole of Electrons

MSC: Micro-Supercapacitor

NMR: Nuclear Magnetic Resonance

NW: Nanowire

OHP: Outer Helmholtz Plane

OLC: Onion-Like Carbon

PC: Propylene Carbonate

PECVD: Plasma-Enhanced Chemical Vapor Deposition

PEMS: Pulsed Electrochemical Mass Spectrometry

ppm: Parts per million

PPy: Polypyrrole

PRI: Pinnacle Research Institute

pzc: Potential of Zero Charge

pzmc: Potential of Zero Mass Change

QCM: Quartz Crystal Microbalance

RF: Radio Frequency

RFID: Radio Frequency Identification

SEI: Solid Electrolyte Interface

SEM: Scanning Electron Microscopy

SiC: Silicon Carbide

SiCNW: Silicon Carbide Nanowire

SiNP: Silicon Nano-Particle

SiNTrs: Silicon Nano-Trees

SiNW: Silicon Nanowire

SLS: Solution-Liquid-Solid

SMES: Superconducting Magnetic Energy Storage

STEM-EELS: Scanning Transmission Electron Microscopy- Electron Energy Loss Spectroscopy

TF: Transfer Function

TOF-SIMS: Time-Of-Flight Secondary Ion Mass Spectrometry

TPD-MS: Temperature-Programmed Desorption coupled with Mass Spectroscopy

VAGNA: Vertically Aligned Graphene Nanosheets Array

VLS: Vapor Liquid Solid

VOGN: Vertically-Oriented Graphene Nanosheet

XPS: X-ray Photoelectron Spectroscopy

Scientific notations

$GaPO_4$: Gallium phosphate

Me_3NHTFSI: Trimethylammonium bis(tetrafluoro-methylsulfonyl)imide

Me_3STFSI: Trimethyl-sulfonium bis[(trifluoromethyl)sulfonyl]imide

N_{1114}TFSI: Butyltrimethylammonium bis(trifluoromethylsulfonyl)imide

NEt_3H-TFSI: Triethylammonium bis(tetrafluoromethylsulfonyl)imide

PANi: Polyaniline

PEDOT: Poly(3,4-ethylenedioxythiophene)

PIP_{13}-FSI: N-methyl-N-propylpiperidinium bis(fluorosulfonyl)imide

PYR_{13}-TFSI: N-methyl- N-propyl-pyrrolidinium bis(trifluoromethanesulfonyl)imide

PYR_{14}-TFSI: N-butyl-N-methylpyrrolidinium bis(trifluoromethanesulfonyl)imide

$PYRNO_3$: Pyrrolidinium nitrate

TBA: Tetrabutylammonium

General Introduction

If we had the ability to see inside any complex material at the molecular level, what could be seen? If this material stores energy by adsorbing ions at it's surface what dynamics could be observed? Advanced microscopy techniques can be used to monitor nanometer-scale details on static and rigid samples, however only numerical simulations and a few characterization techniques can be used to understand the ionic fluxes at the interface between an electrode and an electrolyte.

Supercapacitors are high power density and highly stable energy storage solutions based on the electro-adsorption of ions at the surface of an electrode. Various characterization techniques have been used to understand these ionic exchanges and several models have been developed to describe them. Among these techniques, electrogravimetric measurements use the combination of electrochemical and microbalance analysis to obtain key information about the exchanged species and the dynamics of the system.

Vertically-oriented nanostructuration of supercapacitor electrodes drastically improves their performances as the accessible electrode surface increases along with good electronic conduction to the current collector. Yet, the electrogravimetric study of supercapacitor electrodes has only been performed with materials deposited in a relatively flat manner on a microbalance.

Throughout this Ph.D. work, we have explored the adaptability of electrogravimetric techniques to various types of vertically-oriented nanostructures for supercapacitors and the challenges inherent with such a combination. In some cases we could not overcome these challenges, but in the other cases very valuable information about the ionic exchange mechanisms have been obtained.

Chapter 1:
State of the art

Table of contents

I. Energy storage and supercapacitors

Storing energy is a prerequisite for living organisms to thrive, as there is no life form consuming energy without storing it in some form. Plants store photons energy in the form of sugar molecules. Animals transform this sugar into highly energetic Adenosine Triphosphate (ATP) molecules to store energy. Human societies thrived as they used new energy-rich materials like coal, petroleum, gas fuels or uranium, which act as both the source and the storage medium for energy. During the 20^{th} century, electricity became the main transport method to bring energy from the power plants to households. However each of the energy-rich materials used to produce energy requires a low-efficiency transformation in large power plants to produce electricity and cannot be used reversibly to store energy once again. Moreover, such consumption-based energy sources tend to be slowly replaced by renewable forms of energy due to environmental concerns and the urge to cut down CO_2 emissions. Each of these facts triggered a global demand on multi-scale energy storage solutions that could reversibly store electricity.

This chapter presents a panel of solutions to store electrical energy to then focus on supercapacitor devices. The basic principles that drive these devices will be presented along with the advantages of electrode nanostructuration. To characterize and better understand the electrochemical processes at the interface of supercapacitor electrodes, electrogravimetric techniques will be introduced.

I-1. Storing electrical energy

Storing electrical energy on a large scale is a cornerstone to the energetic transition due to the necessity to solve the gap between intermittent energy production and consumption. Photovoltaic plants and wind turbines are on the front line of renewable energies due to their rapidly dropping costs, with the disadvantage of being intermittent sources of electric energy [1]. To gradually replace the current power plants with such energy sources, energy storage solutions must be installed at the grid and the household levels. For grid level energy storage, more than 330 MWh must be installed to have enough energy for 10.000 people in USA for 1 day [2]. At the household level, residential utility customers in USA consume an average 30 kWh per day.

For middle scale applications, storing electrical energy allows the use of electrical power in transportation without a connection to the grid. As opposed to conventional fuel engines, electric motors do not emit harmful gases, are much more efficient, last for much longer with no maintenance and allow the use of renewable energies. Electric bikes, cars, trucks and prototype airplanes use batteries to store energy. A typical electric bike will store around 500 Wh of energy, while an electric car stores around 50 kWh to last for 350 km [3]. Renewable hydrogen production, storage and use in fuel cells are others alternatives but with still much higher costs.

In the smaller scale, portable electronic devices have experienced a massive expansion in every domain of modern life that could not have been possible without a portable source of electricity. Such devices, like smartphones, watches, laptops, e-readers, toys, MP3 players, used to work with non-reversible alkaline batteries that had to be replaced regularly. However the huge evolution in the Li-ion battery technology has enabled the use of rechargeable batteries in most of these applications. The stored energy ranges from around 0.1 Wh for watches to around 10 Wh for smartphones and 50 Wh for laptops respectively.

Figure I-1: Scales in energy storage needs: **a)** Grid or household level. **b)** Transportation. **c)** Portable electronics. **d)** Micro-devices. Images from [3]-[11].

With recent research progress in the field of wirelessly operating micro-devices, the need to store energy at an even smaller scale arises. Wireless sensor networks (WSNs), implantable medical devices, and active radio frequency identification (RFID) systems, all rely on micrometer scale energy storage solutions directly integrated within the micro-device. Micro-supercapacitors offer a reliable solution for such applications, with many advantages over batteries such as easier integration in microdevices, better cycling lifetime (millions of cycles), ultra-fast charge-discharge rates (ms), excellent efficiency and reversibility, and higher power density [12]. For higher energy density needs, micro-batteries are also being investigated.

To tackle this wide range of needs for electrical energy storage (**Fig. I-1**), a large variety of methods can be used. Electricity, a flow of electrical charges, can only be stored in its pure form using Superconducting Magnetic Energy Storage (SMES) [13]. However due to high costs and technological challenges this energy storage solution is still rarely used. To store electrical energy in a more practical manner, it needs to be transformed into a more stable form. This can be achieved in several ways (**Fig. I-2**), which are described as follow:

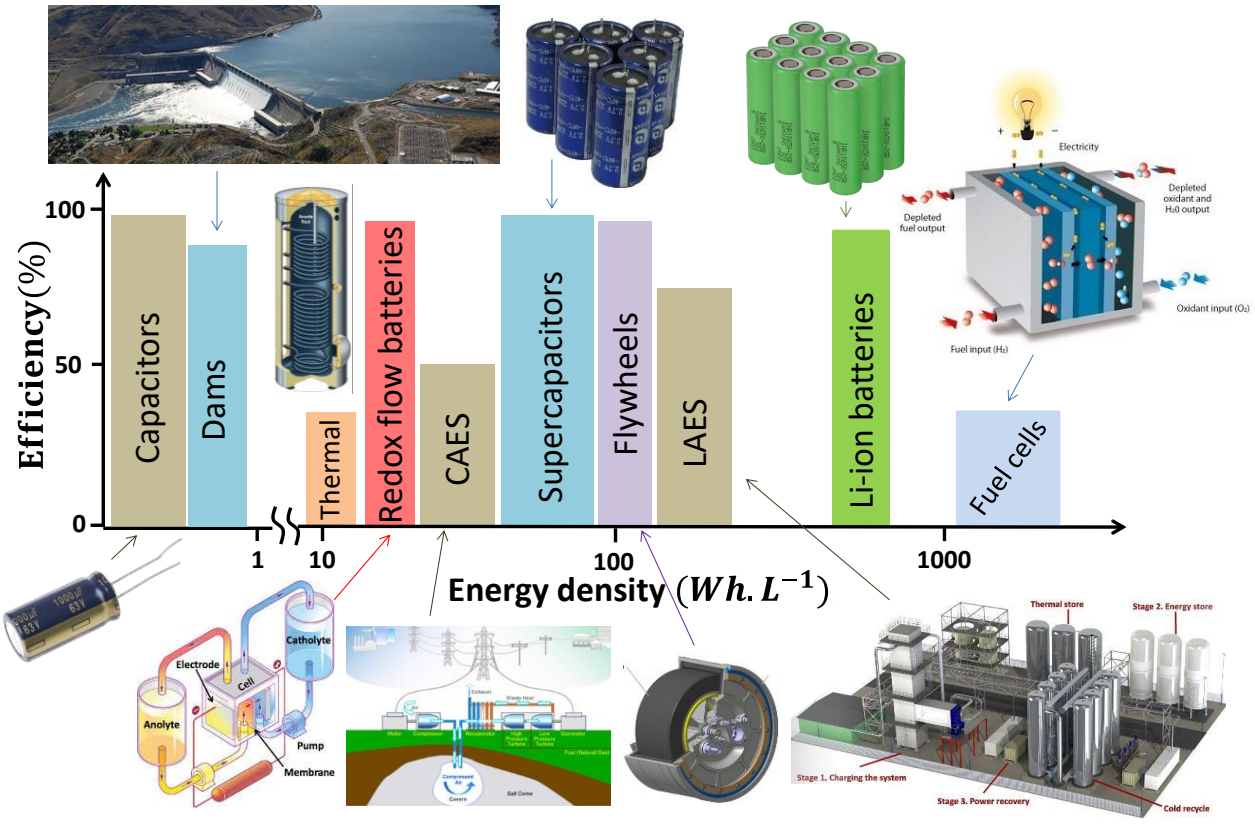

Figure I-2: Reversible energy storage solutions at various scales of energy density. Images from [14]-[22].

i. Mechanically, with the transformation of electrical energy into mechanical motion with reversible electrical motors that can store the energy in various ways: Using water's potential energy (dams), compressed air energy storage (CAES), inertial energy (flywheels) or strain energy (springs). Except for CAES, such systems have a good transformation efficiency in both directions (~90%) but very low energy density. Flywheels can store around 100 $Wh.kg^{-1}$ of energy [23]. The Grand Coulee dam in US (168 m high) can deliver 6.495 GW of power with a peak flow of 4300 $m^3.s^{-1}$, which is equivalent to an energy density around 0.4 $Wh.L^{-1}$ [24]. In the case of CAES, the energy density is much larger (around 50 $Wh.L^{-1}$), however the overall efficiency is lower (~50%). This efficiency can be increased up to 70% in adiabatic systems that also store the heat produced during air compression [25].

ii. Thermally, by heating a large volume with a resistance or a heat pump. This leads to a good efficiency in the heating process (~100%) but a very low efficiency to transform the heat into electricity (up to 40% depending on heat difference between the two thermal sources). The specific heat capacity of liquid water is around 1.2 $Wh.L^{-1}.K^{-1}$ [26]. These low energy densities are greatly increased when harnessing the phase change of a material. In liquid air energy storage (LAES), air is cooled down to reach the liquid phase and stored in tanks with energy densities around 180 $Wh.L^{-1}$. Sophisticated LAES systems using hot and cold thermal stores are being developed by Highview Power in the UK to store energy from the grid with efficiencies around 70% [27].

iii. Electrochemically, with batteries that store energy through redox reactions between the electrodes and an electrolyte. This is the best-know electrical energy storage solution, with astonishing developments in the field of Li-ion batteries leading to energy densities around 690 Wh L^{-1} with around 90% efficiency [28]. The main drawbacks of such batteries are the relatively low power densities (around 500 $W.kg^{-1}$) and the capacity loss after around 1000 cycles, especially if the battery is charged and discharged rapidly. Alternatively, redox flow cells are sometimes used for grid energy storage due to their longer lifetime, but with lower energy density (around 50 $Wh.L^{-1}$) [29]. Electrolysis of water can also be used to produce hydrogen (70-80% efficiency) which can then be transformed back to electricity in fuel cells (40-60% efficiency) [30]. The use of platinum in both electrolysis electrodes and fuel cells and the difficulty to store high pressure H_2

make this solution expensive, but leads to the current highest energy density for storing and restoring electrical energy (around 2500 $Wh.L^{-1}$ for H_2 at 700 bar).

iv. Electrostatically, using capacitors that store electrical energy through the electrostatic attraction between charges of opposite sign. Common capacitors, used in electronic circuits, can operate at high voltages (up to 100 V) and power (>10 000 $W.kg^{-1}$) while being very durable, but they have low energy densities (around 0.06 $Wh.L^{-1}$ for electrolytic capacitors) [31].

For small scale applications, a huge gap can be observed between the highly energetic but low power Li-ion batteries and the low energy but high power electrolytic capacitors. Another kind of energy storage devices, called supercapacitors, fills this gap with an intermediate energy density from 2 to 100 $Wh.L^{-1}$ while keeping a high power density (>6000 $W.kg^{-1}$). Supercapacitors belong to both the electrostatic and the electrochemical types of energy storage, with many advantages over batteries [12]:

- They can last millions of cycles with no degradation.
- They can be made from very abundant materials such as carbon and silicon.
- They can operate in a wider range of temperatures, typically from -40°C to 80 °C.
- They do not contain hazardous materials and therefore do not present risks of explosion.

The following work will now focus on this rising energy storage solution that can be categorized into three main families: Electrochemical double layer capacitors (EDLCs), pseudo-capacitors and hybrid capacitors (**Fig. I-3**).

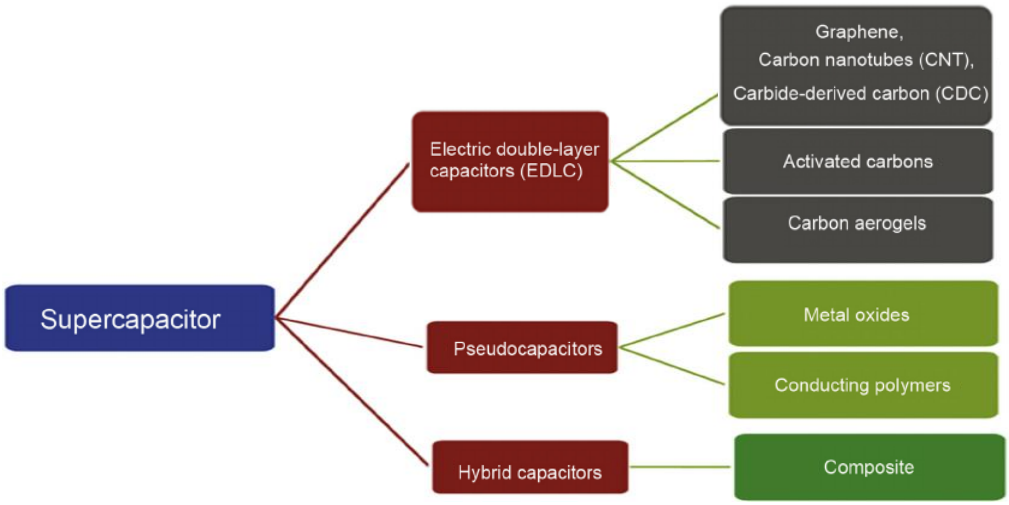

Figure I-3: Supercapacitor families, adapted from [32].

I-2. History of supercapacitors

The basic principles of electrochemical double layer capacitors (EDLCs) were firstly described by Hermann von Helmholtz, who introduced the electrical double-layer model in 1853 [33]. The idea remained theoretical for a century, until H. Becker developed a "Low voltage electrolytic capacitor with porous carbon electrodes" at General Electric in 1957, without knowing about the electrical double-layer [34]. This work was only continued in 1970 with a patent of an “Electrolytic capacitor having carbon paste electrodes” by Donald L. Boos for the Sohio Corporation [35]. Based on activated carbon in a non-aqueous electrolyte, this device was commercialized as a “Supercapacitor” in 1971 by the Japanese company NEC as power supply for computer memory. Similar devices were then commercialized by Panasonic in 1978 (the “Gold Capacitor”) and ELNA in 1987 (the “Dynacap”) [36].

A lower internal series resistance and higher capacitance was obtained by Brian Evans Conway’s group with RuO_2 electrodes between 1975 and 1980. These 10-100 fold higher energy storage performances were achieved with a combination of electrical double-layer and highly reversible faradaic processes, opening a new branch of supercapacitors: Pseudo-capacitors. Nevertheless, military research in the Pinnacle Research Institute (PRI) on EDLCs with a lower internal resistance led to the first high power supercapacitors called “PRI Ultracapacitors” in 1982. This work was carried on by Maxwell laboratories in 1992 with a renewed interest in supercapacitors for their applications in hybrid vehicles [36].

The third branch of supercapacitors, hybrid capacitors, consists of capacitors with asymmetric electrodes combining electrostatic and electrochemical properties. They were firstly introduced in 1994 with the development of high voltage "Electrolytic-Hybrid Electrochemical Capacitor" by David A. Evans [37]. Further works in this field by FDK Corporation led to lithium-ion capacitors in 2007 [38]. Nowadays, commercial supercapacitors are available from a number of sources, such as Maxwell Technologies, Panasonic, NessCap, LS Mtron, and le groupe Bolloré as the main involved companies [36].

I-3. Common applications for supercapacitors

Supercapacitors can provide a large amount of power in a relatively short time, along with a very high number of charge/discharge cycles and a longer lifetime than batteries. These versatile attributes led to their incorporation in a wide range of applications.

In the transportation industry, supercapacitors are used to deliver high bursts of power to electric and hybrid cars and buses, to recover brake energy (**Fig. I-4a**), to enhance stop-start fuel-saving systems, or to start massive motors in military vehicles among others. In Shanghai, an electric bus uses supercapacitors as it's only means to store energy, with enough capacity to go from one stop to another (3-6 km) and recharging the supercapacitors (50% charge in 30 s and 100% in 80 s) at each stop using a pantograph (**Fig. I-4c**) [39]. The same principle is used in some tramways to power them in short sections with no overhead line (**Fig. I-4d**).

An equivalent use of these high power capabilities is made in some hybrid cranes, forklifts and tractors, where supercapacitors are used as energy buffers that are discharged during peak demands in mechanical power (**Fig. I-4b**) [40], [41].

Grid-level energy management is also an important application field for supercapacitors. Short high power consumption events on the grid such as the fast charge of an electric vehicle create spikes of electricity demand that reduce the efficiency of the grid. Supercapacitors could be used to efficiently reduce these spikes and obtain much smoother consumption curves [42].

The possibility to easily downscale supercapacitors also leads to their potential application in various types of electronic micro-devices. With the generalization of Radio Frequency Identification (RFID), Micro Electro-Mechanical Systems (MEMS) (**Fig. I-4e**), bio-sensors (**Fig. I-4f**) and implantable medical devices, important developments of such micro-systems could appear in the near future. In the context of these developments, maintenance-free energy storage solutions that can be charged fast and deliver large amounts of power would be highly beneficial.

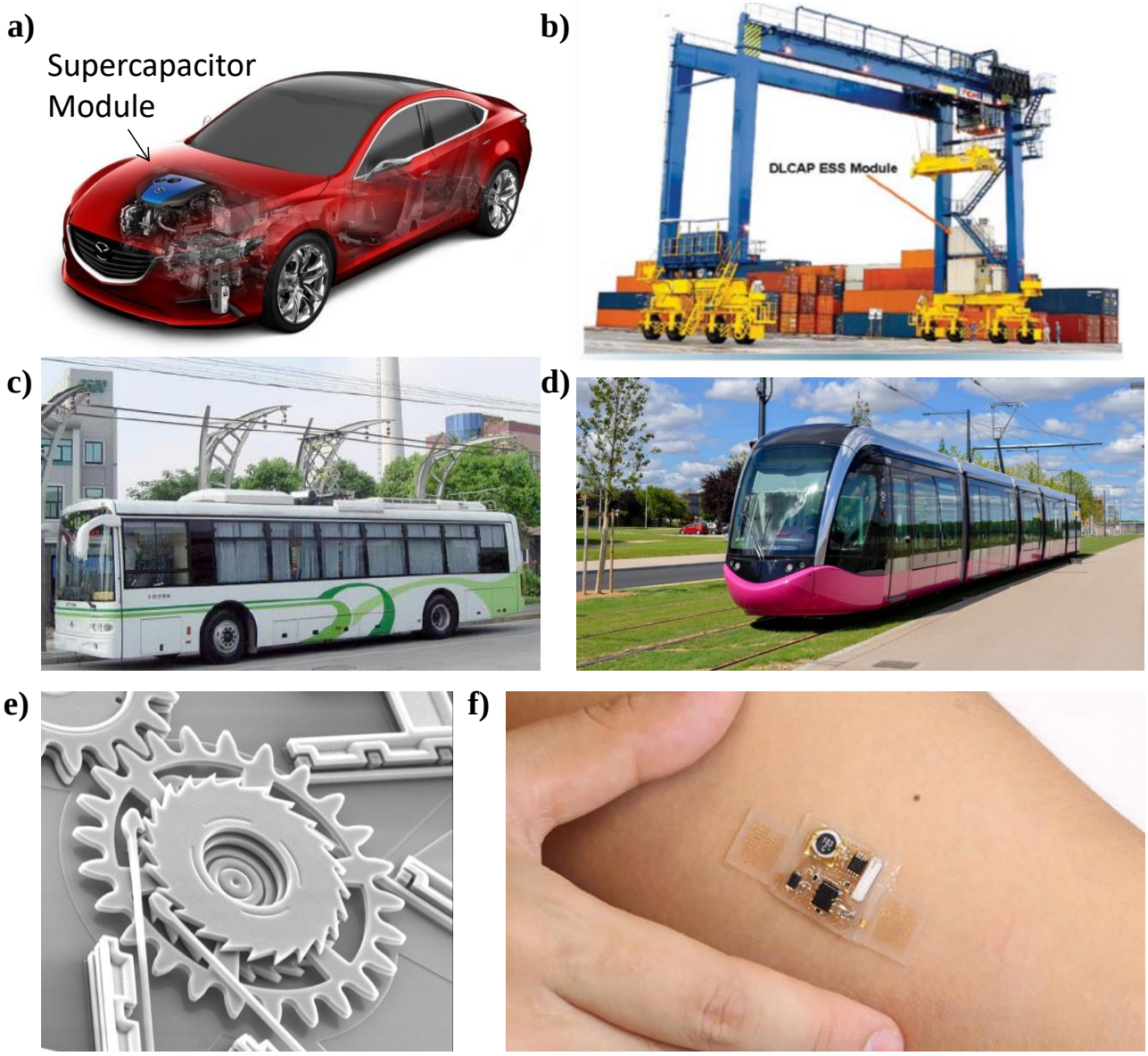

Figure I-4: Range of supercapacitor applications: **a)** Breaking energy recuperation by Mazda. **b)** Hybrid-electric crane. **c)** Supercapacitor electric bus in Shanghai. **d)** Tramway. **e)** MEMS **f)** Bio-sensors. Images from [32],[43]-[47].

Combined with energy harvesting devices such as solar, thermal, vibrational, radiofrequency or biological micro-generators, supercapacitors could be used as main energy sources to power the electrical components. Supercapacitors also offer the possibility of on-chip integration on very small surfaces (<0.1 mm²), increasing the ease of development and speed of deployment. Active RFID devices, wireless sensor arrays, implantable micro-sensors and micro-robots all require a miniaturized form of energy storage that supercapacitors can provide [12], [48]–[50].

I-4. Working principles

I-4.i. Electrochemical double layer capacitors (EDLCs)

The basic mechanisms governing the overall behavior of a supercapacitor take place at the interface between the electrode and the electrolyte. In the case of EDLCs, except for parasitic reactions there are no net charge transfers between the electrode and the electrolyte. The electrode can be considered as an ideal polarizable electrode, also called a blocking electrode. When this electrode is dipped into an electrolyte and submitted to an applied potential, an electrical double layer appears at the electrode/electrolyte interface. The applied potential φ^e, triggers the apparition of a charge q^e at the surface of the electrode, which attracts oppositely charged ions from the electrolyte. These ions are concentrated in a region of the electrolyte close to the electrode, creating an opposite charge $q^s = -q^e$ near the electrode surface to respects the electric neutrality of the system [51]–[54].

The model created by Hermann von Helmholtz is a first approximation theorizing this system where the attracted ions form a layer at the surface of the electrode called the "Helmholtz layer" (**Fig I-5a**). As this region is composed of two layers of opposite charges, the behavior of the electrode/electrolyte interface is similar to a dielectric capacitor. In this model, the potential varies linearly from φ^e at the electrode surface to φ^s, the potential in the solution, at a distance d from the surface. By analogy with a dielectric capacitor, the capacitance of this double layer can be calculated using the following equation:

$$C = \frac{\varepsilon_0 . \varepsilon_r . S}{d} \qquad \textbf{(Eq. I-1)}$$

With ε_0 the permittivity of free space, ε_r the relative permittivity within the Helmholtz layer (often assimilated to that of the electrolyte), *S* the electrode surface and *d* the distance between the electrical centers of the opposite charges. Despite the extreme simplicity of this model, it will be shown in the following section that this equation can explain that nanostructuration is one of the main improvement paths for supercapacitors.

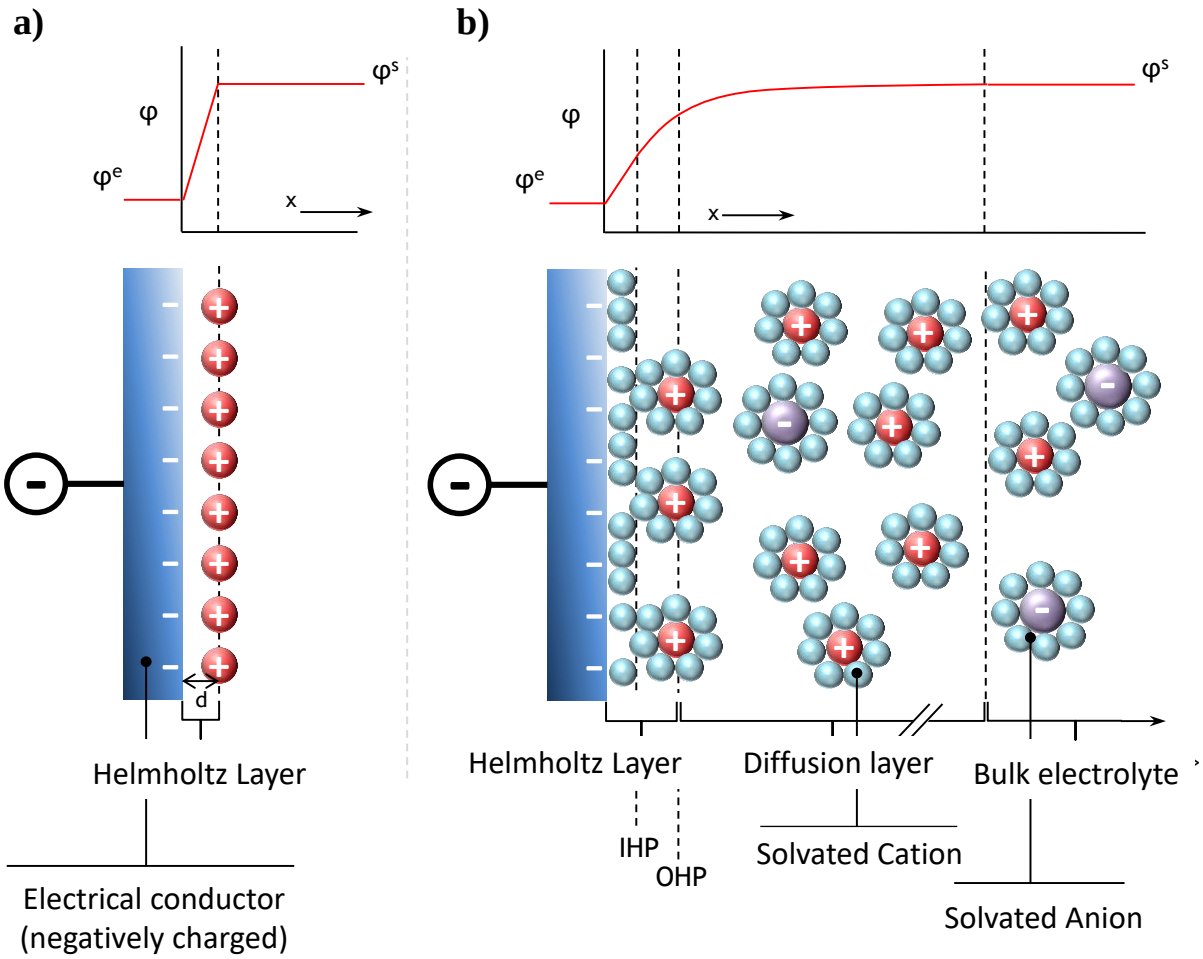

Figure I-5: a) Simplified electrical double layer model from Helmholtz. **b)** More precise model from the work of Gouy, Chapman, Stern, Grahame. Adapted from [52].

In order to enhance this model, the double layer can be described by Gouy and Chapman's model, further improved by Stern and Grahame to take into account the solvation, the diffusion and the adsorption of ions (**Fig. I-5b**). Indeed, for a real double layer system, ions and solvent molecules are subject to thermal agitation that induces their diffusion, reorganizing them following a Maxwell-Boltzmann distribution. Furthermore, the geometry of ions and solvent molecules, as well as their adsorption (specific or not) to the surface will modify the structure of the double layer. Ions and solvent molecules will thus form a structure on the electrolyte's side of the interface consisting of several layers described in **Fig. I-5b**:

- A first layer composed of ions and solvent molecules specifically adsorbed at the surface of the electrode. This layer extends from the electrode surface to the Inner Helmholtz Plane (IHP).

- A second layer composed of solvated ions is located at the closest distance possible to the electrode, at the Outer Helmholtz Plane (OHP).
- A diffusion layer where ions of opposite charge compared to the electrode are attracted by electrostatic interactions and spatially distributed by thermal agitation in the electrolyte.
- Far from the interface, a complete screening of the electrode's charges is obtained with ions from the previous layers. The electrolyte in this region is unmodified compared to the unpolarized state.

This model can be simplified by considering the two first layers united as a single charged layer. In this case the potential varies almost linearly from the electrode surface to the OHP, then as a decreasing exponential from the OHP to the unmodified region of the electrolyte where the potential reaches φ^s. The overall capacitance C of the electrode can then be estimated as a combination of the capacitance C_H due to the Helmholtz layer and the component C_d due to the diffusion layer:

$$\frac{1}{C} = \frac{1}{C_H} + \frac{1}{C_d} \qquad \textbf{(Eq. I-2)}$$

The thickness of the diffusion layer can vary depending on the electrolyte's ionic concentration. It is generally below 10 nm for ionic concentrations above 10^{-2} mol.l^{-1} and often approximated to the electrolyte's Debye length [52], [55]. For planar surfaces, EDLCs can achieve a specific capacitance from 1 to 50 µF.cm^{-2} depending on the electrode material [51], [55]. However a given material will seldom have a planar surface at the nanometer scale, with porosity and surface roughness that can change the potential at the interface and force the partial desolvation of ions [56], [57]. These structural dependencies, coupled with the difficulty to evaluate the effective relative permittivity ε_r and the thickness of the double layer, make the *ab initio* derivation of specific capacitance for a given material and electrolyte extremely complex [55].

The capacitive behavior of the electrical double layer is linked to the charge accumulation in the electrode, which is directly proportional to the applied potential difference φ^e - φ^s, following the equation:

$$\Delta Q = C.(\varphi^e - \varphi^s) \qquad \textbf{(Eq. I-3)}$$

where ΔQ is the charge accumulation and C is the capacitance of the electrode.

When two identical electrodes described by the previous models are combined into the same electrolyte, a complete supercapacitor device is formed. The working principles of these devices are depicted in **Fig. I-6**. In the uncharged state and with an open circuit configuration (**Fig. I-6a**), there is no potential difference between the electrodes because they are identical. A layer of adsorbed ions and solvent molecules is observed on both electrode surfaces and their charge is compensated by the reorganization of ions within the electrolyte. When a potential difference ΔU is applied between these two electrodes, cations and anions will migrate in opposite directions (**Fig. I-6b**). For both sides, the electrical double layers previously described are formed and behave like two capacitors in series. With C_1 the capacitance of the first double layer and C_2, the second, the total capacitance of the supercapacitor C_{tot} can be calculated with equation:

$$\frac{1}{C_{tot}} = \frac{1}{C_1} + \frac{1}{C_2} \qquad \textbf{(Eq. I-4)}$$

If both double layers present the same capacitances ($C_1 = C_2 = C$), then $C_{tot} = \frac{C}{2}$. The charge accumulation for each electrode can then be derived with the equation:

$$\Delta Q = C_{tot}.\Delta U \qquad \textbf{(Eq. I-5)}$$

During the discharge process the ions move in the opposite direction to return to the initial configuration while generating a usable current. An equivalent electrical circuit can be used to describe the overall system, with the capacitances C_1 and C_2 in series and an equivalent series resistance (ESR) (**Fig. I-6d**). The ESR accounts for the unavoidable resistance of the electrical contacts, the double layer and the electrolyte. For each interface, leakage currents can appear which are taken into account by the parallel resistances R_{f1} and R_{f2}.

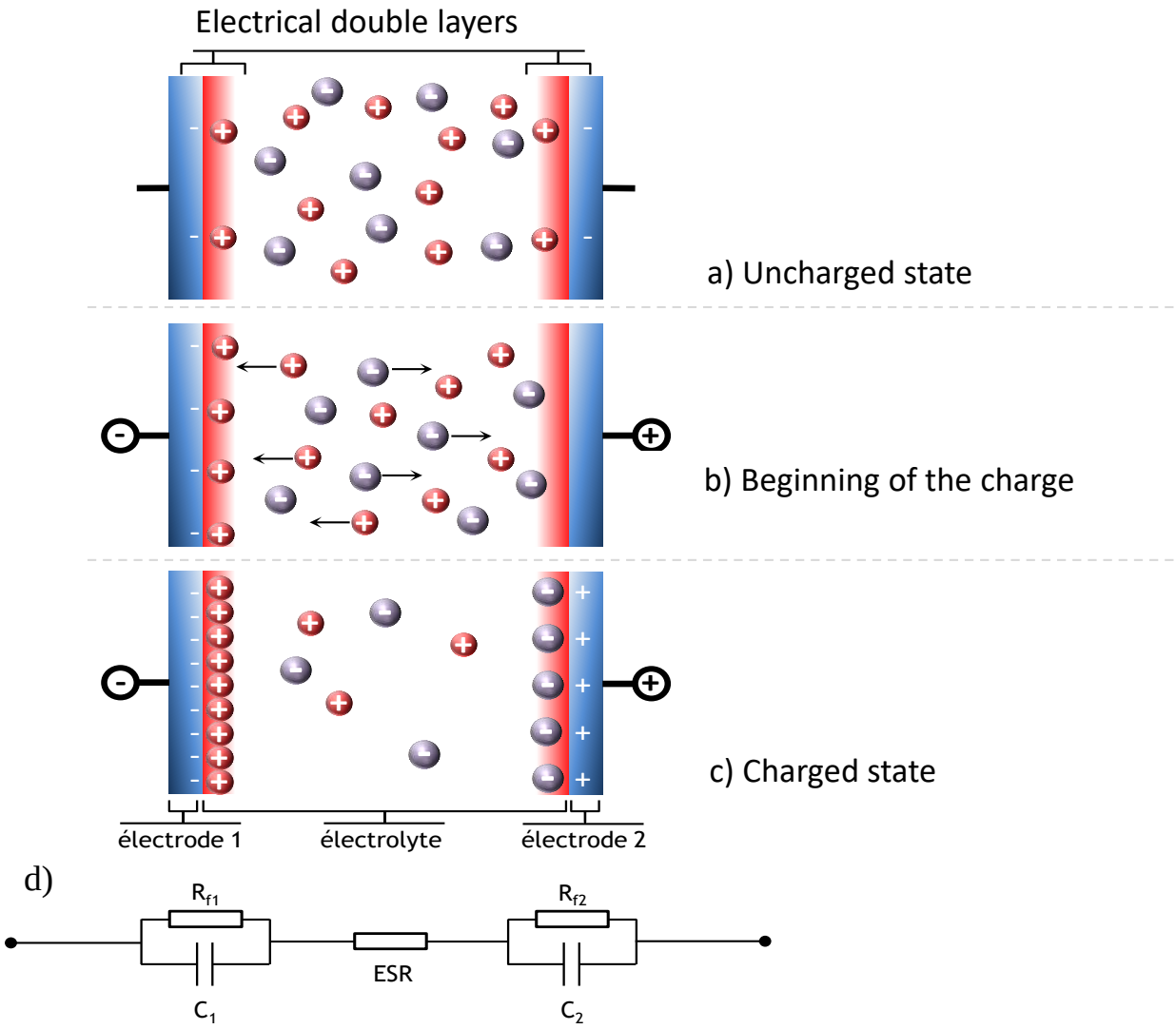

Figure I-6: a) b) c) Schematic representation of the charging process in EDLC devices and **d)** the corresponding equivalent circuit. Adapted from [52],[53].

The energy stored in a supercapacitor can be derived using the same equations as conventional capacitors:

$$E = \frac{1}{2} C_{tot} . \Delta U_{max}{}^2 \qquad \textbf{(Eq. I-6)}$$

where ΔU_{max} is the maximal potential difference that can be applied to the electrodes.

Moreover, the theoretical maximal power output of the supercapacitor while retaining 50% efficiency can be derived from the equivalent circuit:

$$P_{max} = \frac{\Delta U_{max}{}^2}{4. ESR} \qquad \textbf{(Eq. I-7)}$$

The accumulation of charges at an electrode/electrolyte interface is one of the simplest ways to store electrical energy reversibly. Unlike most battery systems, EDLCs can be discharged with no lower potential limit to prevent electrode degradation and perform millions of charge/discharge cycles while retaining most of their capacitance. Furthermore, as the underlying mechanism is simply based on the movement of ions from the electrolyte to the electrode surface, EDLCs can be charged and discharged very fast and thus provide large power densities.

I-4.ii. Pseudo-capacitors

The term pseudo-capacitance, introduced initially by Conway [58], is used to describe electrode materials that display a capacitive behavior and store charges with electronic transfers (faradaic reactions) rather than the electrostatic accumulation of ions in an electrical double layer.

Fast reversible redox reactions are possible with a variety of electrode materials that can achieve much higher energy densities than EDLCs by allowing faradaic reactions to occur simultaneously with the double layer mechanisms. The most common pseudo-capacitive materials are transition metal oxides and metal nitrides (RuO_2, MnO_2, VN, TiN…), hydroxydes and electroactive conductive polymers (PEDOT, PPy, PANi…). For example ruthenium oxide, that has been extensively studied in literature due to its large capacitance, can reach oxidation states between +II and +IV in contact with a proton conductive electrolyte [53]. An applied potential will trigger successive redox reactions of the RuO_2 electrode to switch from an oxidation state to another, allowing an electrochemical accumulation of stored charges near the surface. In the case of RuO_2, the stored charge depends linearly on the applied potential, with no redox peaks observed on a cyclic voltammogram. The higher capacitance that these mechanisms allow compared to EDLCs often come at the cost of the ionic exchange kinetics, with faradaic reactions being slower than electrostatic attraction of ions. Moreover, a small proportion of parasitic irreversible reactions can intervene and slowly degrade the electrode at each cycle. This means that pseudo-capacitors will typically provide less power density and last for less cycles than EDLCs.

Pseudo-capacitive materials store energy using faradaic mechanisms, making the frontier between pseudo-capacitors and batteries very thin. In order to distinguish both energy storage fields, Thierry Brousse *et al.* have proposed that a material could be called “pseudo-capacitive” if the charge stored depends linearly of the applied potential [59]. If this linearity is respected, the

voltammograms will present a rectangular shape and a capacitance value can be extracted using **Eq. I-5**. **Fig. I-7** presents a comparison between voltammograms obtained with Ni-based classical faradaic systems (**Fig. I-7a**) and a pseudo-capacitive material such as MnO_2 (**Fig. I-7.b**). Pseudo-capacitance can also be found as an extrinsic behavior in materials that could be used in bulk as battery electrodes, but exhibit pseudo-capacitive properties once used in thin layers (**Fig. I-8**) [60].

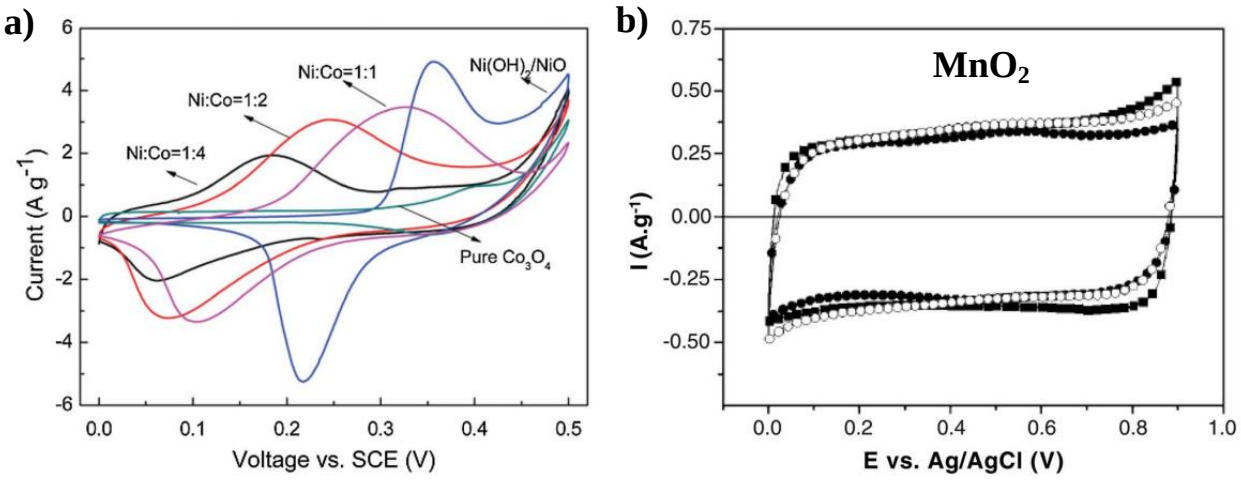

Figure I-7: Cyclic voltammetry results for various oxides and hydroxides: **a)** Purely faradaic behavior, typical for batteries. **b)** Rectangular shaped voltammogram of MnO_2 electrodes, characteristic of pseudo-capacitive materials. [59]

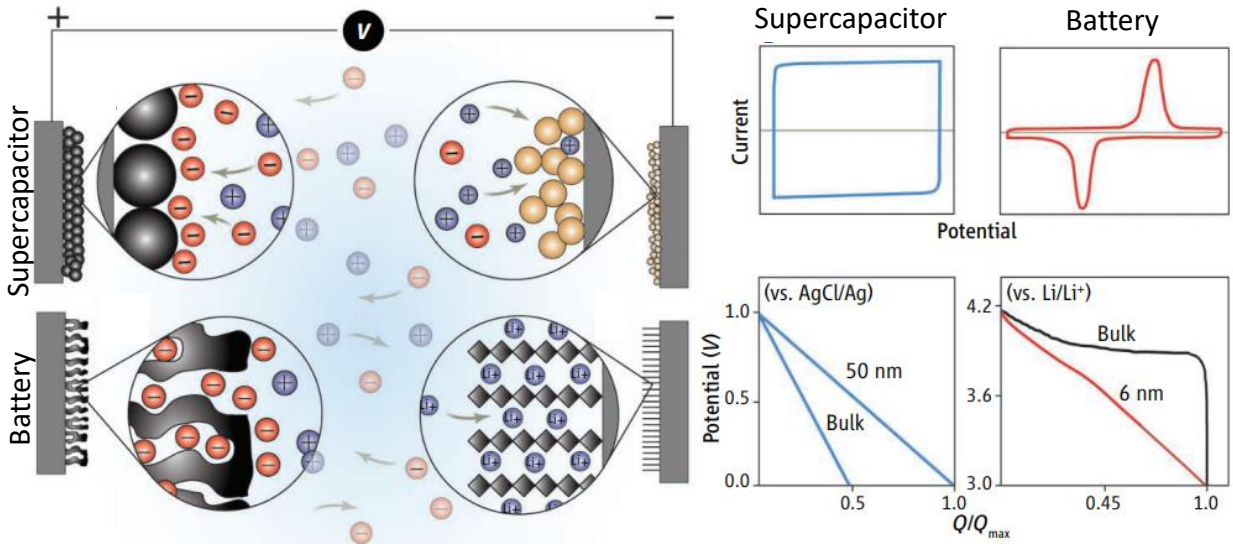

Figure I-8: Illustration comparing the behavior in supercapacitors and batteries, with typical response shapes for each case. [60]

I-4.iii. Hybrid supercapacitors

Both of the previous types of supercapacitors had a symmetric configuration: both electrodes are made from the same material. A new type of supercapacitors called “Hybrid capacitors” has been imagined without this symmetry, with two different types of electrodes working in synergy. The combination of an electrical double layer electrode with a pseudo-capacitive electrode is an interesting solution to obtain intermediate performances between EDLCs and pseudo-capacitors. Such capacitors can take advantage of the high stability of a double layer system while achieving higher capacitance values due to faradaic exchanges on one of the electrodes [55]. Similarly, electrical double layer electrodes can be combined with battery electrodes to obtain intermediate capacitance and stability performances between supercapacitors and batteries. Hybrid capacitors are currently being actively investigated to create the future breakthrough supercapacitors with high energy and power density along with long cycling stability [61]–[64].

I-5. Electrolytes for supercapacitors

The characteristics of a supercapacitor device are strongly linked to both electrode and electrolyte composition. The electrochemical and thermal stability, the ion concentration, the ionic conductivity, the toxicity and the inflammability of the electrolyte drive a large part of the overall properties of a supercapacitor. For a given set of electrodes, the choice of the proper electrolyte is restricted to electrically insulating and chemically inert solutions with a good wettability of the electrode surface.

The electrochemical stability window of the electrolyte determines the maximal operating potential ΔU_{max}. According to **Eq. I-6** and **Eq. I-7**, the energy and power densities of a supercapacitor are proportional to ${\Delta U_{max}}^2$ and can thus be greatly increased with a larger electrochemical window. The ionic conductivity of the electrolyte, which drives the ESR, is directly linked to the maximal power density.

Aqueous, organic and ionic liquids-based electrolytes are the three main classes of electrolytes used for supercapacitor applications. Their respective properties are presented in **Table I-1**.

Type	Aqueous	Organic	Ionic liquid
Electrochemical window*	0.5-1 V (1.23 V)	2.5-3V (3-3.5 V)	3.0-4.0 V (3.0-6.0 V)
Ionic conductivity at 25°C	>400 $\mathrm{mS.cm^{-1}}$	10-50 $\mathrm{mS.cm^{-1}}$	<15 $\mathrm{mS.cm^{-1}}$
Viscosity at 25°C	1 mPa.s	0.3-2.5 mPa.s	50-300 mPa.s
Thermal stability	-20°C ; +80°C	-50°C ; +70°C	-50°C ; +300 °C
Capacitance with activated carbon electrodes	150-300 $\mathrm{F.g^{-1}}$	100-200 $\mathrm{F.g^{-1}}$	60-140 $\mathrm{F.g^{-1}}$
Toxicity	Low	High	Under investigation
Inflammability	None	High	Very low
Cost	Low	High	Very high

* Electrochemical window typically found in literature, with between parenthesis the values obtained with Pt or vitrous carbon electrodes.

Table I-1: Comparison between the three main classes of electrolytes used for supercapacitors. Adapted from [95].

Aqueous electrolyte solutions are the most convenient to use, with many examples in literature of acidic (for example sulfuric acid), basic (using potash) or neutral solutions (Na_2SO_4, KCl, etc.) used for supercapacitors. The higher ionic conductivity of aqueous electrolytes leads to higher specific capacitance values and lower ESR, however the electrochemical stability window of such electrolytes is small compared to organic solutions: 0.5-1 V.

Organic electrolytes are composed of a salt dissolved in an organic solvent such as propylene carbonate (PC) or acetonitrile (ACN). Their ionic conductivity is lower than that of aqueous electrolytes, leading to lower specific capacitance and higher ESR. This is compensated by an electrochemical window around three times larger than aqueous electrolytes: 2.5-3 V. The thermal stability is also wider, with demonstrated operation of supercapacitors at -40°C [25]. Commercially available supercapacitors mostly use organic electrolytes [50].

Finally ionic liquids, composed of salts with a fusion temperature below 100°C, have gained a lot of attention in the last couple of decades for their benefits in batteries and supercapacitors due to their large electrochemical window (3-4 V) and high temperature stability [54]. On the other hand the ionic conductivity of ionic liquids is lower than organic electrolytes, resulting in higher ESR. In chapter 3-II-2 a mixture of an ionic liquid, butyltrimethylammonium bis(trifluoromethylsulfonyl)imide ($N_{1114}TFSI$), and an organic solvent (PC) is investigated at various ratios to obtain an electrolyte with a higher ionic conductivity while maintaining the electrochemical window at 3.5 V.

II. Nanostructured electrodes for supercapacitors

Ever since H. Becker developed the first supercapacitor electrodes based on porous carbon in 1957, the research of new types of electrode materials has rapidly escalated. With the basic understanding of an EDLC that led to **Eq. I-1**, it appears that the capacitance achieved by such supercapacitors is proportional to the electrode's surface. In the case of pseudo-capacitors, the fast reversible redox reactions happen close to the electrode surface, and therefore capacitance is also enhanced with accessible surface. It was then rather clear that large surfaces accessible to the electrolyte and low resistivity to the current collector were essential to increase the performance of supercapacitors. To obtain both of these properties on the limited surface of a current collector, the deposited electrode materials have to be either porous or nanostructured. A large variety of nanostructured materials have widely been developed for supercapacitor applications. Among them, in this section, a special focus will be devoted to carbonaceous, silicon and conductive polymer electrodes due to their great potential for EDLCs and pseudo-capacitors [12], [65].

II-1. Carbon-based electrodes

Carbonaceous materials are the most represented in the field of EDLCs, in both commercial devices and recent research for new double layer electrodes. This predominance is not only due to the full-carbon start in supercapacitor history, but also to the panel of advantages that carbon presents for EDLC electrodes compared to other elements [52], [66]–[68] as for example:

- It's natural abundance in the environment.
- The variety of its allotropes and the excellent control over the various structures that can be achieved.
- The low mass density of these various allotropes.
- Its relatively high electrical conductivity (from 0.5 to 10 $S.cm^{-1}$ for active carbon and up to 1000 $S.cm^{-1}$ for carbon fibers) [53].
- The ease of fabrication, along with low prices depending on the allotropes.
- Its low chemical reactivity in contact with common electrolytes.

Nowadays, most commercial EDLC electrodes are made from activated carbon, which is obtained by high temperature activation of a carbon precursor that can be recovered from organic waste or industrial by-product. The simplicity of this procedure makes activated carbon the cheapest supercapacitor electrode material. Presented as a powder, activated carbon presents a high specific surface area (up to 3000 $m^2.g^{-1}$) and a large porosity (around 1 $cm^3.g^{-1}$). Depending on the electrolyte used, these materials can display an areal capacitance of 5 to 20 $\mu F.cm^{-2}$ (50 to 100 $F.cm^{-3}$ and 100 to 200 $F.g^{-1}$ relative to carbon volume and mass) [55].

Carbide derived carbon (CDC) is another highly porous carbonaceous material actively studied for EDLC electrodes, as it presents a very conductive carbon mesh with finely tuned nano-pores that can go below 2 nm in diameter. Made by high temperature chlorine treatment that eliminates heteroatoms from carbides, CDCs are compatible with clean room processes and can thus be integrated on micro-devices. By tuning the mean pore size, CDCs have been used to study the effect of porosity on capacitance and desolvation of ions upon electroadsorption [57], [69], [70].

Material	Carbon onions	Carbon nanotubes	Graphene	Activated carbon	Carbide derived carbon	Templated carbon
Dimensionality	0-D	1-D	2-D	3-D	3-D	3-D
Conductivity	High	High	High	Low	Moderate	Low
Volumetric Capacitance	Low	Low	Moderate	High	High	Low
Cost	High	High	Moderate	Low	Moderate	High
Structure	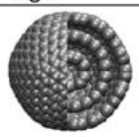	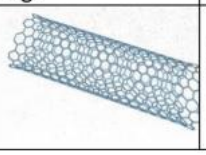	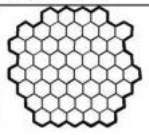	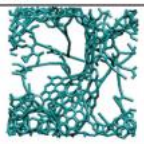	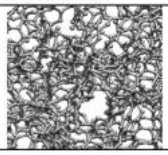	

Figure II-1: Comparison of various porous and nanostructured carbon materials for supercapacitor applications. Adapted from [67].

Porous carbon materials result in high developed surfaces at low fabrication cost. However ions do not always have access to the entire pore network, with some parts not accessible to the electrolyte. Consequently, nanostructured carbon materials with various dimensionalities have been developed to enhance both the electrical conductivity and the electrolyte accessibility to the electrode surface (**Fig. II-1**). Onion-like carbon (OLC) electrodes are made from zero-dimensional (0D) carbon nanoparticles within a conductive binder. A few nanometers in diameter, these nanoparticles are usually prepared by annealing diamond

nanopowders in vacuum or argon. With their high electrical conductivity and a fully accessible specific surface area around 500-600 $m^2.g^{-1}$, OLC electrodes can provide very high power densities but a limited capacitance (around 30 $F.g^{-1}$) [67].

Carbon nano-tubes (CNTs) are 1D carbonaceous materials known for their very high conductivity and tensile strength. Their use in EDLC electrodes has been extensively studied over the past decade, and more specifically for small diameter single-walled CNTs [71]. With an average specific surface area of 1000 $m^2.g^{-1}$ and a capacitance around 50-70 $F.g^{-1}$, CNTs exhibit high power densities like OLCs but still do not yet compete with porous carbon in terms of energy density [67]. They can also be used as a substrate in composite electrodes where the CNTs are covered with pseudo-capacitive materials to achieve high capacitance values [72]–[75].

Graphene, a 2D single layer of carbon atoms arranged in an hexagonal matrix, is the strongest material ever created since its discovery in 2004 by Geim and Novoselov. With its exceptional electronic conductivity of 10^6 $S.cm^{-1}$, good chemical stability and specific surface area over 2600 $m^2.g^{-1}$, graphene has attracted a lot of attention in recent years for its potential use in the energy storage field. In particular, as-grown graphene can be used as EDLC electrode material with very high power densities and capacitance values around 100 $F.g^{-1}$ in non-aqueous electrolytes [41]. However these results were obtained with graphene grown without any structure design, an essential feature that affects the reaction kinetics, the accessibility of the electrolyte and the optimization of the current collector surface. The main challenge for designing graphene-based electrodes is to grow thicker electrodes (to use less current collector surface) and avoid restacking of the graphene sheets during preparation [41], [76]. To face this challenge, two main types of 3D graphene nanostructures have been synthetized (**Fig. II-2**): Graphene foams (GFs) and "Vertically aligned graphene nanosheets arrays" (VAGNAs), also called "Vertically-oriented graphene nanosheets" (VOGNs) [76].

The former, GFs, can be synthetized using various techniques like chemical vapor deposition (CVD) on a sacrificial template [77]–[79], hydrothermal assembly [80] or high-temperature graphitization [81], [82] (**Fig. II-2a-f**) respectively. These electrodes offer very large accessible specific surface areas and globally exhibit capacitance values around 250 $F.g^{-1}$ at current densities larger than 1 $A.g^{-1}$.

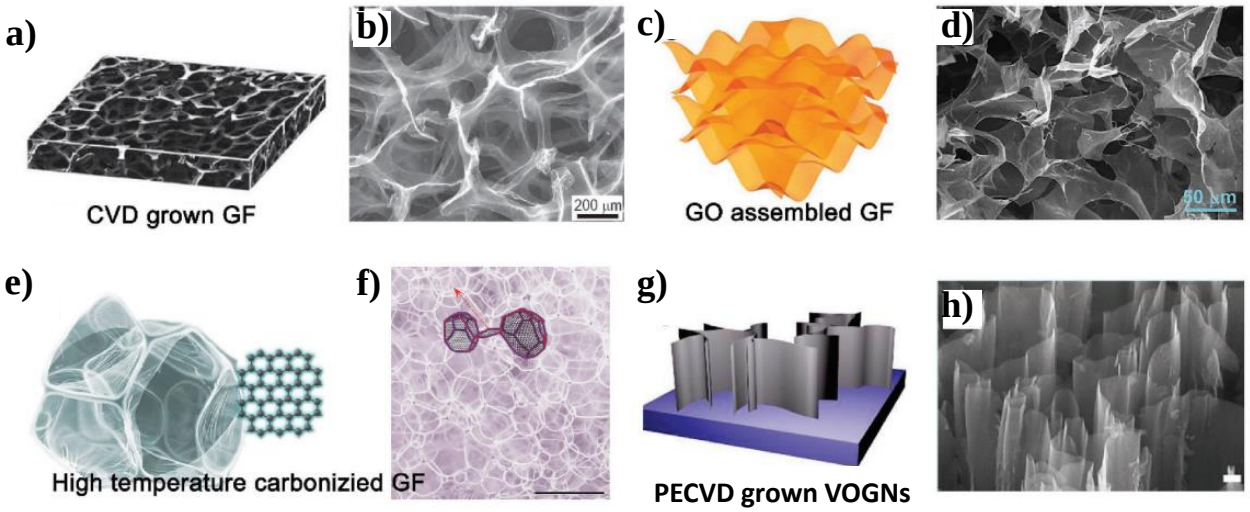

Figure II-2: Illustrations and Scanning Electron Microscopy (SEM) images of 3D graphene architectures: **a-b)** CVD grown GF. **c-d)** Graphene oxide assembled. GF **e-f)** High temperature carbonized GF. **g-h)** PECVD grown VOGNs. [76]

The latter, VOGNs, are generally synthetized with plasma-enhanced chemical vapor deposition (PECVD) on various substrates without metal catalysts. Several atom-thick graphene nanosheets perpendicular to the substrate are obtained in a dense array that presents many advantages over graphene foams (GFs) [76]:

- The graphene nanosheets end with sharp edges which are beneficial for electrocatalytic applications.
- Every graphene nanosheets is directly grown on the substrate, allowing an efficient charge transfer from the current collector to the graphene.
- The structural robustness of the graphene nanosheet array prevents from aggregation.
- VOGNs can easily be decorated or uniformly functionalized with other active materials.
- The synthesis is made at lower temperatures than GFs (from 300 to 800 °C), allowing the use of a larger variety of substrates. It will be shown in chapter III that this point is crucial for our work.

The vertical orientation of the graphene nanosheets offers a large surface-to-volume ratio with an open access for the electrolyte, resulting in higher areal capacitance values than in plane or lateral architectures (**Fig. II-3**) [76]. But in order to use this surface efficiently, the wettability of the VOGN structure has to be optimized. A study by X. Shuai *et al.* has shown that smaller

intersheet distances lead to enhanced wettability due to larger capillarity pressure [83]. VOGNs grown with direct current plasma source PECVD, with an average intersheet distance of 20 nm, led to specific capacitance values around 150 $F.g^{-1}$ in an aqueous electrolyte. In comparison VOGNs grown with micro-wave PECVD have an intersheet distance around 300 nm and exhibit highly hydrophobic properties leading to a specific capacitance around 80 $F.g^{-1}$ [83]. The nature of the electrolyte also has a big influence on wettability, with for example a better wettability of aqueous KOH solutions over K_2SO_4 solutions [84]. Propylene carbonate (PC) has a much higher wettability than water on graphite substrates with a contact angle of 31° in PC [85] versus 90° in water [86]. PC is a commonly used solvent for supercapacitor electrolytes despite a lower ionic conductivity than water, with the advantage of having a wide electrochemical stability window ranging from 2.5 to 3 V. The VOGN studies in this thesis will therefore be conducted with PC-based electrolytes.

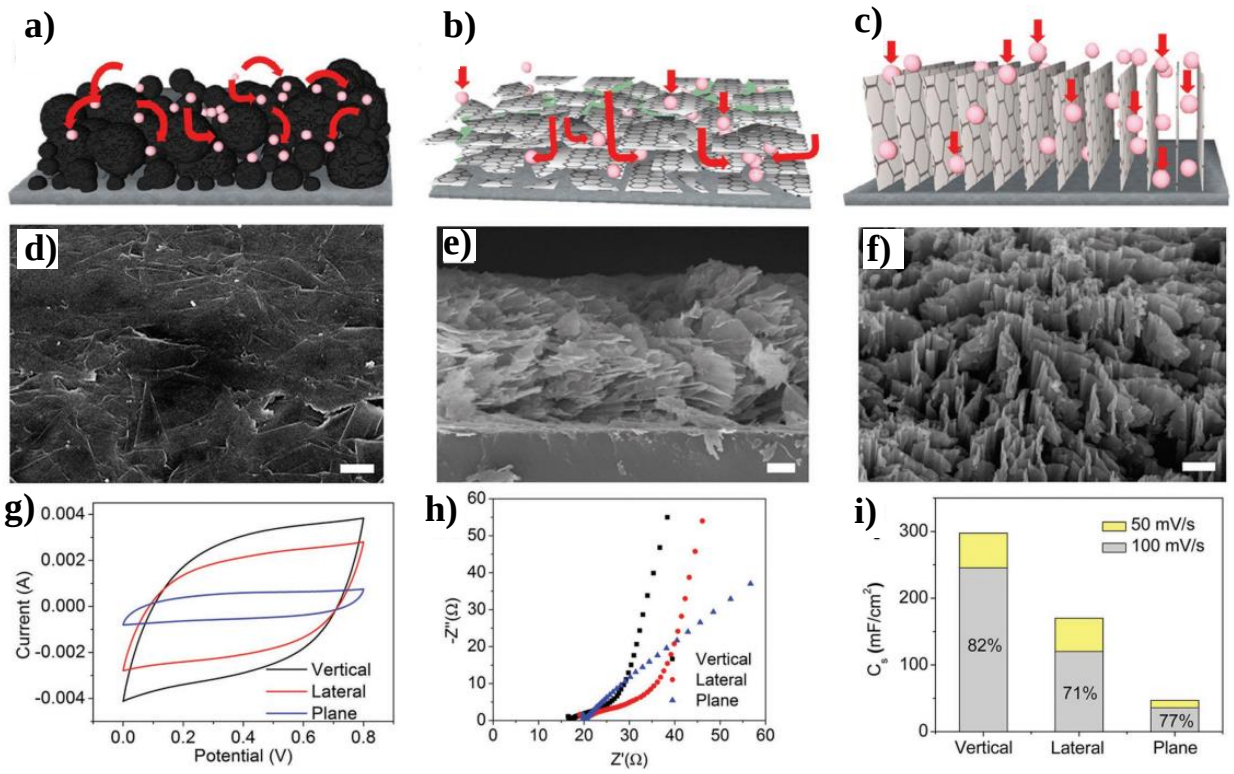

Figure II-3: Illustrations and SEM images of graphene architectures oriented **a,d)** in plane, **b,e)** laterally, **c,f)** vertically. **g)** Corresponding voltammograms. **h)** Electrochemical impedance spectroscopy (EIS) results. **i)** Areal capacitance values for each architecture. [76]

After the growth, applying an NH_3 plasma to the graphene nanosheets has been shown to introduce nitrogen atoms in the graphene lattice, resulting in N-doped VOGNs. This modification is shown to enable n-type conductivity, enhancing the VOGNs reactivity and reducing the equivalent series resistance (ESR) [76]. Supercapacitor devices based on N-doped VOGNs have shown a spectacular increase in specific capacitance, with up to 990 $F.g^{-1}$ at a power density of 14.8 $W.g^{-1}$ in an aqueous electrolyte [87].

Vertically-oriented graphene nanosheets (VOGNs) are currently developed by our team at CEA Grenoble with remarkable results in EDLCs using ionic liquid electrolytes, such as an areal capacitance of 2 $mF.cm^{-2}$ and a current density of 4 $mW.cm^{-2}$. Using ionic liquids presents the advantage of electrochemical stability over a very large potential window (around 4 V) [88]. Grown catalyst-free on any kind of substrate with a modified form of CVD, these VOGNs present both high surface and steady electron transfers as a result of the graphene's renowned conductivity and its direct contact to the current collector.

II-2. Silicon nanowire electrodes

A flourishing alternative to carbon based nanostructures relies on silicon for the conception of micro-supercapacitor electrodes. Compared to other electrode materials, crystalline silicon presents plenty of advantages for energy storage applications [89]:

- Silicon is compatible with micro-electronic fabrication processes. It is the most obvious element to use for on-chip applications.
- Crystalline silicon is a semi-conductor by nature, and it's electrical conductivity can easily be controlled with doping. High doping levels can lead to high electrical conductivity: Around 2000 $S.cm^{-1}$ with 1.3×10^{20} cm^{-3} boron dopant concentrations at room temperature [173].
- Silicon can resist very high temperatures (>500 °C). Ideal for its integration into microelectronics processes (e.g. solder reflow processes, high temperature heating of 240°C during 20s).
- The micro-device fabrication industry provides several methods to create 3D silicon microstructures, as for example lithography and plasma etching.
- Versatility of nanostructures (nanoparticules, nanospheres, nanoneedles, nanowires) as well as a great number of different synthesis methods.
- For Li-ion battery applications, silicon can be used as anode with a theoretical capacity of 3590 $mAh.g^{-1}$ at room temperature (almost ten times higher than graphite) [90].

However, a number of disadvantages are impeding the large scale use of silicon as electrode material:

- For EDLC applications, the double layer specific areal capacitance is between 1 and 5 $\mu F.cm^{-2}$ [91], [92], which is lower than carbon-based materials that achieve around 10 to 20 $\mu F.cm^{-2}$ [52].
- Silicon has a strong surface reactivity with water and oxygen, creating an isolating layer of silicon oxide in aqueous solutions. A thin 1-2 nm SiO_2 layer is also formed in air, decreasing the double layer capacitance. Silicon also easily adsorbs volatile organic compounds which then pollute its surface.

- For high surface-to-volume ratio architectures, the previous point will reduce the overall conductivity of the electrode due to the formation of SiO_2 on a larger surface.
- For battery applications, huge volume changes around 370% upon lithiation lead to structural pulverization of the electrode [90].

Despite these limiting factors, silicon has been extensively studied as electrode material for both supercapacitors and batteries, mainly in a nanostructured form. Nanostructured silicon can take various forms, with nanoporous silicon, silicon nanoparticles (SiNPs), silicon nanowires (SiNWs) and various 2D architectures. SiNPs and SiNWs have attracted a huge interest for their potential in Li-ion battery anodes as they can partially compensate the large volume changes upon lithiation **(Fig. II-4)** [89], [90]. For supercapacitor applications, SiNWs and silicon carbide nanowires (SiCNWs) are the most represented in literature.

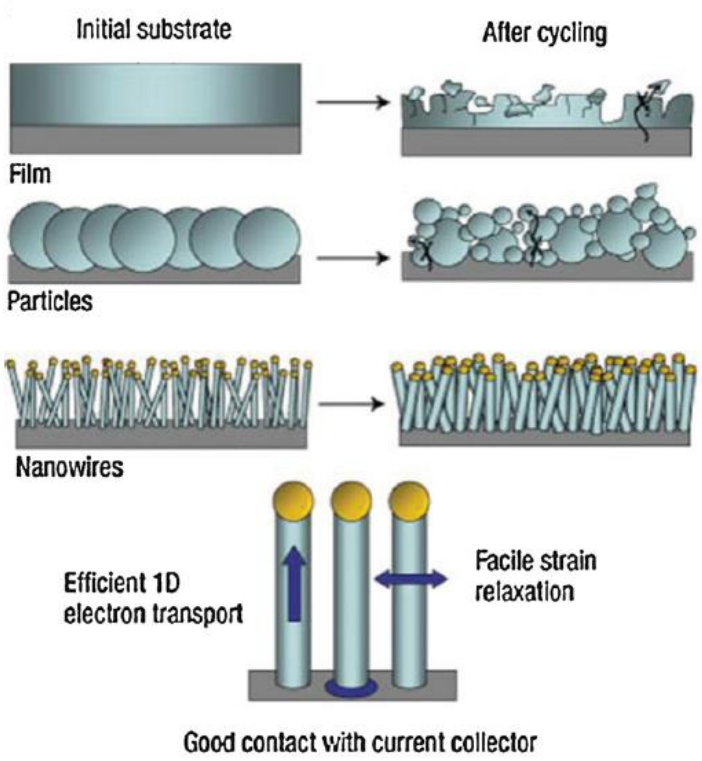

Figure II-4: Compensation for the large volume changes upon lithiation in various silicon architectures: Flat film, SiNPs, SiNWs. [93]

Crystalline SiNWs can be grown directly on silicon substrates with different processes which are adapted to today's micro-fabrication industry and thus simplify on-chip integration. Doped SiNWs grown on doped silicon wafers also impede electrical contact issues, each

nanowire's base being directly connected to the substrate. Moreover, large specific surface areas can be obtained with SiNWs if they are grown in a dense array. This surface can be further increased in silicon nano-trees (SiNTrs) by adding branches to each SiNW in an additional growth step (**Fig. II-5b**) [94].

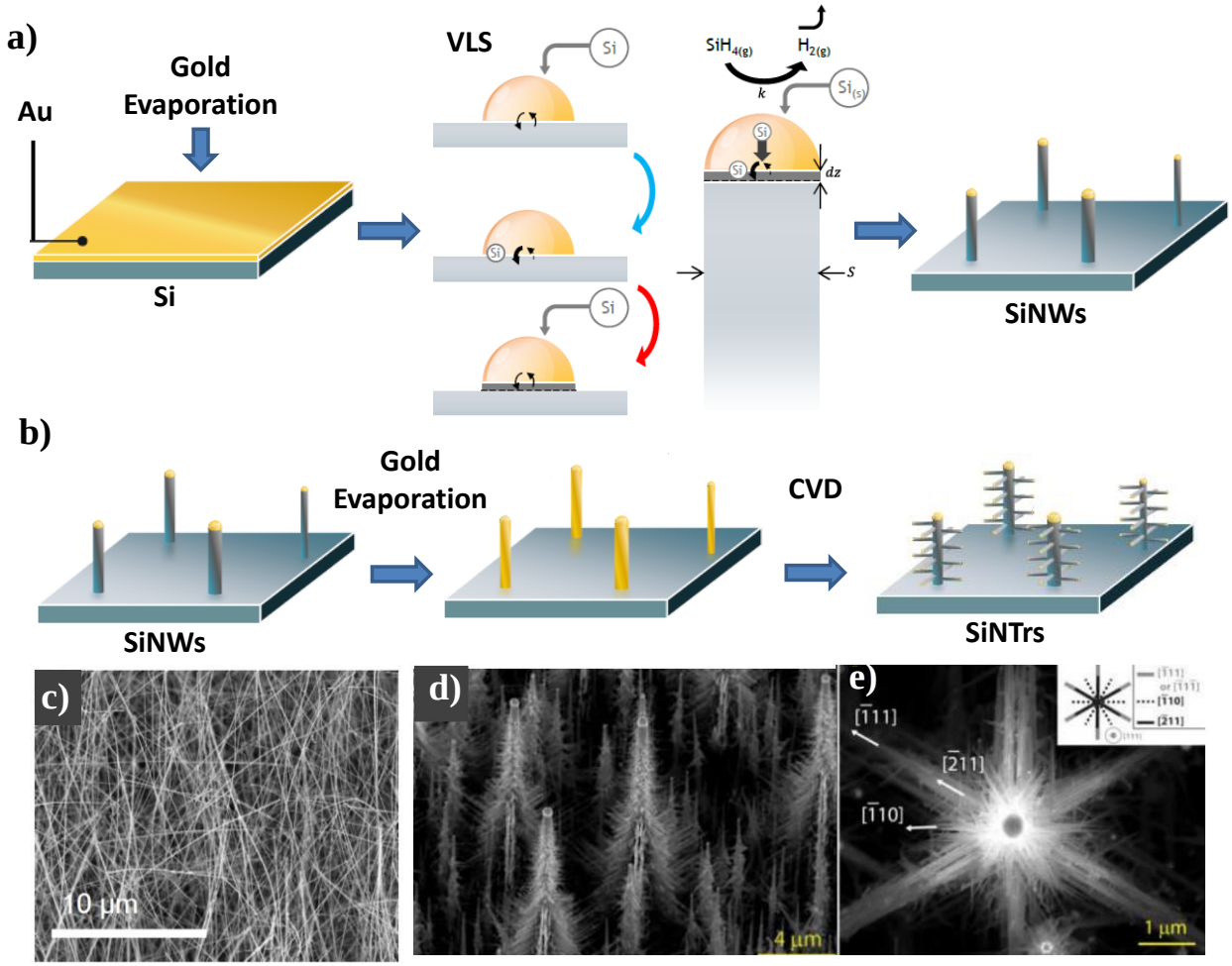

Figure II-5: a) Illustration of the CVD growth of SiNWs and the VLS mechanism. **b)** Process for growing branches on SiNWs to form SiNTrs. **c)** SEM images of SiNWs. **d-e)** SEM images of SiNTrs. Adapted from [95], [96].

These facts have led many research groups to investigate the potential of SiNWs and SiNTrs for EDLC applications [89]. There are various ways to obtain SiNWs that lead to different types of morphologies, either grown on a substrate or etched from a silicon wafer. Chemical vapor deposition (CVD) is the main method used to grow SiNWs, it is based on a catalyzed Vapor Liquid Solid (VLS) reaction taking place in a gas chamber. The catalyst most commonly used for this reaction is gold, which can be deposited as a thin film on the substrate by

evaporation or chemical deposition and then thermally dewetted to form nanoparticles of various diameters. As a result, a high density of SiNWs can be obtained ($\sim 3.10^9\ NW/cm^2$) with various nanowire diameters (20-200 nm) [97]–[99].

Another way of depositing the catalyst on the substrate consists in using a solution of gold colloids, followed by the annealing of the substrate. This method provides a lower density of SiNWs ($\sim 10^8\ NW/cm^2$) but the nanowire diameter is homogeneous and can be precisely chosen with the initial colloid diameters.

Alternatively, an electrochemical growth of SiNWs can be obtained on a conducting surface if a nanoporous template is first deposited on top of it. The template can then be dissolved to release the nanowires. Templateless chemical growth of SiNWs is also possible in solution with solution-liquid-solid (SLS) growth, leading to very thin nanowires that can then be collected as a powder [100].

SiNWs can be etched from a silicon wafer using two different mechanisms:

- Chemical or Electroless etching of SiNWs can be achieved with a metal catalyst, usually silver nanoparticles, and an HF etching solution [101], [102].
- Electrochemical etching can be achieved by applying a potential to the silicon substrate in a HF solution [103], [104].

Both etching mechanisms provide very dense porous SiNWs with an inhomogeneous diameter.

Uncovered SiNWs can be used as EDLC electrodes due to the absence of faradaic interactions with electrolyte ions. For such supercapacitors, the capacitance is proportional to the developed surface that ions can reach. This is verified by the values of specific capacitance obtained in literature for uncovered SiNW and SiNTrs electrodes, which are higher for longer or denser nanowires (**Table I-1**).

The addition of branches to SiNWs, making SiNTrs, also greatly increases the developed surface of the electrode. Such electrodes were able to provide a specific capacitance of up to 900 $\mu F.cm^{-2}$ in a 3-electrodes setup.

Type	Growth conditions	Length (µm)	Capacitance (µF/cm²)	Electrolyte	ΔE (V)	Réf.
N-doped SiNWs	CVD with colloids (50 nm)	5	26	NEt_4BF_4 + PC	0,8	[105]
N-doped SiNWs	CVD with colloids (50 nm)	20	105	NEt_4BF_4 + PC	0,8	[105]
N-doped SiNWs	CVD with dewetting	5	106	NEt_4BF_4 + PC	0,8	[105]
N-doped SiNWs	CVD with dewetting	50	440	NEt_4BF_4 + PC	0,8	[105], [106]
N-doped SiNWs	CVD with colloids (100 nm)	10	34	NEt_4BF_4 + PC	0,8	[91]
P-doped SiNWs	CVD with colloids (100 nm)	11	46	NEt_4BF_4 + PC	0,8	[91]
N-doped SiNWs	CVD with colloids (100 nm)	20	31	EMI-TFSI	4	[92]
N-doped SiNTrs	CVD with dewetting	50	900	NEt_4BF_4 + PC	0,9	[94]
P-doped SiNWs	CVD on porous Al_2O_3	3	110	NEt_4BF_4 + PC	1,5	[107]

Table I-1: Values of specific capacity for uncovered SiNW and SiNTr electrodes obtained in a 3-electrodes setup.

Two-electrode symmetrical devices have also been investigated with symmetrical uncovered SiNW electrodes. The specific capacitance obtained for such devices is lower than the 3-electrode equivalent, going for example from 440 µF.cm^{-2} in a 3-electrode setup to 51 µF.cm^{-2} for a two-electrode device with 50 µm long SiNWs grown by CVD with a dewetted gold layer as catalyst (**Table I-2**).

Symmetrical SiNTr electrode devices achieved higher capacitance values around 80 µF.cm^{-2}, but one particular device stands out with specific capacitance values three orders of magnitude higher. This particular device reported by J.W. Choi *et al.* is made from CVD-grown SiNWs that have been made porous after 5 cycles in Li-ion battery setup. As a result, a high developed surface of ~1070 m^2.g^{-1} and a high specific capacity of 45-90 mF.cm^{-2} is achieved [108]. However no information is given about the behavior under cyclic voltammetry or about the nanowire length, therefore it is unclear whether this device is purely an EDLC or if faradaic reactions occur.

Type	Growth conditions	Length (µm)	Capacitance (µF/cm²)	Energy density (µJ/cm²)	Power density (mW/cm²)	Cycling stability	Electrolyte	ΔE (V)	Réf.
N-doped SiNWs	CVD with colloids (50 nm)	50	23	190	182	75% at 10^6 cycles	PYR13TFSI	4	[109]
Porous SiNWs	CVD with dewetting + cycles as Li-ion battery	----------	45000 - 90000	36000-72000	11-22	----------	NEt4BF4 / LiPF6	2,5	[108]
P-doped SiNWs	CVD colloïdes (100 nm)	11	6,5	3	1,6	99,5% at 200 cycles	NEt4BF4 + PC	1	[91]
N-doped SiNWs	CVD with dewetting	50	51	37	----------	94,4% at 2000 cycles	NEt4BF4 + PC	0,8	[105]
N-doped SiNTrs	CVD with dewetting	50	67,5	66,2	49	97,9% at 10^6 cycles	EMI-TFSI + PC	1,4	[94]
N-doped SiNTrs	CVD with dewetting	50	58,3	262,4	225	82,5% à 10^6 cycles	EMI-TFSI + PC	3	[94]
N-doped SiNTrs	CVD with dewetting	50	83,9	60,4	45	98,8% at 10^6 cycles	NEt4BF4 + PC	1,2	[94]
N-doped SiNTrs	CVD with dewetting	50	73	210,2	180	78,3% at 10^6 cycles	NEt4BF4 + PC	2,4	[94]
P-doped SiNWs	CVD on porous Al_2O_3	6	34,1	272,8	400	90% at 4000 cycles	EMI-TFSI	4	[107]
P-doped SiNWs	CVD on porous Al_2O_3	3	16,5	16,2	16	99,4% at 3.10^5 cycl.	EMI-TFSI	1,4	[107]
N-doped SiNWs	CVD with colloids (50 nm)	35	16	128	4 (moy)	73% at 5.10^6 cycles	NEt3H TFSI	4	[110]

Table I-2: Electrochemical performances of uncovered SiNW and SiNTr electrodes obtained for two-electrode EDLC devices.

The predominant type of electrolyte used in literature with uncovered SiNW and SiNTr electrodes is an organic solution of triethylammonium bis(tetrafluoromethylsulfonyl)imide (NEt_4BF_4) + PC. This choice of an organic electrolyte instead of a more conductive aqueous one is driven by the high reactivity of silicon in water causing it to oxidize. The other alternatives to aqueous electrolytes investigated in literature are ionic liquids and mixtures of ionic liquids with organic solutions. Ionic liquids such as EMI-TFSI, PYR_{13}-TFSI or NEt_3H-TFSI offer the advantage of having a better stability for potential windows up to 4 V while organic electrolytes are limited to 2.5 V by oxidation. However, ionic liquids are more viscous and less conductive than organic electrolytes and will therefore decrease the capacitance obtained. A good balance between a better stability and a lower conductivity was found by mixing ionic liquids with an organic solution [94], [111]. More details will be given on the specific ratio that has been used in this thesis in chapter 3.

Type	Growth conditions	Length (µm)	Capacitance (µF/cm²)	Energy density (µJ/cm²)	Power density (mW/cm²)	Cycling stability	Electrolyte	ΔE (V)	Ref.
Three-electrode measurements									
SiC/ SiNWs	Etching (AgNO3+HF) + CVD	32	1700	850		95% at 1000 cycles	KCl	0,8	[112]
Diamond/ SiNWs	CVD colloids (50 nm) + MWCVD	5	105	84	0,94	93,3% at 10^4 cycles	PMPyrrTFSI +PC	4	[113]
C/SiNWs (porous)	Etching (AgNO3+HF) + Carbonisation	120	325000				EMIM-TFSI	0,7	[114]
TiN/SiNWs (porous)	Electrochemical etching + ALD	6	2600	1280	11,4	Bonne à 5500 cycles	TEABF4+PC	2	[116]
Final devices									
C/SiNWs (porous)	Etching (AgNO3+HF) + Carbonization	120	75000	100000	1	83% at 5000 cycles	EMIM-TFSI	0,8	[114]
Graphene/ SiNWs (porous)	Electrochemical etching + CVD	4	15300	91800	160		EMIBF4	2,7	[115]
C/SiNWs	Chemical etching + Evaporation Substrate: Ti/Au/Si	5	6800				H3PO4 + PVA solid	0,8	[117]
Diamond/ SiNWs	CVD dewetting + MWCVD	50	1500	15000	25	65% at 10^6 cycles	NEt3H TFSI	4	-

Table I-3: Electrochemical performances of covered SiNW electrode EDLCs.

To enhance the capacitive properties of SiNW electrodes, the deposition of various carbon derivatives can be achieved on the surface of SiNWs. The resulting nanowires are passivated, preventing their oxidation in air and allowing their use in aqueous electrolytes without forming an isolating SiO_2 layer. The various methods used to cover the silicon nanowires also improve the specific surface of the electrode, thus enhancing the areal capacitance. In the literature, SiNWs have been covered with amorphous carbon, silicon carbide (SiC), diamond and graphene with outstanding capacitive and stability performances (**Table I-3**).

Finally SiNWs can also been functionalized with pseudo-capacitive materials. Transition metal oxides such as MnO_2, NiO_2 and $Ni(OH)_2$ and conductive polymers like PEDOT and PPy have been used to cover SiNW and SiNTr electrodes to obtain SiNW-based pseudo-capacitors. The covered nanostructures present better characteristics compared to plain SiNWs in terms of structural stability and specific capacitance. The performance of these high energy density supercapacitors are presented in **Table I-4**. **Fig. II-6** presents a summary of the performances found for SiNW-based supercapacitors compared to activated carbon and onion-like carbon (OLC) in the form of a Ragone plot.

Type	Growth conditions	Length (µm)	Capacitance	Energy density (J/cm²)	Power density (mW/cm²)	Cycling stability	Electrolyte	ΔE (V)	Ref.
Three-electrode measurements									
NiO/SiNW	Catalytic Etching + Electrolessly deposited Ni + thermal oxidation	40	787,5 F/g			95% at 500 cycles	KOH	0,4	[118]
NiO/SiNW	Catalytic Etching + Electrolessly deposited Ni + thermal oxidation	20	681,04 F/g 360mF/cm²			97% at 1000 cycles	KOH	0,4	[119]
Ni(OH)2/ SiC NW	CVD/carbon + Electrochemical cathodic deposition		1724 F/g 3,31 F/cm²	0,5	1	70% at 500 cycles	KOH		[120]
Ni(OH)2/ SiC NW	CVD/carbon + Electrochemical cathodic deposition		1412 F/g 2,71 F/cm²	0,41	52,8	70% at 500 cycles	KOH		[120]
Ni(OH)2/ SiC NW	CVD/carbon + Electrochemical cathodic deposition		4,7 mF/cm²			90% at 1000 cycles	Solid KOH/PVA		[120]
Final devices									
PPy/SiNtrs	3 step CVD gold dewetting + Electrochem deposition	50	14 mF/cm²	0,015	0,8	80% at 5000 cycles 70% at 10000 cycles	PYR13TFSI	1,5	[121]
PEDOT/SiNWs	CVD gold colloids + Electrochem deposition	15	8 mF/cm²	0,009	0,8	80% at 3500 cycles	PYR13TFSI	1,5	[122]
MnO2/SiNWs	CVD gold colloids (50nm) + Chemical Bath Deposition	50	13 mF/cm²	0,032	0,388	91% at 5000 cycles	LiClO4-PMPyrrBTA	2,2	[123]

Table I-4: Electrochemical performances of functionalized SiNW/SiNTr/SiCNW electrode pseudo-capacitors.

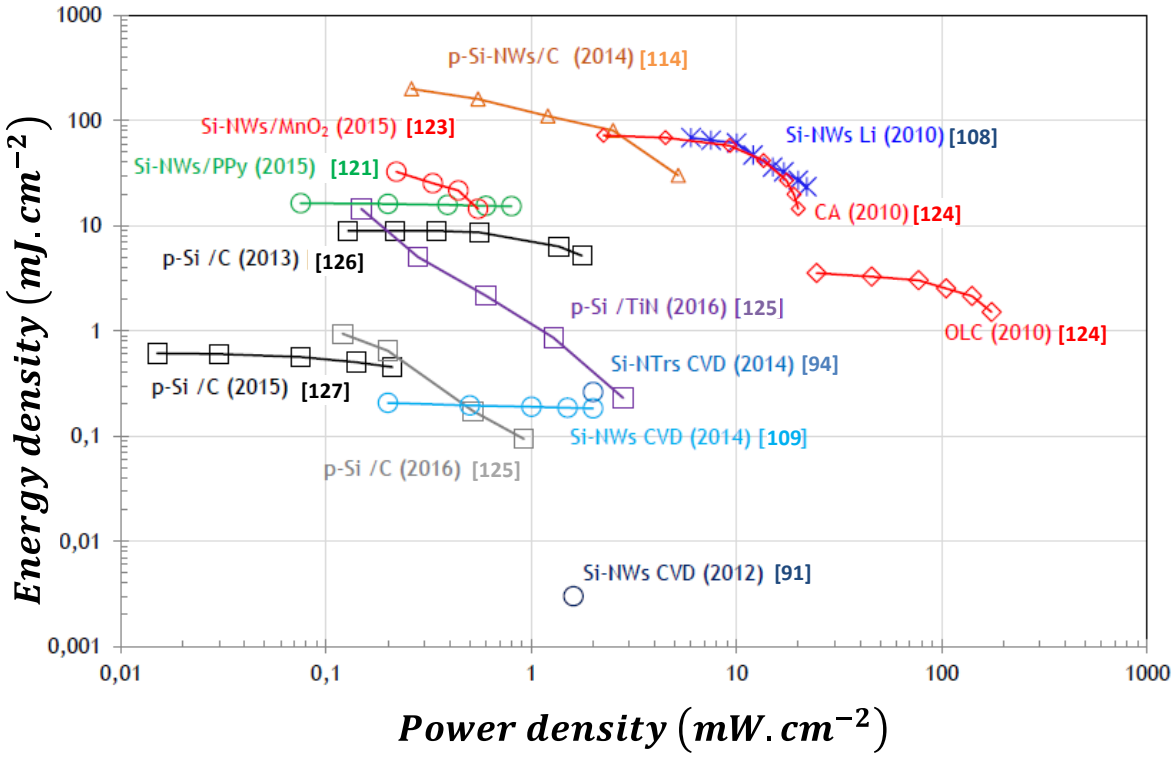

Figure II-6: Ragone plot presenting the performance of SiNW-based electrodes compared to two carbon-based supercapacitors in literature (activated carbon (CA) and OLC). Adapted from [95].

II-3. Conductive polymer electrodes

Among the vast possibilities of electrode materials for pseudo-capacitors, conductive polymers are a very attractive solution due to their low price, non-toxicity and tunable chemical, electrical and physical properties. These polymers can be electrochemically doped in the presence of an electrolyte to obtain very good electrical conductivity (10 to 100 $S.cm^{-1}$) and a wide electrochemical window.

Through the doping process, charges are transferred to the polymer chains with an excess of electrons in the case of n-doping and a lack of electrons in the case of p-doping. Ions from the electrolyte are then inserted within the polymer matrix to maintain electrical neutrality. As the conductive polymer electrode is charged and discharged, the faradaic exchanges with the electrolyte happen very reversibly without damaging the polymer structure. This feature allows conductive polymers to be very good materials for pseudo-capacitors.

The most common conductive polymers used in literature are poly(pyrroles) (PPy), poly(anilines) (PANi), poly(thiophenes) and their derivatives such as PEDOT (poly(3,4-ethylenedioxythiophene)) [128]–[130]. Even though the specific capacitance values achieved with these materials (300-800 $F.g^{-1}$) are lower than those obtained with transition metal oxides, extensive work have been made and reported in the past decades to investigate their potential for supercapacitor applications.

The nanostructuration of conductive polymer electrodes has gained a lot of attention in recent years as it is a key to enhance ion transfers from the electrolyte [128]. This nanostructuration can be achieved in various ways:

- Covering an existing nanostructure like CNTs, VOGNs, SiNWs.
- Synthetizing conductive polymer nanostructures using a template.
- Performing templateless growth of conductive polymer nanowires.

PANi nanowires synthetized by K. Wang *et al.* showed to reach specific capacitance values up to 950 $F.g^{-1}$ (**Fig. II-7**) [131].

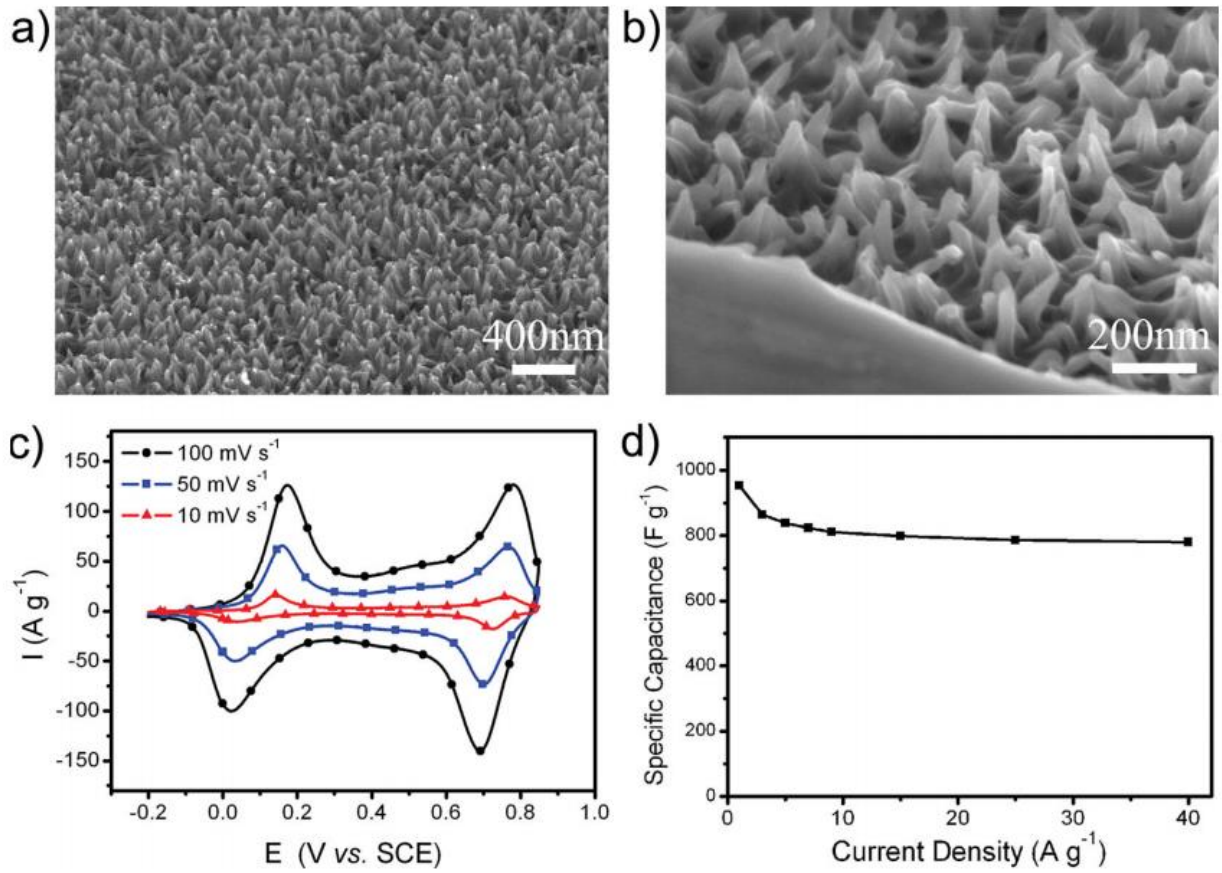

Figure II-7: a-b) SEM images of PANi nanowires. **c)** Cyclic voltammetry results in $HClO_4$ aqueous solution. **d)** Specific capacitance as a function of current density. [131]

III. Electrochemical Quartz Crystal Microbalance

In the first part of this chapter, we presented an overview of the basic working principles for supercapacitors. These simple models are often insufficient to describe the complex reality of the ionic exchange mechanisms occurring at the electrode-electrolyte interface. Thus, more detailed models have been developed to describe such systems, with for example molecular dynamic simulations [132]. However in-situ/operando characterization techniques are still required to complement the simulations and clearly understand the long chain of mechanisms that led to an energy storage system's final properties (specific capacitance, power density, cycling stability, self discharge…). For this purpose, a large panel of cutting-edge spectroscopy, scattering and imaging techniques are available, including Nuclear Magnetic Resonance (NMR), X-ray Photoelectron Spectroscopy (XPS), Time-Of-Flight Secondary Ion Mass Spectrometry (TOF-SIMS), Scanning Transmission Electron Microscopy- Electron Energy Loss Spectroscopy (STEM-EELS), Pulsed Electrochemical Mass Spectrometry (PEMS), temperature-programmed desorption coupled with mass spectroscopy (TPD-MS), Raman, Fourier Transform Infrared Spectroscopy (FTIR), Synchrotron X-rays Reflectivity and Diffraction [133].

Adapting any of these characterization techniques to an in-operando electrochemical system comporting various electrodes in contact with an electrolyte is not an easy task. And since each of these general techniques are not specifically designed for electrochemical systems, interpreting the data to understand the behavior of ions at the electrode surface requires a complementary method. Pure electrochemical methods such as electrochemical impedance spectroscopy (EIS) is a very useful tool to understand some properties of the system, but insufficient to deliver a global understanding of the ionic mechanisms.

The following sections will describe another type of characterization techniques based on the combination of a quartz crystal microbalance (QCM) with conventional electrochemical methods.

III-1. From the Sauerbrey equation to classical EQCM

A QCM is an attractive tool for gravimetric measurements with applications in many research fields such as material deposition, chemical sensors and biosensors [134], [135]. This device permits the measurement of mass variations within a sample deposited on the surface of a piezoelectric crystal (most commonly an AT-cut of quartz). This measurement is made through the change of the crystal's resonant frequency [136]–[139]. The thin quartz crystal is linked to an electrical circuit that is strong enough to create a vibrational motion at its resonant frequency [137], [140]. The microbalance frequency may be followed over time, the precision depending on the stability of the microbalance [141], [142]. The QCM is a high precision instrument which permits the determination of the mass variations with an error around 1 ng in optimal stability conditions.

In 1959, Dr. Günter Sauerbrey established an equation showing the relationship between the mass variations and the resonance frequency changes [143]. When a rigid, purely elastic and electroacoustically thin layer is deposited on the quartz, the relationship between the mass variation of the material and the QCM's frequency change is:

$$\Delta f_m = -k_s \times \Delta m = -\left(\frac{2f_0^2}{S \times n\sqrt{\rho_q \mu_q}}\right)\Delta m \qquad \textbf{(Eq. III-1)}$$

where Δf_m is the frequency change of the microbalance (Hz), Δm is the mass change of the microbalance active surface (g), ρ_q is the quartz density (2.648 g.cm^{-3}), μ_q is the shear modulus of an AT-cut quartz crystal (2.947 x 10^{11} g.cm^{-1}.s^{-2}), f_0 is the fundamental resonance frequency of the quartz (Hz), S is the active surface of the quartz, corresponding to the surface of the metal electrode deposited on it (cm^2), n is the overtone number and k_s is the sensitivity factor of the QCM (Hz.g^{-1}.cm^2).

With a QCM operating at 9 MHz, the theoretical sensitivity factor calculated from the Sauerbrey equation is equal to 18.3 x 10^7 Hz.g^{-1}.cm^2. Bizet *et al.* determined the experimental sensitivity coefficients for QCMs operating at 6, 9 and 27 MHz by copper electrodeposition at a known deposition rate [144]. For resonators operating at 9 MHz, an experimental mass sensitivity factor of 16.31 (± 0.32) ×10^7 Hz.g^{-1}.cm^2 was obtained, which is in fairly good agreement with the theory. For an electrode surface of 0.2 cm^2, this sensitivity factor leads to the fact that a variation

of 1 Hz in resonance frequency corresponds to a mass variation of 1.2 ng on the electrode surface.

Electrochemical quartz crystal microbalance (EQCM) is a method combining QCM with classical electrochemical measurements such as cyclic voltammetry (CV) and galvanostatic charge-discharge cycles [145], [146]. It is capable of quantitatively measuring small mass changes occurring at the electrode surface during an electrochemical process and correlate them to the electrical response. EQCM has been used to investigate diverse phenomena such as metal electrodeposition [147]–[149], electrocrystallization [150], electrochromic reactions [136], electroadsorption [151], [152] and mass changes associated with electrolyte-ion movements [153]–[155].

In the field of supercapacitors, EQCM allows the investigation of the capacitive properties of the electrode by analyzing the capacitive current and the resulting mass changes. The operation principles of the EQCM will be discussed in further detail in Chapter 2-III.

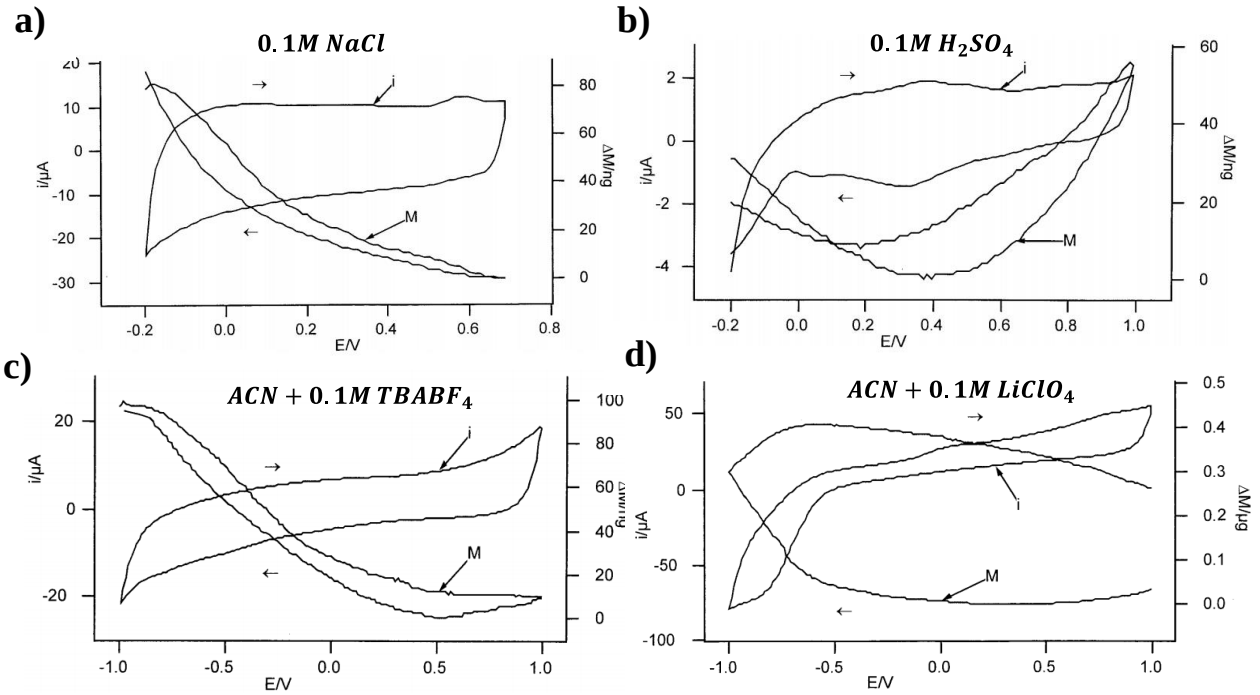

Figure III-1: EQCM study of CNT supercapacitor electrodes in **a-b)** aqueous electrolytes and **c-d)** ACN-based electrolytes. [156]

Reviewing the literature, only a limited number of studies were found to employ EQCM to study carbon nano-materials and none was found concerning Si-based electrodes. Barisci *et al.* reported a study comparing the influence of three different electrolytes on CNT electrodes.

Monitoring the mass changes of CNT films as a function of the applied potential, the authors reported that the ionic exchange behavior is similar in acetonitrile (ACN) solutions and aqueous electrolytes when the cation is tetrabutylammonium (TBA). However, Li^+ cations caused a substantial increase of the CNT film mass associated with cation insertion, which is not readily reversed, thus reflecting slow Li^+ expulsion (**Fig. III-1**) [156].

Maier *et al.* studied the EQCM responses of typical microporous activated carbons. For these porous films, the periodic mass change during cycling was found to be much higher than that of non-porous carbon-black electrodes. This was associated with the sorption of both anions and cations in relation to the microporous volume of the electrode [157]. The authors also studied the effect of specific adsorption of cations and their size on the charge-compensation mechanism in carbon micropores [158]. They reported that this technique reveals a complicated interplay between the adsorption of NH_4^+ cations and the desorption of Cl^- anions inside carbon micropores at low surface charge densities, which results in a failure of their permselectivity. Higher negative surface charge densities induce complete exclusion (desorption) of the Cl^- co-ions, which impedes a purely permselective behavior on the carbon micropores.

Griffin *et al.* reported the combination of EQCM with NMR to further investigate micro-porous carbon electrodes for supercapacitor applications [159]. Using tetraethylphosphonium tetrafluoroborate in acetonitrile, the authors revealed a partial desolvation of ions along with different charge storage mechanisms for positively and negatively polarized electrodes. While cation adsorption dominates for negative polarization, an exchange between cations and anions is observed for positive polarization.

Recently, Tsai *et al.* reported the use of EQCM to study the influence of pore size on ion desolvation in CDC electrodes [155]. In an acetonitrile solution containing 2M EMI-TFSI, the authors showed that the extent of desolvation increased when decreasing the carbon pore size from 1 to 0.65 nm.

Two communications by Levi *et. al.* reported further EQCM studies of micro-porous carbon electrodes using binary aqueous CsCl solutions [153] and various propylene carbonate (PC) electrolytes [160]. Mixed cation and anion contributions were observed, with a huge impact of cation size due to the limited accessibility in the carbon micro-pores (**Fig. III-2**). Overall, EQCM offers a great opportunity to better understand ion transport and solvation in porous

materials, thus enabling the design of optimized porous materials for the next generation of high energy density supercapacitors.

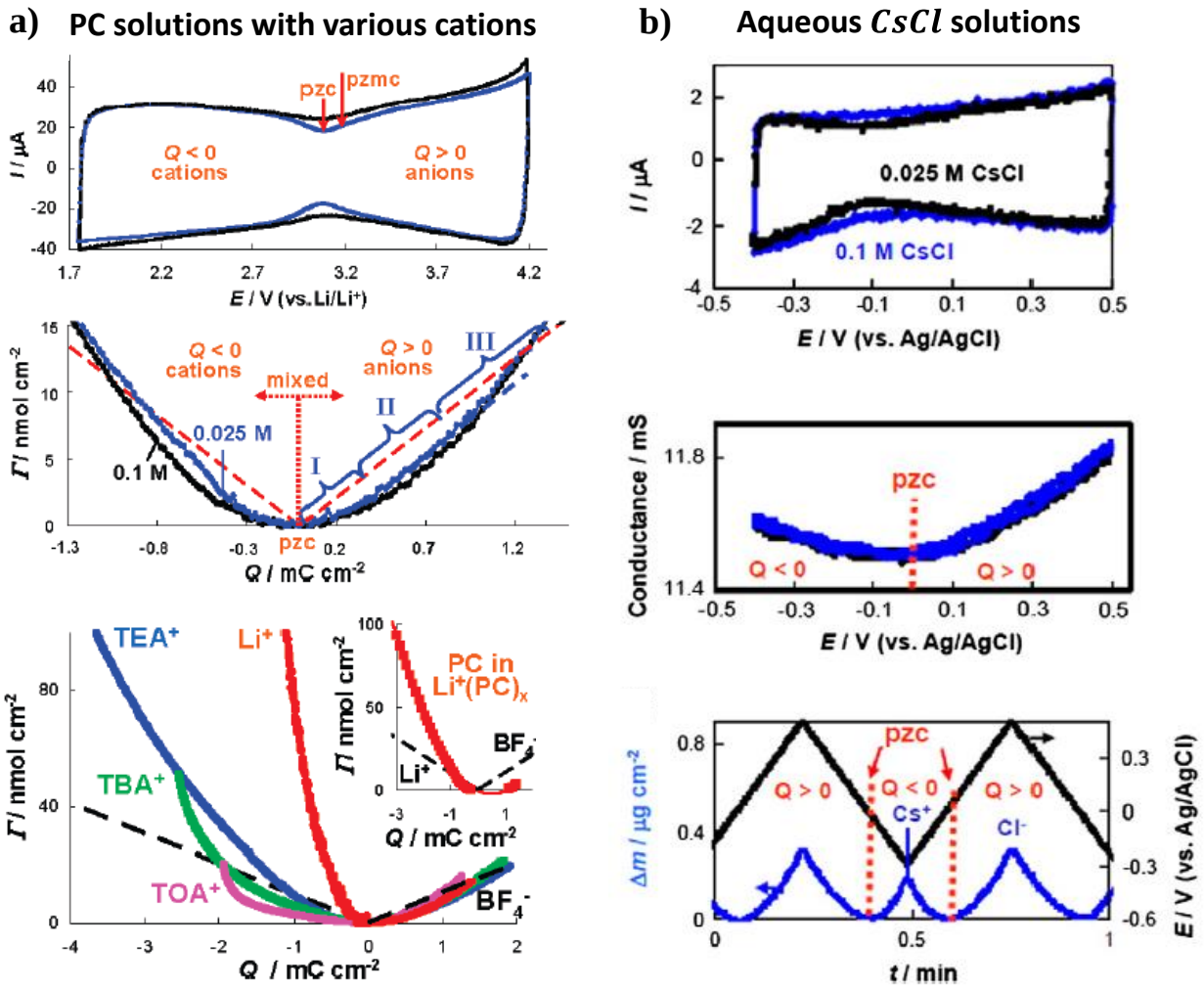

Figure III-2: EQCM study of micro-porous supercapacitor electrodes in **a)** PC-based electrolytes with various cation sizes and **b)** aqueous CsCl electrolytes. [153], [160]

A few pseudo-capacitive materials were also studied with EQCM. Nayak *et al.* investigated the ionic exchange mechanisms in MnO_2 electrodes with electrolytes containing multivalent cations [161]. Cations were found to dominate the exchanges and an increase of the cations valence was shown to increase the specific capacitance. Another study of MnO_2 electrodes was conducted by Chu *et al.* to obtain better electrode stability [162]. The gradual dissolution of MnO_2 while cycling in 10 mM Na_2SO_4 and the effect of adding $NaHCO_3$ or Na_2HPO_4 to the solution were monitored with EQCM. These additives were found to successfully suppress both MnO_2 dissolution and oxygen evolution.

In order to quantitatively correlate the mass changes of the adsorbed ions and solvent molecules with the potential-induced variations of the electrode charge density, two terms are introduced by the previous authors (**Fig. III-2**):

- The potential of zero charge (pzc) describes the potential where the electrode is not polarized. At this potential no charges gather in the electrode and no electrostatic attraction of ions occur.
- The potential of zero mass change (pzcm) describes the potential where the slope of the mass variations measured with EQCM changes in sign.

According to the electrical double layer model described in part I, the pzcm should coincide with the pzc, since, according to this point of view, adsorption of anions and cations into carbon micropores occurs at $Q>0$ and $Q<0$, respectively. However, in practice, the pzcm does not necessarily coincide with the pzc of the electrode, since the former may depend on the dynamics of formation of the double layer. The EQCM is a unique technique for handling this topic and understanding its mechanisms. Nevertheless, this method has some limitations:

- Only the global mass variations of an electrode are measured, thus when multiple species are exchanged simultaneously it is difficult to discriminate between them.
- The dynamics of the exchange mechanisms are unknown.

The following section will introduce another gravimetric technique designed to overcome these limitations.

III-2. *Ac*-electrogravimetry

In 1988, C. Gabrielli *et al.* at LISE laboratory (France) introduced a new in-situ/operando characterization technique based on the combination of QCM and EIS: *ac*-electrogravimetry [163]. Using a small potential perturbation at a varying frequency, both the impedance and the corresponding mass variations are measured. This method can deliver unique species-selective and frequency-dependent information about the ionic exchange mechanisms at the electrode/electrolyte interface. Like in EIS, a model is used to fit *ac*-electrogravimetry data and extract valuable information from these measurements. But rather than being based on a simple electrical circuit, this model describes the specific exchange flux for each species. A description of the experimental features of *ac*-electrogravimetry along with the models used to fit the results will be given in chapter 2-III.

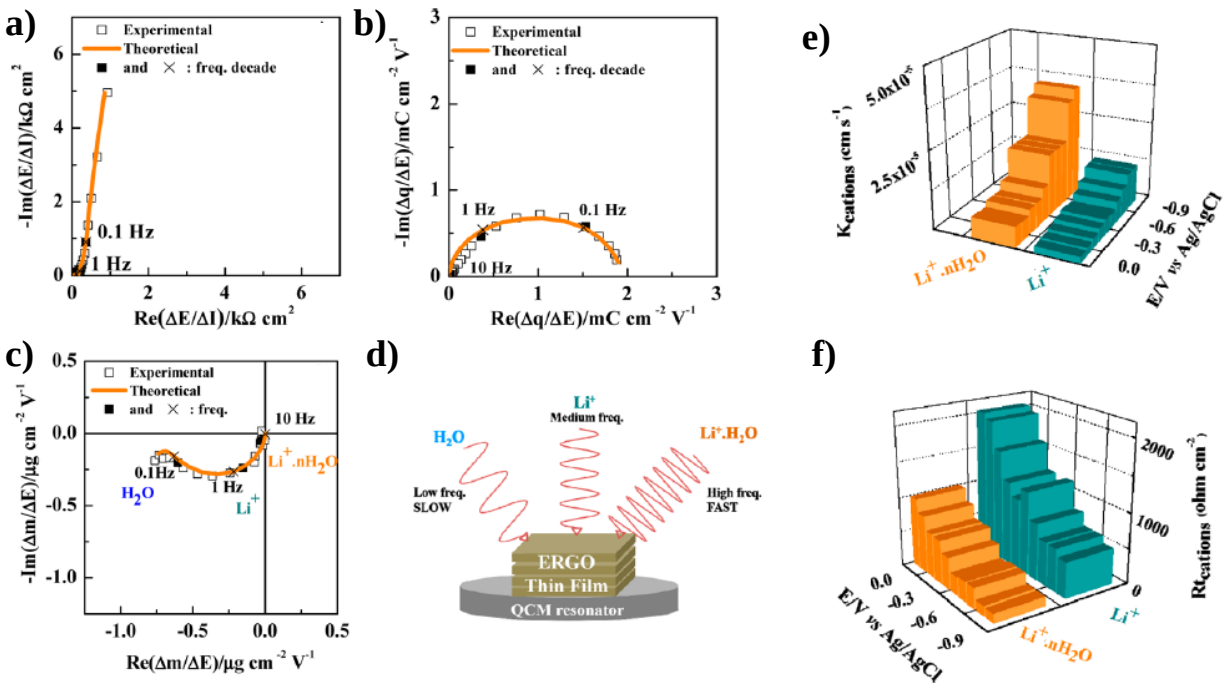

Figure III-3: *Ac*-electrogravimetry study of ERGO thin films in 0.5M LiCl aqueous solution: **a)** The electrochemical impedance. **b)** The charge/potential transfer function. **c)** The mass/potential transfer functions. **d)** A schematic view the exchanged species. **e)** The kinetic and **f)** transfer resistance parameters obtained from the *ac*-electrogravimetry fitting model. [168]

Since its first introduction, *ac*-electrogravimetry was used to characterize various supercapacitor electrode materials such as conducting polymers [164], [165], CNTs [166], CNT/Prussian blue composites [167] and more recently electrochemically reduced graphene

oxide (ERGO) [168]. In each case the dynamics of electroadsorption/desorption of individual ions was derived along with interesting material properties. Garbielli *et al.* reported a potential dependence in the number of solvent molecules exchanged per ion moving through the interface of a polyaniline (PANi) electrode [165]. To Thi Kim *et al.* unveiled a switch of the transfer mechanisms in polypyrrole (PPy) films doped with heteropolyanions: Depending on the applied potential, the global kinetics is controlled by both the ionic and electronic transfers [164].

For both CNT and ERGO electrodes, the *ac*-electrogravimetry results were used to understand the potential dependence on the kinetics of individual species (**Fig. III-3**) and to reconstruct the mass variation response from EQCM with the individual concentration changes of each species (**Fig. III-4**) [166], [168]. *Ac*-electrogravimetry can therefore be used to obtain a full deconvolution of the global EQCM response at both gravimetric and temporal levels.

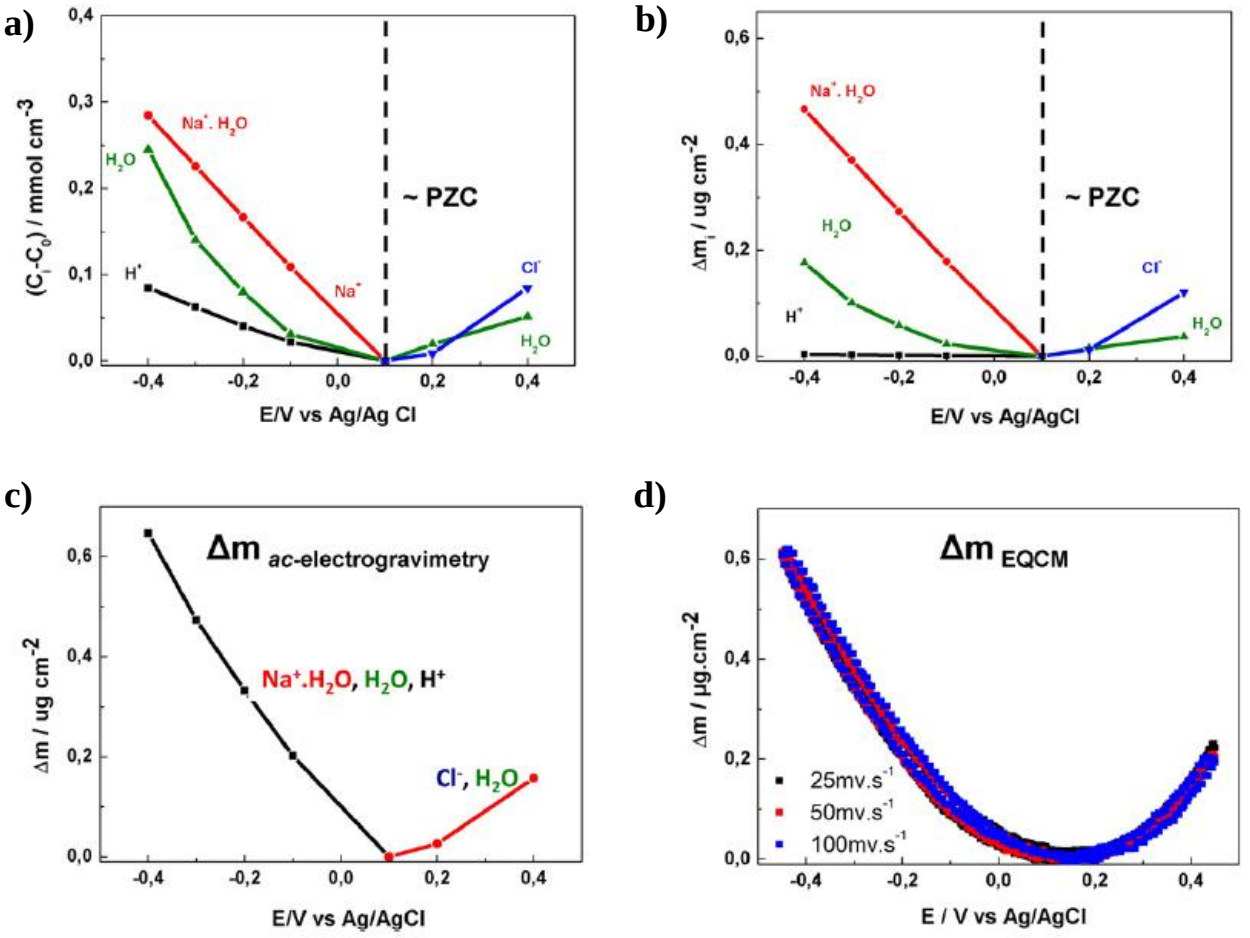

Figure III-4: *Ac*-electrogravimetry study of CNT electrodes in 0.5M NaCl aqueous solution: **a)** Concentration variations for each exchanged species. **b)** The corresponding mass variations due to each species. **c)** The reconstructed total mass variations. **d)** The mass variations measured with EQCM. [166]

III-3. Limits of the gravimetric methods

EQCM and *ac*-electrogravimetry both rely on the good gravimetric properties of a QCM, allowing the use of the Sauerbrey equation. However this simple relation is derived for thin films rigidly attached to the quartz's surface and is no longer valid for too thick or too soft films, or in the case of films presenting a too complex surface structure. In those cases, a clear relation between frequency shift and mass variations cannot be established due to a strong damping of the shear wave generated by the piezoelectric oscillator during QCM operation [169], [170]. For thick or soft films, this damping takes place directly within the film, whereas for surface structures the damping is due to hydrodynamic forces opposite to the film's movement in the solution during QCM oscillations. These hydrodynamic drag forces will vary depending on the surface geometries, the film's velocity (which in turn depends on the QCM's amplitude and frequency) and the solution's dynamic viscosity. For example at low Reynolds numbers, the force experienced by a spherical particle on the electrode surface can be derived with Stoke's law [171]:

$$F_d = 6\pi\eta R v \qquad \textbf{(Eq. III-2)}$$

where F_d is the frictional force (N), also known as Stokes' drag, η is the dynamic viscosity (Pa.s), R is the radius of the spherical particle (m) and v is the flow velocity relative to the object (m.s^{-1}).

These hydrodynamic damping forces could undermine the ability to perform electrogravimetric measurements on nanostructured electrodes depending on their shape and extent in the solution. This would also be the case for thin rigid films if this property is lost in the solution or under applied potential, or in the case where the volume or the porosity of the film changes with potential, which would modify the hydrodynamic liquid-solid interactions respectively.

To validate or invalidate the use of the Sauerbrey equation, the quality factor $Q = \frac{f_0}{W}$ or the dissipation factor $D = \frac{W}{f_0}$ can be evaluated, where W is the full-width at half-height of the resonance peak, and f_0 is the resonance frequency. The methods used to obtain the Q factor and determine the feasibility of gravimetric measurements will be discussed in chapter 2-III.2.

If too large variations of the dissipation factor are obtained due to volume or porosity change in the film, for example during Li-ion insertion and desorption, it is still possible to use the QCM in a "non-gravimetric" regime by performing EQCM with dissipation monitoring (EQCM-D) [169], [170], [172].

This method, also called in-situ hydrodynamic spectroscopy, is based on the simultaneous measurement of the variations of f_0 and W for different values of the decay length of the transverse wave generated by the crystal (**Fig. III-5**) [169]:

$$\delta_n = \sqrt{\frac{\eta}{\pi\, n\, f_0\, \rho}} \qquad \textbf{(Eq. III-3)}$$

where n is the overtone order, η is the electrolyte viscosity and ρ it's density.

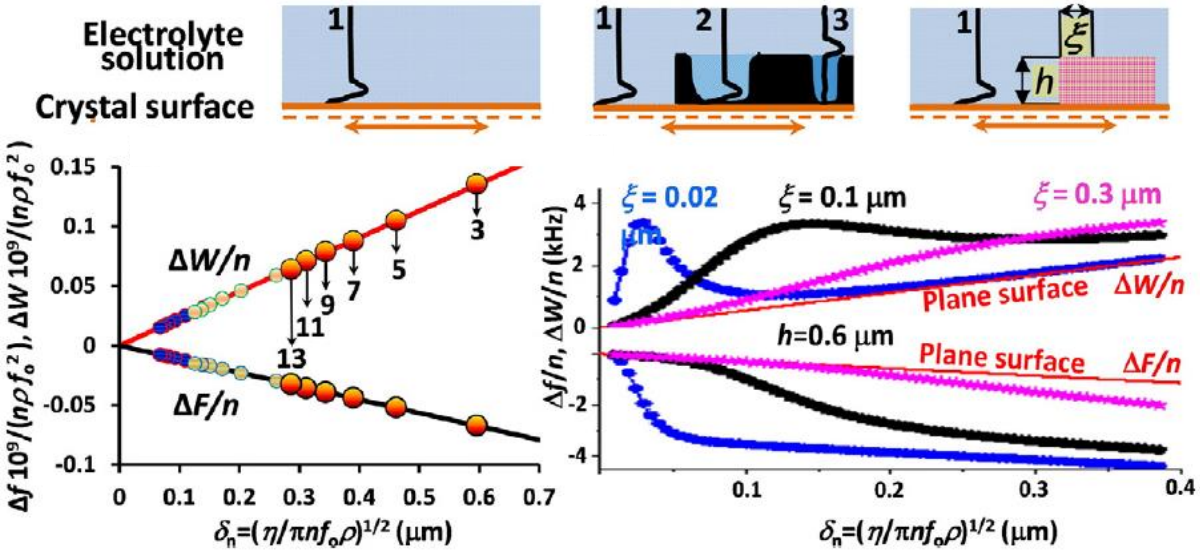

Figure III-5: Hydrodynamic modeling on a porous electrode. The values measured for Δ*f*/*n* and Δ*W*/*n* diverge from the straight lines obtained with an ideal flat surface. [169]

To vary δ_n experimentally, it is possible to either use various liquids with different values of $\frac{\eta}{\rho}$ and thus perform ex-situ hydrodynamic spectroscopy, or to use the multi-harmonic in-situ approach by varying the overtone order *n*.

Once Δ*f* and Δ*W* are measured for different values of δ_n, the results need to be compared with an appropriate hydrodynamic model of the system. Such models have been created and tested for various geometries of porous electrode layers (**Fig. III-6**). Fitting the experimental data

of Δf and ΔW versus δ_n with the appropriate hydrodynamic model enables the determination of the electrode's porous structure parameters such as the permeability length ξ [169].

EQCM-D is a non-invasive technique that can be used to monitor electrode deformations and viscoelastic changes during the charging and discharging of supercapacitor and battery electrodes. This technique has for example been used to follow the rigidity changes of $LiFePO_4$/PVdF electrodes in Li-ion aqueous and organic electrolytes [172].

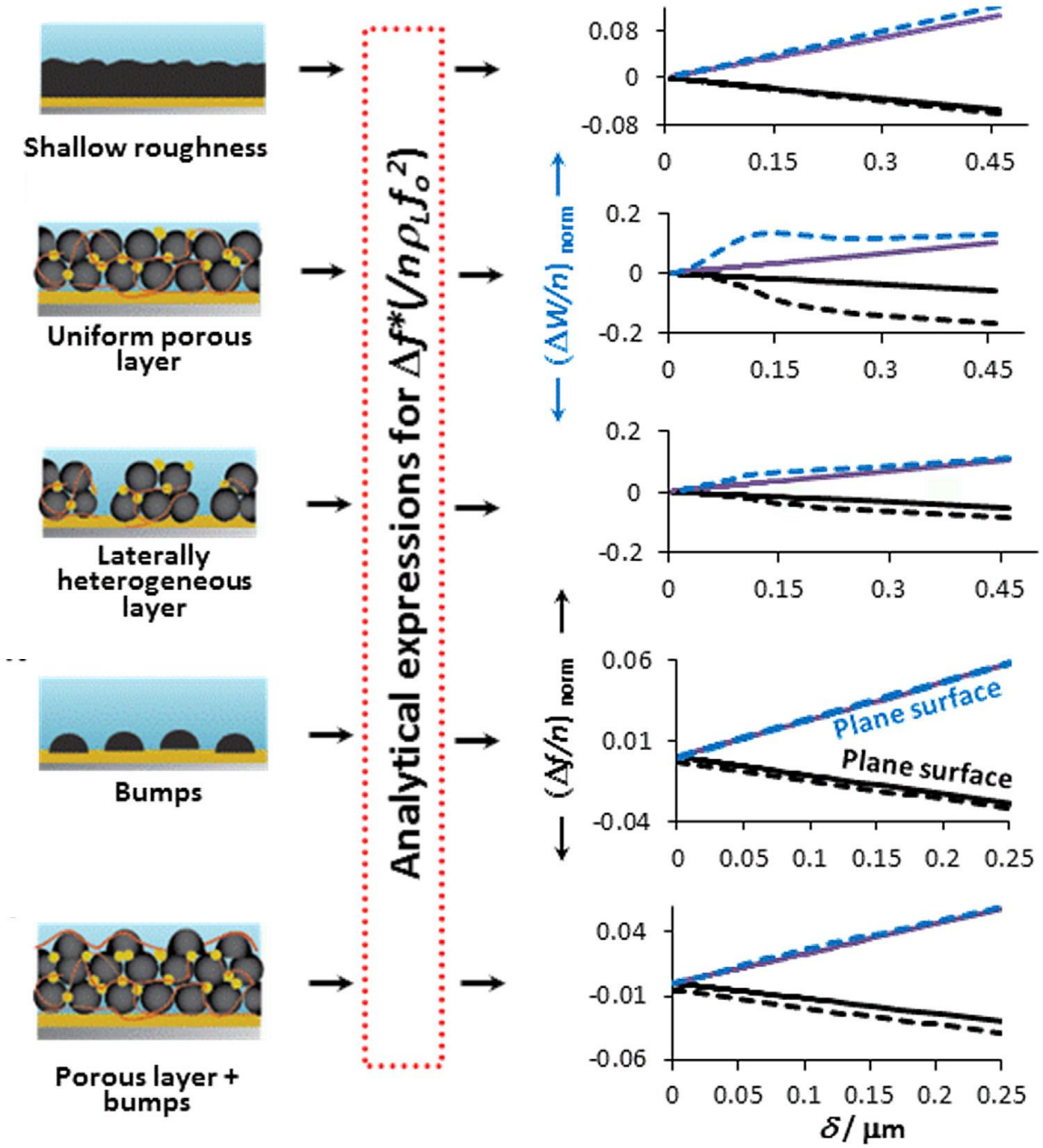

Figure III-6: Hydrodynamic modeling of five types of rough/porous electrode geometries. [169]

IV. Aim of this work

Taking into account the recent advances in the field of supercapacitor, nanostructuration of the electrodes appears to be a key development path to achieve better performances. Understanding the principles governing the ionic exchange mechanisms in nanostructured supercapacitor electrodes is important to shed light on this path and improve current devices. The mechanisms driving a supercapacitor device at the ionic level are much more complicated than the simple view introduced in part-I with the double layer model. The electrode material, type of nanostructuration and electrolyte composition will all affect the ionic exchange mechanisms.

In part III we have seen that EQCM and *ac*-electrogravimetry are very powerful tools to better understand these mechanisms. For instance they brought important insight on the ionic exchanges in CNTs and nanoporous carbon, showing that these methods could be applied to nanostructured material. However, in every case found in literature, the nanostructured materials were deposited on the QCM with a binder and the roughness of the electrode's surface remained low compared to vertical nanostructures such as vertical nanosheets or nanowires. To our knowledge, no study has ever been conducted on as-grown vertically nanostructured materials using EQCM or *ac*-electrogravimetry.

The aim of the work presented in this thesis is to perform the following three steps:

- Synthetize as-grown vertically nanostructured materials used in state-of-the-art supercapacitor electrodes on a QCM while keeping the resonator functional, i.e. without perturbing its piezoelectric properties. This is already a very challenging step for some materials given the high temperatures involved and the sensibility of the microbalance's piezoelectric crystal and electrodes to the growth environment. Peeling-off or degradation of the electrodes and collapse of the piezoelectric properties of the quartz are two post-growth symptoms that had to be solved.
- Demonstrate the feasibility of EQCM and *ac*-electrogravimetry measurements on the as-grown material. These techniques are designed to work on thin rigid films, and the limit imposed by hydrodynamic damping on the surface nanostructuration is still unknown. This work aims at maneuvering around this limit to find the adaptability of

the electro-gravimetric approach for vertically nanostructured supercapacitor materials.

- Perform EQCM and *ac*-electrogravimetry measurements using various electrolyte compositions to understand the ionic exchange mechanisms in these nanostructured materials.

These three steps will be performed with four vertically nanostructured materials. First, the experiments will be conducted on uncovered SiNWs and VOGNs which are both EDLC electrodes. Then SiNWs covered with PEDOT and PEDOT nanowires, both pseudo-capacitive materials, will be synthetized and investigated.

References

[1] I. Dincer, 'Renewable energy and sustainable development: a crucial review', *Renew. Sustain. Energy Rev.*, 4, no. 2, pp. 157–175, Jun. 2000.

[2] 'The World Factbook — Central Intelligence Agency'. https://www.cia.gov/library/publications/the-world-factbook/geos/us.html. 16-Aug-2018.

[3] 'Tesla Model 3 specs: 220-mile standard with 310-mile option for $9k', *TESLARATI.com*, 29-Jul-2017. .

[4] 'Renewable Energy Sources', *CleanTechnica*. https://cleantechnica.com/renewable-energy-sources/. 27-Aug-2018.

[5] '10 best electric bikes', *The Independent*, 05-Jul-2016. http://www.independent.co.uk/extras/indybest/outdoor-activity/cycling/best-electric-bike-rated-under-500-halfords-brompton-brands-reviews-a7120306.html. 27-Aug-2018.

[6] 'Top 10 Best Smartwatches Under $300', *TechCinema*. .

[7] 'HP Windows 10 14" Laptop - Jet Black (14-BW012NR)'. /p/hp-windows-10-14-laptop-jet-black-14-bw012nr/-/A-52948509. 27-Aug-2018.

[8] CSols-Admin, 'RFID labelling for laboratories', 19-Dec-2011. .

[9] 'Smartphone hire - Roma - Snap Phone'. /en-gb/cellphone-and-smartphone-hire. 27-Aug-2018.

[10] A. Kiourti and R. Shubair, 'Implantable and Ingestible Sensors for Wireless Physiological Monitoring: A Review', 2017.

[11] 'Different Types of Sensors Based Engineering Projects And Applications', *Edgefxkits International*, 15-Jun-2017. .

[12] M. Beidaghi and Y. Gogotsi, 'Capacitive energy storage in micro-scale devices: recent advances in design and fabrication of micro-supercapacitors', *Energy Environ. Sci.*, 7, no. 3, pp. 867–884, Feb. 2014.

[13] M. W. Browne, 'BUSINESS TECHNOLOGY: ADVANCES; New Hunt for Ideal Energy Storage System', *The New York Times*, 06-Jan-1988.

[14] 'From hydrogen and oxygen to fuel cell', *Mass Flow ONLINE*, 08-Aug-2017. https://www.massflow-online.com/markets_applications/hydrogen-oxygen-fuel-cell/. 27-Aug-2018.

[15] B. R. Chalamala, T. Soundappan, G. Fisher, M. R. Anstey, V. Viswanathan, and M. Perry, 'Redox Flow Batteries: An Engineering Perspective', *Proc. IEEE*, 102, pp. 976–999, Jun. 2014.

[16] 'Compressed Air Energy Storage: Renewable Energy'. https://phys.org/news/2010-03-compressed-air-energy-storage-renewable.html. 27-Aug-2018.

[17] admin, 'Highview Power Storage using Liquid Air', *Revolution-Green*, 04-Apr-2017. .

[18] 'About Grand Coulee Dam | Bureau of Reclamation'. https://www.usbr.gov/pn/grandcoulee/about/index.html. 27-Aug-2018.

[19] 'Demand For Lithium-Ion Batteries Outpacing Supply | Sensors Magazine'. https://www.sensorsmag.com/components/demand-for-lithium-ion-batteries-outpacing-supply. 27-Aug-2018.

[20] '200F Super Capacitor | Global Sources'. http://www.globalsources.com/si/AS/Green-Tech/6008848812833/pdtl/200F-Super-Capacitor/1111668057.htm. 27-Aug-2018.

[21] 'EEUFC1J102U | Panasonic Aluminium Electrolytic Capacitor FC Radial Series 63V dc 1000µF, Through Hole Electrolytic, ±20% +105°C | RS Components'. https://au.rs-online.com/web/p/aluminium-capacitors/0572215/. 27-Aug-2018.
[22] 'Volvo hybrid drive: 60,000 rpm flywheel, 25% boost to mpg - ExtremeTech'. http://www.extremetech.com/extreme/154405-volvo-hybrid-drive-60000-rpm-flywheel-25-boost-to-mpg. 27-Aug-2018.
[23] I. Hadjipaschalis, A. Poullikkas, and V. Efthimiou, 'Overview of current and future energy storage technologies for electric power applications', *Renew. Sustain. Energy Rev.*, 13, no. 6, pp. 1513–1522, Aug. 2009.
[24] 'Powerplant details - Grand Coulee Powerplant - Bureau of Reclamation', 29-Apr-2014. https://web.archive.org/web/20140429162702/http://www.usbr.gov/projects/Powerplant.jsp?fac_Name=Grand%20Coulee%20Powerplant. 16-Aug-2018.
[25] F. Meyer, 'German AACAES project information. Retrieved February 22, 2008.' .
[26] 'Water - Thermophysical Properties'. https://www.engineeringtoolbox.com/water-thermal-properties-d_162.html. 16-Aug-2018.
[27] 'Technology', *Highview Power*. https://www.highviewpower.com/technology/. 16-Aug-2018.
[28] 'Specifications for NCR18650GA'. Panasonic, 02-Jul-2017.
[29] S. P. S. Badwal, S. S. Giddey, C. Munnings, A. I. Bhatt, and A. F. Hollenkamp, 'Emerging electrochemical energy conversion and storage technologies', *Front. Chem.*, 2, 2014.
[30] 'Products | FUELCELL ENERGY'. .
[31] 'Vishay - 036 RSP - Aluminum Electrolytic Capacitors Radial Semi-Professional'. http://www.vishay.com/ppg?28312&quality. 16-Aug-2018.
[32] A. Anwar, A. Majeed, N. Iqbal, W. Ullah, A. Shuaib, U. Ilyas, F. Bibi, and H. M. Rafique, 'Specific Capacitance and Cyclic Stability of Graphene Based Metal/Metal Oxide Nanocomposites: A Review', Aug. 2015.
[33] H. Helmholtz, 'Ueber einige Gesetze der Vertheilung elektrischer Ströme in körperlichen Leitern mit Anwendung auf die thierisch-elektrischen Versuche', *Ann. Phys.*, 165, no. 6, pp. 211–233, Jan. 1853.
[34] H. I. Becker, 'Low voltage electrolytic capacitor', US2800616 (A), 23-Jul-1957.
[35] L. B. Donald, 'Electrolytic Capacitor Having Carbon Paste Electrodes', US3536963 (A), 27-Oct-1970.
[36] A. M. Namisnyk and J. G. Zhu, 'A SURVEY OF ELECTROCHEMICAL SUPERCAPACITOR TECHNOLOGY', Aug. 2018.
[37] D. A. Evans, 'Capacitor', US5369547 (A), 29-Nov-1994.
[38] 'Corporate Information | FDK History -2000s- | FDK'. http://www.fdk.com/company_e/ayumi2000-e.html. 16-Aug-2018.
[39] 'The supercapacitor electric bus is adopted in China - SupercapTech.com'. https://www.supercaptech.com/the-supercapacitor-electric-bus-is-adopted-in-china. 16-Aug-2018.
[40] J. R. Miller and A. F. Burke, 'Electrochemical Capacitors: Challenges and Opportunities for Real-World Applications', *Electrochem. Soc. Interface*, p. 5, 2008.
[41] L. L. Zhang, R. Zhou, and X. S. Zhao, 'Graphene-based materials as supercapacitor electrodes', *J. Mater. Chem.*, 20, no. 29, pp. 5983–5992, Jul. 2010.
[42] J. R. Miller, 'Capacitors for Power Grid Storage', p. 51.

[43] B. Halvorson, 'Ultracapacitor Resistance Breaking Down Among Automakers?', *Green Car Reports*. https://www.greencarreports.com/news/1098550_ultracapacitor-resistance-breaking-down-among-automakers. 27-Aug-2018.
[44] 'Biosensors History|Scientific India Magazine'. http://www.scind.org/517/Science/biosensors-history.html. 27-Aug-2018.
[45] 'Le tramway à Toulon', *Collectif Tramway Toulon*. http://www.tramwaytoulon.com/. 27-Aug-2018.
[46] 'MEMS Waveguide Switch Controls 500 to 750 GHz', *Microwaves & Radio Frequency*, 02-Aug-2017. https://www.mwrf.com/components/mems-waveguide-switch-controls-500-750-ghz. 27-Aug-2018.
[47] J. R. Miller and P. Simon, 'Electrochemical Capacitors for Energy Management', *Science*, 321, no. 5889, pp. 651–652, Aug. 2008.
[48] S. Pan, J. Ren, X. Fang, and H. Peng, 'Integration: An Effective Strategy to Develop Multifunctional Energy Storage Devices', *Adv. Energy Mater.*, 6, no. 4, p. 1501867, Feb. 2016.
[49] 'Design of Solar Harvested Semi Active RFID Transponder with - PDF Free Download', *zdoc.site*. https://zdoc.site/design-of-solar-harvested-semi-active-rfid-transponder-with.html. 16-Aug-2018.
[50] M.D. Levi, M.R. Lukatskaya, S. Sigalov, M. Beidaghi, N. Shpigel, L. Daikhin, D. Aurbach, M. Barsoum and Y. Gogotsi, 'Solving the Capacitive Paradox of 2D MXene using Electrochemical Quartz-Crystal Admittance and In Situ Electronic Conductance Measurements', Advanced Energy Materials. 5 (2014) 1400815.
[51] A. J. Bard and L. R. Faulkner, 'Electrochemical Methods: Fundamentals and Applications, 2nd Edition', *Wiley.com*. https://www.wiley.com/en-fr/Electrochemical+Methods%3A+Fundamentals+and+Applications%2C+2nd+Edition-p-9780471043720. 16-Aug-2018.
[52] F. Béguin, V. Presser, A. Balducci, and E. Frackowiak, 'Carbons and Electrolytes for Advanced Supercapacitors', *Adv. Mater.*, 26, no. 14, pp. 2219–2251, Apr. 2014.
[53] J.C. Lassègues, 'Supercondensateurs', *Ref : TIP301WEB - 'Conversion de l'énergie électrique'*, 10-May-2001. /base-documentaire/energies-th4/accumulateurs-d-energie-42243210/supercondensateurs-d3334/. 16-Aug-2018.
[54] F. Miomandre, S. Sadki, P. Audebert, and R. Méallet-Renault, *Électrochimie*. 2018.
[55] A. Burke, 'Ultracapacitors: why, how, and where is the technology', *J. Power Sources*, 91, no. 1, pp. 37–50, Nov. 2000.
[56] C. Pean, B. Daffos, B. Rotenberg, P. Levitz, M. Haefele, P.-L. Taberna, P. Simon, and M. Salanne, 'Confinement, Desolvation, And Electrosorption Effects on the Diffusion of Ions in Nanoporous Carbon Electrodes', *J. Am. Chem. Soc.*, 137, no. 39, pp. 12627–12632, Oct. 2015.
[57] C. Largeot, C. Portet, J. Chmiola, P.-L. Taberna, Y. Gogotsi, and P. Simon, 'Relation between the Ion Size and Pore Size for an Electric Double-Layer Capacitor', *J. Am. Chem. Soc.*, 130, no. 9, pp. 2730–2731, Mar. 2008.
[58] B. E. Conway, *Electrochemical Supercapacitors: Scientific Fundamentals and Technological Applications*. Springer US, 1999.
[59] T. Brousse, D. Belanger, and J. W. Long, 'To Be or Not To Be Pseudocapacitive?', *J Electrochem. Soc*, 162, no. 5, pp. A5185–A5189, 2015.
[60] P. Simon, Y. Gogotsi, and B. Dunn, 'Materials science. Where do batteries end and supercapacitors begin?', *Science*, 343, no. 6176, pp. 1210–1211, Mar. 2014.

[61] D. P. Dubal, O. Ayyad, V. Ruiz, and P. Gómez-Romero, 'Hybrid energy storage: the merging of battery and supercapacitor chemistries', *Chem. Soc. Rev.*, 44, no. 7, pp. 1777–1790, Mar. 2015.
[62] A. Du Pasquier, I. Plitz, S. Menocal, and G. Amatucci, 'A comparative study of Li-ion battery, supercapacitor and nonaqueous asymmetric hybrid devices for automotive applications', *J. Power Sources*, 115, no. 1, pp. 171–178, Mar. 2003.
[63] T. Brousse, M. Toupin, and D. Bélanger, 'A Hybrid Activated Carbon-Manganese Dioxide Capacitor using a Mild Aqueous Electrolyte', *J. Electrochem. Soc.*, 151, no. 4, pp. A614–A622, Jan. 2004.
[64] E. Le, T. Brousse, R. Retoux, C. Cougnon, and J. Gaubicher, 'Toward fully organic rechargeable charge storage devices based on carbon electrodes grafted with redox molecules', *J. Mater. Chem. Mater. Energy Sustain.*, 2, Mar. 2014.
[65] G. A. Snook, P. Kao, and A. S. Best, 'Conducting-polymer-based supercapacitor devices and electrodes', *J. Power Sources*, 196, no. 1, pp. 1–12, Jan. 2011.
[66] L. G. H. Staaf, P. Lundgren, and P. Enoksson, 'Present and future supercapacitor carbon electrode materials for improved energy storage used in intelligent wireless sensor systems', *Nano Energy*, 9, pp. 128–141, Oct. 2014.
[67] P. Simon and Y. Gogotsi, 'Capacitive Energy Storage in Nanostructured Carbon–Electrolyte Systems', *Acc. Chem. Res.*, 46, no. 5, pp. 1094–1103, May 2013.
[68] N. N. Greenwood and A. Earnshaw, 'Chemistry of the elements', 1984.
[69] J. Chmiola, G. Yushin, Y. Gogotsi, C. Portet, P. Simon, and P. L. Taberna, 'Anomalous Increase in Carbon Capacitance at Pore Sizes Less Than 1 Nanometer', *Science*, 313, no. 5794, pp. 1760–1763, Sep. 2006.
[70] J. Chmiola, C. Largeot, P.-L. Taberna, P. Simon, and Y. Gogotsi, 'Desolvation of Ions in Subnanometer Pores and Its Effect on Capacitance and Double-Layer Theory', *Angew. Chem. Int. Ed.*, 47, no. 18, pp. 3392–3395, Apr. 2008.
[71] W. L. and L. Dai, 'Carbon Nanotube Supercapacitors', *Carbon Nanotub.*, 2010.
[72] G. Lota, K. Fic, and E. Frackowiak, 'Carbon nanotubes and their composites in electrochemical applications', *Energy Environ. Sci.*, 4, no. 5, pp. 1592–1605, Apr. 2011.
[73] E. Frackowiak, 'Carbon materials for supercapacitor application', *Phys. Chem. Chem. Phys.*, 9, no. 15, pp. 1774–1785, Apr. 2007.
[74] J. W. Long, D. Bélanger, T. Brousse, W. Sugimoto, M. B. Sassin, and O. Crosnier, 'Asymmetric electrochemical capacitors—Stretching the limits of aqueous electrolytes', *MRS Bull.*, 36, no. 7, pp. 513–522, Jul. 2011.
[75] K. Naoi, S. Ishimoto, Y. Isobe, and S. Aoyagi, 'High-rate nano-crystalline $Li_4Ti_5O_{12}$ attached on carbon nano-fibers for hybrid supercapacitors', *J. Power Sources*, 195, no. 18, pp. 6250–6254, Sep. 2010.
[76] Z. Zhang, C.-S. Lee, and W. Zhang, 'Vertically Aligned Graphene Nanosheet Arrays: Synthesis, Properties and Applications in Electrochemical Energy Conversion and Storage', *Adv. Energy Mater.*, 7, no. 23, p. 1700678, Dec. 2017.
[77] X. Cao, Z. Yin, and H. Zhang, 'Three-dimensional graphene materials: preparation, structures and application in supercapacitors', *Energy Environ. Sci.*, 7, no. 6, pp. 1850–1865, 2014.
[78] Z. Chen, W. Ren, L. Gao, B. Liu, S. Pei, and H.-M. Cheng, 'Three-dimensional flexible and conductive interconnected graphene networks grown by chemical vapour deposition', *Nat. Mater.*, 10, no. 6, pp. 424–428, Jun. 2011.

[79] X. Cao, Y. Shi, W. Shi, G. Lu, X. Huang, Q. Yan, Q. Zhang, and H. Zhang, 'Preparation of Novel 3D Graphene Networks for Supercapacitor Applications', *Small*, 7, no. 22, pp. 3163–3168, Nov. 2011.
[80] V. Chabot, D. Higgins, A. Yu, X. Xiao, Z. Chen, and J. Zhang, 'A review of graphene and graphene oxide sponge: material synthesis and applications to energy and the environment', *Energy Environ. Sci.*, 7, no. 5, pp. 1564–1596, Apr. 2014.
[81] Y. Jiao, D. Han, L. Liu, L. Ji, G. Guo, J. Hu, D. Yang, and A. Dong, 'Highly Ordered Mesoporous Few-Layer Graphene Frameworks Enabled by Fe_3O_4 Nanocrystal Superlattices', *Angew. Chem. Int. Ed.*, 54, no. 19, pp. 5727–5731, May 2015.
[82] X. Wang, Y. Zhang, C. Zhi, X. Wang, D. Tang, Y. Xu, Q. Weng, X. Jiang, M. Mitome, D. Golberg, and Y. Bando, 'Three-dimensional strutted graphene grown by substrate-free sugar blowing for high-power-density supercapacitors', *Nat. Commun.*, 4, p. 2905, Dec. 2013.
[83] X. Shuai, Z. Bo, J. Kong, J. Yan, and K. Cen, 'Wettability of vertically-oriented graphenes with different intersheet distances', *RSC Adv.*, 7, no. 5, pp. 2667–2675, 2017.
[84] S. Ghosh, T. Mathews, B. Gupta, A. Das, N. Gopala Krishna, and M. Kamruddin, 'Supercapacitive vertical graphene nanosheets in aqueous electrolytes', *Nano-Struct. Nano-Objects*, 10, pp. 42–50, Apr. 2017.
[85] X. You, M. I. Chaudhari, L. R. Pratt, N. Pesika, K. M. Aritakula, and S. W. Rick, 'Interfaces of propylene carbonate', *J. Chem. Phys.*, 138, no. 11, p. 114708, Mar. 2013.
[86] F. Taherian, V. Marcon, N. F. A. van der Vegt, and F. Leroy, 'What Is the Contact Angle of Water on Graphene?', *Langmuir*, 29, no. 5, pp. 1457–1465, Feb. 2013.
[87] H.-F. Yen, Y.-Y. Horng, M.-S. Hu, W.-H. Yang, J.-R. Wen, A. Ganguly, Y. Tai, K.-H. Chen, and L.-C. Chen, 'Vertically aligned epitaxial graphene nanowalls with dominated nitrogen doping for superior supercapacitors', *Carbon*, 82, pp. 124–134, Feb. 2015.
[88] D. Aradilla, M. Delaunay, S. Sadki, J.-M. Gérard, and G. Bidan, 'Vertically aligned graphene nanosheets on silicon using an ionic liquid electrolyte: towards high performance on-chip micro-supercapacitors', *J. Mater. Chem. A*, 3, no. 38, pp. 19254–19262, Sep. 2015.
[89] K.-Q. Peng, X. Wang, L. Li, Y. Hu, and S.-T. Lee, 'Silicon nanowires for advanced energy conversion and storage', *Nano Today*, 8, no. 1, pp. 75–97, Feb. 2013.
[90] B. Liang, Y. Liu, and Y. Xu, 'Silicon-based materials as high capacity anodes for next generation lithium ion batteries', *J. Power Sources*, 267, pp. 469–490, Dec. 2014.
[91] F. Thissandier, A. Le Comte, O. Crosnier, P. Gentile, G. Bidan, E. Hadji, T. Brousse, and S. Sadki, 'Highly doped silicon nanowires based electrodes for micro-electrochemical capacitor applications', *Electrochem. Commun.*, 25, pp. 109–111, Nov. 2012.
[92] N. Berton, M. Brachet, F. Thissandier, J. Le Bideau, P. Gentile, G. Bidan, T. Brousse, and S. Sadki, 'Wide-voltage-window silicon nanowire electrodes for micro-supercapacitors via electrochemical surface oxidation in ionic liquid electrolyte', *Electrochem. Commun.*, 41, pp. 31–34, Apr. 2014.
[93] C. K. Chan, H. Peng, G. Liu, K. McILWRATH, X. F. Zhang, R. A. Huggins, and Y. Cui, 'High-performance lithium battery anodes using silicon nanowires', in *Materials for Sustainable Energy*, 0 vols, Co-Published with Macmillan Publishers Ltd, UK, 2010, pp. 187–191.
[94] F. Thissandier, P. Gentile, T. Brousse, G. Bidan, and S. Sadki, 'Are tomorrow's micro-supercapacitors hidden in a forest of silicon nanotrees?', *J. Power Sources*, 269, pp. 740–746, Dec. 2014.
[95] D. Gaboriau, *Nanostructures de silicium par croissance chimique catalysée : une plate-forme pour des applications micro-supercondensateurs*. Grenoble Alpes, 2016.

[96] F. Oehler, P. Gentile, T. Baron, M. D. Hertog, J. Rouvière, and P. Ferret, 'The morphology of silicon nanowires grown in the presence of trimethylaluminium', *Nanotechnology*, 20, no. 24, p. 245602, 2009.
[97] D. Wang and C. M. Lieber, 'Inorganic materials: Nanocrystals branch out', *Nat. Mater.*, 2, no. 6, pp. 355–356, Jun. 2003.
[98] V. Schmidt, J. V. Wittemann, and U. Gösele, 'Growth, Thermodynamics, and Electrical Properties of Silicon Nanowires', *Chem. Rev.*, 110, no. 1, pp. 361–388, Jan. 2010.
[99] R. S. Wagner and W. C. Ellis, 'Vapor-liquid-solid mechanism of single crystal growth', *Appl. Phys. Lett.*, 4, no. 5, pp. 89–90, Mar. 1964.
[100] A. T. Heitsch, D. D. Fanfair, H.-Y. Tuan, and B. A. Korgel, 'Solution−Liquid−Solid (SLS) Growth of Silicon Nanowires', *J. Am. Chem. Soc.*, 130, no. 16, pp. 5436–5437, Apr. 2008.
[101] H. Han, Z. Huang, and W. Lee, 'Metal-assisted chemical etching of silicon and nanotechnology applications', *Nano Today*, 9, no. 3, pp. 271–304, Jun. 2014.
[102] C.-Y. Chen and C.-P. Wong, 'Unveiling the shape-diversified silicon nanowires made by HF/HNO3 isotropic etching with the assistance of silver', *Nanoscale*, 7, no. 3, pp. 1216–1223, Dec. 2014.
[103] S. Desplobain, G. Gautier, J. Semai, L. Ventura, and M. Roy, 'Investigations on porous silicon as electrode material in electrochemical capacitors', *Phys. Status Solidi C*, 4, no. 6, pp. 2180–2184, May 2007.
[104] S. E. Rowlands, R. J. Latham, and W. S. Schlindwein, 'Supercapacitor devices using porous silicon electrodes', *Ionics*, 5, no. 1–2, pp. 144–149, Jan. 1999.
[105] F. Thissandier, P. Gentile, N. Pauc, E. Hadji, A. L. Comte, O. Crosnier, G. Bidan, S. Sadki, and T. Brousse, 'Highly N-doped Silicon Nanowires as a Possible Alternative to Carbon for On-chip Electrochemical Capacitors', *Electrochemistry*, 81, no. 10, pp. 777–782, Oct. 2013.
[106] F. Thissandier, P. Gentile, N. Pauc, T. Brousse, G. Bidan, and S. Sadki, 'Tuning silicon nanowires doping level and morphology for highly efficient micro-supercapacitors', *Nano Energy*, 5, pp. 20–27, Apr. 2014.
[107] F. Thissandier, L. Dupré, P. Gentile, T. Brousse, G. Bidan, D. Buttard, and S. Sadki, 'Ultra-dense and highly doped SiNWs for micro-supercapacitors electrodes', *Electrochimica Acta*, 117, pp. 159–163, Jan. 2014.
[108] J. W. Choi, J. McDonough, S. Jeong, J. S. Yoo, C. K. Chan, and Y. Cui, 'Stepwise Nanopore Evolution in One-Dimensional Nanostructures', *Nano Lett.*, 10, no. 4, pp. 1409–1413, Apr. 2010.
[109] D. Aradilla, P. Gentile, G. Bidan, V. Ruiz, P. Gómez-Romero, T. J. S. Schubert, H. Sahin, E. Frackowiak, and S. Sadki, 'High performance of symmetric micro-supercapacitors based on silicon nanowires using N-methyl-N-propylpyrrolidinium bis(trifluoromethylsulfonyl)imide as electrolyte', *Nano Energy*, 9, pp. 273–281, Oct. 2014.
[110] D. Aradilla, P. Gentile, V. Ruiz, P. Gómez-Romero, J. Wimberg, B. Iliev, T. J. S. Schubert, S. Sadki, and G. Bidan, 'SiNWs-based electrochemical double layer micro-supercapacitors with wide voltage window (4 V) and long cycling stability using a protic ionic liquid electrolyte', *Adv. Nat. Sci. Nanosci. Nanotechnol.*, 6, no. 1, p. 015004, 2015.
[111] T. Lé, P. Gentile, G. Bidan, and D. Aradilla, 'New electrolyte mixture of propylene carbonate and butyltrimethylammonium bis(trifluoromethylsulfonyl)imide (N1114 TFSI) for high performance silicon nanowire (SiNW)-based supercapacitor applications', *Electrochimica Acta*, 254, pp. 368–374, Nov. 2017.

[112] J. P. Alper, M. Vincent, C. Carraro, and R. Maboudian, 'Silicon carbide coated silicon nanowires as robust electrode material for aqueous micro-supercapacitor', *Appl. Phys. Lett.*, 100, no. 16, p. 163901, Apr. 2012.

[113] F. Gao, G. Lewes-Malandrakis, M. T. Wolfer, W. Müller-Sebert, P. Gentile, D. Aradilla, T. Schubert, and C. E. Nebel, 'Diamond-coated silicon wires for supercapacitor applications in ionic liquids', *Diam. Relat. Mater.*, 51, pp. 1–6, Jan. 2015.

[114] J. P. Alper, S. Wang, F. Rossi, G. Salviati, N. Yiu, C. Carraro, and R. Maboudian, 'Selective Ultrathin Carbon Sheath on Porous Silicon Nanowires: Materials for Extremely High Energy Density Planar Micro-Supercapacitors', *Nano Lett.*, 14, no. 4, pp. 1843–1847, Apr. 2014.

[115] S. Chatterjee, R. Carter, L. Oakes, W. R. Erwin, R. Bardhan, and C. L. Pint, 'Electrochemical and Corrosion Stability of Nanostructured Silicon by Graphene Coatings: Toward High Power Porous Silicon Supercapacitors', *J. Phys. Chem. C*, 118, no. 20, pp. 10893–10902, May 2014.

[116] K. Grigoras, J. Keskinen, L. Grönberg, J. Ahopelto, and M. Prunnila, 'Coated Porous Si for High Performance On-Chip Supercapacitors', *J. Phys. Conf. Ser.*, 557, no. 1, p. 012058, 2014.

[117] L. Sun, X. Wang, K. Zhang, J. Zou, Z. Yan, X. Hu, and Q. Zhang, 'Bi-functional electrode for UV detector and supercapacitor', *Nano Energy*, 15, pp. 445–452, Jul. 2015.

[118] F. Lu, M. Qiu, X. Qi, L. Yang, J. Yin, G. Hao, X. Feng, J. Li, and J. Zhong, 'Electrochemical properties of high-power supercapacitors using ordered NiO coated Si nanowire array electrodes', *Appl. Phys. A*, 104, no. 2, pp. 545–550, Aug. 2011.

[119] B. Tao, J. Zhang, F. Miao, J. Zhang, and L. Wan, 'Preparation and electrochemistry of NiO/SiNW nanocomposite electrodes for electrochemical capacitors', *Electrochimica Acta*, 55, pp. 5258–5262, Jul. 2010.

[120] L. Gu, Y. Wang, R. Lu, W. Wang, X. Peng, and J. Sha, 'Silicon carbide nanowires@$Ni(OH)_2$ core–shell structures on carbon fabric for supercapacitor electrodes with excellent rate capability', *J. Power Sources*, 273, pp. 479–485, Jan. 2015.

[121] D. Aradilla, D. Gaboriau, G. Bidan, P. Gentile, M. Boniface, D. Dubal, P. Gómez-Romero, J. Wimberg, T. J. S. Schubert, and S. Sadki, 'An innovative 3-D nanoforest heterostructure made of polypyrrole coated silicon nanotrees for new high performance hybrid micro-supercapacitors', *J. Mater. Chem. A*, 3, no. 26, pp. 13978–13985, Jun. 2015.

[122] D. Aradilla, G. Bidan, P. Gentile, P. Weathers, F. Thissandier, V. Ruiz, P. Gómez-Romero, T. J. S. Schubert, H. Sahin, and S. Sadki, 'Novel hybrid micro-supercapacitor based on conducting polymer coated silicon nanowires for electrochemical energy storage', *RSC Adv.*, 4, no. 50, pp. 26462–26467, Jun. 2014.

[123] D. P. Dubal, D. Aradilla, G. Bidan, P. Gentile, T. J. S. Schubert, J. Wimberg, S. Sadki, and P. Gomez-Romero, '3D hierarchical assembly of ultrathin MnO_2 nanoflakes on silicon nanowires for high performance micro-supercapacitors in Li- doped ionic liquid', *Sci. Rep.*, 5, p. 9771, May 2015.

[124] D. Pech, M. Brunet, H. Durou, P. Huang, V. Mochalin, Y. Gogotsi, P.-L. Taberna, and P. Simon, 'Ultrahigh-power micrometre-sized supercapacitors based on onion-like carbon', *Nat. Nanotechnol.*, 5, pp. 651–4, Sep. 2010.

[125] D. S. Gardner, C. W. Holzwarth, Y. Liu, S. B. Clendenning, W. Jin, B. K. Moon, C. Pint, Z. Chen, E. Hannah, R. Chen, C. P. Wang, C. Chen, E. Mäkilä, and J. L. Gustafson, 'Integrated on-chip energy storage using porous-silicon electrochemical capacitors', in *2014 IEEE International Electron Devices Meeting*, 2014, pp. 8.2.1-8.2.4.

[126] L. Oakes, A. Westover, J. W. Mares, S. Chatterjee, W. R. Erwin, R. Bardhan, S. M. Weiss, and C. L. Pint, 'Surface engineered porous silicon for stable, high performance electrochemical supercapacitors', *Sci. Rep.*, 3, p. 3020, Oct. 2013.
[127] A. P. Cohn, W. R. Erwin, K. Share, L. Oakes, A. S. Westover, R. E. Carter, R. Bardhan, and C. L. Pint, 'All Silicon Electrode Photocapacitor for Integrated Energy Storage and Conversion', *Nano Lett.*, 15, pp. 2727–2731, Apr. 2015.
[128] K. Wang, H. Wu, Y. Meng, and Z. Wei, 'Conducting Polymer Nanowire Arrays for High Performance Supercapacitors', *Small*, 10, no. 1, pp. 14–31, Jan. 2014.
[129] G. Wang, L. Zhang, and J. Zhang, 'A review of electrode materials for electrochemical supercapacitors', *Chem. Soc. Rev.*, 41, no. 2, pp. 797–828, Jan. 2012.
[130] S. Sadki, P. Schottland, N. Brodie, and G. Sabouraud, 'The mechanisms of pyrrole electropolymerization', *Chem. Soc. Rev.*, 29, no. 5, pp. 283–293, Jan. 2000.
[131] K. Wang, J. Huang, and Z. Wei, 'Conducting Polyaniline Nanowire Arrays for High Performance Supercapacitors', *J. Phys. Chem. C*, 114, no. 17, pp. 8062–8067, May 2010.
[132] C. Merlet, B. Rotenberg, P. A. Madden, P.-L. Taberna, P. Simon, Y. Gogotsi, and M. Salanne, 'On the molecular origin of supercapacitance in nanoporous carbon electrodes', *Nat. Mater.*, 11, no. 4, pp. 306–310, Apr. 2012.
[133] Z. Lin, P.-L. Taberna, and P. Simon, 'Advanced analytical techniques to characterize materials for electrochemical capacitors', *Curr. Opin. Electrochem.*, 9, pp. 18–25, Jun. 2018.
[134] F.-G. Banica, in *Chemical Sensors and Biosensors: Fundamentals and Applications*, John Wiley & Sons, 2012, pp. 1–20.
[135] Calvo E., 'Chapter 9', in *Piezoelectric Transducers and Applications*, Springer Science & Business Media, 2008, pp. 241–257.
[136] G. S. Ostrom and D. A. Buttry, 'Quartz crystal microbalance studies of deposition and dissolution mechanisms of electrochromic films of diheptylviologen bromide', *J. Electroanal. Chem. Interfacial Electrochem.*, 256, no. 2, pp. 411–431, Dec. 1988.
[137] D. A. Buttry and M. D. Ward, 'Measurement of interfacial processes at electrode surfaces with the electrochemical quartz crystal microbalance', *Chem. Rev.*, 92, no. 6, pp. 1355–1379, Sep. 1992.
[138] S. Bruckenstein and M. Shay, 'Experimental aspects of use of the quartz crystal microbalance in solution', *Electrochimica Acta*, 30, no. 10, pp. 1295–1300, Oct. 1985.
[139] F. N. Dultsev, E. A. Kolosovsky, and I. A. Mik, 'New Procedure to Record the Rupture of Bonds between Macromolecules and the Surface of the Quartz Crystal Microbalance (QCM)', *Langmuir*, 28, no. 39, pp. 13793–13797, Oct. 2012.
[140] A. A. Vives, 'Chapter 5', in *Piezoelectric Transducers and Applications*, Springer Science & Business Media, 2008, pp. 177–186.
[141] L. Rodriguez-Pardo, J. F. Rodriguez, C. Gabrielli, H. Perrot, and R. Brendel, 'Sensitivity, noise, and resolution in QCM sensors in liquid media', *IEEE Sens. J.*, 5, no. 6, pp. 1251–1257, Dec. 2005.
[142] L. Rodriguez-Pardo, J. Fariña, C. Gabrielli, H. Perrot, and R. Brendel, 'Resolution in quartz crystal oscillator circuits for high sensitivity microbalance sensors in damping media', *Sens. Actuators B Chem.*, 103, no. 1, pp. 318–324, Sep. 2004.
[143] G. Sauerbrey, 'Verwendung von Schwingquarzen zur Wägung dünner Schichten und zur Mikrowägung', *Z. Für Phys.*, 155, no. 2, pp. 206–222, Apr. 1959.
[144] K. Bizet, C. Gabrielli, and H. Perrot, 'Immunodetection by quartz crystal microbalance', *Appl. Biochem. Biotechnol.*, 89, no. 2–3, p. 139, Nov. 2000.

[145] F. Scholz, Ed., 'Chapter 13', in *Electroanalytical Methods: Guide to Experiments and Applications*, 2nd ed., Berlin Heidelberg: Springer-Verlag, 2010, pp. 257–270.
[146] S. Sigalov, M. D. Levi, L. Daikhin, G. Salitra, and D. Aurbach, 'Electrochemical quartz crystal admittance studies of ion adsorption on nanoporous composite carbon electrodes in aprotic solutions', *J. Solid State Electrochem.*, 18, no. 5, pp. 1335–1344, May 2014.
[147] S. Bruckenstein and S. Swathirajan, 'Potential dependence of lead and silver underpotential coverages in acetonitrile using a piezoelectric crystal oscillator method', *Electrochimica Acta*, 30, no. 7, pp. 851–855, Jul. 1985.
[148] M. Hepel and S. Bruckenstein, 'Tracking anion expulsion during underpotential deposition of lead at silver using the quartz microbalance', *Electrochimica Acta*, 34, no. 11, pp. 1499–1504, Nov. 1989.
[149] M. Hepel, K. Kanige, and S. Bruckenstein, 'In situ underpotential deposition study of lead on silver using the electrochemical quartz crystal microbalance: Direct evidence for lead(II) adsorption before spontaneous charge transfer', *J. Electroanal. Chem. Interfacial Electrochem.*, 266, no. 2, pp. 409–421, Jul. 1989.
[150] R. Schumacher, G. Borges, and K. K. Kanazawa, 'The quartz microbalance: A sensitive tool to probe surface reconstructions on gold electrodes in liquid', *Surf. Sci. Lett.*, 163, no. 1, pp. L621–L626, Nov. 1985.
[151] C. R. Arias, C. Debiemme-Chouvy, C. Gabrielli, C. Laberty-Robert, A. Pailleret, H. Perrot, and O. Sel, 'New Insights into Pseudocapacitive Charge-Storage Mechanisms in Li-Birnessite Type MnO2 Monitored by Fast Quartz Crystal Microbalance Methods', *J. Phys. Chem. C*, 118, no. 46, pp. 26551–26559, Nov. 2014.
[152] M. D. Levi, S. Sigalov, D. Aurbach, and L. Daikhin, 'In Situ Electrochemical Quartz Crystal Admittance Methodology for Tracking Compositional and Mechanical Changes in Porous Carbon Electrodes', *J. Phys. Chem. C*, 117, no. 29, pp. 14876–14889, Jul. 2013.
[153] S. Sigalov, M. D. Levi, G. Salitra, D. Aurbach, and J. Maier, 'EQCM as a unique tool for determination of ionic fluxes in microporous carbons as a function of surface charge distribution', *Electrochem. Commun.*, 12, no. 12, pp. 1718–1721, Dec. 2010.
[154] S. Sigalov, M. D. Levi, G. Salitra, D. Aurbach, A. Jänes, E. Lust, and I. C. Halalay, 'Selective adsorption of multivalent ions into TiC-derived nanoporous carbon', *Carbon*, 50, no. 10, pp. 3957–3960, Aug. 2012.
[155] W.-Y. Tsai, P.-L. Taberna, and P. Simon, 'Electrochemical Quartz Crystal Microbalance (EQCM) Study of Ion Dynamics in Nanoporous Carbons', *J. Am. Chem. Soc.*, 136, no. 24, pp. 8722–8728, Jun. 2014.
[156] J. N. Barisci, G. G. Wallace, and R. H. Baughman, 'Electrochemical quartz crystal microbalance studies of single-wall carbon nanotubes in aqueous and non-aqueous solutions', *Electrochimica Acta*, 46, no. 4, pp. 509–517, Dec. 2000.
[157] M. D. Levi, G. Salitra, N. Levy, D. Aurbach, and J. Maier, 'Application of a quartz-crystal microbalance to measure ionic fluxes in microporous carbons for energy storage', *Nat. Mater.*, 8, no. 11, pp. 872–875, Nov. 2009.
[158] M. D. Levi, S. Sigalov, G. Salitra, D. Aurbach, and J. Maier, 'The Effect of Specific Adsorption of Cations and Their Size on the Charge-Compensation Mechanism in Carbon Micropores: The Role of Anion Desorption', *ChemPhysChem*, 12, no. 4, pp. 854–862, Mar. 2011.
[159] J. M. Griffin, A. C. Forse, W.-Y. Tsai, P.-L. Taberna, P. Simon, and C. P. Grey, '*In situ* NMR and electrochemical quartz crystal microbalance techniques reveal the structure of the electrical double layer in supercapacitors', *Nat. Mater.*, 14, no. 8, pp. 812–819, Aug. 2015.

[160] M. D. Levi, N. Levy, S. Sigalov, G. Salitra, D. Aurbach, and J. Maier, 'Electrochemical Quartz Crystal Microbalance (EQCM) Studies of Ions and Solvents Insertion into Highly Porous Activated Carbons', *J. Am. Chem. Soc.*, 132, no. 38, pp. 13220–13222, Sep. 2010.

[161] P. K. Nayak and N. Munichandraiah, 'An EQCM investigation of capacitance of MnO_2 in electrolytes containing multivalent cations', *J. Electroanal. Chem.*, 685, pp. 37–40, Oct. 2012.

[162] Y.-H. Chu, C.-C. Hu, and K.-H. Chang, 'Electrochemical quartz crystal microbalance study of amorphous MnO_2 prepared by anodic deposition', *Electrochimica Acta*, 61, pp. 124–131, Feb. 2012.

[163] S. Bourkane, C. Gabrielli, and M. Keddam, 'Kinetic study of electrode processes by ac quartz electrogravimetry', *J. Electroanal. Chem. Interfacial Electrochem.*, 256, no. 2, pp. 471–475, Dec. 1988.

[164] L. To Thi Kim, C. Debiemme-Chouvy, C. Gabrielli, and H. Perrot, 'Redox Switching of Heteropolyanions Entrapped in Polypyrrole Films Investigated by ac Electrogravimetry', *Langmuir*, 28, no. 38, pp. 13746–13757, Sep. 2012.

[165] C. Gabrielli, M. Keddam, N. Nadi, and H. Perrot, 'Ions and solvent transport across conducting polymers investigated by ac electrogravimetry. Application to polyaniline', *J. Electroanal. Chem.*, 485, no. 2, pp. 101–113, May 2000.

[166] F. Escobar-Teran, A. Arnau, J. V. Garcia, Y. Jiménez, H. Perrot, and O. Sel, 'Gravimetric and dynamic deconvolution of global EQCM response of carbon nanotube based electrodes by Ac-electrogravimetry', *Electrochem. Commun.*, 70, pp. 73–77, Sep. 2016.

[167] F. Escobar-Teran, H. Perrot, and O. Sel, 'Charge storage properties of single wall carbon nanotubes/Prussian blue nanocube composites studied by multi-scale coupled electrogravimetric methods', *Electrochimica Acta*, 271, pp. 297–304, May 2018.

[168] H. Goubaa, F. Escobar-Teran, I. Ressam, W. Gao, A. El Kadib, I. T. Lucas, M. Raihane, M. Lahcini, H. Perrot, and O. Sel, 'Dynamic Resolution of Ion Transfer in Electrochemically Reduced Graphene Oxides Revealed by Electrogravimetric Impedance', *J. Phys. Chem. C*, 121, no. 17, pp. 9370–9380, May 2017.

[169] M. D. Levi, N. Shpigel, S. Sigalov, V. Dargel, L. Daikhin, and D. Aurbach, 'In Situ Porous Structure Characterization of Electrodes for Energy Storage and Conversion by EQCM-D: a Review', *Electrochimica Acta*, 232, pp. 271–284, Apr. 2017.

[170] M. D. Levi, L. Daikhin, D. Aurbach, and V. Presser, 'Quartz Crystal Microbalance with Dissipation Monitoring (EQCM-D) for in-situ studies of electrodes for supercapacitors and batteries: A mini-review', *Electrochem. Commun.*, 67, pp. 16–21, Jun. 2016.

[171] K. J. Laidler and J. H. Meiser, in *Physical chemistry*, Menlo Park, Calif.: Benjamin/Cummings Pub. Co., 1982, p. 833.

[172] N. Shpigel, M. D. Levi, S. Sigalov, O. Girshevitz, D. Aurbach, L. Daikhin, N. Jäckel, and V. Presser, 'Non-Invasive In Situ Dynamic Monitoring of Elastic Properties of Composite Battery Electrodes by EQCM-D', *Angew. Chem. Int. Ed.*, 54, no. 42, pp. 12353–12356, Oct. 2015.

[173] P. W. Chapman, O. N. Tufte, J. D. Zook, and D. Long, 'Electrical Properties of Heavily Doped Silicon', J. Appl. Phys., 34, no. 11, pp. 3291–3295, Nov. 1963.

Chapter 2:

Methods

Table of contents

I. Morphological characterization

Characterizing the morphology of the vertical nanostructures grown on microbalance electrodes for this study is a primordial step. Before addressing the need to characterize the electrochemical processes at the interface of these materials, it is important to make sure that they entail the expected morphology.

For this thesis, the morphology of the electrodes was studied using scanning electron microscopy (SEM). **Fig. I-1** shows a schematic description of a SEM set-up. The electron gun generates a primary electron beam in a vacuum. The beam is collimated by electromagnetic condenser lenses, focused by an objective lens, and scanned across the surface of the sample by electromagnetic deflection coils [1]. As a consequence of the primary beam's interaction with the sample, secondary electrons are emitted [2]. These electrons are selectively collected in the secondary electron detector through a grid held at a low positive potential with respect to the sample [1]. There, the secondary electrons are counted (number of electrons arrived/unit time) and the count rate is translated into an electrical signal, which is then used to obtain a visualization of the sample [2].

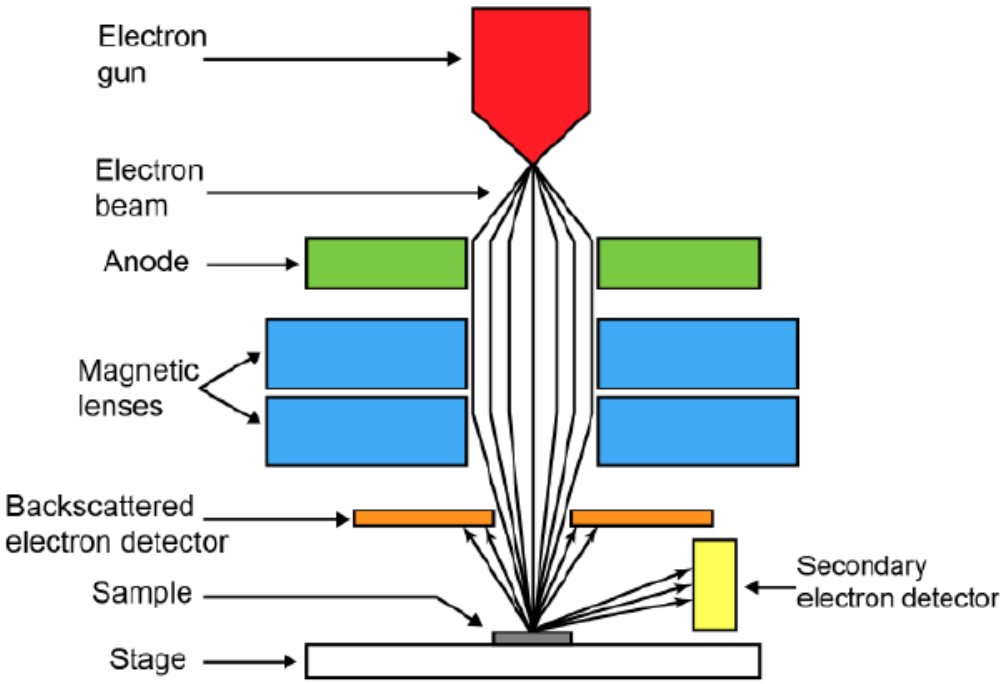

Figure I-1: Simplistic view of a scanning electron microscope in operation. [3]

The resulting image reflects the surface topology, since the number of electrons that are collected from each point is dependent on surface topology. In shallow surfaces fewer emitted electrons reach the detector, resulting in darker areas, as opposite to edges and convex surfaces where more electrons escape and reach the detector resulting in brighter areas. Charge builds up on the sample surface due to the electron bombardment of the primary beam and in the case of non-conductive samples this charge cannot be dissipated. This results in images that are too bright throughout the sample. To avoid this phenomena, samples can be sputtered with a very thin layer of metals such as gold or gold/palladium [1], however this was not necessary for our electrodes because they all present good electrical contact with the current collector.

There are various types of electron guns. In comparison to thermionic electron guns, field emission guns (FEGs) provide enhanced electron brightness (approximately x 100) and longer lifetime. Furthermore, because of the lower electron energy spread (0.3 eV), the chromatic aberration is significantly reduced and probes smaller than 2 nm can be formed, thus, providing much higher resolution for SEM images [2].

In this Ph.D. thesis, the morphology and the thickness of the nanostructured electrodes were investigated with FEGSEM (Zeiss, Ultra 55) at an accelerating voltage of 10 kV. Before the analysis, the samples were fixed onto an aluminum stub with two pincers. Images were taken at two different angles:

- At 45° in order to investigate surface topology and morphology.
- At 90° (cross-sectional view) after cleavage of the sample to investigate the height of the nanostructures.

II. Electrochemical characterization of supercapacitors

Supercapacitors, also called “Ultracapacitors”, are electrochemical capacitors where the dielectric material between the two electrodes in a classical capacitor has been replaced by an electrolyte. The performances of a supercapacitor are therefore driven by the electrochemical properties of the electrode and the electrolyte. These properties are commonly investigated with electrochemical measurements such as cyclic voltammetry (CV), galvanostatic charge/discharge (GCD) cycles and electrochemical impedance spectroscopy (EIS), providing key information about a given supercapacitor configuration: Adequate potential window, specific capacitance, equivalent series resistance (ESR), energy and power densities, cycling stability, etc. In a second step, electrogravimetric explorations were preformed namely classical EQCM, *ac*-electrogravimetry and electroacoustic impedance. These techniques were selected to deeper examine the mechanism of interaction between the electrolyte and the nanostructured electrodes.

This section describes how the first measurements were performed on SiNW, VOGN and PEDOT nanowire electrodes before using the electrogravimetric techniques in order to get a first idea of the behavior and performances of these materials prior to their successful growth on a microbalance. Two different methods were adopted:

- Using a three electrode configuration set-up to obtain general information over the electrochemical processes involved: The studied material is the working electrode, a platinum wire is used as a counter electrode and a commercial non-aqueous Ag/Ag^+ electrode from ALS Japan is used as a reference electrode (**Fig. II-1a**).
- Using two electrodes in a symmetric coin cell device (CR2032) to provide the realistic performances of the final supercapacitor (**Fig. II-1b**).

The experiments were performed with a VSP-300 potentiostat/galvanostat/EIS from Bio-Logic. All the electrochemical experiments were conducted in an Ar-filled glove box under water and oxygen levels below 1 ppm to avoid the presence of water in the organic and ionic liquid-based electrolytes used in this thesis.

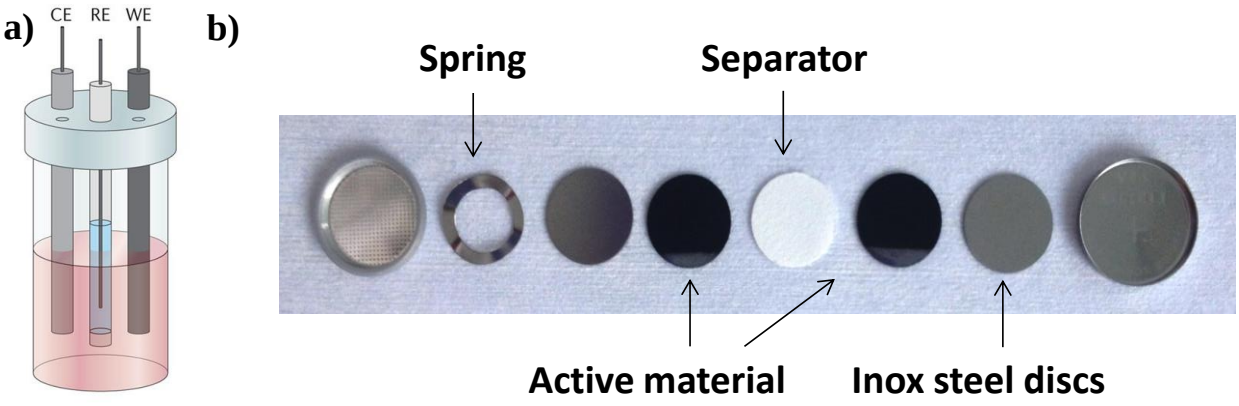

Figure II-1: a) Three-electrode characterization cell, image from [4]. **b)** Components that are stacked together to form a coin cell.

II-1. CV and galvanostatic charge/discharge cycles

CV is a potentiodynamic electrochemical measurement technique that measures current versus potential. The principle is to perform successive cyclic scans by setting the potential between the working electrode and the reference electrode while the current is measured across the working electrode and the counter electrode [5]. For two-electrode setups, the counter electrode is considered as the reference. The resulting data are plotted as current versus applied potential to give the cyclic voltammograms. The potential range is in general limited by the electrolyte stability window.

Cyclic voltammetry provides quantitative and qualitative information on the capacitive behavior between the electrolyte and the active materials. The presence of parasitic faradaic reactions can also be identified. A typical cyclic voltammogram curve, for capacitance diagnosis, is shown in **Fig. II-2**.

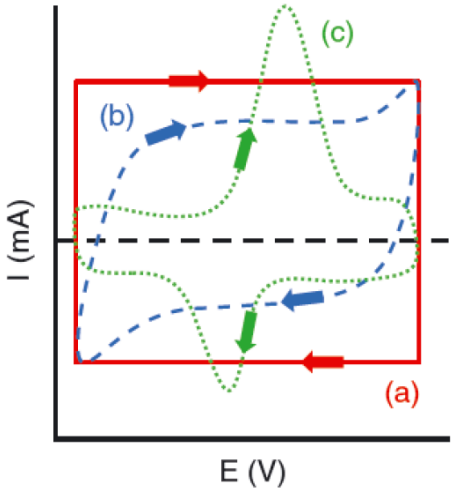

Figure II-2: Voltammograms for **a)** an ideal supercapacitor, **b)** typical supercapacitor response, **c)** faradaic reactions. [6]

In **Fig. II-2a**, the rectangular CV represents an ideal supercapacitor response. However, in practice, a more or less deformed rectangular shape is obtained due to contact resistance and electrolyte resistance in the pores (**Fig. II-2b**). Two redox peaks due to faradaic reactions can be also observed in **Fig. II-2c**. The charge (Q) stored in the electrochemical system can be calculated using the following equation:

$$Q = \int i(t).dt = \frac{1}{v}\int i(E).dE \qquad \textbf{(Eq. II-1)}$$

where i is the current, E is the potential and $v = \frac{dE}{dt}$ is the CV scan rate.

In the case of a capacitive behavior, this charge can be divided by the potential range (ΔV) to obtain a capacitance value (C) in Farads:

$$C = \frac{Q}{\Delta V} \qquad \textbf{(Eq. II-2)}$$

From **Eq. II-1&2**, if the CV result is rectangular ($i(t) = \pm I$) we deduce the following expression for the capacitance:

$$C = \frac{I}{v} \qquad \textbf{(Eq. II-3)}$$

Galvanostatic charge/discharge (GCD) cycling is an alternative method to measure the capacitance, resistance and cycling stability of the electrode materials. This technique consists in performing charge/discharge cycles at a constant current density (I) while the potential response

(V) is measured over time. From the slope of the discharge curve, the cell capacitance (C) can be calculated using the following equation [7]:

$$C = \frac{I}{\frac{dV}{dt}} \quad \textbf{(Eq. II-4)}$$

Using **Eq. II-4**, the evolution of the capacitance as a function of the GCD cycle number is calculated to estimate the cycling stability of the supercapacitor device. The restituted energy (W_D) and power output (P) of the supercapacitor can also be calculated using the following equations:

$$W_D = \frac{1}{2}C(\Delta V)^2 = \frac{1}{2}I \times \Delta V \Delta t_D$$
$$P = \frac{W}{\Delta t_D} = \frac{1}{2}I \times \Delta V \quad \textbf{(Eq. II-5)}$$

where Δt_D is the discharging time of the device.

The energy needed to charge the supercapacitor (W_C) can be calculated with **Eq. II-5** by replacing Δt_D with the charging time (Δt_C). Thus, the overall device efficiency (η) can be estimated with the following equation [8]:

$$\eta = \frac{W_D}{W_C} = \frac{\Delta t_D}{\Delta t_C} \quad \textbf{(Eq. II-6)}$$

II-2. Electrochemical impedance spectroscopy (EIS)

The EIS measurements, based on frequency modulation, provide qualitative and quantitative information on the studied electrochemical system (capacitive, resistive, diffusive behavior etc.). In contrast to cyclic voltammetry, electrochemical impedance is based on the collection of an alternating current (*ac*) resulting from applying a sinusoidal potential perturbation with a small amplitude (typically about tens of mV) [5]. The frequency modulation allows the separation of the different reactions kinetics: fast phenomena occur at high frequencies while slower phenomena are visible at lower frequencies [9]. In general, electrochemical systems have a nonlinear current-voltage characteristic curves I=f(V) (**Fig. II-3**). However, working only on a small portion of this curve, the relationship between ΔV (low amplitude sinusoidal perturbation imposed around the stationary potential) and ΔI (low amplitude sinusoidal response in current) may be considered as linear (**Fig. II-3**). [10]

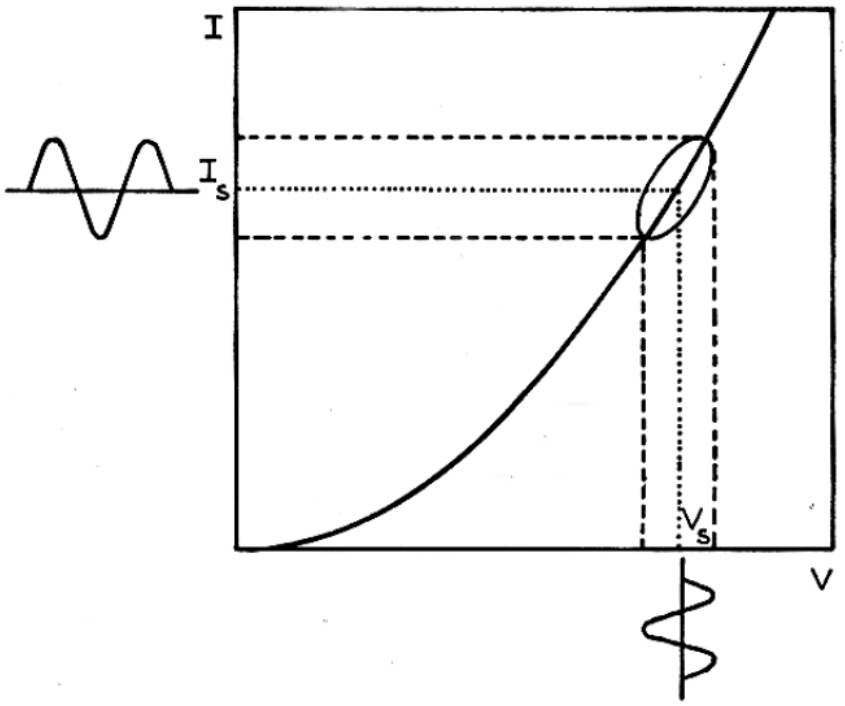

Figure II-3: Linear current response to a low amplitude sinusoidal perturbation potential around a stationary value. [10]

Therefore, by applying a low amplitude sinusoidal perturbation (ΔV) to the system around a stationary potential (V_s) the current response (ΔI) will also be sinusoidal in shape with a small amplitude around a stationary value I_s. The concept of impedance is a generalization of the

concept of resistance, applicable to sinusoidal functions with the application of Fourier transforms to the current and potential time-dependent functions. The electrochemical impedance Z(ω) can then be defined as the following transfer function:

$$Z(\omega) = \frac{\Delta V}{\Delta I}(\omega) \qquad \textbf{(Eq. II-7)}$$

where $\omega = 2\pi f$ corresponds to the pulsation and f to the frequency.

Z(ω) is a complex number that can be represented either in polar coordinates (|Z|,φ), or cartesian coordinates (Re(Z), Im(Z)). The Nyquist diagram is a representation of -Im(Z) versus Re(Z) in cartesian coordinates (**Fig. II-4**) while the Bode diagram plots the measured impedance in polar coordinates within two graphs: |Z|(ω) and φ(ω) (**Fig. II-5b**). [11]

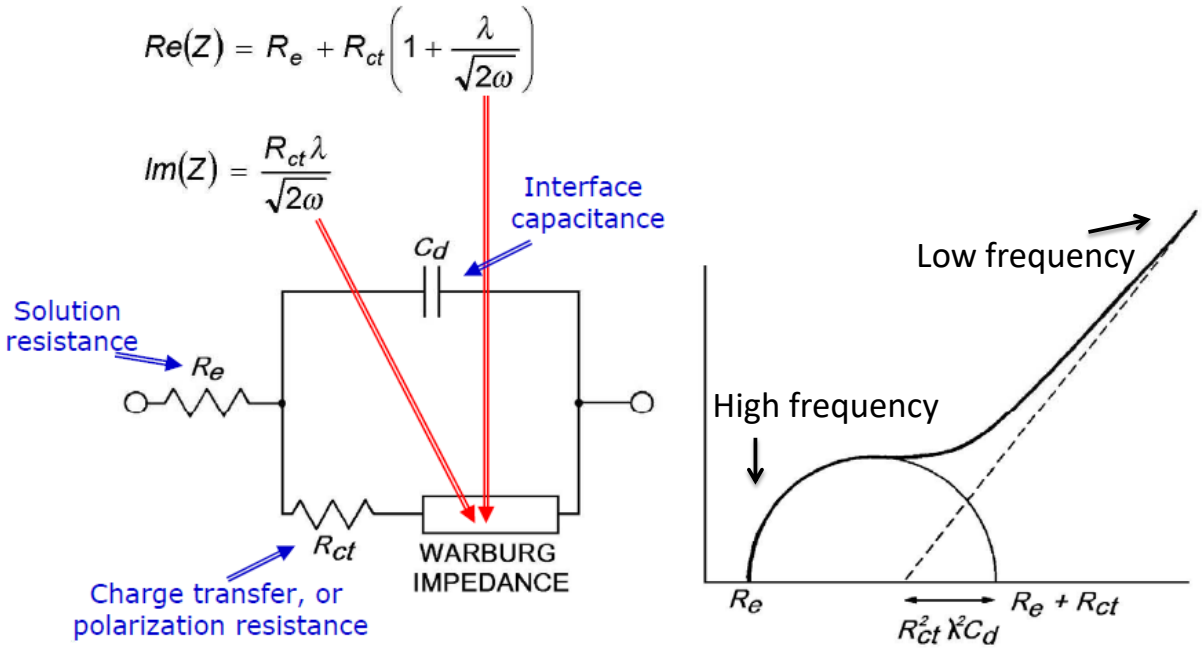

Figure II-4: Typical equivalent circuit used to fit EIS data for supercapacitors and the resulting impedance Nyquist diagram. Adapted from [11].

Fig. II-5 depicts an example of Nyquist and Bode diagrams for EIS measurements performed on MoS_2 nanosheet supercapacitor electrodes [12]. From the Nyquist diagram, qualitative and quantitative information can be obtained on the electrode's capacitive behavior and the system's equivalent series resistance (ESR) R_e can be easily extracted from the point of intersection between the impedance curve and the abscise axis (where Im(Z)=0) (**Fig. II-4**). The slope of the low frequency line is linked to the capacitive behavior of the electrochemical system,

with mostly capacitive electrodes presenting a nearly vertical line. Diffusion of ions results in a deviation of the experimental data from the vertical line. The imaginary part of the impedance can be used to estimate the frequency dependence of the capacitance with the following equation [13]:

$$C = -\frac{1}{2\pi f \times Im(Z)} \quad \textbf{(Eq. II-8)}$$

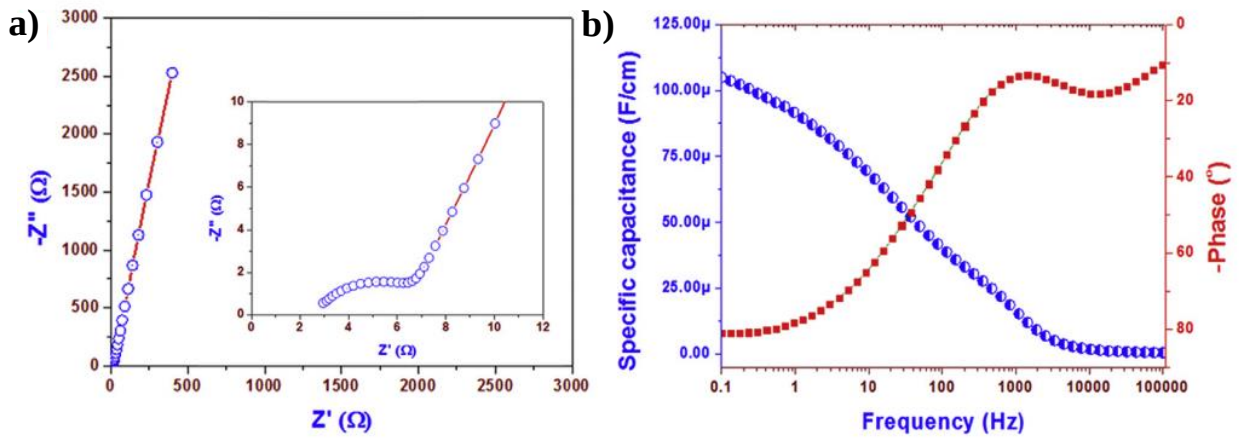

Figure II-5: a) EIS Nyquist plot of MoS_2 nanosheet supercapacitor electrodes. A zoom at high frequencies is shown as inset. **b)** Corresponding specific capacitance and Bode phase φ(ω). [12]

The Bode diagram can be used to obtain further details from EIS data (**Fig. II-5b**). For pure EDLC behavior, the impedance phase φ(ω) at low frequencies is around -90°. This value is closer to -45° for pseudo-capacitors [12]. The intersection of φ(ω) with -45° at a given frequency $f_{45°}$ provides the relaxation time constant $\tau_0 = \frac{1}{f_{45°}}$, corresponding to the minimum time needed to discharge all the energy from the device with an efficiency of more than 50% [14].

In order to extract more information from EIS measurements, a model should be used to fit the data. **Fig. II-4** depicts the electrical model and the corresponding impedance equations used in this thesis that are often used to describe a supercapacitor electrode/electrolyte interface. This model takes into account the electrolyte's resistance R_e in a series resistance and the double layer capacitance in a capacitor C_d. In parallel with C_d, a transfer resistance R_{ct} and a Warburg element are added. The Warburg element has the following impedance:

$$Z_W(\omega) = \frac{\lambda}{\sqrt{\omega}} + \frac{\lambda}{j\sqrt{\omega}} \quad \textbf{(Eq. II-9)}$$

where λ is the Warburg coefficient that accounts for diffusion.

This model is used to fit the experimental data within the EC-Lab software and it allows the derivation of the capacitance C_d, the transfer resistance R_{ct} and the influence of diffusion with the Warburg coefficient λ.

III. Electrogravimetric characterization

III-1. Resonator electrode preparation

A piezoelectric crystal has the very interesting property of converting a mechanical stress into an electrical signal, which can be used to make a transducer or a sensor. [15]. The piezoelectric transducer is the essential component of a quartz crystal microbalance (QCM), a very precise and attractive tool for gravimetric measurements [16].

Designed with a specific shape and thickness, the quartz crystal and its electrodes make up a piezoelectric resonator: Connected to an oscillator circuit, the QCM triggers an oscillating potential at a resonance frequency determined by its shape. The resonant frequency of the quartz resonator then varies under the effect of changes in mass, viscoelasticity and shape of the electrode surface [5], [15], [17].

In the present thesis, various types of vertical nanostructures were grown on the surface of piezoelectric resonator. SiNW grown by CVD and VOGN synthesized from a PECVD derivative technique (ECR-CVD) were performed at high temperatures (more than 400°C) under harsh conditions (presence of reactive gases and/or plasma). Under such temperatures, the standard quartz crystals change phase and lose their piezoelectric properties [18]. More robust, piezoelectric crystals made from $GaPO_4$ can maintain their piezoelectric properties up to around 800°C. Therefore, $GaPO_4$ piezoelectric resonators have been used for our studies on both SiNWs and VOGNs nanostructures. In the case of electropolymerized PEDOT nanowires, harsh growth conditions were not necessary and classical quartz resonators could be used.

The piezoelectric crystals are not the only parts of the resonator suffering from the harsh growth conditions of SiNWs and VOGNs. The patterned electrodes deposited on both sides of the crystal to form the resonator can peel off or be oxidized and thus lose their conducting properties. And in the case of SiNW growth, not all metals can be used: Gold, tin and silver are known to catalyze the VLS reaction and form an alloy with silicon during the CVD process. To achieve the growth of these nanostructures while maintaining the QCM functional, various electrode configurations have been tested. Thus, patterned depositions of various metals were performed on plain $GaPO_4$ crystals provided from AWS (Spain).

In every electrode configuration, thin layers of around 10 nm of chromium or titanium were used as adhesion layers in order to prevent the electrode from peeling off during growth. These layers were deposited by evaporation in a low pressure chamber. The core of the electrode was made from a thicker layer of titanium, platinum or gold (200-400 nm) deposited by radio-frequency sputtering on the adhesion layer (**Fig. III-1**).

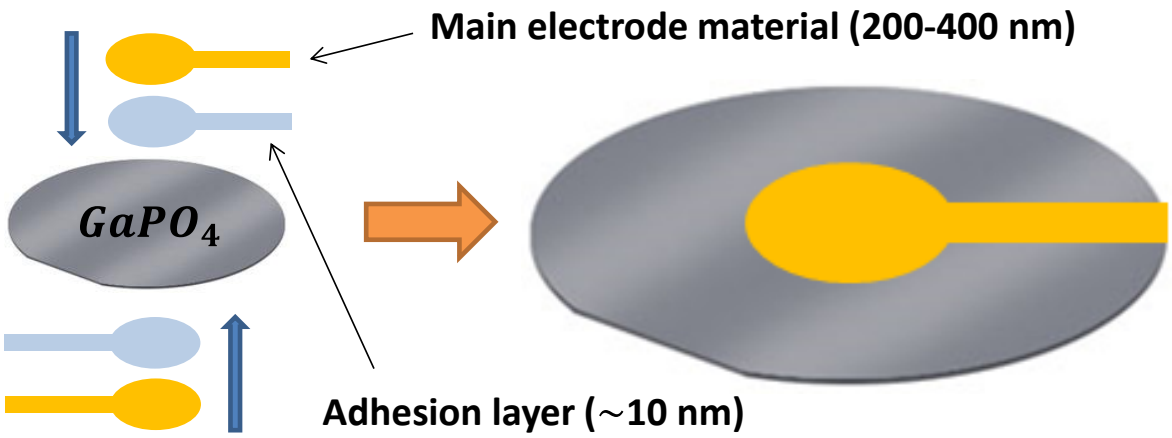

Figure III-1: QCM electrode layer configuration.

Radio frequency (RF) sputtering is a deposition process whereby particles are ejected from a solid target material due to bombardment of the target by energetic particles. In this process, the substrates are placed into a vacuum chamber, also known as the sputter chamber, pumped until sufficient vacuum (10^{-5} torr or less) is obtained. Argon (Ar) gas is then introduced into the chamber. Within the chamber there may be one or multiple sputter guns onto which targets are placed; targets are disks made out of the materials that are to be deposited, or their metal counterparts that will be oxidized during the deposition. A RF power supply is connected to the sputter gun and when the power is turned on an electric field is generated between the target and the substrate. The current is alternating, so free electrons are alternately attracted to and repelled from the target. As the electrons move between the target and the substrate they collide with argon atoms and knock off more electrons. This process continues exponentially until a cloud of argon ions (Ar^+) and electrons, called plasma, is generated. The argon ions bombard the surface of the target and physically knock off pieces which are ballistically ejected and deposited onto the substrate (**Fig. III-2**). To prevent the same process at the surface of the substrate, magnets are placed within the sputter gun to confine the plasma in a region

immediately above the target. In this way, atoms from the target material are sputtered onto the substrate and over time a thin film is deposited. [19]

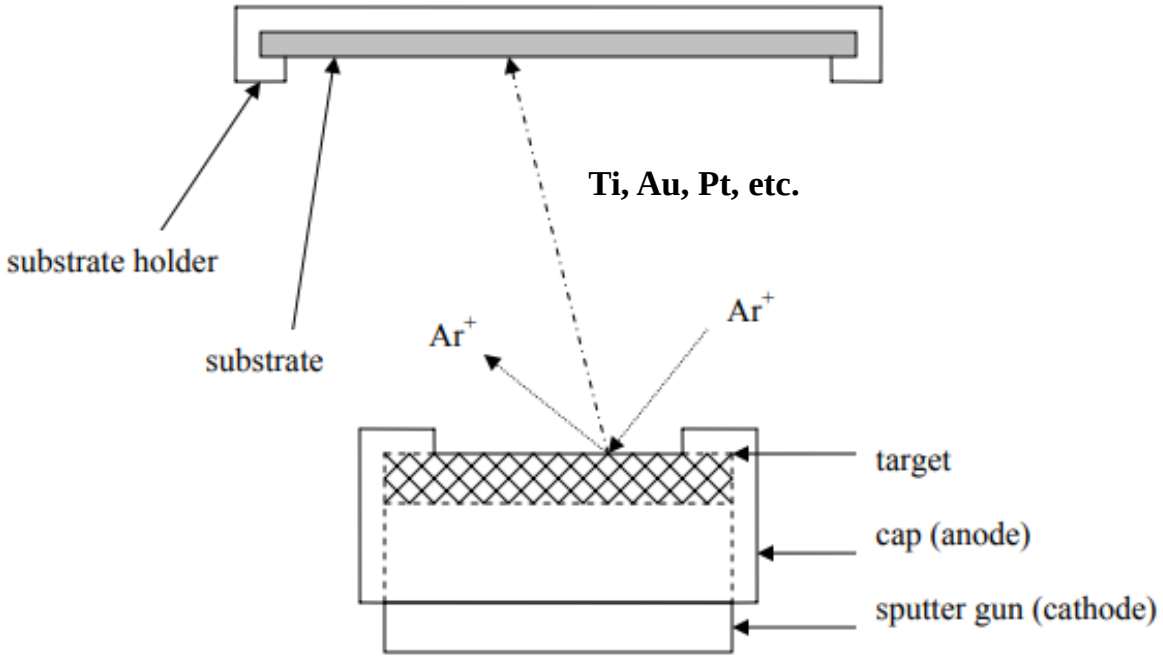

Figure III-2: RF Sputtering deposition process. Adapted from [19].

III-2. Electroacoustic admittance measurements

In chapter 1-III.3, we have seen that the investigation of nanostructured electrodes with electrogravimetric measurements is limited by hydrodynamic damping in the presence of the electrolyte. The viscous drag force exerted on the electrode nanostructures causes a shift and a damping of the resonance frequency peak of the QCM. To understand if this damping will interfere too strongly with the electrogravimetric measurement, it is first needed to quantify this damping (**Fig. III-3**). The dissipation factor $D = \frac{W}{f_0}$, where W is the full-width at half-height of the resonance peak and f_0 is the resonance frequency, has been proposed by Levi et. al. to quantify the hydrodynamic damping of a QCM sensor [20], [21]. The quality factor $Q = \frac{f_0}{W}$ is the inverse of dissipation factor and can equally be used to quantify the degradation of the resonator's quality. For this thesis the latter will be used.

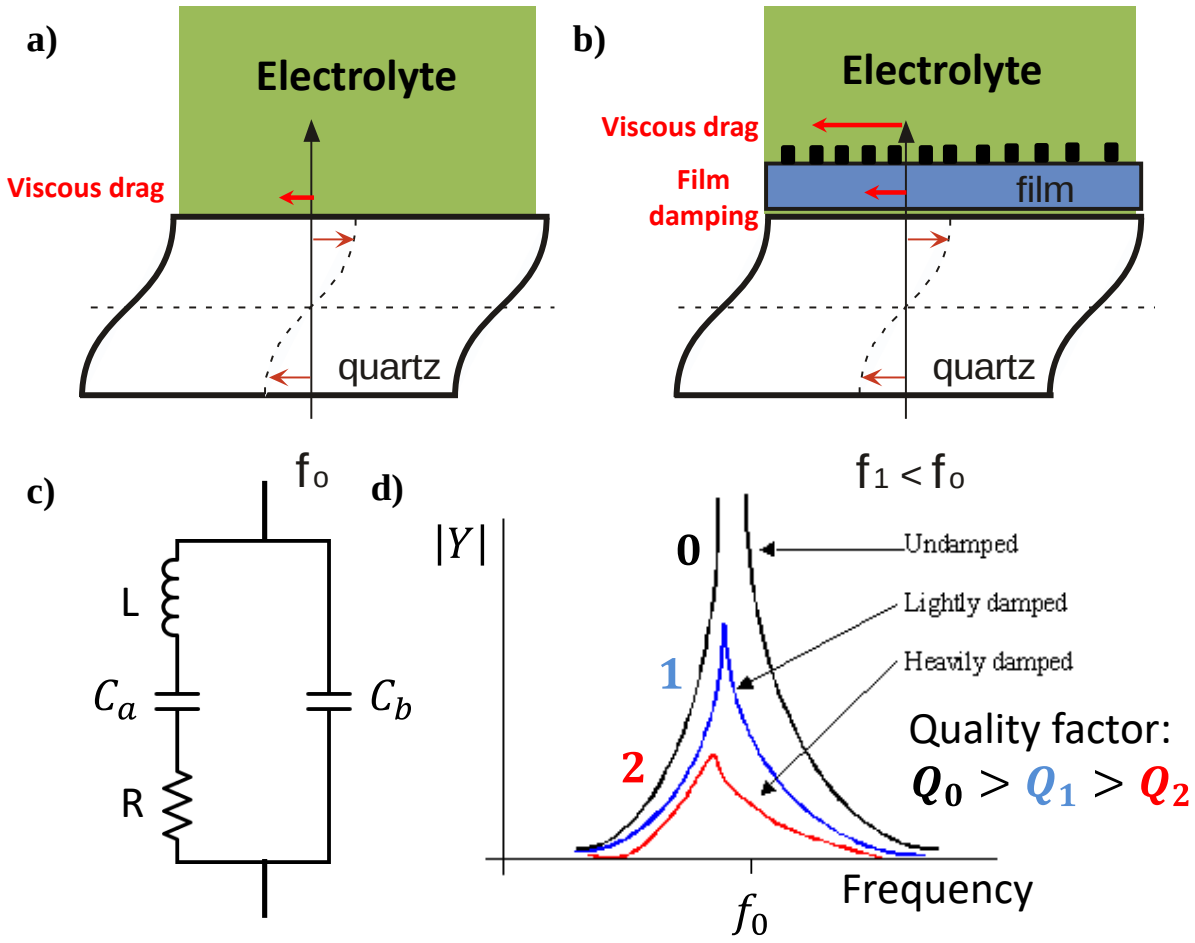

Figure III-3: Schematic of the sources of damping on a resonator **a)** before film growth and **b)** after film growth. **c)** Equivalent circuit of a QCM. **d)** Admittance modulus plots around resonance frequency for undamped, lightly damped and heavily damped resonators.

To calculate the quality factor, electroacoustic admittance measurements were performed using a network analyzer (Agilent 4194A). In a range of frequencies around the resonant frequency of the QCM, the network analyzer is used to measure the electrical admittance $Y = \frac{1}{Z}$ of the resonator, where Z is the impedance. A peak of admittance is measured at the resonant frequency f_0 (**Fig. III-3d**) and fitted by the frequency analyzer with the electrical circuit shown in **Fig. III-3c**. The values of L, C_a, C_b and R are extracted with a Lab-made software and the width of the peak at mid-height is calculated. The value of the resistance R is especially useful to obtain information about the quality of the resonator: around 10-20 Ω without film, its value shouldn't go beyond a few hundred ohms with the film in air. The quality factor $Q = \frac{f_0}{W}$ is then derived from the resonance frequency f_0 and the width at mid-height W. Alternatively Q can be derived from the values of L and R in the resonator's equivalent circuit: $Q = \frac{\omega L}{R} = \frac{2\pi f_0 L}{R}$. This value is compared in four different configurations as follow:

- In air before film growth.
- In air after film growth.
- In solution before film growth (**Fig. III-3a**).
- In solution after film growth (**Fig. III-3b**).

In literature, no clear protocol or quality factor limits have been described to arbitrate whether the resonator can be used for electrogravimetric measurements or not. In this thesis we make the assumption that the contribution of viscous dynamic damping is considered small compared to the gravimetric contribution if the shift in resonance frequency Δf after film deposition is much larger than the shift in peak width ΔW and also if the quality factor is not considerably reduced. The experiments performed with various Q factors throughout this PhD work have shown that a precise limit for good measurements cannot be defined as the results also depend on the amplitude of the mass variations to measure. With electrochemical systems presenting large mass variations, lower values of Q are acceptable.

III-3. Classical EQCM measurements

The first electrogravimetric technique used for characterizing the nanostructured materials is the electrochemical quartz crystal microbalance (EQCM), a combination of CV and microbalance frequency measurements. The overall set-up used for these experiments is depicted in **Fig. III-4a**. A lab made microbalance developed at the LISE laboratory is used to measure mass/frequency changes. The QCM resonator is inserted in an electrochemical cell (AWS Company, Spain) and connected to the oscillator circuit (**Fig. III-4b-c**). Then the electrolyte, a Pt grid as counter electrode and a non-aqueous Ag/Ag^+ reference electrode (ALS Japan) were added to the cell and connected to the potentiostat (Bio-Logic VSP-300), with the top electrode of the QCM as the working electrode. A Fluke PM6685 frequency counter is connected to the oscillator circuit to measure the resonance frequency and it's 5V analogic output is connected to the potentiostat's auxiliary input. To prevent water and oxygen contamination of the electrolyte and avoid electrical noise in the oscillator circuit, both the electrochemical cell and the oscillator circuit were introduced in an argon-filled glove box with oxygen and water levels less than 1 ppm (**Fig. III-4d**).

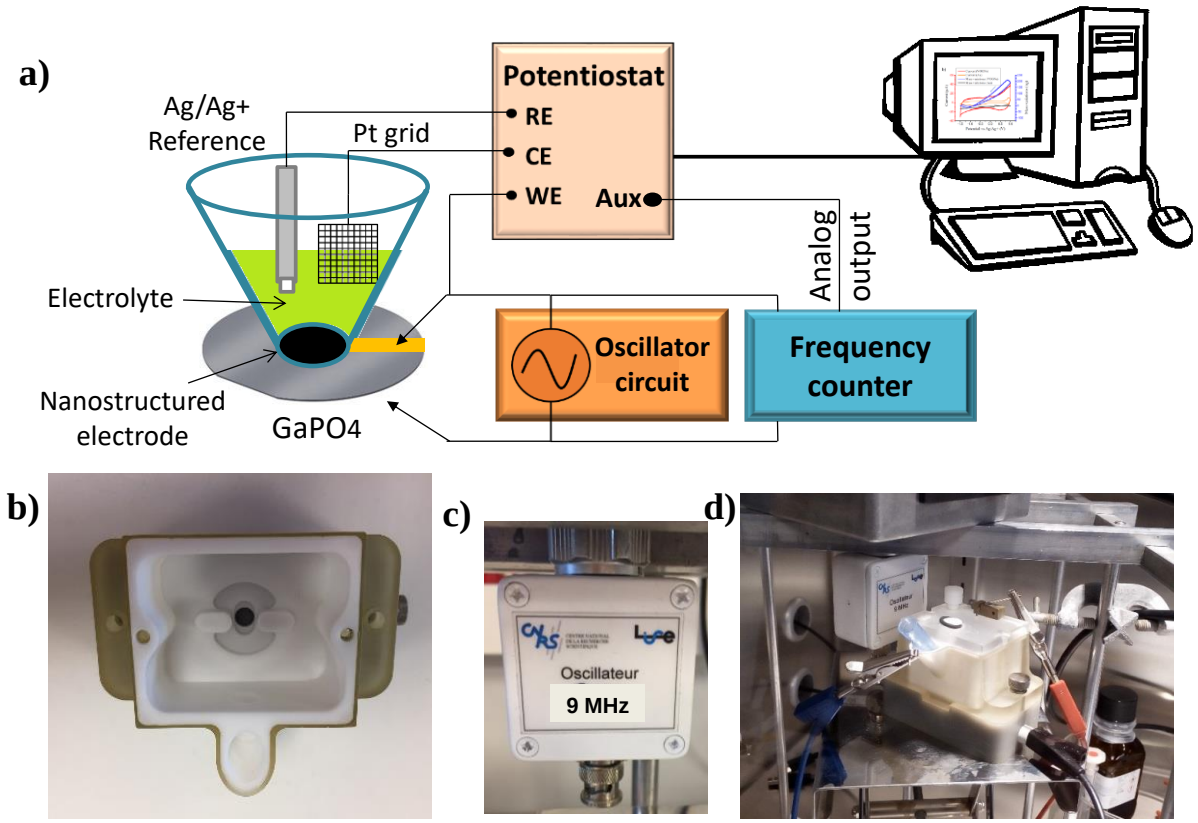

Figure III-4: a) Experimental set-up for EQCM measurements. **b)** Electrogravimetry cell. **c)** Oscillator circuit. **d)** Set-up inside a glove box.

With the computer, the auxiliary input values of the potentiostat (a voltage value from 0 to 5 V) are converted into relative frequency values (Δf_m), that are in turn converted into mass variation values (Δm) with the Sauerbrey equation:

$$\Delta f_m = -k_s \times \Delta m \qquad \textbf{(Eq. III-1)}$$

where k_s is the sensitivity factor of the QCM. For a 9 MHz piezoelectric quartz crystal the theoretical value is $k_s^{th} \cong 16.7 \times 10^7\ Hz.g^{-1}.cm^2$. For a 6 MHz piezoelectric $GaPO_4$ crystal the theoretical value is $k_s^{th} \cong 7.92 \times 10^7\ Hz.g^{-1}.cm^2$ [22].

The combination of CV with mass variation measurements leads to important qualitative information on the ionic exchange mechanisms between the electrode and the electrolyte: A major cation (resp. anion) contribution is obtained if the mass of the electrode decreases (resp. increases) as the potential increases. If both contributions are observed at different potentials, the point of zero mass change (pzmc) can be derived and compared to the point of zero charge (pzc). A description of the pzmc and the pzc can be found in chapter 1-III.1.

An additional step of calculation is needed to obtain more quantitative information from the EQCM data. The analysis of EQCM data by means of the mass per mole of electron (MPE) function gives the mass/charge ratio values at each applied potential during a voltammetric scan, which provides information on the apparent mass of the ions involved in the charge compensation. The MPE can be derived according to the following equation [23], [24]:

$$MPE = F\frac{\Delta m}{\Delta q} = F\frac{\Delta m/\Delta t}{\Delta q/\Delta t} \qquad \textbf{(Eq. III-2)}$$

where F = 96485.332 C.mol^{-1} is the Faraday constant, $\Delta \boldsymbol{m}$ and $\Delta \boldsymbol{q}$ are the mass and charge variations respectively.

The absolute value of the MPE will correspond to the molar mass of the exchanged ion if only one cation or one anion is exchanged as an electron passes through the electrodes. If the MPE is positive, then anions are exchanged. If the MPE is negative, then cations are exchanged. If there are other species participating, for example multiple ions or free solvent molecules, this method reaches its limitation as only a global molar mass that represents the contribution of all species can be estimated. Under such circumstances, it is hard to discriminate between the contributions of different species solely based on the EQCM approach.

III-4. *Ac*-electrogravimetry experimental setup

As mentioned in chapter 1-III.2, *ac*-electrogravimetry consists in coupling EIS measurements with a fast response QCM used in dynamic mode. This technique, first proposed by Gabrielli *et al.* at the LISE laboratory (France) [25], can be used to discriminate the activity of the different species involved in the charge transfer during an electrochemical process. More precisely, it provides access to relevant information on the kinetics of species transferred at the electrode/electrolyte interface and their transport in the bulk of the materials, the nature of these species as well as their relative concentration within the material.

The principle of *ac*-electrogravimetry is analogous to the principle of the EIS described in the previous section with the addition of mass measurement. A low amplitude sinusoidal perturbation (ΔE) applied to an electrochemical system can lead to changes in the mass of the film placed on the microbalance surface (Δm), allowing the measurement of the electrogravimetric transfer function (TF) $\frac{\Delta m}{\Delta E}(\omega)$ and the electrochemical impedance $\frac{\Delta E}{\Delta I}(\omega)$ simultaneously [26]–[28]. When the low amplitude sinusoidal perturbation is applied, some of the charged species in the solution participate in the charge compensation process within the electroactive material. This insertion/removal of species into/from the film is detectable through the microbalance frequency changes converted into mass changes using the Sauerbrey equation (**Eq. III-1**) if the gravimetric regime is kept. Modulating the frequency of the perturbation signal allows the separation of the contribution of different species involved in the charge compensation, thus differentiating species exchanged at different rates of transfer.

The complete set-up is depicted in **Fig. III-5**. Experiments are controlled by a computer using FRACOM, a software developed at the LISE laboratory. The measurements are made with the same three-electrode cell, reference and counter electrodes as described in section III-3. The QCM working electrode is polarized by a SOTELEM PG-STAT 100 potentiostat at a chosen potential. Then, the generator part of a Solartron 1254 delivers a low amplitude sinusoidal perturbation (ΔV') at a modulation frequency f. This signal is superimposed on the polarization potential supplied by the potentiostat (V'_S). [29]

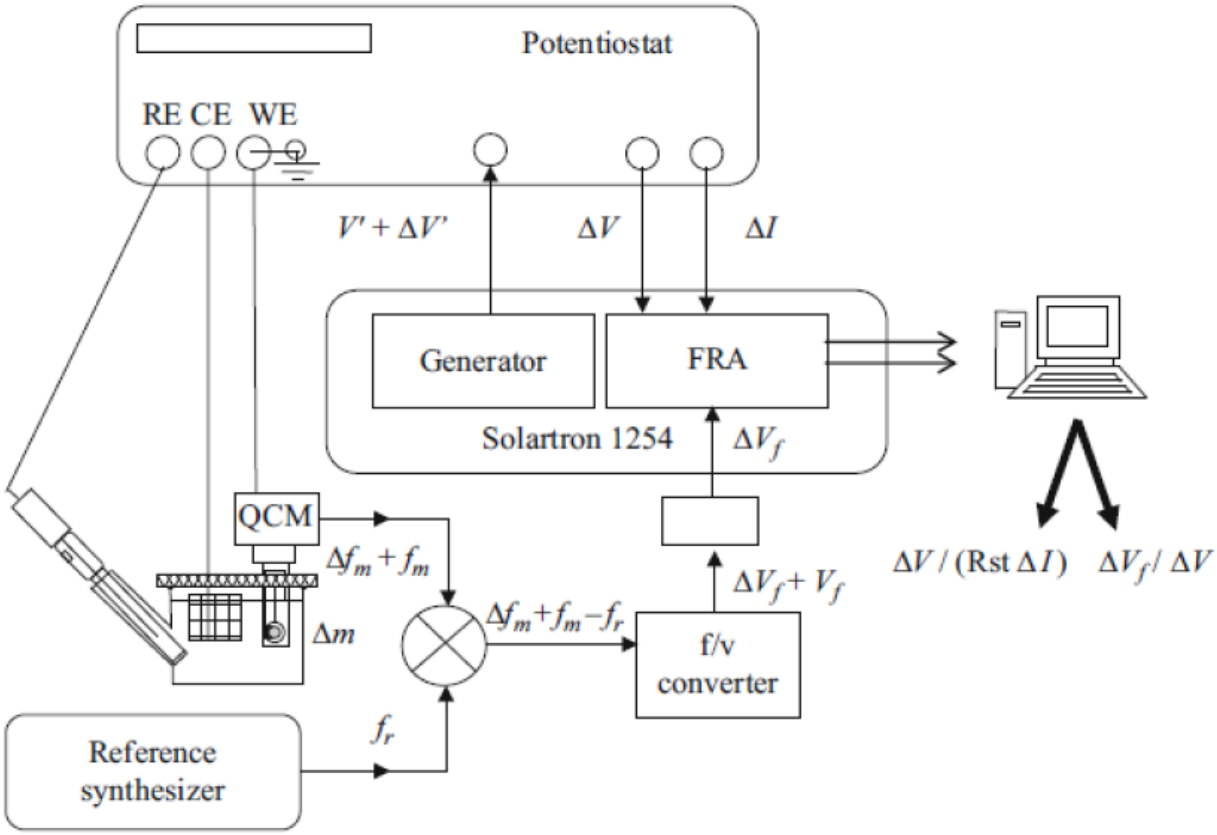

Figure III-5: Experimental set-up for *ac*-electrogravimetry measurements. [29]

To measure the transfer functions, a multi-channel frequency response analyzer (FRA) Solartron 1254 was used, allowing the simultaneous determination of the electrochemical impedance $\frac{\Delta E}{\Delta I}(\omega)$ and the corresponding mass/potential TF. In fact, $\frac{\Delta m}{\Delta E}(\omega)$ is not directly measurable. Instead, a frequency/voltage converter must be used in order to convert the microbalance frequency signal, Δf_m, into a measurable voltage signal, ΔV_f. **Fig. III-6** shows the implemented steps to obtain the electrogravimectric TF $\frac{\Delta m}{\Delta E}(\omega)$. In order to extract a few Hz of modulation on the signal of f_m, a differentiation with a reference signal of fixed frequency f_r is performed. A frequency synthesizer (Marconi-2023) generates this stable frequency while an electronic module allows the differentiation of f_m and f_r to extract a variable signal Δf_d in the range of a few hundred Hz. A frequency counter then transforms these frequency variations into potential variations ΔV_f. Finally, these potential variations are collected by the FRA to calculate the TF $\frac{\Delta V_f}{\Delta V}$. We will see in the following section that it is possible to extrapolate Δm from the ΔV_f

signal for a given configuration and type of measurement. This is achieved by calibrating the frequency/voltage conversion system before the measurement.

The electrochemical impedance TF is also retrieved in a raw form from the FRA: $\frac{\Delta V}{R_s \times \Delta I}(\omega)$ with where R_s is the resistance used in the counter electrode circuit to determine the current value. A transformation described in the next section is required to obtain the classical impedance TF $\frac{\Delta E}{\Delta I}$.

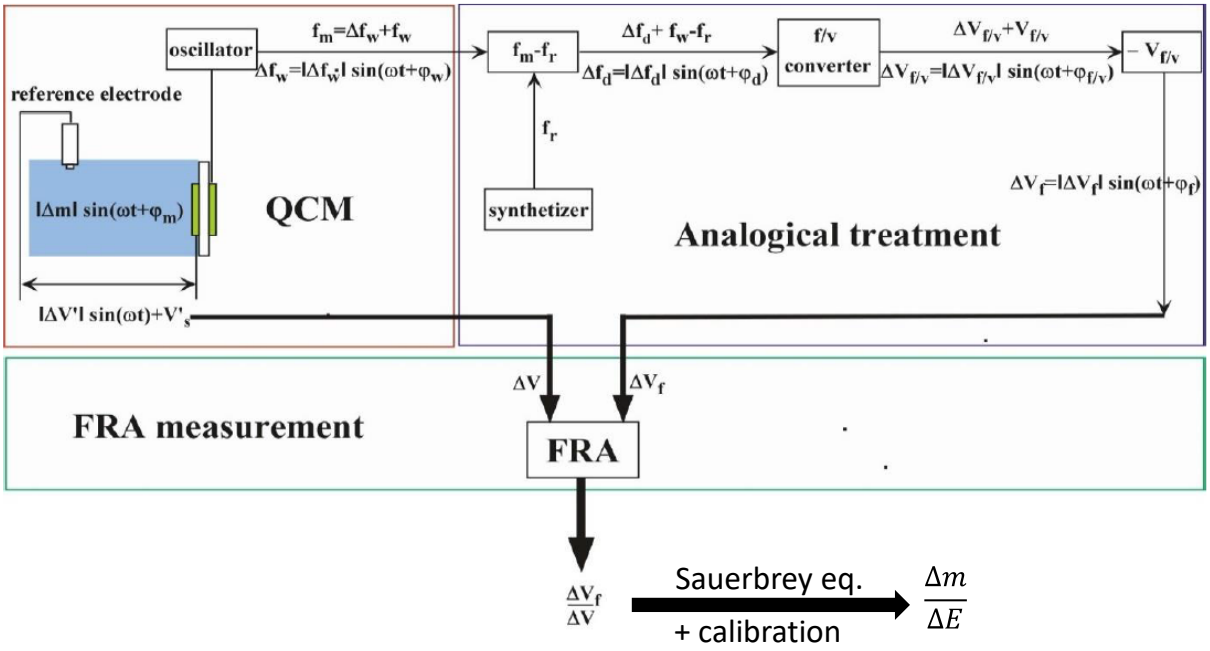

Figure III-6: Schematic of the electronic signal transformations performed by the *ac*-electrogravimetry set-up in order to obtain the final transfer functions.

III-5. *Ac*-electrogravimetry data treatment

III.5.i. Transforming the experimental transfer functions

Ac-electrogravimetry data, acquired in the form of two transfer functions ($\frac{\Delta V}{R_t \times \Delta I}$ and $\frac{\Delta V_f}{\Delta V}$), requires several treatments and fitting steps in order to obtain meaningful information about the electrochemical system. First of all, both TFs must be transformed into their usable form.

To obtain the experimental electrochemical impedance TF $\frac{\Delta E}{\Delta I}$, the following equation is used:

$$\left.\frac{\Delta E}{\Delta I}\right|_{exp}(\omega) = \left[\frac{\Delta V}{R_t \times \Delta I} \times R_t\right] - R_e \qquad \textbf{(Eq. III-3)}$$

where R_t is the resistance used in the counter electrode circuit, incorporated in the potentiostat for measuring the current, and R_e is the electrolyte resistance taken from the high frequency value of $\frac{\Delta V}{\Delta I}(\omega)$.

The charge/potential TF $\frac{\Delta q}{\Delta E}$ is then derived from $\frac{\Delta E}{\Delta I}$ using the following equation, derived from the relation $\Delta I = j\omega\Delta q$:

$$\left.\frac{\Delta q}{\Delta E}\right|_{exp}(\omega) = \frac{1}{j\omega} \times \frac{\Delta I}{\Delta E} \qquad \textbf{(Eq. III-4)}$$

The mass/potential TF $\frac{\Delta m}{\Delta E}$ is derived from $\frac{\Delta V_f}{\Delta V}$ by multiplying it to three other transfer functions:

$$\left.\frac{\Delta m}{\Delta E}\right|_{exp}(\omega) = \frac{\Delta m}{\Delta f_m} \times \frac{\Delta f_m}{\Delta V_f} \times \frac{\Delta V_f}{\Delta V} \times \frac{\Delta V}{\Delta E} \qquad \textbf{(Eq. III-5)}$$

where:

- $\frac{\Delta m}{\Delta f_m}$ is calculated from the Sauerbrey equation (**Eq. III-1**): $\frac{\Delta m}{\Delta f_m} = -\frac{1}{k_s}$.
- $\frac{\Delta f_m}{\Delta V_f}$ is the inverse of the frequency-to-voltage converter sensitivity that can be estimated using the following equation: $\frac{\Delta f_m}{\Delta V_f} = \frac{\Delta f_m}{\Delta e} \times \frac{\Delta e}{\Delta V_f}$. With $\frac{\Delta f_m}{\Delta e} = \frac{\Delta f_s}{\Delta e}$ the sensitivity of the

reference synthesizer and $\frac{\Delta e}{\Delta V_f}$ the inverse of the global calibration TF, recorded in a calibration file.

- $\frac{\Delta V_f}{\Delta V}$ is the raw output TF from the FRA.
- $\frac{\Delta V}{\Delta E}$ is the Ohmic drop correction to be done by taking into account the electrolyte resistance R_e. This Ohmic drop is derived from **Eq. III-3**: $\frac{\Delta V}{\Delta E}(\omega) = \frac{R_e}{\frac{\Delta E}{\Delta I}(\omega)} + 1$.

The *ac*-electrogravimetry data analysis is essentially done using both $\frac{\Delta q}{\Delta E}(\omega)$ and $\frac{\Delta m}{\Delta E}(\omega)$ TFs. Unlike electrochemical impedance, the mass/potential TF, $\frac{\Delta m}{\Delta E}(\omega)$, can occupy all the four quadrants of a Nyquist diagram. To rapidly designate a given quadrant, each of them has an attributed number according to **Fig. III-7a**. Just like for EIS, the Nyquist plot of $\left.\frac{\Delta m}{\Delta E}\right|_{exp}(\omega)$ alone gives some first insights on the overall electrochemical exchanges. A pure anion contribution will result in a suppressed loop in the 1st quadrant while a pure cation contribution will result in a suppressed loop in th 3rd quadrant (**Fig. III-7a**). For multiple species exchanged at the same time but with different speeds, they can be discriminated with their range in frequencies: Slower exchanges are represented in the lower frequency range while faster exchanges are represented in the high frequency range (closer to the center of the diagram). [24]

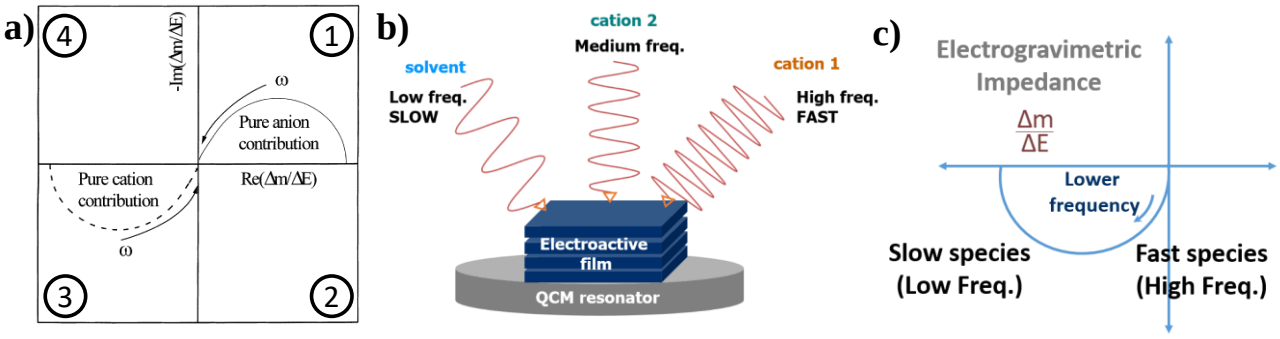

Figure III-7: a) Nyquist diagram of $\frac{\Delta m}{\Delta E}(\omega)$ for pure cation and pure anion contributions, along with quadrant numbers. **b)** Schematic of three species exchanged at various speeds with an electroactive film and **c)** the resulting Nyquist diagram $\frac{\Delta m}{\Delta E}(\omega)$. Adapted from [24].

To extract a deeper understanding from *ac*-electrogravimetry data, the experimental values of these both $\frac{\Delta q}{\Delta E}(\omega)$ and $\frac{\Delta m}{\Delta E}(\omega)$ need to be fitted with theoretical values provided by the model described in the next section.

III.5.ii.Model used to fit *ac*-electrogravimetry data

Fitting the experimental TFs with the theoretical TFs allows the extraction of pertinent information on the electrochemical process. Specifically, fitting the data from an experiment is performed by calculating the electrochemical impedance, the charge/potential TF and the mass/potential TF at all frequencies using the same set of parameters respectively. The fitting procedure respects the strict criteria that a good agreement between the experimental and the theoretical functions in terms of shape and frequencies is achieved.

The model used for this thesis is based on the description of the fluxes of anions, cations and solvent molecules between the nanostructured film and the electrolyte. Fluxes J_i, where i corresponds to a given species (anion, cation or free solvent molecule), are positive in the increasing x direction, as is indicated in **Fig. III.8**. The flux conservation law is:

$$\left(\frac{\partial C_i}{\partial t}\right)_x = -\left(\frac{\partial J_i}{\partial x}\right)_t \qquad \textbf{(Eq. III-6)}$$

where C_i corresponds to concentration of species i in the film.

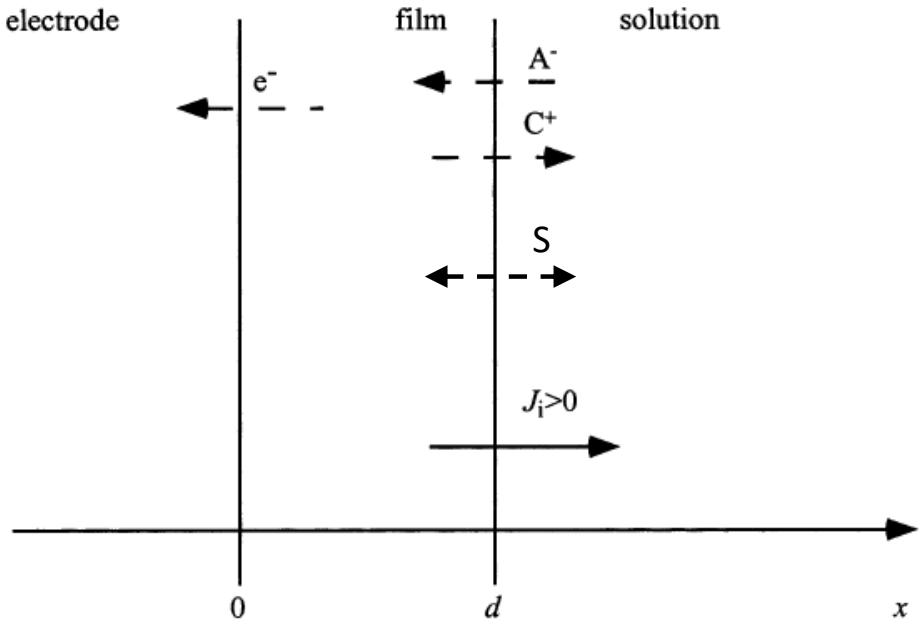

Figure III-8: Schematic of the electrochemical system modeled with the flux of various species. A^- represents a flux of anions, C^+ a flux of cations, S a flux of free solvent molecules and e^- a flux of electrons.

Let us consider the following electroadsorption/desorption mechanism which intervenes in the electrochemical system:

$$Cation: \ < P > + e^- + C^+ \underset{k_c'}{\overset{k_c}{\rightleftarrows}} < P^-, C^+ >$$

$$Anion: \ < P > + A^- \underset{k_a'}{\overset{k_a}{\rightleftarrows}} < P^+, A^- > + e^-$$

where $< P >$ is a free site on the film surface, $< P^-, C^+ >$ is the site occupied with a monovalent cation and $< P^+, A^- >$ is the site occupied with a monovalent anion. The k_i and k_i' are constants related to the transfer kinetic rates.

In this situation, the instantaneous flux of cations and anions for x=d, the film thickness, can be written as follows [30]:

$$J_c(d) = k_c'(C_c - C_{cmin}) - k_c(C_{cmax} - C_c)C_{csol} \quad \textbf{(Eq. III-7)}$$

$$J_a(d) = k_a(C_a - C_{amin}) - k_a'(C_{amax} - C_a)C_{asol} \quad \textbf{(Eq. III-8)}$$

where $C_{imax} - C_i$ is the concentration of free sites for species i in the film, $C_i - C_{imin}$ the concentration of inserted species i available for expulsion and C_{isol} the concentration of species i in the electrolyte.

When a small sine wave potential (ΔE) is superimposed onto the polarization potential difference applied to the electrochemical system, low amplitude sine wave concentrations (ΔC_i) and fluxes (ΔJ_i) are observed, and **Eq. III-6** is transformed into:

$$j\omega \Delta C_i = -\left(\frac{\partial \Delta J_i}{\partial x}\right)_t \quad \textbf{(Eq. III-9)}$$

where $\omega = 2\pi f$ is the pulsation and f the frequency of the sine wave.

At x=d, electroneutrality imposes the condition that the charges crossing the film-electrolyte interface through the fluxes of cations and anions are balanced by the electrons entering/leaving the electrode:

$$-\Delta J_a(d) + \Delta J_c(d) = \frac{j_F}{F} \quad \textbf{(Eq. III-10)}$$

where j_F is the flux of electrons and *F* the Faraday number.

The flux oscillations $\Delta J_i(d)$ are considered very small, thus a linear regime approximation is used to rewrite $\Delta J_i(d)$ as a function of $\Delta C_i(d)$ and ΔE:

$$\Delta J_i(d) = K_i \Delta C_i(d) + G_i \Delta E \qquad \textbf{(Eq. III-11)}$$

where $K_i = \left(\frac{\partial J_i}{\partial C_i}\right)_E$ is a kinetic parameter representing how fast species i are exchanged, and $G_i = \left(\frac{\partial J_i}{\partial E}\right)_{C_i}$ the parameter related to the ease of interfacial transfer.

In the linear regime at x=d, **Eq. III-9** leads to:

$$j\omega \Delta C_i(d) \cong -\left(\frac{\Delta J_i(d)}{d}\right) \qquad \textbf{(Eq. III-12)}$$

Using **Eq. III-12** in **Eq. III-11** leads to:

$$\frac{\Delta C_i(d)}{\Delta E} \cong \frac{-G_i}{K_i + j\omega d} \qquad \textbf{(Eq. III-13)}$$

Then, we define Δm_i as the mass change per unit surface in the film due to the concentration change of species i ($\Delta C_i(d)$) with molar mass M_i: $\Delta m_i = d.M_i \Delta C_i(d)$. From **Eq. III-13** we deduce:

$$\frac{\Delta m_i}{\Delta E} \cong d.M_i \frac{-G_i}{K_i + j\omega d} \qquad \textbf{(Eq. III-14)}$$

Similarly, the charge variations per unit surface (Δq_i) due to the concentration change of the charged species i ($\Delta C_i(d)$) with a valence v_i and a charge sign s_i can be written as: $\Delta q_i = s_i.d.F.v_i \Delta C_i(d)$. From **Eq. III-13** we deduce:

$$\frac{\Delta q_i}{\Delta E} \cong s_i.d.F.v_i \frac{-G_i}{K_i + j\omega d} \qquad \textbf{(Eq. III-15)}$$

To fit the data from a given experiment, the different species present in the electrolyte must be introduced in the model. For example if the electrolyte contains a monovalent cation, a monovalent anion and free solvent molecules, these three species will be taken into account and the total mass and charge variations of the film per surface unit will be calculated as:

$$\begin{aligned} \Delta m &= \Delta m_c + \Delta m_a + \Delta m_s \\ \Delta q &= \Delta q_c + \Delta q_a \end{aligned} \qquad \textbf{(Eq. III-16)}$$

Combining these relations with **Eq. III-14&15**, the mass/potential and charge/potential TFs can then be calculated with the following equations:

$$\left.\frac{\Delta q}{\Delta E}\right|_{th}(\omega) = \mathrm{F}\cdot\mathrm{d}\left(\frac{\mathrm{G_a}}{\mathrm{j}\omega d+K_a}-\frac{\mathrm{G}_c}{\mathrm{j}\omega d+K_c}\right) \quad \textbf{(Eq. III-17)}$$

$$\left.\frac{\Delta m}{\Delta E}\right|_{th}(\omega) = -\mathrm{d}\left(\mathrm{M_a}\frac{\mathrm{G_a}}{\mathrm{j}\omega d+K_a}+\mathrm{M_c}\frac{\mathrm{G}_c}{\mathrm{j}\omega d+K_c}+\mathrm{M_s}\frac{\mathrm{G_s}}{\mathrm{j}\omega d+K_s}\right) \quad \textbf{(Eq. III-18)}$$

If a charged species *i* is exchanged with the film with a solvation shell of n_i solvent molecules, this must be taken into account in the above model by ascribing to this element an effective molar mass M_i' that encompasses the mass of n_i solvent molecules: $M_i' = M_i + n_i \times M_s$.

III.5.iii. Development of a fitting software

The fitting process that consists in finding the proper values of G_i and K_i for each species of the model is usually done at LISE laboratory (France) using a Mathcad code. As the Mathcad software could not be used in the context of this Ph.D., an original software was created to perform *ac*-electrogravimetry fitting. Using python, the interface was made more dynamic than the Mathcad code, allowing faster data treatments. **Fig. III-9** depicts the main fitting interface of this software, that consists of four Nyquist diagrams ($\frac{\Delta E}{\Delta I}$, $\frac{\Delta q}{\Delta E}$, $\frac{\Delta q_{ion}}{\Delta E}$, $\frac{\Delta m}{\Delta E}$) and various components to change the parameters of the model. The red squares are the experimental points, while the blue squares correspond to the theoretical values from the model. For most samples, some parasitic reactions appear in the low frequency range, creating a slight rise in the Nyquist plot of $\frac{\Delta q}{\Delta E}$. These are numerically suppressed in the Nyquist plot of $\frac{\Delta q_{ion}}{\Delta E}$, with the substraction of a parasitic contribution calculated as a TF: $Z_p = R_p + \frac{1}{j\omega C_p}$, where R_p and C_p are parasitic resistances and capacitances respectively.

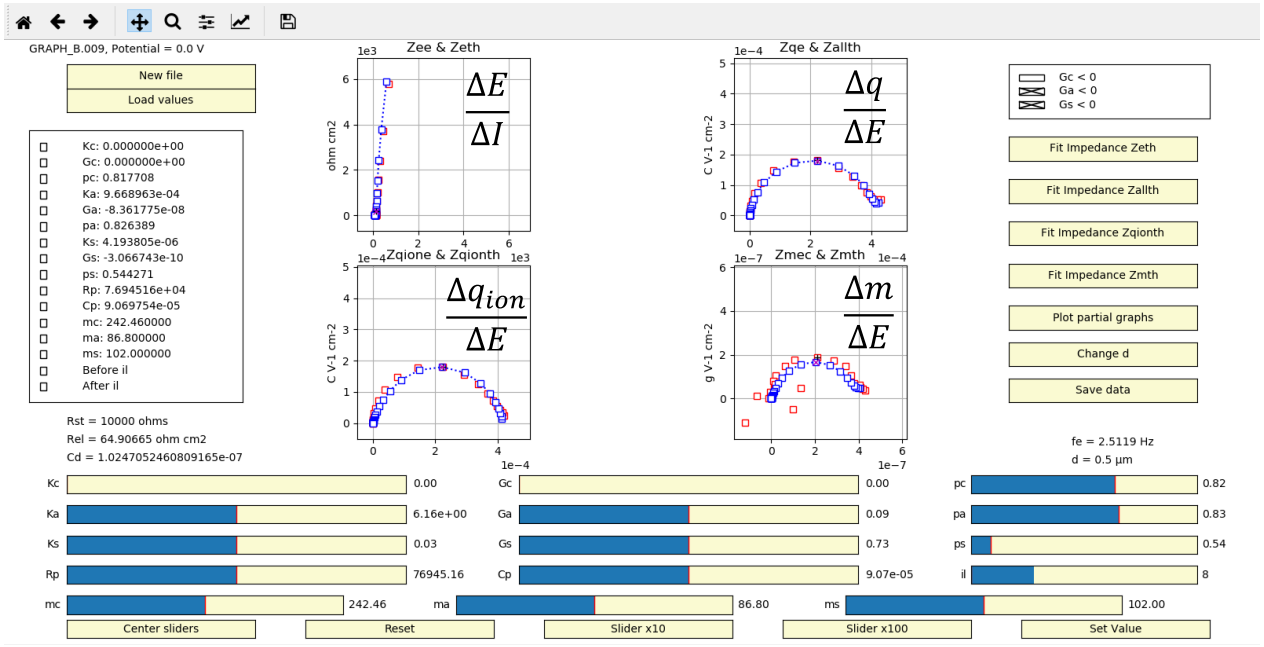

Figure III-9: Software developed to fit *ac*-electrogravimetry data, with experimental data in red and theoretical values in blue.

By finding the proper values of G_i and K_i for each species, it is possible to match the experimental and theoretical values for the four TFs simultaneously with the same set of parameters. Once these values are found, they give very valuable information on the kinetics and ease of transport for each species being exchanged.

III.5.iv. Further use of *ac*-electrogravimetry data

Just like the parasitic TF Z_p was substracted from the electrochemical impedance TF to obtain $\frac{\Delta q_{ion}}{\Delta E}$, it is possible to remove a part of the contributions from $\frac{\Delta m}{\Delta E}$. The resulting TFs are called the partial transfer functions. For example, in the case of three exchanged species where $\left.\frac{\Delta m}{\Delta E}\right|_{th}$ is derived from **Eq. III-18**, it is possible to remove the cation contribution to obtain the anion-solvent partial TF $\left.\frac{\Delta m}{\Delta E}\right|^{as}$. It is also possible to remove the anion contribution to obtain the cation-solvent partial TF $\left.\frac{\Delta m}{\Delta E}\right|^{cs}$. The experimental values of these two TFs is derived from the following equations:

$$\left.\frac{\Delta m}{\Delta E}\right|^{as}_{exp}(\omega) = \left.\frac{\Delta m}{\Delta E}\right|_{exp}(\omega) + \frac{M_c}{F}\left.\frac{\Delta q}{\Delta E}\right|_{exp}(\omega) \qquad \textbf{(Eq. III-19)}$$

$$\left.\frac{\Delta m}{\Delta E}\right|^{cs}_{exp}(\omega) = \left.\frac{\Delta m}{\Delta E}\right|_{exp}(\omega) - \frac{M_a}{F}\left.\frac{\Delta q}{\Delta E}\right|_{exp}(\omega) \qquad \textbf{(Eq. III-20)}$$

And the following equations allow the derivation of the theoretical values for these two partial TFs:

$$\left.\frac{\Delta m}{\Delta E}\right|^{as}_{th}(\omega) = \mathrm{d}\left[(\mathrm{M_a} + M_c)\frac{\mathrm{G_a}}{\mathrm{j}\omega d + K_a} + \mathrm{M_s}\frac{\mathrm{G_s}}{\mathrm{j}\omega d + K_s}\right] \qquad \textbf{(Eq. III-21)}$$

$$\left.\frac{\Delta m}{\Delta E}\right|^{cs}_{th}(\omega) = \mathrm{d}\left[(\mathrm{M_c} + M_a)\frac{\mathrm{G_c}}{\mathrm{j}\omega d + K_c} + \mathrm{M_s}\frac{\mathrm{G_s}}{\mathrm{j}\omega d + K_s}\right] \qquad \textbf{(Eq. III-22)}$$

These TFs allow us to see how the Nyquist diagram would look like with one less species, and show graphically the contributions from the remaining species. When two species of opposite fluxes are exchanged at the same time (like anions and cations), these TFs allow us to see their contributions separately and not a mutually reduced mass response.

Any information extracted from *ac*-electrogravimetry data can be obtained for another fixed potential, and so on over the entire potential window, opening the access to the potential dependence of the electrochemical exchanges. In particular, the potential dependence of the

concentration of individual species within the electroactive film can be obtained by using **Eq. III-13** with $\omega = 0$:

$$\frac{\Delta C_i(d)}{\Delta E}(\omega = 0) = \frac{-G_i}{K_i} \qquad \textbf{(Eq. III-23)}$$

The integration of **Eq. III-23** over a range of potential values leads to a profile of concentration variations $(C_i - C_{i0})$ for each species. These concentration variations can then be transformed into mass variations due to individual species:

$$\Delta m_i(E) = M_i(C_i - C_{i0}) = M_i \int \frac{-G_i}{K_i}(\mathrm{E})\mathrm{dE} \qquad \textbf{(Eq. III-24)}$$

The potential dependence of the total mass variations of the electrode can then be reconstructed:

$$\Delta m = \sum_i \Delta m_i = \sum_i M_i \int \frac{-G_i}{K_i}(\mathrm{E})\mathrm{dE} \qquad \textbf{(Eq. III-25)}$$

These mass variations are meant to be compared with the EQCM results in order to validate or invalidate the model used for *ac*-electrogravimetry. An example of this comparison is shown in **Fig. III-4** of chapter 1 for carbon nanotube-based electrodes [23]. When successful, the huge interest of *ac*-electrogravimetry is that it performs a deconvolution of the global EQCM results to obtain individual information for each exchanged species.

References

[1] Ozlem Sel, 'Hierarchical meso- and micropore architectures by liquid crystlline and polymer colloid templating', Universität Potsdam, 2006.

[2] W. Zhou and Z. L. Wang, *Scanning Microscopy for Nanotechnology: Techniques and Applications*. Springer Science & Business Media, 2007.

[3] M. MASSEY, 'Electrical Properties of Single-Walled Carbon Nanotube Networks Produced by Langmuir-Blodgett Deposition', Doctoral, Durham University, 2013.

[4] K. J. Lee, N. Elgrishi, B. Kandemir, and J. L. Dempsey, 'Electrochemical and spectroscopic methods for evaluating molecular electrocatalysts', *Nat. Rev. Chem.*, 1, no. 5, p. 0039, May 2017.

[5] L. To Thi Kim, 'Study of electroactive films by coupling electrochemical and gravimetric techniques : application to the characterization of proton conductive membrane.', Theses, Université Pierre et Marie Curie, 2009.

[6] B. K. Kim, S. Sy, A. Yu, and J. Zhang, 'Electrochemical Supercapacitors for Energy Storage and Conversion', in *Handbook of Clean Energy Systems*, American Cancer Society, 2015, pp. 1–25.

[7] C. Portet, P. L. Taberna, P. Simon, E. Flahaut, and C. Laberty-Robert, 'High power density electrodes for Carbon supercapacitor applications', *Electrochimica Acta*, 50, no. 20, pp. 4174–4181, Jul. 2005.

[8] A. Laheäär, P. Przygocki, Q. Abbas, and F. Béguin, 'Appropriate methods for evaluating the efficiency and capacitive behavior of different types of supercapacitors', *Electrochem. Commun.*, 60, pp. 21–25, Nov. 2015.

[9] M. E. Orazem and B. Tribollet, *Electrochemical Impedance Spectroscopy*. John Wiley & Sons, 2011.

[10] L. D. Santos, 'Mécanisme de conduction protonique au sein de membranes hybrides pour piles à combustible', phdthesis, Université Pierre et Marie Curie - Paris VI, 2014.

[11] C. Reece, 'An Introduction to Electrochemical Impedance Spectroscopy (EIS)'. .

[12] K. Krishnamoorthy, P. Pazhamalai, G. Kumar, and S. Jae Kim, 'Mechanically delaminated few layered MoS2 nanosheets based high performance wire type solid-state symmetric supercapacitors', *J. Power Sources*, 321, pp. 112–119, Jul. 2016.

[13] R. B. Rakhi, B. Ahmed, M. N. Hedhili, D. H. Anjum, and H. N. Alshareef, 'Effect of Postetch Annealing Gas Composition on the Structural and Electrochemical Properties of Ti_2CT_x MXene Electrodes for Supercapacitor Applications', *Chem. Mater.*, 27, no. 15, pp. 5314–5323, Aug. 2015.

[14] D. Pech, M. Brunet, H. Durou, P. Huang, V. Mochalin, Y. Gogotsi, P.-L. Taberna, and P. Simon, 'Ultrahigh-power micrometre-sized supercapacitors based on onion-like carbon', *Nat. Nanotechnol.*, 5, pp. 651–4, Sep. 2010.

[15] H. Perrot, 'Piezoelectric Transduction (QCM)', in *Chemical Sensors and Biosensors*, Wiley-Blackwell, 2013, pp. 71–91.

[16] F.-G. Banica, in *Chemical Sensors and Biosensors: Fundamentals and Applications*, John Wiley & Sons, 2012, pp. 1–20.

[17] K. A. Marx, 'Quartz Crystal Microbalance: A Useful Tool for Studying Thin Polymer Films and Complex Biomolecular Systems at the Solution−Surface Interface', *Biomacromolecules*, 4, no. 5, pp. 1099–1120, Sep. 2003.

[18] X. Jiang, K. Kim, S. Zhang, J. Johnson, G. Salazar, X. Jiang, K. Kim, S. Zhang, J. Johnson, and G. Salazar, 'High-Temperature Piezoelectric Sensing', *Sensors*, 14, no. 1, pp. 144–169, Dec. 2013.

[19] D. Sporar, 'Sputter deposition of iron oxide and tin oxide based films and the fabrication of metal alloy based electrodes for solar hydrogen production', p. 92.

[20] M. D. Levi, L. Daikhin, D. Aurbach, and V. Presser, 'Quartz Crystal Microbalance with Dissipation Monitoring (EQCM-D) for in-situ studies of electrodes for supercapacitors and batteries: A mini-review', *Electrochem. Commun.*, 67, pp. 16–21, Jun. 2016.

[21] M. D. Levi, N. Shpigel, S. Sigalov, V. Dargel, L. Daikhin, and D. Aurbach, 'In Situ Porous Structure Characterization of Electrodes for Energy Storage and Conversion by EQCM-D: a Review', *Electrochimica Acta*, 232, pp. 271–284, Apr. 2017.

[22] S. Jakab, S. Picart, B. Tribollet, P. Rousseau, H. Perrot, and C. Gabrielli, 'Study of the Dissolution of Thin Films of Cerium Oxide by Using a $GaPO_4$ Crystal Microbalance', Analytical Chemistry. 81 (2009) 5139–5145.

[23] F. Escobar-Teran, A. Arnau, J. V. Garcia, Y. Jiménez, H. Perrot, and O. Sel, 'Gravimetric and dynamic deconvolution of global EQCM response of carbon nanotube based electrodes by Ac-electrogravimetry', *Electrochem. Commun.*, 70, pp. 73–77, Sep. 2016.

[24] H. Goubaa, F. Escobar-Teran, I. Ressam, W. Gao, A. El Kadib, I. T. Lucas, M. Raihane, M. Lahcini, H. Perrot, and O. Sel, 'Dynamic Resolution of Ion Transfer in Electrochemically Reduced Graphene Oxides Revealed by Electrogravimetric Impedance', *J. Phys. Chem. C*, 121, no. 17, pp. 9370–9380, May 2017.

[25] S. Bourkane, C. Gabrielli, and M. Keddam, 'Kinetic study of electrode processes by ac quartz electrogravimetry', *J. Electroanal. Chem. Interfacial Electrochem.*, 256, no. 2, pp. 471–475, Dec. 1988.

[26] C. R. Arias, C. Debiemme-Chouvy, C. Gabrielli, C. Laberty-Robert, A. Pailleret, H. Perrot, and O. Sel, 'New Insights into Pseudocapacitive Charge-Storage Mechanisms in Li-Birnessite Type MnO_2 Monitored by Fast Quartz Crystal Microbalance Methods', *J. Phys. Chem. C*, 118, no. 46, pp. 26551–26559, Nov. 2014.

[27] C. Gabrielli, J. J. Garcia-Jareño, and H. Perrot, 'Charge compensation process in polypyrrole studied by ac electrogravimetry', *Electrochimica Acta*, 46, no. 26, pp. 4095–4103, Aug. 2001.

[28] C. Gabrielli, H. Perrot, D. Rose, A. Rubin, J. P. Toqué, M. C. Pham, and B. Piro, 'New frequency/voltage converters for ac-electrogravimetric measurements based on fast quartz crystal microbalance', *Rev. Sci. Instrum.*, 78, no. 7, p. 074103, Jul. 2007.

[29] Gabrielli, C. and Perrot, H., 'Chapter 5', in *Modern Aspects of Electrochemistry*, pp. 151–238.

[30] C. Gabrielli, M. Keddam, N. Nadi, and H. Perrot, 'Ions and solvent transport across conducting polymers investigated by ac electrogravimetry. Application to polyaniline', *J. Electroanal. Chem.*, 485, no. 2, pp. 101–113, May 2000.

Chapter 3:

Nanowires as supercapacitor electrodes

Table of contents

I. Introduction

Supercapacitors have in common the fact that large surface-to-volume ratios along with easy ion accessibility and good electrical conductivity to the current collector are primordial to obtain higher capacitance and power density. Vertical nanostructures grown directly on the current collector are designed to offer these advantageous properties over a controlled thickness. Among the vast geometrical possibilities to achieve these nanostructures, vertically-grown nanowires have attracted a lot of attention due to the vast panel of other possible applications: Sensors arrays [1], electronic transistors [2], photovoltaic cells [3], batteries [4] and lasers [5].

The strong research efforts conducted on nanowire-based technologies has led to a variety of well-controlled growth procedures for nanowires made from diverse metallic, semi-conducting or insulating materials. Benefiting from these well-known growth processes, nanowires have been investigated as high performance electrodes for EDLCs [6], pseudo-capacitors [7] and even hybrid supercapacitors [8]. However, vertically-oriented nanowire structures have never been investigated with electrogravimetric characterization techniques before.

This chapter covers our results regarding the synthesis of vertically-oriented nanowires on a QCM and their characterization with EQCM and *ac*-electrogravimetry. Three types of nanowires have been investigated: Silicon nanowires (SiNWs), PEDOT nanowires and PEDOT-coated SiNWs.

II. Silicon nanowires

II-1. Chemical vapor deposition on a microbalance

II-1.i. CVD growth principles

The bottom-up synthesis of materials with chemical vapor deposition (CVD) has become common nowadays in both industrial and research laboratories, with applications ranging from large scale protective layers on industrial parts to micro-electronic devices [9], [10]. Indeed, the large diversity of existing CVD processes allows the controlled growth of nearly all metals, alloys and semiconductors on conductive or insulating substrates. This variety of options is multiplied by the numerous alternative types of CVD (high and low pressure, static and dynamic environment, etc.).

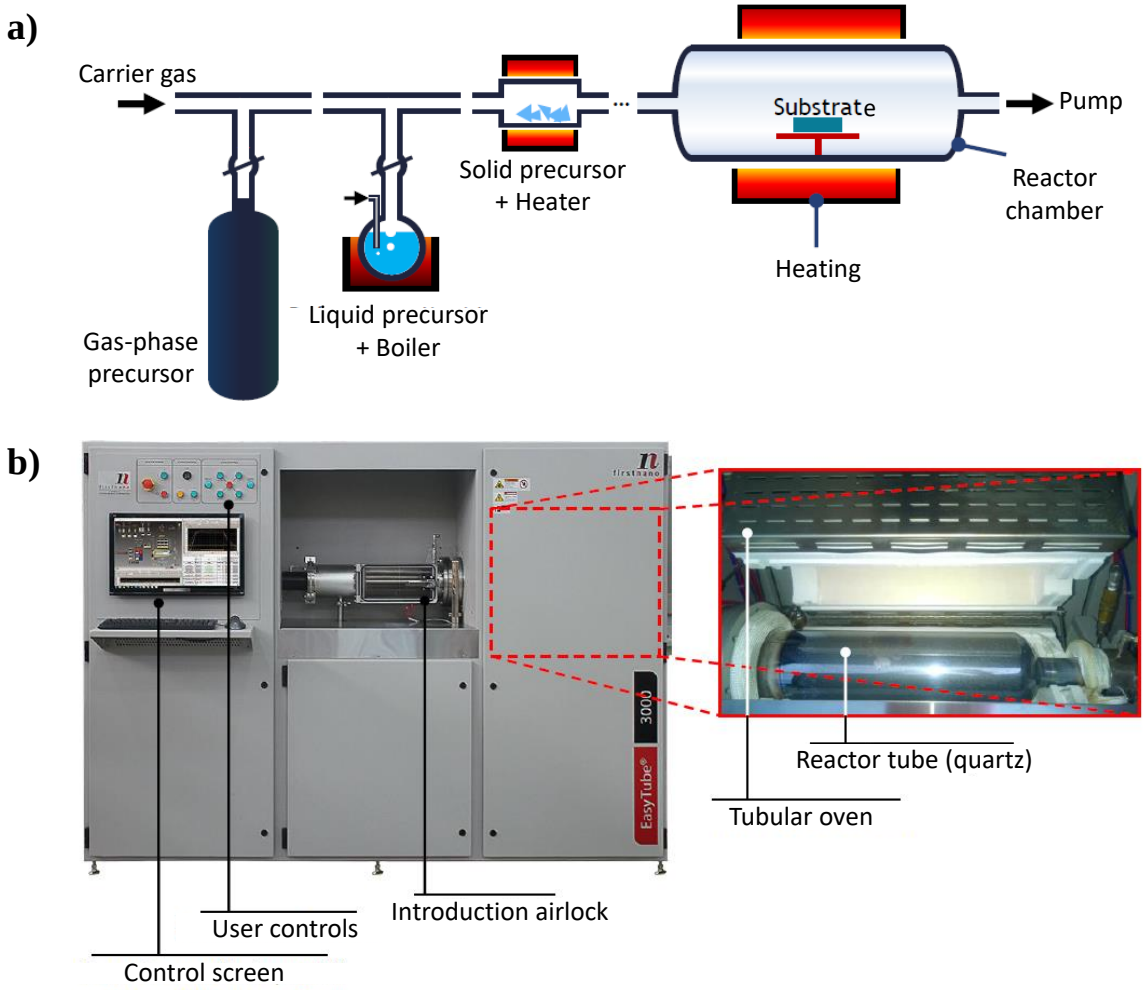

Figure II-1: a) Schematic of the process and equipment in classical CVD. **b)** Pictures of the "EasyTube 3000" LPCVD reactor. [11]

CVD consists in one or several chemical reactions of volatile reactants in a gas phase that produce at least one solid-state product at the substrate's surface. The reaction can take place either between different gas phase reactants or with a material from the solid substrate. The activation energy needed to trigger the chemical reaction can be provided by heating the substrate (classical CVD) or with non-thermal sources (plasma, laser, etc.) and reduced by using a catalyzer. **Fig. II-1a** shows a schematic of the process and equipment used for classical CVD.

The growth of silicon nanowires is achieved in a low pressure CVD (LPCVD) reactor called "EasyTube 3000" (FirstNano, USA) (**Fig. II-1b**) by using gas-phase SiH_4 as the main precursor and gold as catalyst. The growth process is based on the vapor liquid solid (VLS) mechanism in which crystalline silicon grows beneath the gold catalyst in the <111> direction. The VLS mechanism is described below and sketched in **Fig. II-2c**.

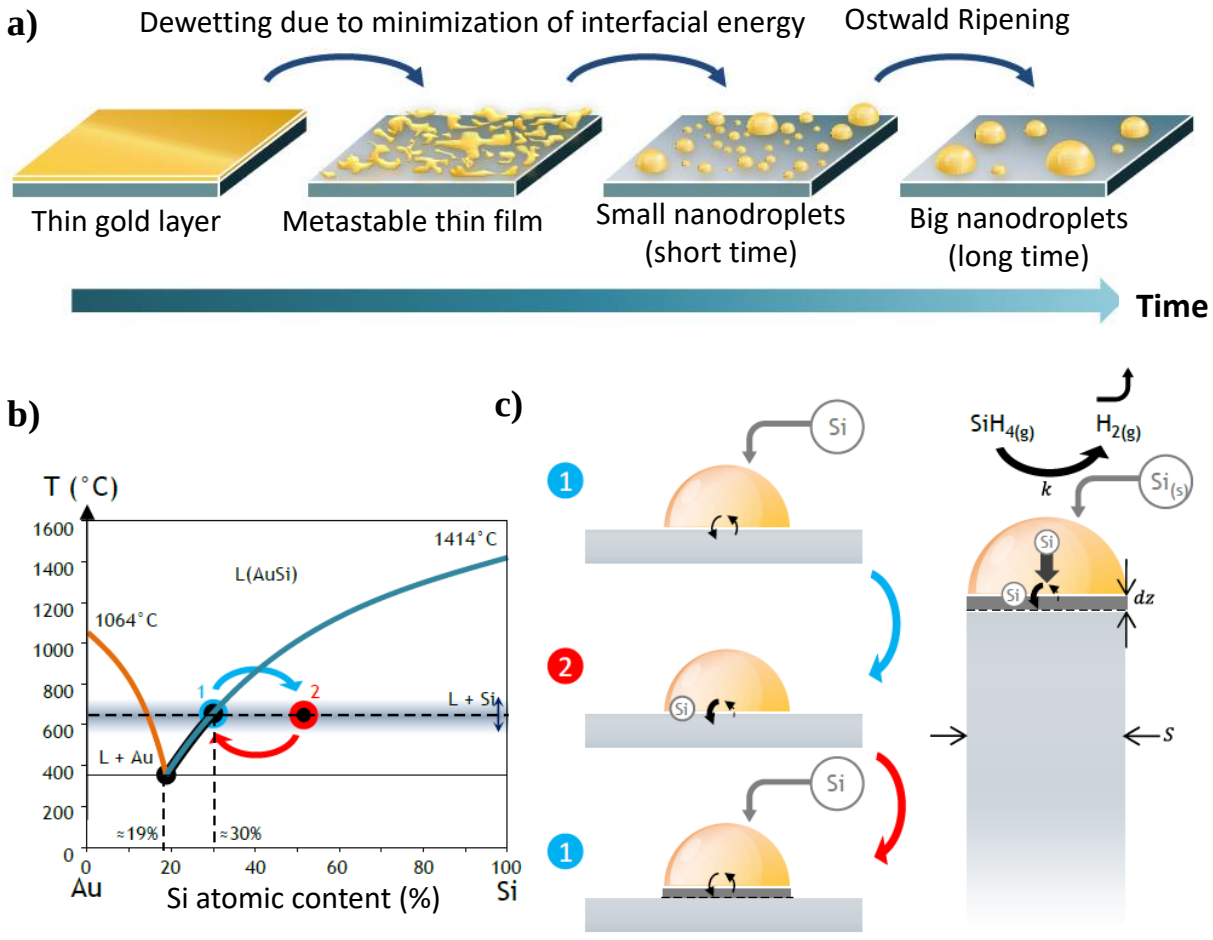

Figure II-2: a) Schematic of the dewetting process. **b)** Binary phase diagram for Au-Si. **c)** Schematic of the VLS mechanism. [11]

Silane (SiH_4) is inserted inside the reaction chamber and gold acts as a catalyst to its dismutation. Above 370°C, gold and silicon form an eutectic mixture in a liquid form (**Fig. II-2b**). Si atoms diffuse in the Au-Si liquid, and as the dissociation of silane continues the liquid Au-Si becomes saturated in silicon. Silicon will then solidify at the Au-Si/substrate interface to reduce the Si content of the saturated liquid. This precipitation of Si happens at the substrate's surface and not within the liquid Au-Si because the latter would require an additional energy to form a new liquid/solid interface (**Fig. II-2c**).

If the liquid Au-Si on the substrate has the form of nano-droplets, the Si precipitation under the droplet will have a linear shape, gradually forming a crystalline silicon nanowire. To obtain high density Au-Si nanodroplets evenly spread across the substrate, a 12 nm layer of gold was evaporated on the substrate. As the temperature rises and the dissociation of silane occurs, a larger Si content within the thin gold layer will trigger the dewetting process shown **Fig. II-2a**. The dewetting of the liquid Au-Si layer, caused by the minimization of the liquid/solid interfacial energy, will form Au-Si nanodroplets with various diameters which depend on the growth conditions [12].

This procedure allows the growth of pure semiconducting SiNWs with a gold droplet at their end. To obtain electrically conductive nanowires, dopants have to be inserted within the SiNW crystalline matrix. For this study, n-type doped SiNWs are grown by adding phosphine (PH_3) to the carrier gas (N_2+H_2). In our lab, HCl is also added to the reactor, as it has been shown to prevent the Au-Si droplet from diffusing along the nanowire during the growth. This stabilizes the structure of the nanowire and allows the growth of long SiNWs with a constant diameter [13].

For this study, SiNW growth was performed using two different kinds of substrates:

- n-type doped silicon wafers were first used in order to calibrate the growth parameters and to perform a series of electrochemical measurements.
- Microbalance electrodes were then used as substrates to perform electrogravimetric measurements.

II-1.ii. Growth on a microbalance electrode

The growth process described above is usually performed at 600°C on silicon wafers, and transposing it to QCM electrodes has been more challenging than expected. First of all, usual QCM electrodes are composed of quartz discs (around 180 µm in thickness) with a Ti or Cr adhesion layer (10-20 nm) and a thick gold electrode (200-250 nm). A growth test on such QCM has shown that in such conditions the gold layer is too thick to be dewetted, and therefore nanowire growth cannot be achieved. Microbalance electrodes especially designed for this application had to be prepared with evaporation and sputtering techniques, as described in chapter 2-III-1.

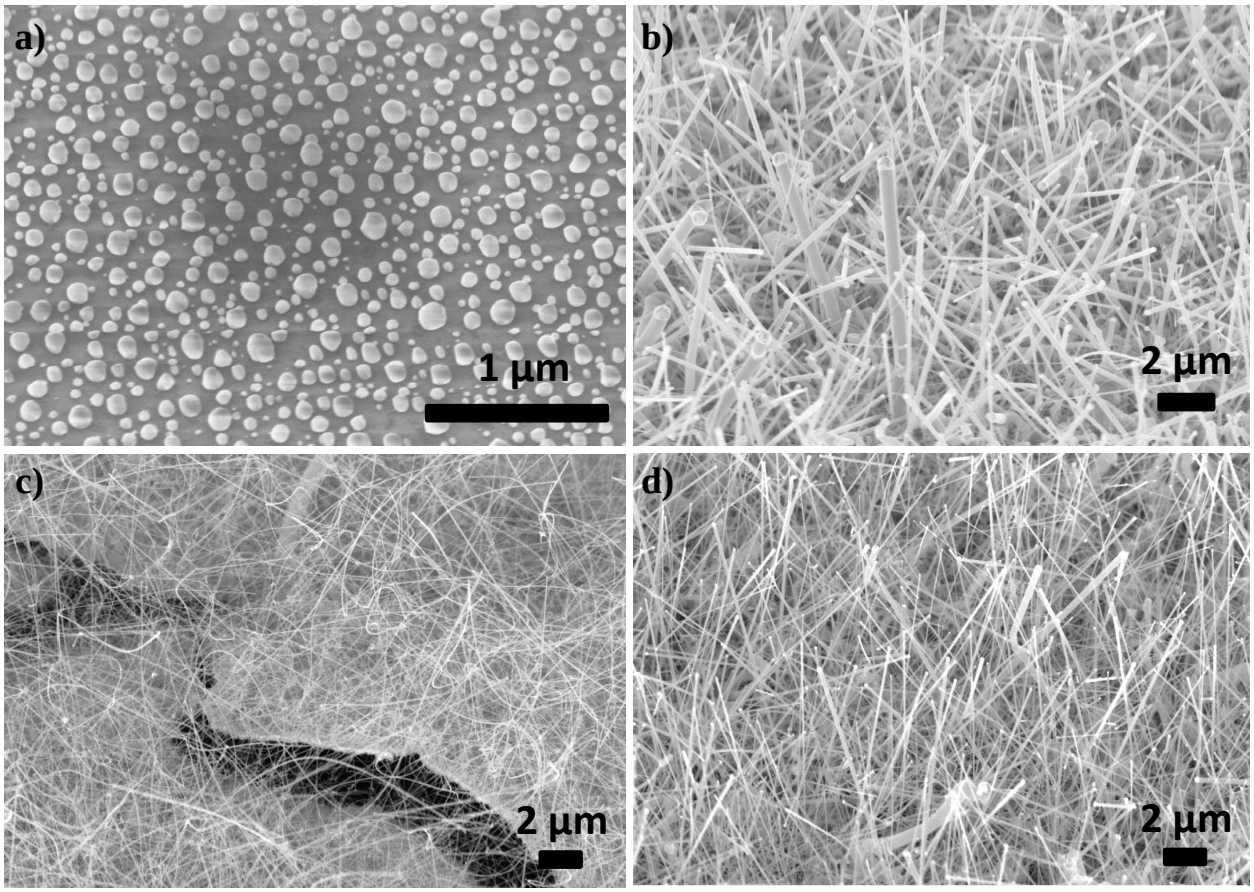

Figure II-3: SEM images of **a)** SiNW growth attempt on quartz with 100 nm Ti, **b)** SiGeNWs grown on quartz with 100 nm Ti, **c)** SiGeNWs grown on quartz with 100 nm Pt and **d)** SiNWs grown on $GaPO_4$ with 10 nm Ti+200 nm Pt. In each case the growth was achieved with the dewetting of a 10 nm Au layer.

Substrate temperature and reactor pressure are two important parameters to control the speed of nanowire growth, with lower temperatures and pressures leading to slower growth.

However in the case where the substrate is a QCM electrode, temperature should be kept as low as possible: The piezoelectric properties of quartz suffer high losses over 350°C and a change in phase from quartz-α to quartz-β at 573°C makes them completely inoperative [14]. Nevertheless, the growth of SiNWs was attempted on quartz with 100 nm Ti electrodes covered with 10 nm Au at 380°C under 18 Torr (the highest pressure accepted for this LPCVD reactor). The corresponding SEM images depicted in **Fig. II-3a** show that the dewetting of the gold layer was successful but not the nanowire growth.

Germanium (Ge) is known to have a lower melting point eutectic temperature with Au (340-350°C), and Ge nanowires have even been shown to grow below this eutectic temperature, as low as 260°C [15]. Si-Ge alloy nanowires have therefore been investigated as a way to grow vertical nanowires at 380°C on a QCM with 50, 100 and 200 nm Ti electrodes covered with a 10 nm Au layer. The growth was successful in the sense that nanowires were obtained, as shown in **Fig. II-3b**, however the QCM was not responding after the growth. This is either due to a too high loss of piezoelectric properties in the quartz or a loss of conductivity of the Ti electrode due to oxidation. The same tests were performed with quartz covered with Pt electrodes, however this time the electrodes cracked and detached from the quartz after the growth (**Fig. II-3c**).

The temperature induced issue of piezoelectricity loss in quartz can be solved by using $GaPO_4$, an alternative piezoelectric crystal that can maintain it's properties up to around 800°C [14]. Thus, the track of Si-Ge alloy nanowires was set aside to focus on pure SiNW growth, which was successfully performed on $GaPO_4$ piezoelectric crystals (~6 MHz in resonance frequency) with 10 nm Ti + 200 nm Pt + 12 nm Au electrodes after several adjustments in electrode configuration and growth conditions (**Fig. II-3d**). The growth of SiNWs on these $GaPO_4$ substrates was found reproducible when performed with the following steps:

- Evaporation of a 12 nm gold layer in the central part of the QCM to catalyze the growth.
- Introducing the samples in the CVD reactor, pumping and heating the QCM up to 600°C.
- Introducing silane and phosphine under a pressure of 6 Torr for 5 minutes, but no HCl to allow a better nucleation of gold nanoparticles.

- Introducing silane, phosphine and HCl to grow SiNWs with a pressure of 6 Torr for 15 minutes.

Fig. II-3d depicts a SEM image of a $GaPO_4$ electrode after SiNW growth. Dense arrays of nanowires with various diameters ranging from 50 to 500 nm and mean lengths around 10 µm are observed. The resonance frequency of each QCM was measured before and after the growth and was found mainly stable in both air and PC. For the sample depicted **Fig. II-3d** the resonance frequency decrease in air due to nanowire growth is 16.4 kHz. If the Sauerbrey equation is valid, this frequency shift corresponds to a mass augmentation of 44 µg, or 220 $\mu g.cm^{-2}$. In comparison Thissandier *et al.* estimated the SiNW mass loading around 750 $\mu g.cm^{-2}$ for a mean length of 50 µm [16].

While SiNW growth on a microbalance electrode constituted a challenge, obtaining the same growth on doped silicon wafers was very easy. Thus, electrochemical characterization of SiNW-based supercapacitor electrodes has been achieved in parallel to the growth tests described in this section.

II-2. Electrochemical analysis of SiNWs in a mixture of PC+N_{1114} TFSI

II-2.i. Electrochemical characterization with various mixture ratios

In spite of the excellent results reported in literature for SiNW-based supercapacitors [6], [16]–[20], important efforts should be still investigated concerning high voltage electrolytes for micro-supercapacitor (MSC) applications. In this regard, new strategies focused on mixtures made of organic and nitrile-based solvents with ionic liquid electrolytes [21]–[23] or eutectic ionic liquids (e.g. PIP_{13}-FSI / PYR_{14}-FSI) [24], [25] have emerged as promising alternatives in order to achieve excellent electrochemical performances in carbon-based SCs at a wide range of temperatures Accordingly, to the best of our knowledge, very preliminary results dealing with organic solvent/ionic liquid electrolyte mixtures (e.g. EMIM TFSI (1M) – PC) were addressed to SiNW-based symmetric MSCs [26], demonstrating the potential of such strategy for doped silicon nanostructures in the field of supercapacitors. Therefore, in this work, we present for the first time a complete and exhaustive electrochemical study focused on a new electrolyte mixture (PC-N_{1114} TFSI) to be employed as electrolyte in electrochemical double-layer (EDL) MSCs made of SiNW electrodes able to operate at a wide operating temperature range (from 0 to 80°C) within a large cell voltage of 3.5V. The choice of employing N_{1114} TFSI as electrolyte for the mixture of this study is ascribed to its excellent performance reported in previous work dealing with SiNWs for supercapacitor devices [27] and its potential also for battery applications [28], [29]. Additionally, ammonium structure-based ionic liquids have already demonstrated their enormous potential as electrolytes for carbon supercapacitors [30].

Fig. II-4a depicts the cross-sectional view of SiNWs grown on p-doped silicon substrates by CVD, with a length of 50 µm and a diameter range between 20 and 200 nm. Regarding the electrochemical performances no significant differences were observed between p and n type doped SiNWs for supercapacitor applications [17]. Using a MMultyConductimeter from MaterialsMates, the variation of conductivity versus the content of PC in N_{1114} TFSI was measured at various temperatures (**Fig. II-4b**). As it can be seen, the maximal conductivity (σ) was obtained at 50% w.t PC in N_{1114} TFSI for all temperatures. For this ratio, σ values of 3.7, 4.7 and 5.6 $mS.cm^{-1}$ were obtained at 5°C, 25°C and 50°C respectively. This trend was found in good agreement with similar electrolyte mixture configurations based on PYR_{14}TFSI and nitrile or carbonate solvents (e.g. maximal conductivity values around of 50% w.t) [21]. Particularly, the

properties of PYR_{14} TFSI, in terms of viscosity (η: 62 mPa s) and conductivity (σ: 2.6 mS cm^{-1}) [31], were found similar to N_{1114} TFSI (η: 95 mPa s and σ: 2 mS cm^{-1}) at room temperature. In this direction, a ratio of 50% w.t using different mixtures of ionic liquids (e.g. PYR_{14} TFSI or Me_3STFSI) and organic solvents (e.g. PC) showed η and σ values close to pure PC containing 1M Et_4NBF_4, which exhibited the highest conductivity and lowest viscosity values by comparison between both the pure ionic liquids and the corresponding mixtures [31], [32]. Based on this criterion, this mixture ratio was chosen as an optimal electrolyte for the electrochemical performances reported in this PhD work.

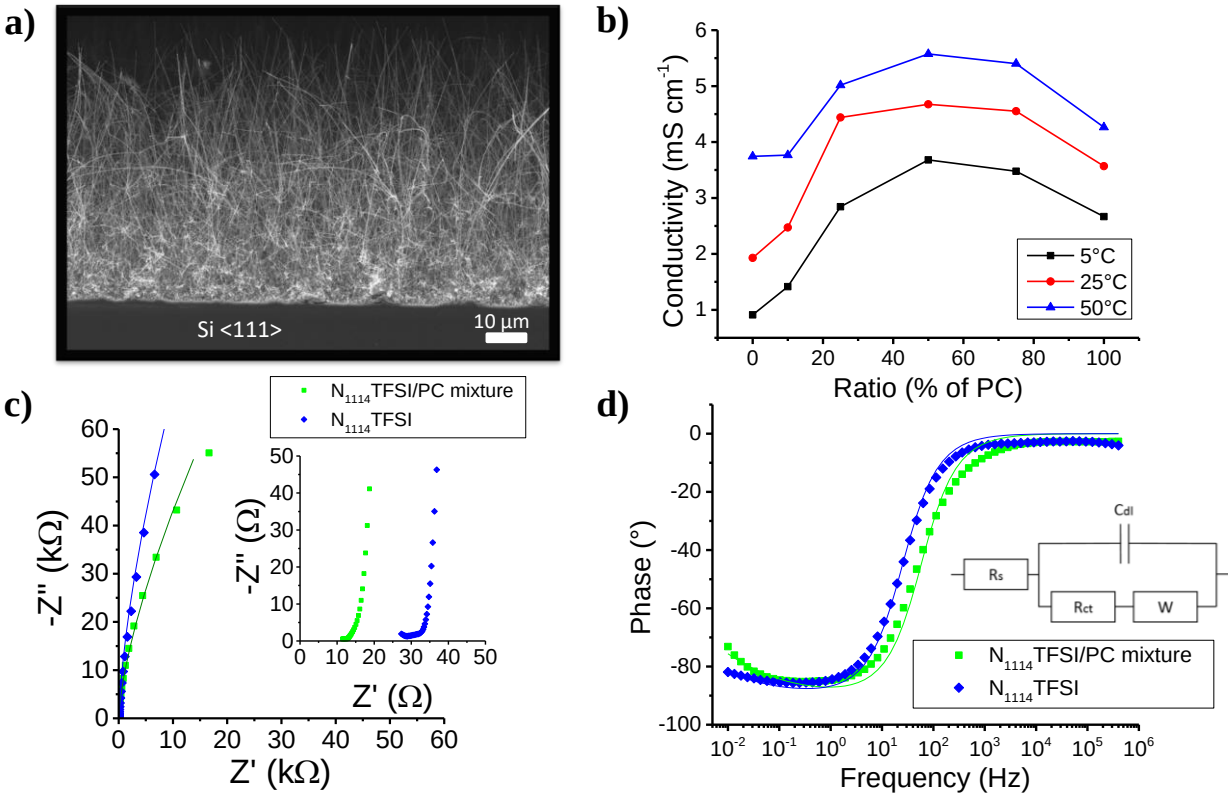

Figure II-4: a) SEM image of SiNWs grown on silicon substrates. **b)** Conductivity of N_{1114} TFSI as a function of volume percentage in PC. **c)** EIS Nyquist plot for a frequency range from 400 kHz to 10 mHz for a SiNW-MSC using N_{1114} TFSI (blue diamond) and PC:N_{1114} TFSI (50-50% w.t) (green square) electrolytes. The inset corresponds to the enlarged view of the high frequency region. **d)** EIS Bode plot of the device obtained from Nyquist plot for N_{1114} TFSI and PC:N_{1114} TFSI (50-50% w.t). Solid lines correspond to the fitting of the experimental data to the equivalent circuit displayed in the inset.

EIS technique is a useful tool to evaluate the electrode-electrolyte interface of a SC device. **Fig. II-4c** illustrates the Nyquist plot at a frequency range from 400 kHz to 10 mHz for SiNW-based MSCs using both N_{1114} TFSI and the corresponding optimal mixture electrolyte. The

plot shows two important regions at high and low frequency range. At high frequency, the intersection of the semi-circle with the x-axis represents an ESR value of 11 Ω for the mixture electrolyte, whereas an ESR value of 27 Ω was estimated for pure ionic liquid. This value was found close to another pure ionic liquids, as for example PYR_{13} TFSI (22 Ω) [19] or EMIM TFSI (17 Ω) [33] employing SiNW electrodes. Thus, the decrease of ESR through the dilution of PC in N_{1114} TFSI results in a very interesting strategy owing to the increase of conductivity and lower viscosity in mixtures, which represent one of the most important drawbacks for pure ionic liquids [34]. At low frequency, the slight deviation of the vertical line demonstrates the good ionic diffusion and capacitive behaviour predominated by an electrical double layer mechanism. Based on these results, an equivalent circuit was proposed in the inset of **Fig. II-4d**, which was expressed as $R_s[C_{dl}(R_{ct}W)]$, where R_s is the internal resistance of the supercapacitor, C_{dl} is the double layer capacitance, R_{ct} is the charge transfer resistance in serial connection with a Warburg element, W, associated to the diffusion process of the electrolyte ions. EIS technique can also provide an important insight on the electrochemical characterisation of supercapacitor devices by evaluating the relaxation time constant (τ_0), which is defined as the minimum time needed to discharge all the energy from the device with an efficiency of more than 50% [35]. This property was determined from Bode plot (phase angle versus frequency) using the following relation $\tau_0 = 1/f_{45°}$, where $f_{45°}$ corresponds to the frequency at 45° phase angle [36]. Thus, a τ_0 value of 19.7 ms and 39.5 ms was calculated for the mixture and pure ionic liquid respectively (**Fig. II-4d**). These values were found similar to those related to SiNW-µSCs using pure ionic liquid electrolytes (e.g. values ranging from 4 ms to 32 ms for EMIM TFSI, PYR_{13}TFSI or NEt_3H TFSI respectively) [18]–[20], [33].

The determination of an operating electrochemical window (ECW) is also a crucial parameter for evaluating the capacitive properties of a supercapacitor device. **Fig. II-5a** displays the CV curves at various ECWs (1, 2, 3, 3.5 and 4 V) at a scan rate of 1 $V.s^{-1}$. The CV curves reflect a good capacitive behavior with a slight distortion of the profile from 3V, which was ascribed to silicon oxidation [6]. This effect was evidenced during the first cycles and subsequently a disappearance of the peak was observed due to the passivation of the surface [6]. As a result, wide ECWs up to 4V evidenced an excellent capacitive behaviour (quasi-ideal rectangular CV shapes) even after long cycling tests [19]. Taking into account this phenomenon, an ECW of 3.5 V was considered as an appropriate cell voltage for further analysis of this study.

In order to provide a better comprehension of the importance of such electrolyte mixture, a comparative electrochemical study with pure N_{1114} TFSI ionic liquid was conducted using CV curves. **Fig. II-5b** shows the relationship between the current density (j) and the scan rate (v) for both electrolytes. The linear regression depicted in the plot demonstrates the predominant effect of a double layer capacitive behaviour. Accordingly, areal capacitance (AC) values of 0.13 and 0.12 mF.cm^{-2} $\left(AC = \frac{j}{v}\right)$ were obtained for the mixture and pure ionic liquid electrolytes respectively. This tendency illustrates that the effect of dilution preserves the large electrochemical window (3.5V) and capacitive properties maintaining an excellent capacitive behaviour even at high scan rates.

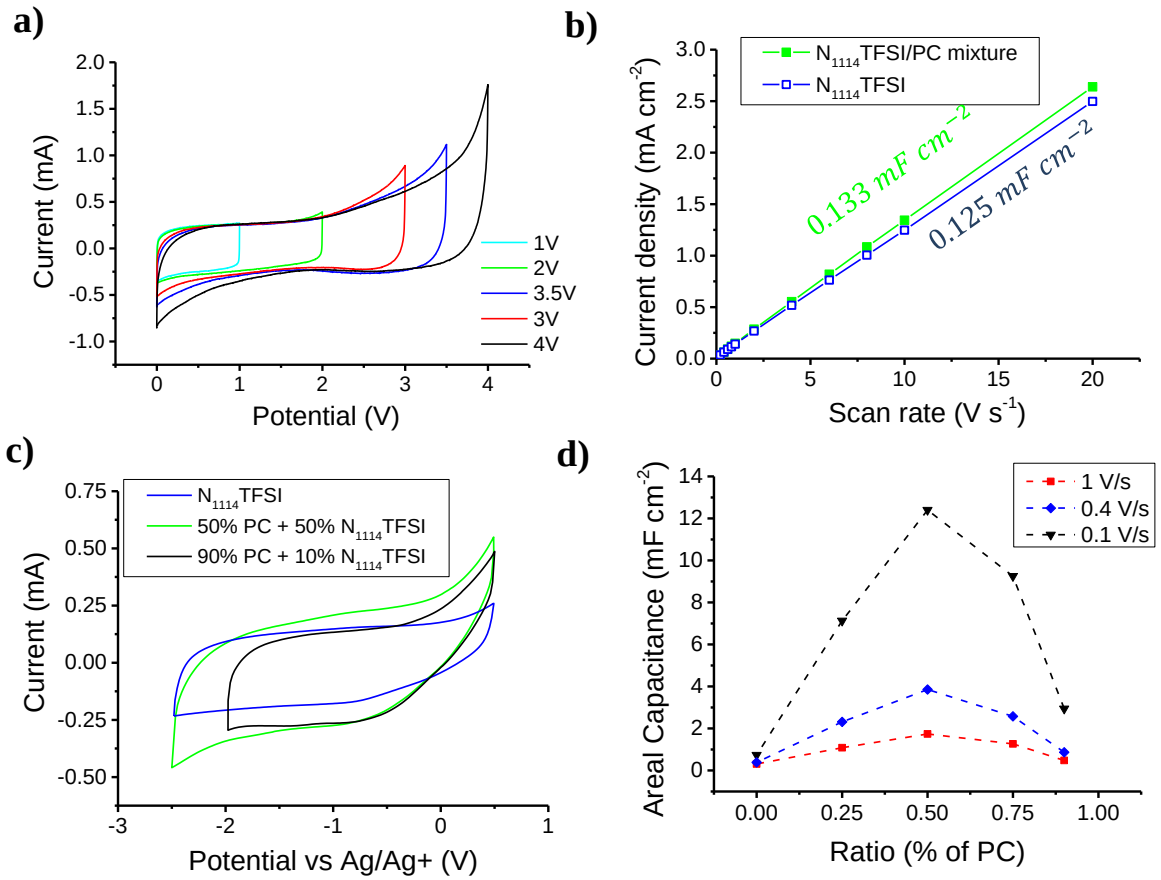

Figure II-5: a) CV curves of a SiNW-based MSC using different ECWs from 1 to 4 V at a scan rate of 1 V.s^{-1}. **b)** Current density (j) versus scan rate (v) for SiNW-based MSCs using PC:N_{1114} TFSI (50-50% w.t) (green line) and N_{1114} TFSI (blue line). **c)** CV curves of SiNW electrodes using different electrolyte mixture ratio at a scan rate of 1 V.s^{-1}. **d)** Variation of the AC of SiNWs as a function of the PC volume percentage in N_{1114} TFSI obtained from the CV curves at scan rates of 0.1 V.s^{-1} (black triangle), 0.4 V.s^{-1} (blue diamond) and 1 V.s^{-1} (red square) respectively.

In this direction, a comparative study concerning different mixture configurations was reported in **Fig. II-5c-d** using a 3-electrode cell configuration. The CV curves displayed in

Figure II-5c reflect the clear enhancement of the stored charge by the optimal 50:50 w.t ratio compared to both the pure ionic liquid and the 90 (PC):10 (N_{1114} TFSI) w.t mixture. The electrochemical behaviour was also analyzed in terms of AC with other mixture ratios. As it can be seen in **Fig. II-5d**, the maximal AC value was obtained using the PC-N_{1114} TFSI (50:50 % w.t) mixture, which corresponds to the maximal conductivity value (**Fig. II-4b**). This optimal ratio (50:50% w.t) has been widely employed as mixture electrolyte for electrochemical energy storage devices in presence of different ionic liquid chemical structures, as for example Me_3NHTFSI:PC, $PYRNO_3$:PC, Me_3STFSI:PC or PYR_{14}TFSI:PC in the field of supercapacitors [30]–[32]. This ratio demonstrated in all the aforementioned cases physical-chemical properties (η and σ) close to pure PC containing salt electrolytes (e.g. NEt_4BF_4) and ECWs larger than 2.7V (e.g. ECW used commonly for PC containing electrolyte salts). Such characteristics play a key role on the electrochemical performances of supercapacitors since the dilution effect reduces the viscosity, enhances the diffusion of the ions, which enlarges the ionic conductivity [34], [37]. This effect has been demonstrated in the literature by the solvent-solute interaction and solvation effects as the main driving forces to improve the ionic conductivity of the mixtures [21], [38].

II-2.ii. SiNW-based coin cell performances

Symmetric supercapacitor coin cells were assembled using two identical SiNW electrodes in order to obtain the final device performances with the new electrolyte developed in the previous section. **Fig. II-6** shows the electrochemical performance of the SiNW-based MSC using the PC-N_{1114} TFSI (50:50 % w.t) mixture at a wide cell voltage of 3.5V. **Fig. II-6a** shows the galvanostatic charge-discharge cycles at different intensities from 1 to 20 mA. Accordingly, the profiles reflect an excellent reversibility, a good capacitive behaviour as well as an extraordinary fast charge-discharge rate at high current densities (e.g. < 10 ms at 20 mA) predominated by an EDL mechanism. The AC was calculated from the discharge profiles displayed in **Fig. II-6a**. Initially, a drop of AC from 0.18 to 0.14 $mF.cm^{-2}$ at low current densities ranging from 0.1 to 2.3 $mA.cm^{-2}$ was observed (**Fig. II-6b**). This decay was attributed mainly to the surface reactions occurring on SiNWs surface due to the formation of a 1-2 nm nanometric native silicon oxide layer by the presence of water traces, which was recently confirmed by XPS [39]. Thus, a distortion of the symmetry and linearity of GCD cycles was evidenced because of electrolyte impurities such as halides, surface defects because of inhomogeneous silicon oxidation layer or chemical reactions between SiNW surface and the electrolyte. This

electrochemical tendency at low current densities and scan rates was already evidenced in previous works [19], [20], [33].

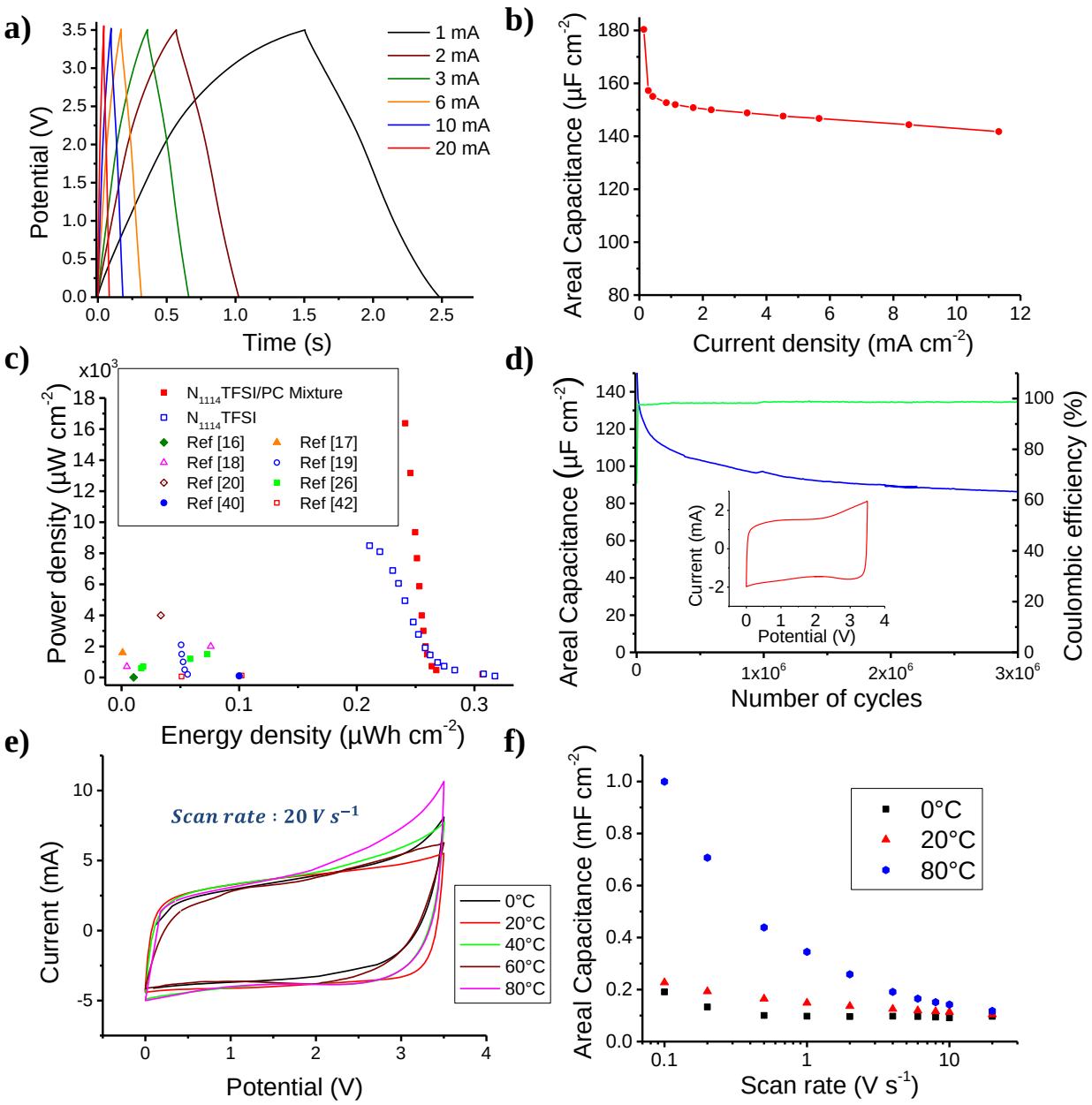

Figure II-6: Electrochemical performance of a symmetric SiNWs-based micro-supercapacitor. **a)** Galvanostatic charge-discharge cycles at different intensities from 1 to 20 mA. **b)** Areal capacitance versus current density. **c)** Ragone plot (P vs E) of the device. The plot shows also the state-of-the-art dealing with previous SiNW-MSCs. **d)** Cycling stability test (blue line) and coulombic efficiency (green line) over 3×10^6 GCD cycles at a current density of 2.3 mA.cm^{-2}. Inset shows the CV curve after the cycling test at a scan rate of 10 V.s^{-1}. **e)** CV curves at different operating temperatures ranging from 0 to 80°C at a scan rate of 20 V.s^{-1}. **f)** Areal capacitance versus scan rate at different working temperatures, 0°C (black square), 20°C (red triangle) and 80°C (blue circle) respectively.

Subsequently, the device exhibited an AC value of approximately 140 µF cm^{-2} at current densities higher than 2 mA cm^{-2} (**Fig. II-6b**). This value was found higher than the previous results reported in literature concerning SiNW-based MSCs using organic solvent (AC: 7-51 $\mu F.cm^{-2}$, average values depending on morphological characteristics of SiNWs and electrochemical conditions) [27], ionic liquids (PYR_{13}TFSI, AC: 23 $\mu F.cm^{-2}$ or EMIM TFSI, AC: 13 $\mu F.cm^{-2}$) [19], [41], or ionogels (AC: 60 $\mu F.cm^{-2}$) [42] electrolytes. This tendency demonstrates the potential of this mixture for MSC applications. Apart from AC, energy and power density are also two key properties to characterize the performance of a supercapacitor device. For that purpose, a Ragone plot (P vs E) was analyzed in **Fig. II-6c**. Power and energy density values were ranged from $0.2 \cdot 10^3$ to $16 \cdot 10^3$ $\mu W.cm^{-2}$ (around 1 to 50 $mW.cm^{-3}$) and from 0.25 to 0.3 $\mu Wh.cm^{-2}$ (around 0.7 to 1 $mWh.cm^{-3}$) at current densities ranging from 0.1 to 11 $mA.cm^{-2}$ respectively. These values were compared to the state-of-the-art using similar studies dealing with silicon nanostructures such as CVD-SiNWs [17]–[20], [42]–[45], silicon nanotrees (SiNTrs) [26] or silicon carbide nanowires (SiCNWs) [40] in presence of various electrolytes. Additionally, a comparison with other MSC based on the functionalization of CVD-SiNWs by using pseudocapacitive materials such as electroactive conducting polymers (PEDOT and PPy) [46], [47] or transition metal oxides (MnO_2) [48] has been also reported. In this direction, as expected according to the working principle of pseudocapacitors, energy density (2.5 - 5 $\mu Wh.cm^{-2}$) was found to be higher than the results reported in this study, whereas the power density (0.6 - $1 \cdot 10^3$ $\mu W.cm^{-2}$) was lower compared to pure SiNW EDLCs (>$2 \cdot 10^3$ $\mu W.cm^{-2}$) [27]. Consequently, this PhD work reports one of the best electrochemical performances of SiNW-based MSC in terms of AC, E and P thanks to both:

- A new configuration of device (coin cell), which was never reported before for SiNWs.
- The corresponding PC-N_{1114} TFSI electrolyte mixture.

The cycling stability is another crucial factor to evaluate the performance of a supercapacitor. From this point of view, the end of life criterion for supercapacitor devices is 20% or 30% loss in capacitance or doubling of the internal resistance [49]. In this PhD work, this property was evaluated by applying $3 \cdot 10^6$ GCD cycles at a current density of 2.3 $mA.cm^{-2}$. A capacitance retention of 63 % was determined after the cycling test with an excellent coulombic

efficiency (~ 99 %) as illustrated in **Fig. II-6d**. The lifetime of the device in this study is very satisfying taking into account the results reported for pure protic and aprotic ionic liquids with stability values around 70-80% after millions of GCD cycles [18], [19], [33], [42]. Based on the criteria aforementioned, a loss of capacitance of 30% was achieved after 380000 cycles, which can be considered still an excellent result based on EDLCs [50]. Furthermore, an excellent EDL capacitive behavior was kept even after 3×10^6 GCD cycles, as reflected the CV curve in inset in **Fig. II-6d**. Finally, the potential of this new electrolyte was analyzed at various operating temperatures. **Fig. II-6e** shows the CV curves at 0, 20, 40, 60 and 80°C using a scan rate of 20 Vs^{-1} at a large cell voltage of 3.5V respectively. Interestingly, the quasi-ideal rectangular shape of the curves, which corroborates a pure EDL capacitive behavior, is maintained at a wide range of temperatures from 0 to 80°C. The variation of AC versus scan rate at different working temperatures is displayed in **Fig. II-6f**. As can be seen, the areal capacitance increases with the temperature leading to values of 94 $\mu F.cm^{-2}$ (0°C), 147 $\mu F.cm^{-2}$ (20°C) and 344 $\mu F.cm^{-2}$ (80°C°) at a scan rate of 1 $V.s^{-1}$.

The results presented in this section have shown the great advantages of using a mixture of PC-N_{1114} TFSI, with a larger usable ECW compared to PC-based electrolytes and a greater ionic conductivity than pure N_{1114} TFSI. In the next section presenting the microbalance results obtained with SiNWs, this particular mixture could not be used as it is too viscous to be used with the morphology of our samples. However this mixture has later been used in the electrogravimetric study of VOGN electrodes presented in chapter 4.

II-3. Microbalance results

II-4.i. Network Analyzer measurements

Once a successful growth of SiNWs was achieved on an operational $GaPO_4$ resonator with Pt electrodes, the possibility of using them as QCM for electrogravimetric measurements was investigated with a network analyzer. This instrument measures the real and imaginary parts of the electrode admittance $Y = \frac{1}{Z}$ as a function of the applied frequency and calculates the equivalent circuit of the resonator shown as inset of **Fig. II-7**. These measurements were performed on the same resonator by using 6 configurations: Before SiNW growth, with the Pt electrode in contact with air, acetonitrile (ACN) and propylene carbonate (PC), followed by measurements in the same three mediums after SiNW growth. **Fig. II-7** depicts the admittance modulus near the resonance frequency for each of these configurations. From these resonance peaks it is clearly observed that SiNWs cause a very important damping of the shear wave in ACN, and an even greater damping in PC. The better results obtained in ACN are due to a lower dynamic viscosity ($\mu_{ACN} = 0.34\ mPa.s$) compared to PC ($\mu_{PC} = 2.5\ mPa.s$).

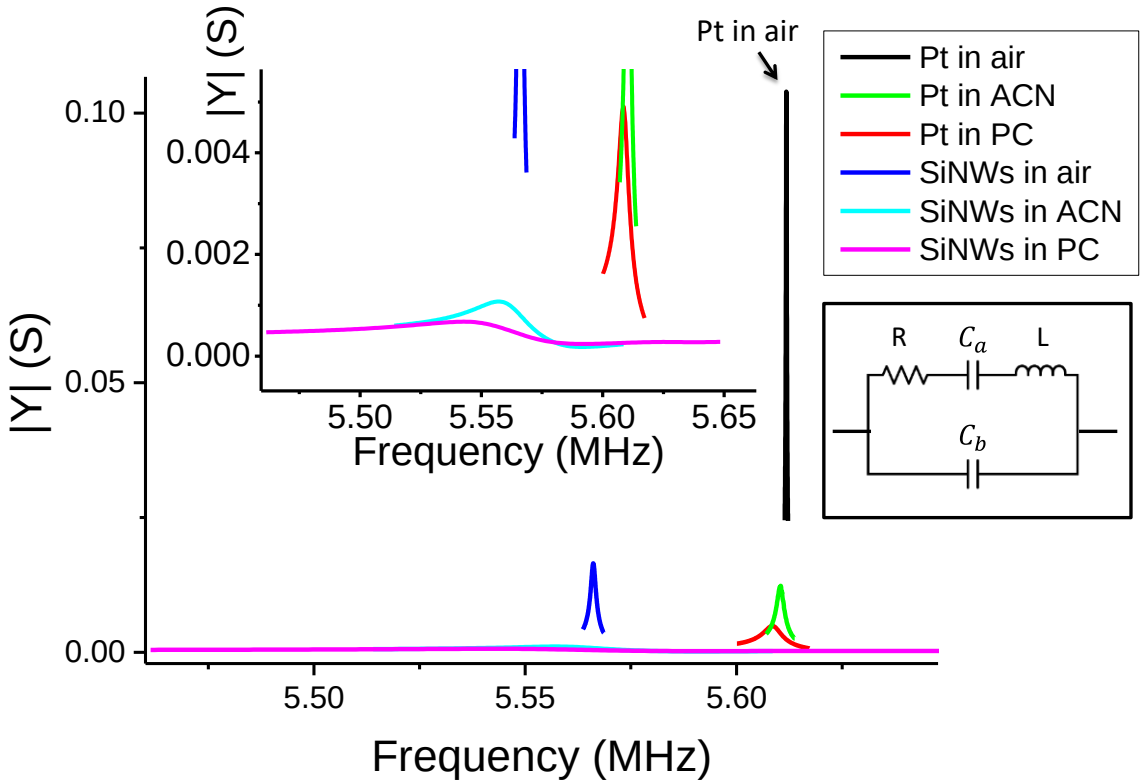

Figure II-7: Admittance modulus of the $GaPO_4$ resonator in air, ACN and PC before and after SiNW growth. A zoom-in with lower admittance values and the equivalent circuit of the resonator are shown as insets.

From the experimental data obtained with the network analyzer, the values of the resonance frequency (f_0), peak width at half height (W), resistance (R), inductance (L) and quality factor (Q) are estimated for each configuration and shown in **Table II-1**.

Configuration	Fluid visc. ($mPa.s$)	Fluid density ($kg.m^{-3}$)	Resonance frequency (MHz)	Peak width (Hz)	R (Ω)	L (H)	Quality factor
Pt in air	0.0184	1.17	5.612	192	9.6	0.00796	29191
Pt in ACN	0.34	786	5.610	1602	77.7	0.00772	3502
Pt in PC	2.5	1200	5.608	4292	206	0.00763	1307
SiNWs in air	0.0184	1.17	5.566	1207	60	0.00791	4610
SiNWs in ACN	0.34	786	5.561	23519	1070	0.00724	236
SiNWs in PC	2.5	1200	5.555	46659	2122	0.00724	119

Table II-1: Values obtained for the resonance frequency, peak width at half height, resistance, inductance and quality factor for a $GaPO_4$ resonator with Pt electrodes in air, ACN and PC before and after SiNW growth.

In the presence of PC, the variations in resonance frequency and peak width after SiNW growth are $\Delta f_{PC} = 53\ kHz$ and $\Delta W_{PC} = 42\ kHz$ respectively. The fact that both of these values are of the same magnitude and that Q dramatically drops from 1307 to 119 clearly indicates that this $GaPO_4$ resonator cannot be used for gravimetric measurements in the presence of PC due to hydrodynamic damping of the SiNWs in this viscous solvent. Thus, ACN was used as an alternative solvent with a very low viscosity to reduce the damping effect. As seen in **Table II-1**, the low viscosity of ACN was shown to reduce the hydrodynamic damping by a factor 2, with W=23.5 kHz and R=1 kΩ compared to W=46.6 kHz and R=2 kΩ in PC. The variations in resonance frequency and peak width after SiNW growth obtained in ACN are $\Delta f_{ACN} = 49\ kHz$ and $\Delta W_{ACN} = 21.9\ kHz$ respectively. The difference between these values is small, and the quality factor drop from 3502 to 236 is still very important, meaning that the contribution of hydrodynamic damping cannot be neglected. Nevertheless, EQCM and *ac*-electrogravimetry experiments were conducted on SiNWs in both PC and ACN to investigate the possibility of extracting the gravimetric response from the QCM in spite of the observed damping.

II-4.ii. EQCM and *ac*-electrogravimetric measurements

EQCM measurements were conducted on $GaPO_4$ resonators with Pt electrodes densely covered with SiNWs (**Fig. II-8a-b**). Two electrolytes based on ACN and PC were used for these measurements: ACN + 0.5M $TBABF_4$ and PC+0.5M $TBABF_4$. In both cases the results were highly non-reproducible from one sample to another. Many samples exhibited unstable frequency variations such as the results with ACN shown in **Fig. II-8c**.

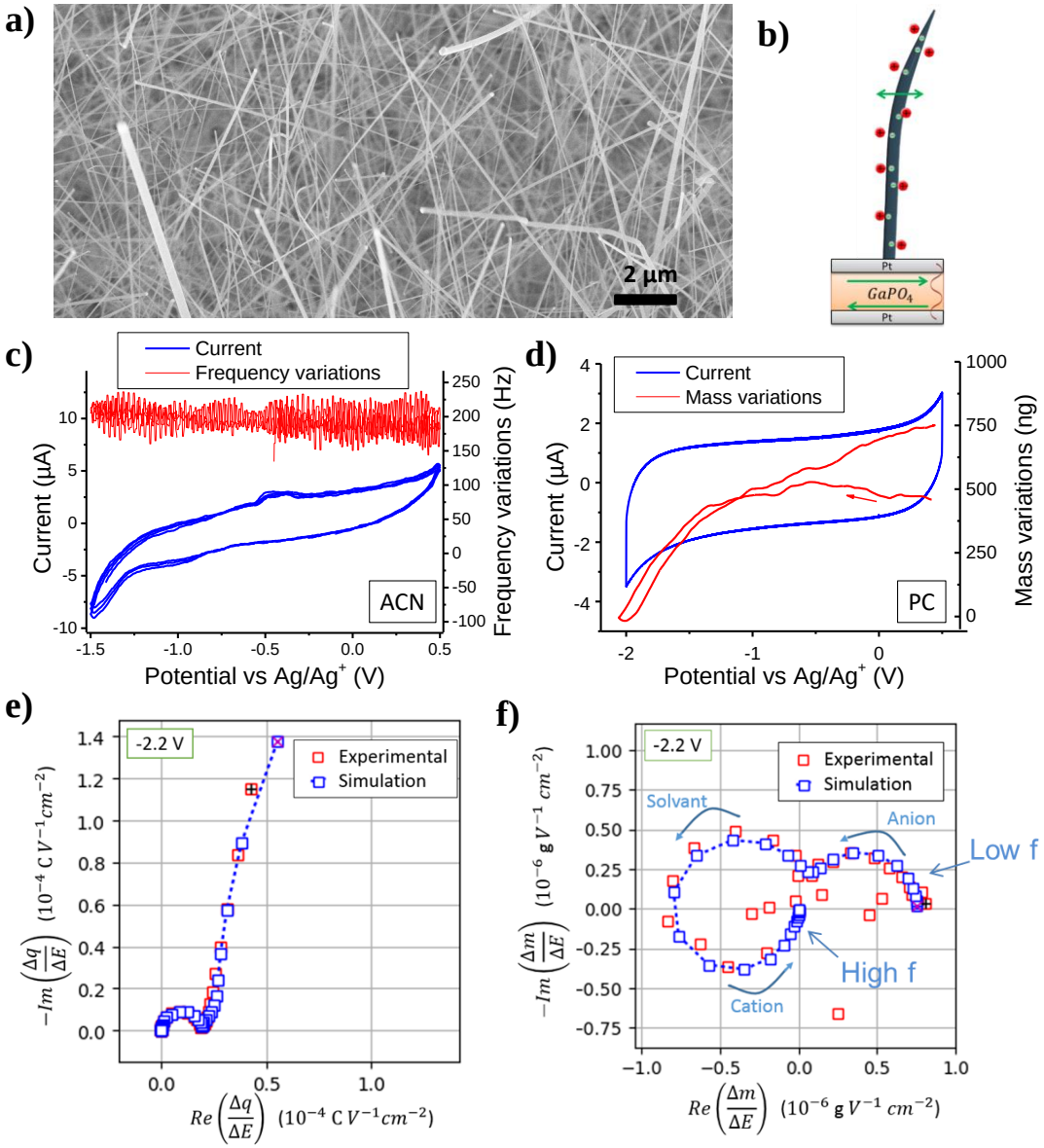

Figure II-8: a) SEM image of SiNWs on a $GaPO_4$ resonator. **b)** Schematic of a polarized SiNW moving at the surface of an operating QCM. **c)** EQCM results with unstable frequency on SiNWs with ACN+0.5M $TBABF_4$ at 100 $mV.s^{-1}$. **d)** EQCM result with the mass response of SiNWs in PC+0.5M $TBABF_4$ at 100 $mV.s^{-1}$. **e-f)** Nyquist plots of *ac*-electrogravimetric TFs $\frac{\Delta q}{\Delta E}$ and $\frac{\Delta m}{\Delta E}$ and a fit with very large masses.

For a part of the measured samples using PC+0.5M $TBABF_4$, large periodic frequency shifts of 100-250 Hz were observed as CV cycles were performed. Then, the Sauerbrey equation was applied to obtain the gravimetric response (Δm) of the system presented **Fig. II-8d**. From this experimental response, the mass per mole of electrons ($MPE = F\frac{\Delta m}{\Delta q}$) was estimated. If the shifts in resonance frequency correspond to the exchange of one charged species with the electrolyte, then the molar mass of this species corresponds to the MPE. The highest slopes for Δm are obtained for potentials below -1 V vs Ag/Ag^+. The samples displaying an EQCM response such as **Fig. II-8d** resulted in MPE values ranging from 1000 to 4000 $g.mol^{-1}$ below -1 V vs Ag/Ag^+. Such molar masses are an order of magnitude higher than the molar mass of the ions in the electrolyte: $M_{TBA+} = 242.46\ g{\cdot}mol^{-1}$ and $M_{BF4-} = 86.8\ g{\cdot}mol^{-1}$. Even taking into account a solvation shell, the frequency shifts observed in PC+0.5M $TBABF_4$ cannot be attributed to gravimetric changes of the SiNW electrode. To explain these large and unpredicted values, it is possible that the hydrodynamic contribution or the viscoelastic properties of the SiNWs mask totally the gravimetric response. This effect was demonstrated during the measurements of the electroacoustic impedance of our resonators covered with SiNWs and filled with the different solvents. Indeed, the Q factors were drastically reduced in this case indicating this strong damping contribution.

To further confirm this statement, *ac*-electrogravimetry measurements were performed on the same samples to separate the contributions to these frequency shifts. Most of the resulting data for the mass/potential transfer function ($\frac{\Delta m}{\Delta E}$) had not well defined loops that could not be fitted with our *ac*-electrogravimetry model. In one case shown in **Fig. II-8f** it was possible to distinguish three loops that could correspond respectively to anion, solvent and cation contributions from low to high frequencies. However in order to fit this data with our model, ionic masses 50 to 100 times greater than the real values would be required. The data for the charge/potential transfer function ($\frac{\Delta q}{\Delta E}$) shown in **Fig. II-8e** led to similar results as the EIS measurements presented in the previous section.

With both EQCM and *ac*-electrogravimetry, it was confirmed that the frequency shifts observed in PC+0.5M $TBABF_4$ are not induced by mass changes of the electrode, but rather by hydrodynamic or perhaps viscoelastic changes within the SiNW array. The following

phenomenon is proposed: As the electrode is polarized and ions gather at the surface of the SiNWs (**Fig. II-8b**), the flow of the electrolyte is modified in a way that changes the hydrodynamic contribution to the resonance frequency shift. This phenomenon is not observed in ACN-based electrolytes because of the lower viscosity of ACN that leads to much lower hydrodynamic perturbations. The reduced length the SiNWs used here (10 µm) leads to reduced current densities that trigger very low mass variations. Measuring these low mass variations would require a very stable QCM with very low hydrodynamic perturbations. Reducing the nanowire length is not a solution because it would reduce the current and the mass variations at the same time as the hydrodynamic perturbations. In fact we obtained a strong contribution of a viscous drag and the real mass response is very small. The difficulty is to extract the pure gravimetric response.

II-4.iii. Viscous drag simulations

The goal here will be to estimate this viscous drag contribution over our QCM response. As a resonator operates, the electrode surface experiences low amplitude shear oscillations at high frequencies that lead to accelerations a million times stronger than the gravitation constant $g = 9.81\, m.s^{-2}$ [51]. When vertically-oriented nanostructures in a fluid are exposed to such oscillations, hydrodynamic forces can bring perturbations to the QCM response. First, a part of the fluid can be trapped within the nanostructures and add it's inertia to the QCM. Second, viscous drag forces apply to the nanostructures moving in the fluid. To better understand the second mechanisms taking place in SiNW arrays, the following simplified simulation is proposed.

We define the system as an homogeneous array of 10^9 vertical SiNWs per cm² represented by cylinders with a diameter D=100 nm and a length L=10 µm on top of a QCM operating at a power P=100 µW. The mass of this nanowire array (m) can be calculated as:

$$m = \rho_{Si} N_{SiNWs} \frac{D^2 \pi}{4} L \qquad \textbf{(Eq. II-1)}$$

where $\rho_{Si} = 2329\, kg.m^{-3}$ is the density of c-Si and $N_{SiNWs} = 10^9\, cm^{-2}$ is the number of nanowires per surface unit.

The resulting mass, $m = 183\ \mu g.cm^{-2}$ is close to the average mass of SiNWs on our samples. We then define $x(t) = A_0.\sin(\omega t)$ as the displacement of the surface during the QCM operation, where $\omega = 2\pi f$ and A_0 is the oscillation amplitude that can be derived with the following equations [51]:

$$\begin{aligned} A_0 &= CQV_d \\ V_d &= \sqrt{2PR} \end{aligned} \qquad \textbf{(Eq. II-2)}$$

where $C = 1.4 \times 10^{-12} m.V^{-1}$, $Q = \frac{\omega L}{R}$ is the quality factor, V_d is the peak voltage applied on the resonator electrodes. The values of f, R, L and Q are taken from **Table II-1**.

Oscillation amplitudes of 0.153 and 0.108 nm are found for ACN and PC respectively. The speed ($v(t)$) and acceleration ($a(t)$) of the QCM surface are then derived as:

$$v(t) = A_0\omega\cos(\omega t)$$
$$a(t) = -A_0\omega^2\sin(\omega t) \quad \textbf{(Eq. II-3)}$$

The Reynolds number is calculated with:

$$Re = \rho\frac{v_{max}D}{\mu} \quad \textbf{(Eq. II-4)}$$

where ρ is the fluid density, μ is the fluid's dynamic viscosity and $v_{max} = A_0\omega$ is the maximal speed of the electrode surface.

In every configuration, the resulting Reynolds numbers are always very low (around 10^{-4}). We could thus use Lamb's equation to derive the drag coefficient (C_D) of the cylindrical SiNWs [52]:

$$C_D = \frac{8\pi}{Re\left(\frac{1}{2}-\gamma-\ln\left(\frac{Re}{8}\right)\right)} \quad \textbf{(Eq. II-5)}$$

where $\gamma = 0.5772$ is the Euler constant.

The drag force F_d acting on the SiNW array could then be derived:

$$F_d(t) = N_{SiNWs} \times \frac{1}{2}\rho\, v(t)^2 DL\, C_D \times \left(-\frac{v(t)}{|v(t)|}\right) \quad \textbf{(Eq. II-6)}$$

where $\left(-\frac{v(t)}{|v(t)|}\right)$ is multiplied to give F_d the opposite sign of $v(t)$ and thus take into account the direction of the force.

Within this model, the maximal values of $F_d(t)$ are 0.03 and 0.13 $N.cm^{-2}$ using ACN and PC respectively, showing that a large reduction in drag force is obtained for low viscosity solutions. However in practice the mean speed of the fluid relative to the nanowires is reduced in PC compared to ACN because of their large difference in viscosity (**Fig. II-9a**). Thus for this simulation a reduction factor of ½ was applied to $F_d(t)$ in the case of PC. The drag forces are then compared to the inertial force F_i exerted by the nanowire array on the surface of the electrode as it oscillates, which is opposite to the acceleration:

$$F_i = -m\, a(t) \quad \textbf{(Eq. II-7)}$$

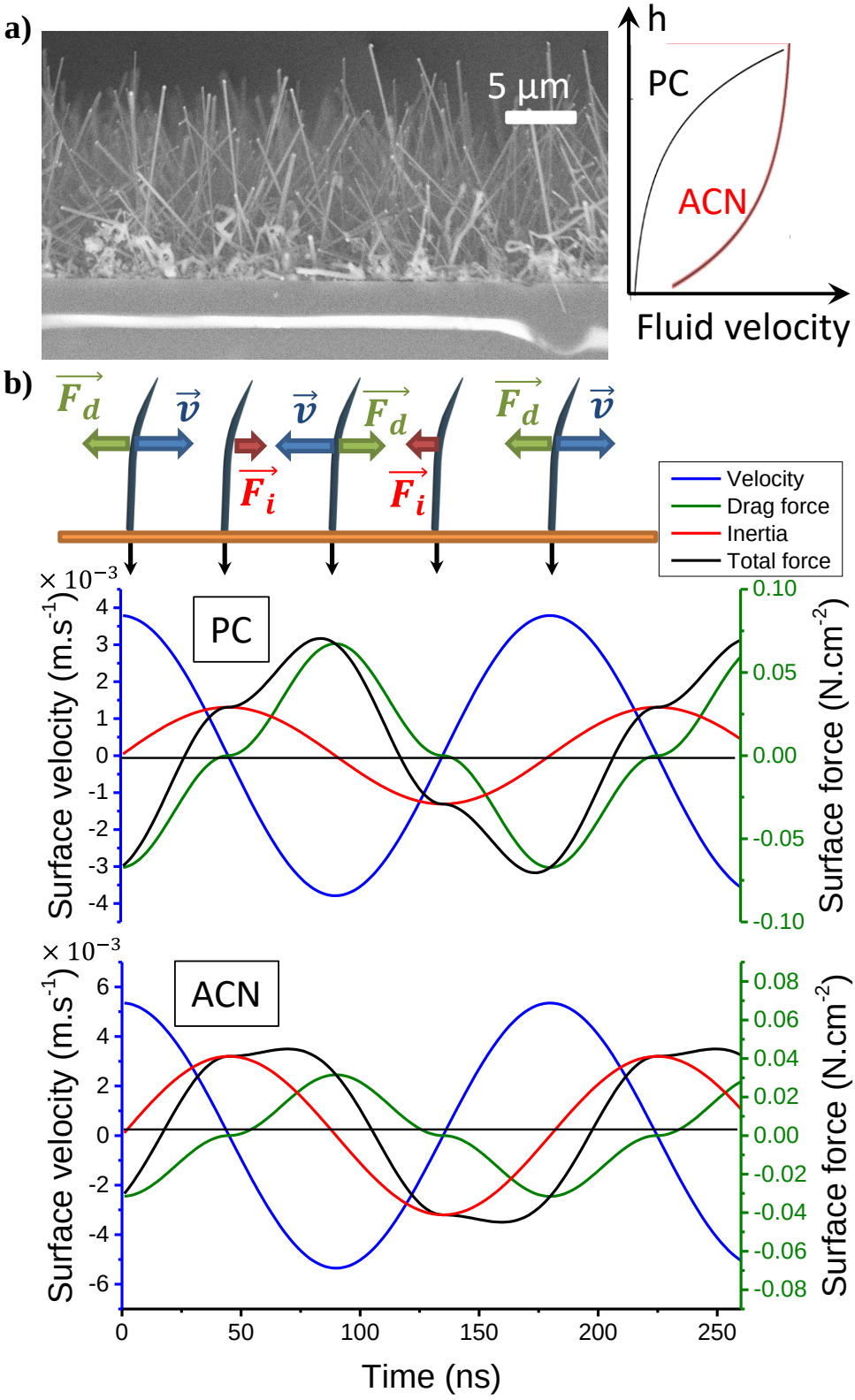

Figure II-9: a) Cross-section view of SiNWs along with the hypothetic shape of the fluid velocity as a function of height in PC and ACN. **b)** Variations of surface speed, drag force, inertial force and total force over an oscillation period for both PC and ACN.

Fig. II-9b depicts the variations of speed (blue), drag force (green) and inertial force (red) over an oscillation period for both PC and ACN as fluids. It is clearly seen that the drag forces have a phase shift of $\frac{\pi}{2}$ compared to the inertial force. This shows that the drag forces do not only enhance or reduce the effect of inertia: they create a distortion of the force experienced by the QCM. The sum of the drag and inertial forces depicted in black shows the total force exerted by the SiNW array on the operating QCM, although the inertial force of the trapped fluid is not considered here. In the case of PC, the hydrodynamic drag forces are larger than the inertial forces, showing that they have become predominant over the inertia of the system. In the case of ACN both forces have approximately the same magnitude, however the phase-shift between the two creates a distortion in the sum of forces. This distortion may be the cause for the QCM instability obtained in EQCM measurements performed previously.

From this simplified model, a better understanding of the issue raised by SiNWs for electrogravimetric characterization is obtained. The drag forces acting on the nanowires, which are proportional to the nanowire length, trigger a distortion of the force experienced by the resonating QCM that lowers it's precision. However reducing the length of the nanowires would also reduce the current proportionally, reducing the mass variations. Using an alternative expression of the MPE (**Eq. II-8**), we find that if only BF_4^- anions are exchanged with a current value (I) around 2 µA at a scan rate $v = 100\ mV.s^{-1}$ then a reasonable mass variation of 35 ng needs to be measured over $\Delta E = 2\ V$ (**Eq. II-9** with $MPE = M_{BF_4^-} = 86.8\ g.mol^{-1}$).

$$MPE = F\frac{\Delta m}{\Delta q} = F\frac{v}{I}\frac{\Delta m}{\Delta E} \qquad \textbf{(Eq. II-8)}$$

$$\Delta m = MPE \times \frac{I\Delta E}{Fv} \qquad \textbf{(Eq. II-9)}$$

A current of 2 µA was obtained with 10 µm long SiNWs with the surface of 0.2 cm^2 imposed by the QCM. If the nanowire length is decreased to 2 µm, a current of around 0.4 µA would be obtained and a mass variation for only anions of 7 ng over 2 V would have to be measured, which is too small unless the QCM is very stable. Thus, raising the precision with shorter nanowires is not a solution to the dual issue of current and drag. In the next section, super-capacitive conductive polymer nanowires are used to solve the issue of current.

III. PEDOT nanowires

III-1. Electropolymerization of nanowires on a QCM

Template-free electropolymerization of conducting polymer nanowire electrodes is becoming a very mature process with many recent developments reported in literature [53]–[57]. The principle of this nanowire growth process is based on the electropolymerization of the monomer in the presence of some particular ions and under specific pH conditions. The polymer becomes conducting as a result of doping from ions of the solution during the monomer oxidation. The formation of conductive polymer nanowires usually implies stepwise electrodeposition with a nucleation step followed by a growth step [53]. In the case of pyrrole, the presence of only weak-acid anions during potentiostatic electrooxidation leads to a 10-20 nm thin non-conductive overoxidized polypyrrole (OPPy) film. Debiemme-Chouvy *et al.* demonstrated that this film could be modified to obtain a one-step nanowire growth process: When non-acidic anions are added to the solution in the presence of K_2HPO_4, PPy nanowires grow surrounded by the OPPy film (**Fig. III-1**) [54], [56].

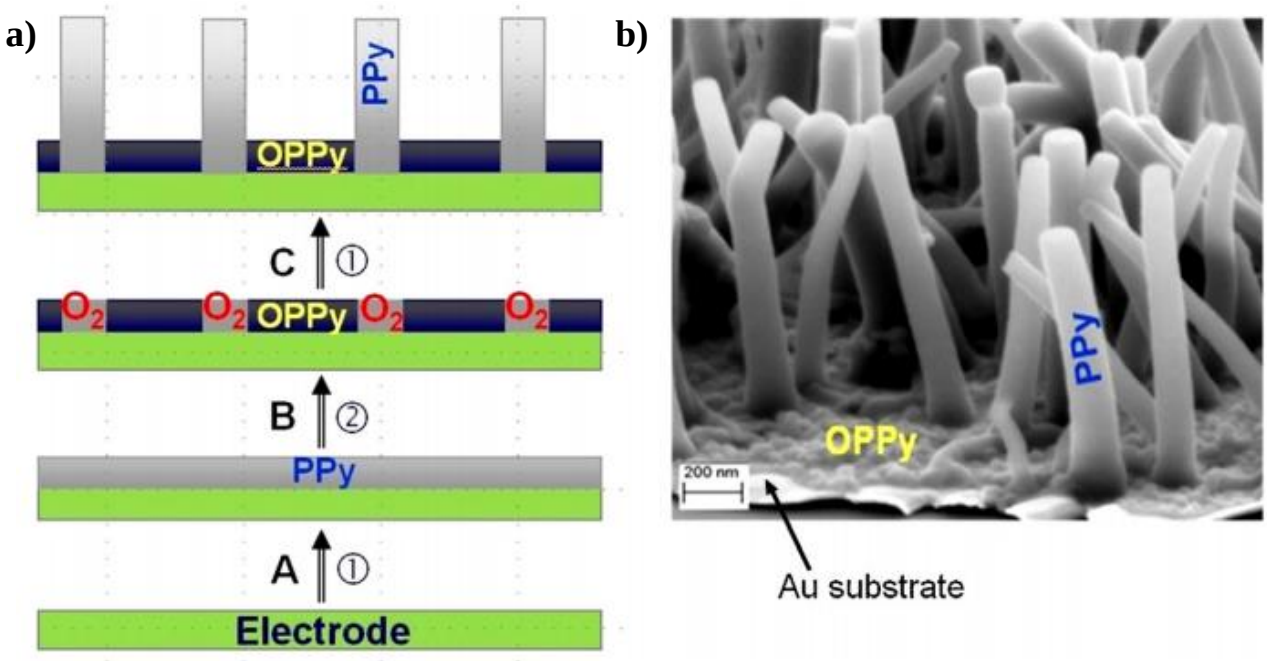

Figure III-1: a) Schematic view of the growth process. **b)** SEM image of PPy nanowires grown template-free. [57]

The method used in this PhD work is a variation of this technique developed by Debiemme-Chouvy *et al.* in order to grow PEDOT nanowires in a single template-free step. The QCM used for the growth is a classical AT-cut 9 MHz quartz microbalance from AWSensors with gold electrodes. A few adaptations from the original growth conditions have been made to achieve a successful and dense growth of nanowires on the QCM, as described in **Fig. III-2**.

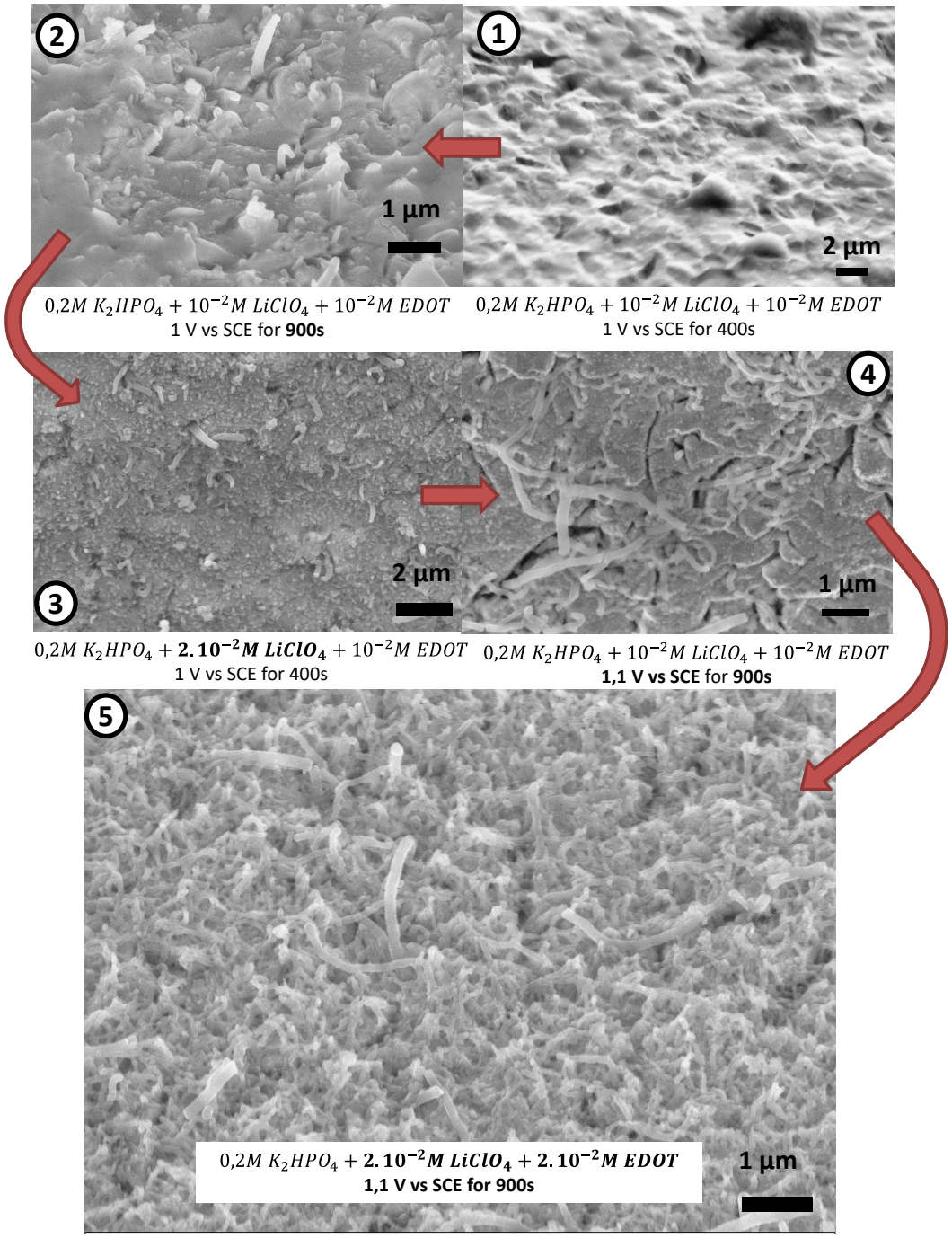

Figure III-2: Adaptations of the one-step PEDOT NW electropolymerization process on the gold electrode of a QCM with SEM images resulting from each growth condition.

The adapted growth conditions consist of the following two steps:

- Preparing an aqueous solution containing $0.2M\ K_2HPO_4 + 2.10^{-2}M\ LiClO_4 + 2.10^{-2}M$ 3,4 − $Ethylenedioxythiophene$ $(EDOT)$.
- Adding the solution to the 3-electrode QCM cell and applying 1.1 V vs Saturated Calomel Electrode (SCE) for 900s.

Fig. III-2-step 5 depicts a SEM image showing the morphology of the resulting nanowires. This electropolymerization process results in PEDOT nanowires with a diameter around 100 nm and a length of 1-2 µm. A total PEDOT nanowire mass of 28 µg.cm^{-2} was estimated from microbalance measurements, which is around 10 times lower than the 10 µm-long SiNW samples used in the previous section. These properties have been reproduced on several samples under the same growth conditions in a reasonable way. As opposite to CVD, this grow process is very well adapted for QCMs because it doesn't require high temperatures or harsh growth conditions that could harm the resonator's properties.

Once the growth successful, the properties of the quartz resonators were investigated using a network analyzer in air and ACN and reported in **Table III-1**.

Configuration	Fluid visc. $(mPa.s)$	Fluid density $(kg.m^{-3})$	Resonance frequency (MHz)	Peak width (Hz)	R (Ω)	L (H)	Quality factor
PEDOT NW in air	0.0184	1.17	8.983	922	67	0.01164	9734
PEDOT NW in ACN	0.34	786	8.980	4002	273	0.01086	2243

Table III-1: Values obtained for the resonance frequency, peak width at half height, resistance, inductance and quality factor for a quartz resonator with Au electrodes covered with PEDOT NWs in air and ACN.

The quality factor obtained with PEDOT NWs in ACN (Q_{ACN} = 2243) is ten times higher than SiNW electrodes in the same solvent (Q = 236), and almost as high as $GaPO_4$ resonators without SiNWs in ACN (Q = 3500). This is due to the naturally higher quality factors obtained with quartz resonators compared to $GaPO_4$ resonators, the absence of high temperature annealing and the shorter length of these nanowires (1-2 µm) compared to SiNWs (10 µm).

This high quality factor, along with a low resistance of 273Ω, allows the use of these quartz resonators for gravimetric measurements in ACN-based electrolytes.

III-2. EQCM measurements

As presented in chapter 1-III.2, conducting polymer electrodes such as PANi and PPy have been previously studied with EQCM and *ac*-electrogravimetry techniques [58], [59]. However no gravimetric study has been reported on conducting polymer nanowires. For this PhD work PEDOT has been selected among other conducting polymers due to it's significant advantages for energy storage applications: A reversible doping state, an excellent stability, a regular structure and low redox potentials [60].

After the successful growth of PEDOT NWs on a QCM (**Fig. III-3a**), EQCM measurements were conducted from -1.5 V to 0.7 V vs Ag/Ag^+ in ACN+0.5 M $TBABF_4$ in order to have a low viscosity electrolyte along with a wide electrochemical window compared to aqueous electrolytes. An important microbalance frequency shift was observed up to one hour after electrolyte introduction in the electrochemical cell, indicating mass-loss inducing mechanisms were taking place as the electrode was stabilizing in the solution. This is attributed to the partial dissolution of the doping ions from the PEDOT NWs.

Fig. III-3b-c depicts the EQCM measurements performed on PEDOT NWs at the following scan rates: 100, 50, 20 and 10 $mV.s^{-1}$. No significant changes in both current and mass variations were observed when the scan rate was changed. The shape of the CV showed in **Fig. III-3b** is similar to previously reported results on PEDOT in ACN with $LiClO_4$ and $TBAClO_4$ [61], [62]. A large residual current is observed after the oxidation wave, associated with pseudo-capacitive behavior [61]. This is especially seen at 50 $mV.s^{-1}$ and below. An areal capacitance (AC) value of 715 $\mu F.cm^{-2}$ and a specific capacitance of 25 $F.g^{-1}$ are obtained at 100 $mV.s^{-1}$ using **Eq. II-1&2** from chapter 2 and an electrode surface of 0.2 cm^{-2}. Stable and periodic mass variations of around 200 ng are observed at all measured scan rates, with the mass increasing during reduction and decreasing rapidly just after the oxidation peak (**Fig. III-3c**). This is associated with periodic doping of the PEDOT NWs with cations during reduction and undoping oxidation. A mean MPE value of -70 $g.mol^{-1}$ is derived right after the oxidation peak for potentials between 0 V and 0.7 V vs Ag/Ag^+. This value is decreased down to around -10 $g.mol^{-1}$ during reduction. The negative sign of the MPE corresponds to a predominant exchange of cations. However these values are lower than the mass of TBA^+ cations (M_{TBA+} = 242.46 $g{\cdot}mol^{-1}$), which could be explained by two possible phenomena:

- BF_4^- anions are expulsed at more or less the same time as TBA^+ cations are adsorbed, leading to a partial cancellation of the observed mass variations.
- Li^+ cations from the initial doping of the PEDOT NWs are exchanged at the same time as TBA^+ cations, leading to a mean MPE in between the molar mass of these two cations.

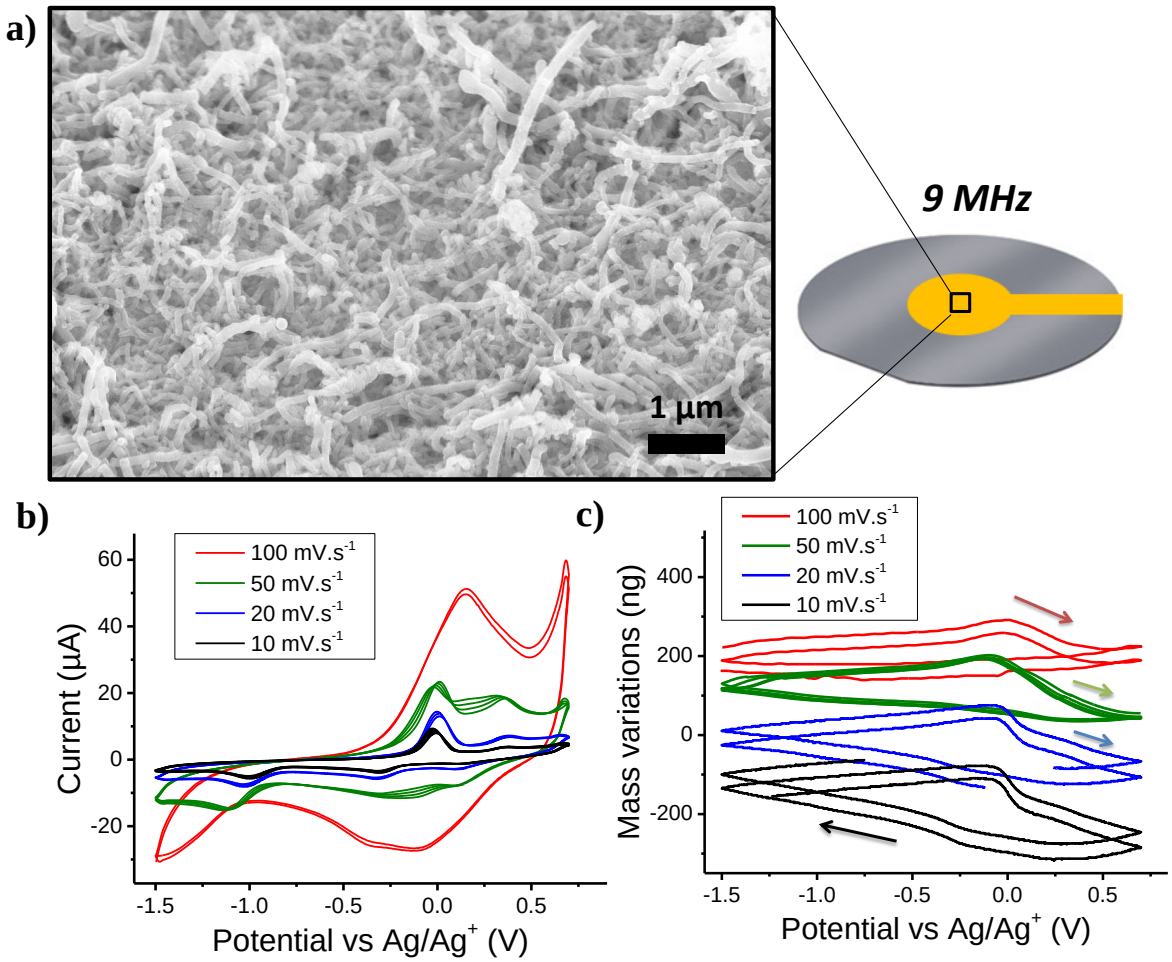

Figure III-3: a) SEM image of PEDOT NWs on the surface of a 9 MHz QCM. **b)** CV measurements on PEDOT NWs in ACN+0.5M $TBABF_4$ at various scan rates and **c)** the corresponding mass variations derived with the microbalance (two cycles).

The data retrieved from EQCM measurements cannot be used to distinguish between these two cases and obtain an answer. To unveil the mechanisms occurring in this pseudo-capacitive material and separate the contributions of the exchanged species, *ac*-electrogravimetric measurements were performed on the same PEDOT NW samples.

III-3. *Ac*-Electrogravimetric measurements

Ac-electrogravimetric measurements were performed on PEDOT NWs in ACN+0.5M $TBABF_4$ with perturbation frequencies ranging from 0.01 Hz to 63 kHz and polarization potentials ranging from -1.4 V to 0.6 V vs Ag/Ag^+ each 0.2 V. The experimental results for $\frac{\Delta m}{\Delta E}$ below -0.2 V were too small and non-exploitable. The results between -0.2 V and 0.6 V vs Ag/Ag^+ were exploitable for frequencies above 0.3 Hz. The points obtained below 0.3 Hz were scattered due to insufficient microbalance stability. This could be caused by hydrodynamic drag forces acting on the nanowires. **Fig. III-4a-d** depicts the Nyquist plots of *ac*-electrogravimetric results obtained at 0 V and 0.4 V. To fit these results, the model described in chapter 2-III was used in two different configurations:

- Using only TBA^+ cations and BF_4^- anions as exchanged species.
- Using only TBA^+ and Li^+ cations as exchanged species.

The first configuration of the model could successfully fit the data for $\frac{\Delta q}{\Delta E}$ in every experiment, however the data for $\frac{\Delta m}{\Delta E}$ could not be fitted with the same set of parameters. Adding free ACN solvent molecules as exchanged species in the same direction as TBA^+ cations partially solved the issue.

The second configuration could successfully fit the data from both $\frac{\Delta q}{\Delta E}$ and $\frac{\Delta m}{\Delta E}$ at all the valid potentials without adding a third exchanged species (**Fig. III-4a-d**). Thus, this second configuration seems a more adequate model to explain the exchange mechanism between the PEDOT NWs and the electrolyte. Li^+ cations from the initial doping of the PEDOT NWs diffused into the electrolyte upon first exposure, explaining the mass loss measured for some time at the beginning of the experiment. Li^+ and TBA^+ cations are reabsorbed within the PEDOT NWs upon reduction and released back into the electrolyte after the oxidation peak at 0 V.

Using the *ac*-electrogravimetry fitting model, the mutual contributions of Li^+ and TBA^+ were obtained: The transfer resistance $R_{t_i} = \frac{1}{G_i}$, where G_i is the parameter for ease of transfer for species i, was derived for both species at each measured potential. Both Li^+ and TBA^+ cations were found to have a mean transfer resistance around $2\ k\Omega.\mathrm{cm}^{-2}$.

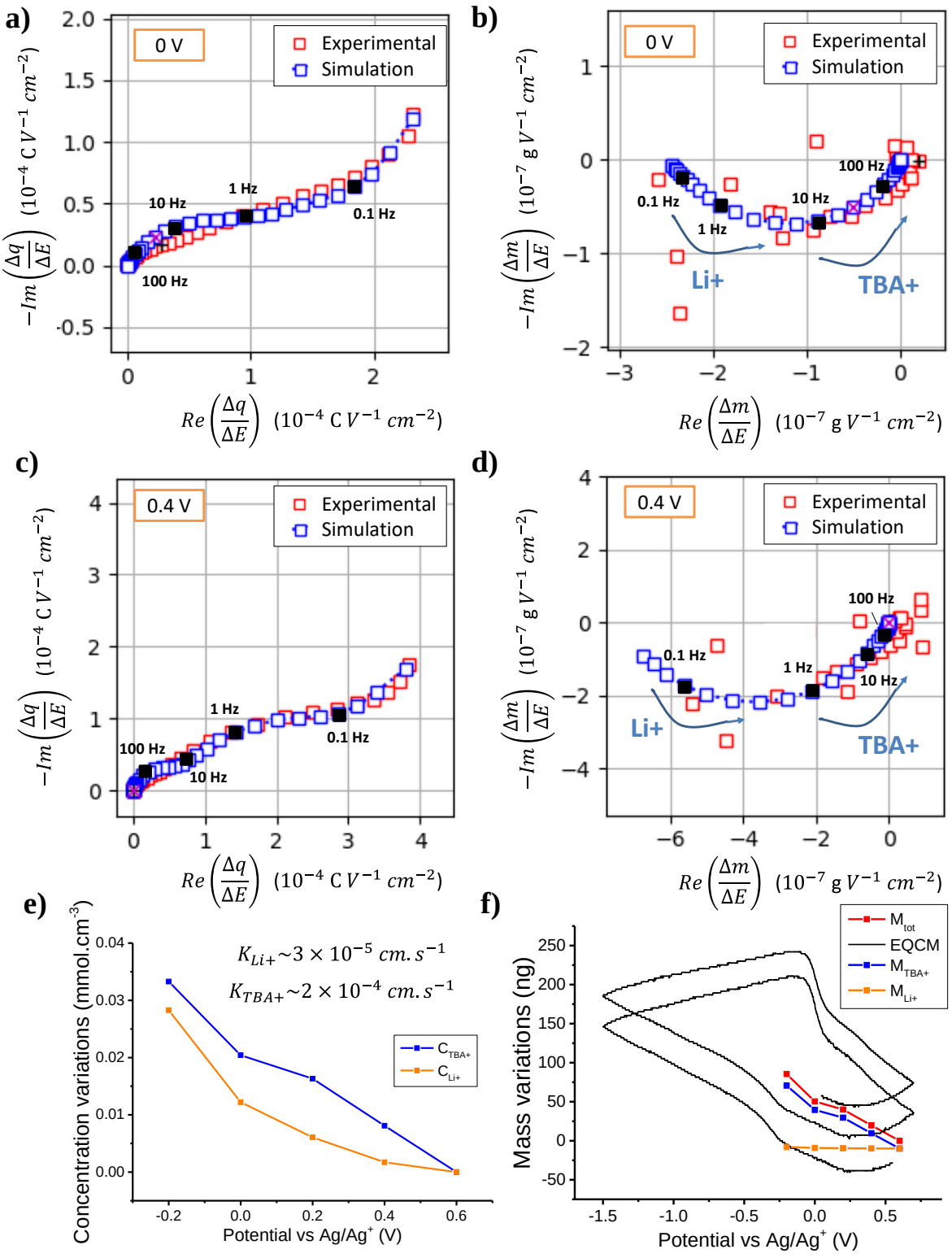

Figure III-4: a-d) Nyquist plots of *ac*-electrogravimetry TFs $\frac{\Delta q}{\Delta E}$ and $\frac{\Delta m}{\Delta E}$ acquired at 0V (**a-b**) and 0.4 V (**c-d**) vs Ag/Ag^+ with PEDOT NWs and fitted using Li^+ and TBA^+ cations. **e)** Concentration variations calculated for Li^+ and TBA^+ cations from *ac*-electrogravimetric data. **f)** Mass variations measured with EQCM at 10 $mV.s^{-1}$ and derived from *ac*-electrogravimetry between -0.2 V and 0.6 V vs Ag/Ag^+.

TBA^+ cations, with an average kinetic parameter $K_{TBA+} \sim 2 \times 10^{-4}\ cm.s^{-1}$, were found to be exchanged at higher frequencies than Li^+, with an average kinetic parameter $K_{Li+} \sim 3 \times 10^{-5}\ cm.s^{-1}$. The concentration variations ΔC_i between -0.2 V and 0.6 V for both species could be derived through the integration of the following equation:

$$\frac{\Delta C_i}{\Delta E}(\omega = 0) = \frac{-G_i}{K_i} \qquad \textbf{(Eq. III-1)}$$

The resulting concentration variations, depicted in **Fig. III-4e**, show that both Li^+ and TBA^+ cations are exchanged in almost similar quantities. However, Li^+ cations are much lighter than their TBA^+ counterpart, leading to the averaged mass variations obtained with EQCM. Using the concentration variations derived above, the mass variations induced by each species upon introduction are calculated and shown in **Fig. III-4f** along with the sum of both contributions and the EQCM result at 10 $mV.s^{-1}$. From this graph we observe that the contribution of Li^+ cations to the mass variations is negligible compared to TBA^+ cations, and that the results obtained with *ac*-electrogravimetry are in good agreement with the EQCM results from the previous section. These results confirm that *ac*-electrogravimetry is a very useful tool to operate a deconvolution of the EQCM measurements and unveil the ionic exchange mechanisms at the electrode/electrolyte interface.

IV. Silicon nanowires covered with PEDOT

EQCM and ac-electrogravimetry were successfully used to characterize the ionic exchange mechanisms in PEDOT NW electrodes, however the characterization of bare SiNWs using electrogravimetric techniques is hindered by the dual issue of generating too low mass variations in short nanowires (due to low currents) and too high QCM resonance damping in long nanowires. In the previous section PEDOT NWs have been shown to overcome these issues owing to their pseudo-capacitive behavior, generating higher currents and thus higher mass variations in comparison to hydrodynamic perturbations. In this section, the electrogravimetric response in PEDOT-covered SiNW electrodes was examined.

This novel electrode architecture has been designed to combine the advantages of both materials, with the higher conductance of highly doped SiNWs and the higher capacitance of PEDOT due to their pseudo-capacitive behavior. Directly grown on the substrate, SiNWs are used both as a deposition template to obtain long and dense nanowires and as highly conductive current collector to bring charges all along the nanowires to the conducting polymer coating. This hybrid electrode was shown to significantly improve the performances of conductive polymer pseudo-capacitors with a specific capacitance of 32 $F.g^{-1}$ and a maximal power density of 85 $kW.kg^{-1}$ [46].

PEDOT was electrodeposited on the surface of 10 µm long N-doped SiNWs grown on top of Au(12 nm)/Pt(200nm)/Ti(10nm)/$GaPO_4$ resonators as described in section II. Prior to the electropolymerization, the samples were introduced in the electrochemical cell with PC+0.1M $TBABF_4$+10 mmol EDOT and three CV cycles were performed. An oxidation peak starting at 0.75 V vs Ag/Ag^+ and corresponding to the polymerization of EDOT was identified. The electropolymerization was performed with chronoamperometry at 0.9 V vs Ag/Ag^+ for 1h. A SEM picture of the resulting PEDOT-covered SiNWs is shown **Fig. IV-1a**. After deposition, the resonance frequency of the resonator had decreased of 8 kHz, which corresponds to a deposited PEDOT mass of 125 $µg.cm^{-2}$ (compared to a bare SiNW mass of 220 $µg.cm^{-2}$). This nearly 100 nm thick PEDOT loading has increased the nanowire diameters from 100-500 nm to 400-700 nm, as measured from SEM images.

After polymerization, the $GaPO_4$ resonator supporting the PEDOT-covered SiNWs was monitored with a network analyzer in air, ACN and PC. The properties extracted from these measurements are presented in **Table IV-1**.

Configuration	Fluid visc. ($mPa.s$)	Fluid density ($kg.m^{-3}$)	Resonance frequency (MHz)	Peak width (Hz)	R (Ω)	L (H)	Quality factor
PEDOT/SiNWs in air	0.0184	1.17	5.699	12385	528	0.00679	460
PEDOT/SiNWs in ACN	0.34	786	5.698	25599	1013	0.0063	223
PEDOT/SiNWs in PC	2.5	1200	5.688	69997	2436	0.00554	81

Table IV-1: Values obtained for the resonance frequency, peak width at half height, resistance, inductance and quality factor for a $GaPO_4$ resonator with PEDOT-covered SiNW electrodes in air, ACN and PC.

The quality factor of these resonators with PEDOT/SiNWs in air is very low (<500) compared to those obtained with SiNWs (around 4600). The low value of 81 obtained in PC completely hinders the use of these resonators with such high viscosity solvents. However, in ACN the quality factor is not reduced in as great proportions and is therefore equivalent to that of bare SiNWs in the same solvent (223). Even though a relatively low stability is expected with such quality factors and peak width, this might be compensated by the large currents and thus large mass variations obtained in pseudo-capacitive materials.

Therefore, EQCM measurements were performed on PEDOT-covered SiNWs in ACN+0.5M $TBABF_4$ (**Fig. IV-1b**). The shape of the CV obtained with these electrodes is very similar to the shape obtained in the previous section with PEDOT NWs. An AC value of 17 $mF.cm^{-2}$ and a specific capacitance value of 50 $F.g^{-1}$ were obtained at 100 $mV.s^{-1}$ by considering a global electrode mass of 345 $\mu g.cm^{-2}$. As expected from the Q factor of the resonator, low microbalance stability was obtained due to hydrodynamic damping of the resonance. However large periodic mass variations of around 700 ng could be observed between -0.75 V and -0.2 vs Ag/Ag^+. The shape of these mass variations is completely different from the behavior observed in the previous section where only cations where exchanged. In this covering PEDOT electrode the mass variations are concentrated around the oxidation peak and show a major anion contribution. These differences can be explained with the fact that in this case the initial doping of PEDOT was

performed in the presence of $TBABF_4$ while in the previous section $LiClO_4$ was used and we have shown that Li^+ cations had a great impact on the exchanges.

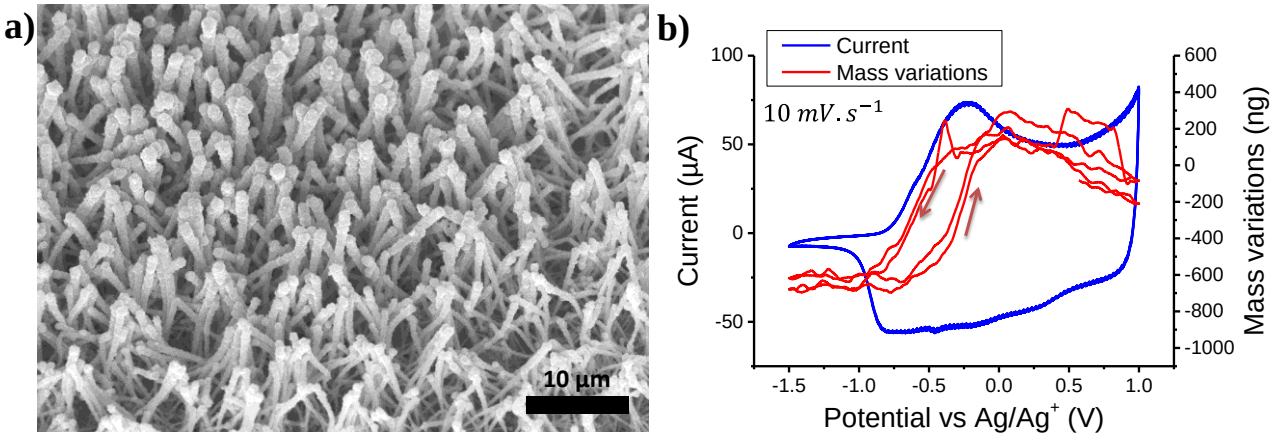

Figure IV-1: a) SEM image of PEDOT-covered SiNWs on a $GaPO_4$ resonator and **b)** two cycles of CV and mass variations obtained at 10 $mV.s^{-1}$ in ACN+0.5M $TBABF_4$.

Between -0.75 V and -0.2 vs Ag/Ag^+ the value of the MPE is around 26 $g.mol^{-1}$, which is much lower than the molar mass of BF_4^- anions (86.8 $g{\cdot}mol^{-1}$). This indicates that cations are exchanged at the same time as the anions in a way that during the oxidation peak TBA^+ cations are expelled from the PEDOT and replaced with the adsorption of BF_4^- anions. *Ac*-electrogravimetric measurements would be very helpful to better understand the mutual contributions from both ions, however the experimental data obtained with these samples did not lead to useable results. The abundance of noise in these measurements is associated to a too large hydrodynamic damping of the resonance due to the nanostructures. Nevertheless, the study presented here shows that the mass variations obtained in this configuration are very large, which paves the way to new experiments on PEDOT-covered SiNWs with shorter nanowires and thus better stability.

Conclusions

Three kinds of nanowire electrode configurations made from silicon, PEDOT and a combination of both were successfully grown on QCM resonators. The challenge of retaining a functional microbalance after the CVD growth of SiNWs was overpassed using $GaPO_4$ as piezoelectric material, Ti as adhesion layer and Pt as oxidation-resistant electrode material. The development of a new mixture of PC+N_{1114}TFSI with optimized electrochemical properties was conducted on SiNW supercapacitor devices, leading to a significant improvement of their performances.

A dual issue of low currents and significant drag forces concerning the electrogravimetric characterization of bare SiNW electrodes hindered their investigation with EQCM and *ac*-electrogravimetry. A simplified model was used to better understand the action of the drag forces relative to inertial forces on the QCM electrode.

The issue of current was then bypassed using pseudo-capacitive PEDOT NW electrodes and EQCM was successfully used to find a major cation contribution in ACN+$TBABF_4$. To operate a deconvolution of the EQCM signal, *ac*-electrogravimetry was employed and unveiled an equal contribution of Li^+ and TBA^+ cations to the exchange mechanisms.

Hybrid PEDOT/silicon nanowires were developed on $GaPO_4$ resonators and significant mass variations were measured with EQCM. As opposite to the previous example, a major anion contribution to the ionic exchanges was discovered in this pseudo-capacitive electrode using ACN+$TBABF_4$. However no results could be obtained using *ac*-electrogravimetry due to hydrodynamic damping of the QCM.

References

[1] G. Zheng, F. Patolsky, Y. Cui, W. U. Wang, and C. M. Lieber, 'Multiplexed electrical detection of cancer markers with nanowire sensor arrays', *Nat. Biotechnol.*, 23, no. 10, pp. 1294–1301, Oct. 2005.

[2] T. Bryllert, L.- Wernersson, L. E. Froberg, and L. Samuelson, 'Vertical high-mobility wrap-gated InAs nanowire transistor', *IEEE Electron Device Lett.*, 27, no. 5, pp. 323–325, May 2006.

[3] T. J. Kempa, B. Tian, D. R. Kim, J. Hu, X. Zheng, and C. M. Lieber, 'Single and Tandem Axial p-i-n Nanowire Photovoltaic Devices', *Nano Letters.* 8 (2008) 3456–3460.

[4] C. K. Chan, H. Peng, G. Liu, K. McILWRATH, X. F. Zhang, R. A. Huggins, and Y. Cui, 'High-performance lithium battery anodes using silicon nanowires', in *Materials for Sustainable Energy*, 0 vols, Co-Published with Macmillan Publishers Ltd, UK, 2010, pp. 187–191.

[5] A. B. Greytak, C. J. Barrelet, Y. Li, and C. M. Lieber, 'Semiconductor nanowire laser and nanowire waveguide electro-optic modulators', *Appl. Phys. Lett.*, 87, no. 15, p. 151103, Oct. 2005.

[6] N. Berton, M. Brachet, F. Thissandier, J. Le Bideau, P. Gentile, G. Bidan, T. Brousse, and S. Sadki, 'Wide-voltage-window silicon nanowire electrodes for micro-supercapacitors via electrochemical surface oxidation in ionic liquid electrolyte', *Electrochem. Commun.*, 41, pp. 31–34, Apr. 2014.

[7] L.-Q. Mai, F. Yang, Y.-L. Zhao, X. Xu, L. Xu, and Y.-Z. Luo, 'Hierarchical $MnMoO_4/CoMoO_4$ heterostructured nanowires with enhanced supercapacitor performance', *Nat. Commun.*, 2, p. 381, Jul. 2011.

[8] Q. Wang, Z. H. Wen, and J. H. Li, 'A Hybrid Supercapacitor Fabricated with a Carbon Nanotube Cathode and a TiO_2–B Nanowire Anode', *Adv. Funct. Mater.*, 16, no. 16, pp. 2141–2146, Oct. 2006.

[9] T. Belmonte, *Dépôts chimiques à partir d'une phase gazeuse*. Tech. l'ingénieur, 2010.

[10] A. C. Jones and M. L. Hitchman, *Chemical Vapour Deposition: Precursors, Processes and Applications*. Royal Society of Chemistry, 2009.

[11] D. Gaboriau, *Nanostructures de silicium par croissance chimique catalysée : une plate-forme pour des applications micro-supercondensateurs*. Grenoble Alpes, 2016.

[12] B. Ressel, K. C. Prince, S. Heun, and Y. Homma, 'Wetting of Si surfaces by Au–Si liquid alloys', *J. Appl. Phys.*, 93, no. 7, pp. 3886–3892, Mar. 2003.

[13] P. Gentile, A. Solanki, N. Pauc, F. Oehler, B. Salem, G. Rosaz, T. Baron, M. D. Hertog, and V. Calvo, 'Effect of HCl on the doping and shape control of silicon nanowires', *Nanotechnology*, 23, no. 21, p. 215702, 2012.

[14] X. Jiang, K. Kim, S. Zhang, J. Johnson, G. Salazar, X. Jiang, K. Kim, S. Zhang, J. Johnson, and G. Salazar, 'High-Temperature Piezoelectric Sensing', *Sensors*, 14, no. 1, pp. 144–169, Dec. 2013.

[15] S. Kodambaka, J. Tersoff, M. C. Reuter, and F. M. Ross, 'Germanium Nanowire Growth Below the Eutectic Temperature', *Science*, 316, no. 5825, pp. 729–732, May 2007.

[16] F. Thissandier, P. Gentile, N. Pauc, E. Hadji, A. L. Comte, O. Crosnier, G. Bidan, S. Sadki, and T. Brousse, 'Highly N-doped Silicon Nanowires as a Possible Alternative to Carbon for On-chip Electrochemical Capacitors', *Electrochemistry*, 81, no. 10, pp. 777–782, Oct. 2013.

[17] F. Thissandier, A. Le Comte, O. Crosnier, P. Gentile, G. Bidan, E. Hadji, T. Brousse, and S. Sadki, 'Highly doped silicon nanowires based electrodes for micro-electrochemical capacitor applications', *Electrochem. Commun.*, 25, pp. 109–111, Nov. 2012.
[18] F. Thissandier, L. Dupré, P. Gentile, T. Brousse, G. Bidan, D. Buttard, and S. Sadki, 'Ultra-dense and highly doped SiNWs for micro-supercapacitors electrodes', *Electrochimica Acta*, 117, pp. 159–163, Jan. 2014.
[19] D. Aradilla, P. Gentile, G. Bidan, V. Ruiz, P. Gómez-Romero, T. J. S. Schubert, H. Sahin, E. Frackowiak, and S. Sadki, 'High performance of symmetric micro-supercapacitors based on silicon nanowires using N-methyl-N-propylpyrrolidinium bis(trifluoromethylsulfonyl)imide as electrolyte', *Nano Energy*, 9, pp. 273–281, Oct. 2014.
[20] D. Aradilla, P. Gentile, V. Ruiz, P. Gómez-Romero, J. Wimberg, B. Iliev, T. J. S. Schubert, S. Sadki, and G. Bidan, 'SiNWs-based electrochemical double layer micro-supercapacitors with wide voltage window (4 V) and long cycling stability using a protic ionic liquid electrolyte', *Adv. Nat. Sci. Nanosci. Nanotechnol.*, 6, no. 1, p. 015004, 2015.
[21] V. Ruiz, T. Huynh, S. R. Sivakkumar, and A. G. Pandolfo, 'Ionic liquid–solvent mixtures as supercapacitor electrolytes for extreme temperature operation', *RSC Adv.*, 2, no. 13, pp. 5591–5598, Jun. 2012.
[22] C. Schütter, A. R. Neale, P. Wilde, P. Goodrich, C. Hardacre, S. Passerini, J. Jacquemin, and A. Balducci, 'The use of binary mixtures of 1-butyl-1-methylpyrrolidinium bis{(trifluoromethyl)sulfonyl}imide and aliphatic nitrile solvents as electrolyte for supercapacitors', *Electrochimica Acta*, 220, pp. 146–155, Oct. 2016.
[23] S. Leyva-García, D. Lozano-Castelló, E. Morallón, T. Vogl, C. Schütter, S. Passerini, A. Balducci, and D. Cazorla-Amorós, 'Electrochemical performance of a superporous activated carbon in ionic liquid-based electrolytes', *J. Power Sources*, 336, pp. 419–426, Dec. 2016.
[24] R. Lin, P.-L. Taberna, S. Fantini, V. Presser, C. R. Pérez, F. Malbosc, N. L. Rupesinghe, K. B. K. Teo, Y. Gogotsi, and P. Simon, 'Capacitive Energy Storage from −50 to 100 °C Using an Ionic Liquid Electrolyte', *The Journal of Physical Chemistry Letters*. 2 (2011) 2396–2401.
[25] W.-Y. Tsai, R. Lin, S. Murali, L. Li Zhang, J. K. McDonough, R. S. Ruoff, P.-L. Taberna, Y. Gogotsi, and P. Simon, 'Outstanding performance of activated graphene based supercapacitors in ionic liquid electrolyte from −50 to 80°C', *Nano Energy*, 2, no. 3, pp. 403–411, May 2013.
[26] F. Thissandier, P. Gentile, T. Brousse, G. Bidan, and S. Sadki, 'Are tomorrow's micro-supercapacitors hidden in a forest of silicon nanotrees?', *J. Power Sources*, 269, pp. 740–746, Dec. 2014.
[27] D. Aradilla, F. Gao, G. Lewes-Malandrakis, W. Müller-Sebert, P. Gentile, M. Boniface, D. Aldakov, B. Iliev, T. J. S. Schubert, C. E. Nebel, and G. Bidan, 'Designing 3D Multihierarchical Heteronanostructures for High-Performance On-Chip Hybrid Supercapacitors: Poly(3,4-(ethylenedioxy)thiophene)-Coated Diamond/Silicon Nanowire Electrodes in an Aprotic Ionic Liquid', *ACS Appl. Mater. Interfaces*, 8, no. 28, pp. 18069–18077, Jul. 2016.
[28] V. Chakrapani, F. Rusli, M. A. Filler, and P. A. Kohl, 'Quaternary Ammonium Ionic Liquid Electrolyte for a Silicon Nanowire-Based Lithium Ion Battery', *The Journal of Physical Chemistry C.* 115 (2011) 22048–22053.
[29] V. Chakrapani, F. Rusli, M. A. Filler, and P. A. Kohl, 'Silicon nanowire anode: Improved battery life with capacity-limited cycling', *J. Power Sources*, 205, pp. 433–438, May 2012.

[30] A. Brandt, J. Pires, M. Anouti, and A. Balducci, 'An investigation about the cycling stability of supercapacitors containing protic ionic liquids as electrolyte components', *Electrochimica Acta*, 108, pp. 226–231, Oct. 2013.
[31] A. Krause and A. Balducci, 'High voltage electrochemical double layer capacitor containing mixtures of ionic liquids and organic carbonate as electrolytes', *Electrochem. Commun.*, 13, no. 8, pp. 814–817, Aug. 2011.
[32] A. Brandt, C. Ramirez-Castro, M. Anouti, and A. Balducci, 'An investigation about the use of mixtures of sulfonium-based ionic liquids and propylene carbonate as electrolytes for supercapacitors', *J. Mater. Chem. A*, 1, no. 40, pp. 12669–12678, Sep. 2013.
[33] D. Gaboriau, D. Aradilla, M. Brachet, J. L. Bideau, T. Brousse, G. Bidan, P. Gentile, and S. Sadki, 'Silicon nanowires and nanotrees: elaboration and optimization of new 3D architectures for high performance on-chip supercapacitors', *RSC Adv.*, 6, no. 84, pp. 81017–81027, Aug. 2016.
[34] F. Gao, G. Lewes-Malandrakis, M. T. Wolfer, W. Müller-Sebert, P. Gentile, D. Aradilla, T. Schubert, and C. E. Nebel, 'Diamond-coated silicon wires for supercapacitor applications in ionic liquids', *Diam. Relat. Mater.*, 51, pp. 1–6, Jan. 2015.
[35] D. Pech, M. Brunet, H. Durou, P. Huang, V. Mochalin, Y. Gogotsi, P.-L. Taberna, and P. Simon, 'Ultrahigh-power micrometre-sized supercapacitors based on onion-like carbon', *Nat. Nanotechnol.*, 5, pp. 651–4, Sep. 2010.
[36] P. L. Taberna, P. Simon, and J. F. Fauvarque, 'Electrochemical Characteristics and Impedance Spectroscopy Studies of Carbon-Carbon Supercapacitors', *J. Electrochem. Soc.*, 150, no. 3, pp. A292–A300, Jan. 2003.
[37] D. Y. Kim, J. C. Yang, H. W. Kim, and G. M. Swain, 'Heterogeneous electron-transfer rate constants for ferrocene and ferrocene carboxylic acid at boron-doped diamond electrodes in a room temperature ionic liquid', *Electrochimica Acta*, 94, pp. 49–56, Apr. 2013.
[38] Y. François, K. Zhang, A. Varenne, and P. Gareil, 'New integrated measurement protocol using capillary electrophoresis instrumentation for the determination of viscosity, conductivity and absorbance of ionic liquid–molecular solvent mixtures', *Anal. Chim. Acta*, 562, no. 2, pp. 164–170, Mar. 2006.
[39] D. Gaboriau, M. Boniface, A. Valero, D. Aldakov, T. Brousse, P. Gentile, and S. Sadki, 'Atomic Layer Deposition Alumina-Passivated Silicon Nanowires: Probing the Transition from Electrochemical Double-Layer Capacitor to Electrolytic Capacitor', *ACS Appl. Mater. Interfaces*, 9, no. 15, pp. 13761–13769, Apr. 2017.
[40] C.-H. Chang, B. Hsia, J. P. Alper, S. Wang, L. E. Luna, C. Carraro, S.-Y. Lu, and R. Maboudian, 'High-Temperature All Solid-State Microsupercapacitors based on SiC Nanowire Electrode and YSZ Electrolyte', *ACS Appl. Mater. Interfaces*, 7, no. 48, pp. 26658–26665, Dec. 2015.
[41] A. Soam, N. Arya, A. Singh, and R. Dusane, 'Fabrication of silicon nanowires based on-chip micro-supercapacitor', *Chem. Phys. Lett.*, 678, pp. 46–50, Jun. 2017.
[42] M. Brachet, D. Gaboriau, P. Gentile, S. Fantini, G. Bidan, S. Sadki, T. Brousse, and J. L. Bideau, 'Solder-reflow resistant solid-state micro-supercapacitors based on ionogels', *J. Mater. Chem. A*, 4, no. 30, pp. 11835–11843, Jul. 2016.
[43] F. Thissandier, P. Gentile, N. Pauc, T. Brousse, G. Bidan, and S. Sadki, 'Tuning silicon nanowires doping level and morphology for highly efficient micro-supercapacitors', *Nano Energy*, 5, pp. 20–27, Apr. 2014.
[44] F. Thissandier, N. Pauc, T. Brousse, P. Gentile, and S. Sadki, 'Micro-ultracapacitors with highly doped silicon nanowires electrodes', *Nanoscale Res. Lett.*, 8, no. 1, p. 38, Jan. 2013.

[45] N. A. Kyeremateng, T. Brousse, and D. Pech, 'Microsupercapacitors as miniaturized energy-storage components for on-chip electronics', *Nat. Nanotechnol.*, 12, no. 1, pp. 7–15, Jan. 2017.
[46] D. Aradilla, G. Bidan, P. Gentile, P. Weathers, F. Thissandier, V. Ruiz, P. Gómez-Romero, T. J. S. Schubert, H. Sahin, and S. Sadki, 'Novel hybrid micro-supercapacitor based on conducting polymer coated silicon nanowires for electrochemical energy storage', *RSC Adv.*, 4, no. 50, pp. 26462–26467, Jun. 2014.
[47] D. Aradilla, D. Gaboriau, G. Bidan, P. Gentile, M. Boniface, D. Dubal, P. Gómez-Romero, J. Wimberg, T. J. S. Schubert, and S. Sadki, 'An innovative 3-D nanoforest heterostructure made of polypyrrole coated silicon nanotrees for new high performance hybrid micro-supercapacitors', *J. Mater. Chem. A*, 3, no. 26, pp. 13978–13985, Jun. 2015.
[48] D. P. Dubal, D. Aradilla, G. Bidan, P. Gentile, T. J. S. Schubert, J. Wimberg, S. Sadki, and P. Gomez-Romero, '3D hierarchical assembly of ultrathin MnO_2 nanoflakes on silicon nanowires for high performance micro-supercapacitors in Li- doped ionic liquid', *Sci. Rep.*, 5, p. 9771, May 2015.
[49] D. Weingarth, A. Foelske-Schmitz, and R. Kötz, 'Cycle versus voltage hold – Which is the better stability test for electrochemical double layer capacitors?', *J. Power Sources*, 225, pp. 84–88, Mar. 2013.
[50] R. Kötz and M. Carlen, 'Principles and applications of electrochemical capacitors', *Electrochimica Acta*, 45, no. 15, pp. 2483–2498, May 2000.
[51] V. M. Mecea, 'Is quartz crystal microbalance really a mass sensor?', *Sens. Actuators Phys.*, 128, no. 2, pp. 270–277, Apr. 2006.
[52] Burke Huner, 'Cylinder Drag at Low Reynolds Number', 1977.
[53] J. Liu, Y. Lin, L. Liang, J. A. Voigt, D. L. Huber, Z. R. Tian, E. Coker, B. Mckenzie, and M. J. Mcdermott, 'Templateless Assembly of Molecularly Aligned Conductive Polymer Nanowires: A New Approach for Oriented Nanostructures', *Chem. – Eur. J.*, 9, no. 3, pp. 604–611, Feb. 2003.
[54] C. Debiemme-Chouvy, 'Template-free one-step electrochemical formation of polypyrrole nanowire array', *Electrochem. Commun.*, 11, no. 2, pp. 298–301, Feb. 2009.
[55] L. Al-Mashat, C. Debiemme-Chouvy, S. Borensztajn, and W. Wlodarski, 'Electropolymerized Polypyrrole Nanowires for Hydrogen Gas Sensing', *J. Phys. Chem. C*, 116, no. 24, pp. 13388–13394, Jun. 2012.
[56] A. Fakhry, H. Cachet, and C. Debiemme-Chouvy, 'Mechanism of formation of templateless electrogenerated polypyrrole nanostructures', *Electrochimica Acta*, 179, pp. 297–303, Oct. 2015.
[57] M. Li, Z. Wei, and L. Jiang, 'Polypyrrole nanofiber arrays synthesized by a biphasic electrochemical strategy', *J. Mater. Chem.*, 18, no. 19, pp. 2276–2280, Apr. 2008.
[58] L. To Thi Kim, C. Debiemme-Chouvy, C. Gabrielli, and H. Perrot, 'Redox Switching of Heteropolyanions Entrapped in Polypyrrole Films Investigated by ac Electrogravimetry', *Langmuir*, 28, no. 38, pp. 13746–13757, Sep. 2012.
[59] C. Gabrielli, M. Keddam, N. Nadi, and H. Perrot, 'Ions and solvent transport across conducting polymers investigated by ac electrogravimetry. Application to polyaniline', *J. Electroanal. Chem.*, 485, no. 2, pp. 101–113, May 2000.
[60] Y. Wang, 'Research progress on a novel conductive polymer–poly(3,4-ethylenedioxythiophene) (PEDOT)', *J. Phys. Conf. Ser.*, 152, no. 1, p. 012023, 2009.
[61] J. C. Carlberg and O. Inganäs, 'Poly(3,4-ethylenedioxythiophene) as Electrode Material in Electrochemical Capacitors', *J. Electrochem. Soc.*, 144, no. 4, pp. L61–L64, Jan. 1997.

[62] D. K. Bhat and M. Selva Kumar, 'N and p doped poly(3,4-ethylenedioxythiophene) electrode materials for symmetric redox supercapacitors', *J. Mater. Sci.*, 42, no. 19, pp. 8158–8162, Oct. 2007.

Chapter 4:

Vertically-oriented graphene nanosheets grown on a microbalance electrode

Table of contents

I. Introduction

The stunning capabilities of supercapacitor devices in terms of power density and cycling stability has led many research groups to focus on nanostructured carbonaceous materials with enhanced capacitance and lifetime performances [1]. Among such materials, VOGNs have recently shown a great potential as electrodes for electrochemical double layer capacitors (EDLCs) due to their peculiar characteristics such as high conductivity, ion access facility and open structure with high surface area [2-4]. In spite of the numerous conventional morphological, structural and physical-chemical techniques employed for their characterization, a better understanding of the electrochemical processes involved in VOGN electrodes has not yet been provided with in-situ characterization techniques. A graphical view of the exchange mechanisms is shown **Fig I-1** with Donnan permselectivity of the electrode upon ion adsorption, meaning that only ions of opposite charge are adsorbed. However the real mechanisms at the electrode interface might differ completely from this view.

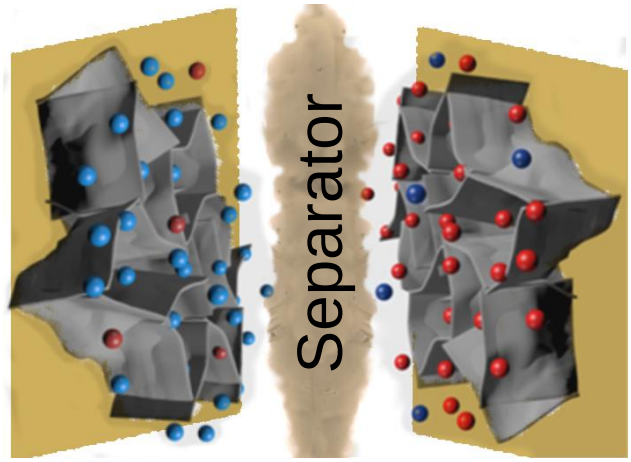

Figure I-1: Schematic view of a VOGN-based supercapacitor and the ionic exchange process which is the main focus of this chapter. Cations are depicted in red and anions in blue.

This chapter presents the results obtained with EQCM and *ac*-electrogravimetry techniques on VOGN electrodes. Using propylene carbonate (PC)-based organic electrolytes, the adaptability of these electrogravimetric methods on the graphene nanostructures is investigated. After validation of this step, an analysis comparing the influence of various salts is proposed. The first results were obtained with PC+0.5M $TBABF_4$, and were published in Electrochemistry communications [5]. We then switched to PC+0.5M $TBAClO_4$ to investigate the changes in ionic

exchanges induced by a slight anion mass and size increase. Further experiments were performed with PC+0.5M $LiClO_4$ to examine the effects of an important cation mass decrease. The behaviour of ions from an ionic liquid was then probed in a mixture of PC and N_{1114}TFSI. This mixture was shown in chapter 3-II to offer a higher conductivity than pure N_{1114}TFSI and an electrochemical window of up to 3.5 V in contact with SiNWs. The addition of PC also counter-balances the fact that pure N_{1114}TFSI ionic liquids were found too viscous to be used with the vertically-oriented nanostructures in this study due to hydrodynamic damping. The investigation of the electrolyte composition effect is followed by the N-doping of the VOGN electrodes to study the induced changes on the ionic exchange processes.

II. Synthesis of VOGNs on a microbalance electrode

The growth of VOGNs is achieved by electron cyclotron resonance-plasma enhanced chemical vapor deposition (ECR-CVD). This patented growth technique was developed at CEA Grenoble in order to enable a catalyst-free growth of VOGNs on various types of substrates (quartz, metals, ceramic…) [6, 7]. The growth temperature, normally around 800°C, was lowered to a value of around 480°C to avoid the degradation of the piezoelectric substrate. However such temperatures would still cause a systematic degradation of the piezoelectric properties in common quartz crystals, impeding their use for EQCM [8]. Thus a gold-patterned piezoelectric $GaPO_4$ crystal was used instead of quartz as the substrate for the VOGN synthesis. Gold patterns with a thickness of 200 nm were deposited by sputtering on the masked $GaPO_4$ crystal. A Ti sublayer of 10 nm prevents the electrode from peeling off.

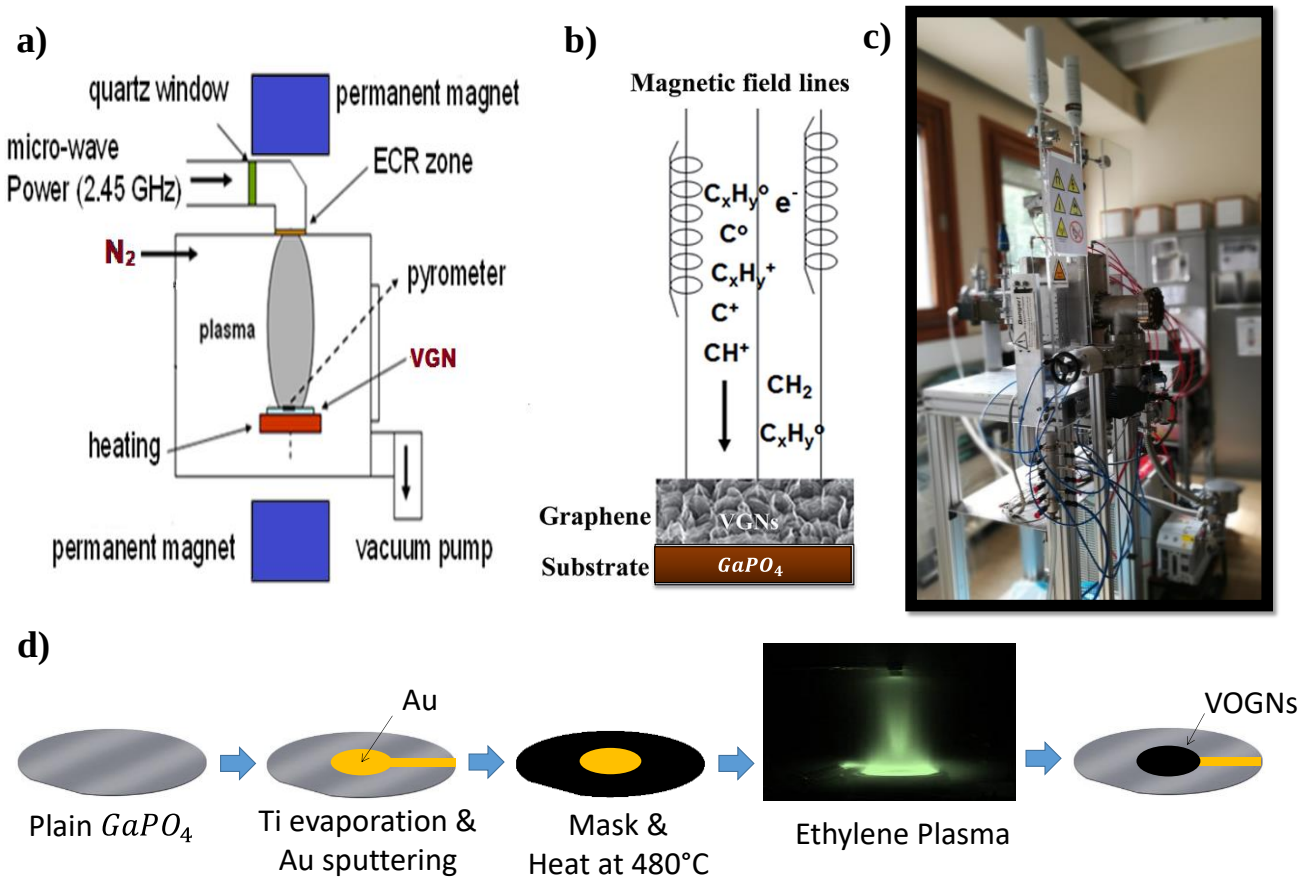

Figure II-1: Experimental setup of ECR-CVD: **a)** Schematic of the components. **b)** Schematic of the growth mechanism. **c)** Picture of the setup. **d)** Sample preparation process.

The substrate is placed in a chamber with $3 \cdot 10^{-4}$ mbar of ethylene perpendicular to static magnetic field lines (**Fig. II-1**). A microwave source of 300 W is directed towards the chamber to trigger the formation of plasma at the surface of the electrode. The dissociation and ionization of ethylene occurs and the produced ions and electrons are guided by the static magnetic field to collide with the electrode. The repeated collisions of carbon radicals at the electrode surface induce the growth of the graphene nanosheets perpendicular to the substrate. A mask was used to allow the growth only in the central part of the $GaPO_4$ resonator. The exposure time for the growth drives the final thickness of VOGNs on the substrate, and a series of growth tests with various exposure times were performed to obtain adequate samples for EQCM measurements. The growth time was set to 80 minutes, resulting in around 7 µg of VOGNs (derived from microbalance frequency variation between the neat and VOGN modified $GaPO_4$) over a surface of 0.2 cm^2 with ~1 µm thickness. This corresponds to a microbalance mass loading of 35 $\mu g.cm^{-2}$, a lot less than for SiNWs presented in chapter 3-II (220 $\mu g.cm^{-2}$). This thickness was found ideal for EQCM measurements as it was thin enough to obtain a suitable gravimetric behavior and thick enough to obtain significant mass changes upon cycling. Before opening the chamber to retrieve the sample, an additional step can be performed to obtain nitrogen-doping (N-doping) of the VOGNs. This step adds nitrogen sites within the graphene matrix by exposing the sample to a plasma of N_2 for 3 minutes at a power of 280 W. These experimental conditions reported a doping level of approximately 17% a.t (determined by XPS), which was found as one of the highest values described in the literature.

III. Microbalance results and discussion

III-1. Scanning electron microscopy of the resonators and electroacoustic measurements

Following each growth of VOGNs, the resulting morphology was investigated with scanning electron microscopy (SEM). **Fig. III-1a** depicts the SEM image of VOGNs directly grown in the central part of a $GaPO_4$ resonator, shown fully in the inset. A good coverage of the gold electrode with graphene nanosheets perpendicular to the substrate was observed. The gap between these nanosheets will ensure a good accessibility of the electrode surface to the electrolyte over the whole thickness. **Fig. III-1b** shows a SEM image of a cross-sectional view of the VOGN sample, showing that the thickness is around 1 µm. To determine whether this morphology was deteriorated upon electrolyte addition and cycling, new SEM images were taken after around 100 cycles. No changes in morphology were observed on any sample, as observed in **Fig. III-1c** for the case of VOGNs after 100 cycles in PC+0.5M $LiClO_4$.

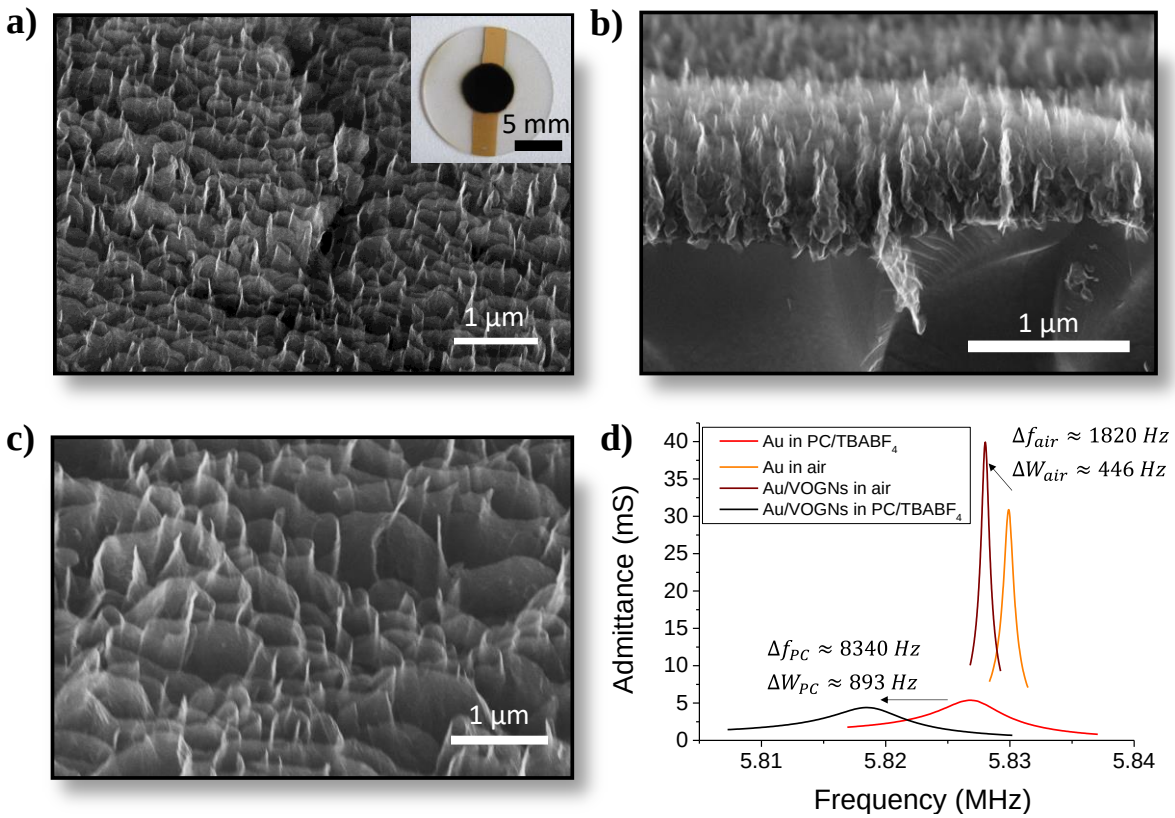

Figure III -1: a) SEM image of VOGNs grown on a gold-patterned $GaPO_4$ electrode (full electrode pictured in inset). **b)** Cross-sectional view of VOGNs on $GaPO_4$. **c)** VOGNs after 100 cycles in PC+0.5M $LiClO_4$. **d)** Electrical admittance of the $GaPO_4$ electrode at resonance frequency before growth in air (orange) and in PC (red), and after VOGN growth in air (brown) and in PC (black).

The excellent cycling stability of VOGNs was reported in our previous studies dealing with VOGN electrodes in the presence of ionic liquid electrolytes, preserving entirely the morphological structure even after 200 000 cycles [9]. Previous works by our team also reported the results of other microscopy techniques like TEM as well as Raman spectroscopy, electrical conductivity and specific surface area measurements by gas adsorption with Brunauer-Emmett-Teller (BET) analysis which characterized VOGN morphology and composition with greater accuracy [9, 10].

The resonator's behavior was investigated in a PC-based electrolyte before and after VOGN growth with electroacoustic measurements. **Fig. III-1d** displays the electrical admittance $|Y| = \left|\frac{1}{Z}\right|$ of the resonator near the resonance frequency in four configurations: Before growth with and without PC electrolyte, and after VOGN growth with and without PC electrolyte. For each resonance peak measured, the resonance frequency f and the full width at half height W are extracted and the quality factor $Q = \frac{f}{W}$ is derived. The electroacoustic results are summarized in **Table III-1**.

Configuration	Fluid visc. $(mPa.s)$	Fluid density $(kg.m^{-3})$	Resonance frequency (MHz)	Peak width (Hz)	R (Ω)	L (H)	Quality factor
Au in air	0.0184	1.17	5.830	700	33	0.00668	8300
Au in PC	2.5	1200	5.827	5046	188	0.00592	1155
VOGNs in air	0.0184	1.17	5.828	756	24	0.00652	7700
VOGNs in PC	2.5	1200	5.819	5726	229	0.00636	1016

Table III-1: Values obtained for the resonance frequency, peak width at half height, resistance, inductance and quality factor for a $GaPO_4$ resonator with Au electrodes in air and PC before and after VOGN growth.

As suggested in chapter 2-III-2, the contribution of viscous dynamic damping due to the electrode's nanostructures is considered small compared to the gravimetric contribution if the shift in resonance frequency Δf is larger than the shift in peak width ΔW and if the quality factor is not considerably reduced. This is obviously the case in air, where the VOGN growth triggers a resonance frequency shift $\Delta f_{air} \approx 1820\ Hz$, a peak width shift $\Delta W_{air} \approx 50\ Hz$, and a quality factor shifting from $Q_{Au-air} \approx 8300$ to $Q_{VOGN-air} \approx 7700$. When a PC-based electrolyte is added, we observe that after VOGN growth the shift in resonance frequency $\Delta f_{PC} \approx 8340\ Hz$ is much greater than the peak width shift $\Delta W_{PC} \approx 700\ Hz$. The quality factor also changes from

$Q_{Au-PC} \approx 1155$ to $Q_{VOGN-PC} \approx 1016$. The quality factor obtained here is much higher than the previous results with SiNWs in the same solvent ($Q_{SiNWs-PC} \approx 120$), which is attributed to the reduced height of VOGNs compared to SiNWs. We deduce from these observations that gravimetric properties of the resonator with VOGNs in PC are suitable for using the Sauerbrey equation (**Eq. III-1** in chapter 2-III) to understand the following measurements.

III-2. EQCM on VOGNs

Electrochemical quartz crystal microbalance measurements have never been reported before on VOGN electrodes. The most similar study has been reported by H. Goubaa *et al.* in our group on electrochemically reduced graphene oxides (ERGO) thin films studied in aqueous electrolytes [11]. These materials share the attribute of being graphene-based with VOGNs but present a completely different morphology, where the graphene oxide sheets are parallel to the substrate and are subjected to electrochemical reduction before the measurements. The morphological difference of the VOGNs to ERGO thin films originated from the parallel to vertical orientation of the nanosheets is considered to be an asset for the accessible electrode surface area and interactions with the electrolyte. Therefore, the following results will compare the behavior in various electrolytes. PC is used as electrolyte solvent due to it's large stable electrochemical window compared to aqueous electrolytes. Specifically, the VOGN electrode's behavior was investigated in PC with three different salts ($TBABF_4$, $TBAClO_4$ and $LiClO_4$) as well as the mixture of PC and N_{1114}TFSI optimized in chapter 3-II-2. The ions and PC molecules contained in each of these electrolytes are described in **Table III-2**. Classical EQCM measurements were performed for each electrolyte, resulting in the CV with mass variations depicted in **Fig. III-2**.

Ion or Molecule	Molar mass ($g.mol^{-1}$)	Estimated size (pm)	Structure	Graphical view
PC	102	550	$H_3C_2H_3O_2CO$	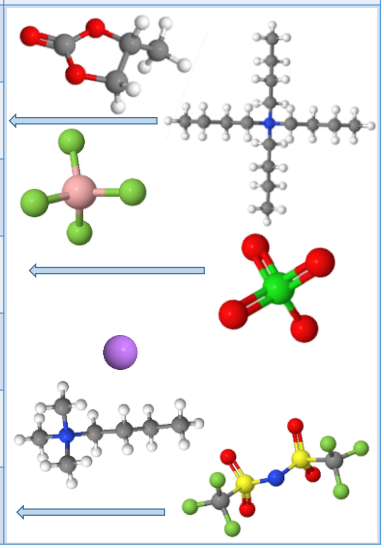
TBA^+	242	880	$[N(C_4H_9)_4]^+$	
BF_4^-	86.8	230	BF_4^-	
ClO_4^-	99.4	240	ClO_4^-	
Li^+	6.94	76	Li^+	
N_{1114}^+	106	530	$C_7H_{18}N^+$	
$TFSI^-$	280	450	$C_2F_6NO_4S_2^-$	

Table III-2: Properties of each ion or molecule in the studied electrolytes. [12]-[13]

Two comparable salts, $TBABF_4$ and $TBAClO_4$, were used to investigate the changes in charge storage mechanisms with a very small change of anion size and mass. Then $LiClO_4$ was used to determine the effects of a much smaller cation on the exchange mechanisms. Ultimately a mixture of PC and $N_{1114}TFSI$ (50% w.t.) was used to study the evolution of these mechanisms in the presence of an ionic liquid which reported excellent electrochemical performances for SiNW-based micro-supercapacitors [14].

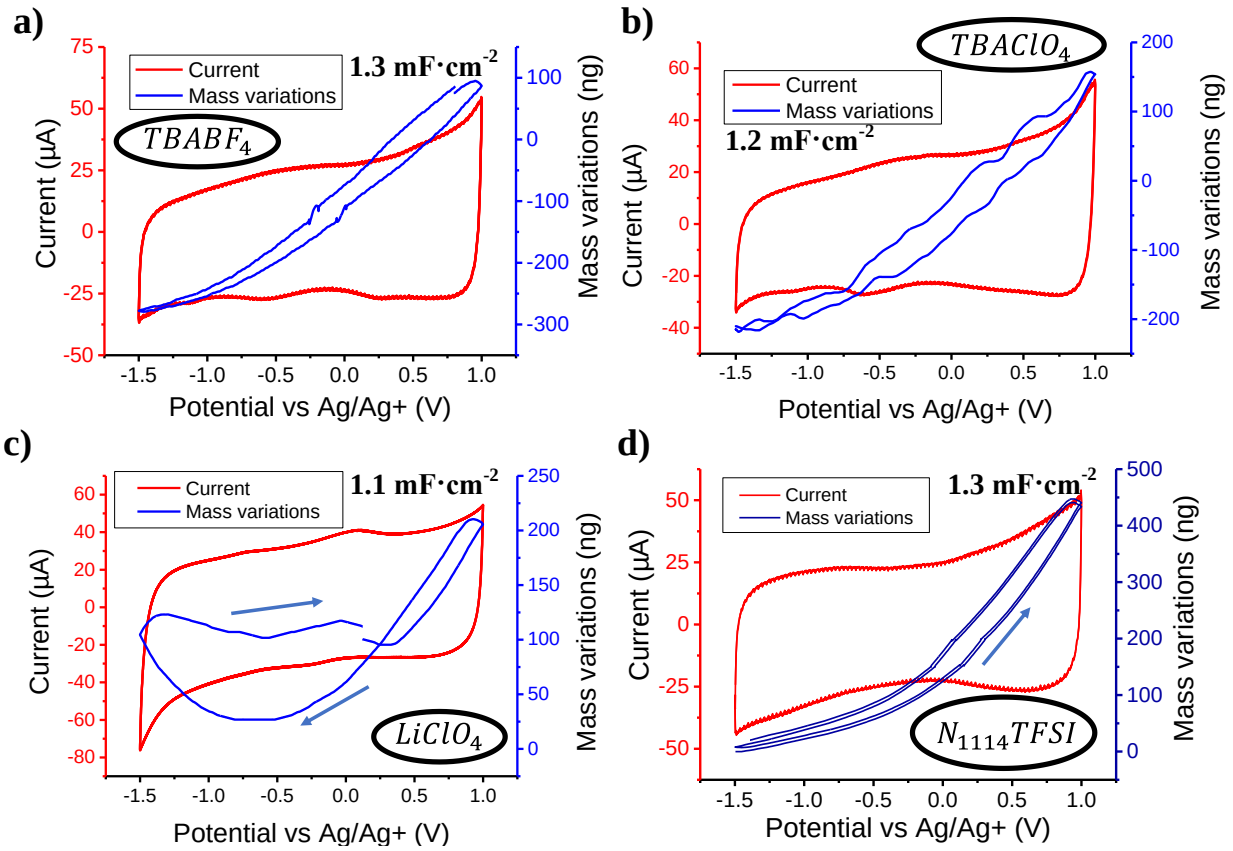

Figure III-2: Cyclic voltammetry (red) coupled with the mass measurement (blue) at 100 $mV{\cdot}s^{-1}$ on a VOGN electrode in various electrolytes: **a)** PC+0.5M $TBABF_4$, **b)** PC+0.5M $TBAClO_4$, **c)** PC+0.5M $LiClO_4$, **d)** PC+$N_{1114}TFSI$.

For each electrolyte, the overall charge stored in the electrode at each cycle was calculated with an integration of the current: $Q = \int i(t).dt$. The corresponding areal capacitance $AC = \frac{Q}{\Delta V \cdot A}$ was then calculated with ΔV the potential range (2.5 V) and A the electrode surface (0.2 cm^2). All capacitance values obtained were close, with 1.3 $mF{\cdot}cm^{-2}$ for PC+0.5M $TBABF_4$, 1.2 $mF{\cdot}cm^{-2}$ for PC+0.5M $TBAClO_4$, 1.1 $mF{\cdot}cm^{-2}$ for PC+0.5M $LiClO_4$ and 1.3 $mF{\cdot}cm^{-2}$ for

PC+N_{1114}TFSI (values shown in **Fig. III-2**). With a mass loading of 35 µg.cm^{-2}, the average specific capacitance for these four configurations is 35 F.g^{-1}.

The EQCM measurements with $TBABF_4$ (**Fig. III-2a**) resulted in very stable current and mass variations. A reversible mass increase of 365 ng is observed from -1.5 V to 1 V vs Ag/Ag^+, associated to anions being predominantly exchanged with the electrode. A slight decrease in the mass variation slope below -1 V vs Ag/Ag^+ suggests that cations are likely to play a role in this potential region. EQCM results with $TBAClO_4$ (**Fig. III-2b**) show the same behavior with a reversible mass increase of 350 ng from -1.5 V to 1 V vs Ag/Ag^+, suggesting that ClO_4^- anions (slightly bigger and heavier than BF_4^- anions) are predominant to the energy storage mechanisms in the entire potential window.

A more quantitative analysis is obtained by calculating the exchanged mass per mole of electrons MPE$= \frac{F\Delta m}{\Delta Q}$, where F is the Faraday number, Δm is the mass variation of the electrode and ΔQ is the charge variations. With $TBABF_4$, we obtain an MPE of 65 g.mol^{-1} (**Table III-3**). Positive values of the MPE correspond to species being attracted to the VOGN surface when the potential is increased: Anions with/without free solvent molecules exchanged in the same direction [15]. The BF_4^- anion molar mass is 86.8 g.mol^{-1}, therefore mainly anions are exchanged. With $TBAClO_4$ the MPE is around 70 g.mol^{-1} above -1 V and around 30 g·mol^{-1} below -1 V vs Ag/Ag^+ compared with the ClO_4^- anion mass of 99.4 g.mol^{-1} (**Table III-3**). Therefore the ionic exchange mechanisms appear to be very close between these two electrolytes: Anions are predominant in the entire potential window, while only low concentrations of cations are exchanged at lower potentials. This is attributed to the fact that TBA^+ cations occupy a much bigger space than both types of anions used here, with an estimated size of 880 pm without solvation shell and probably beyond 1 nm with the solvation with PC molecules. It seems that these dimensions are a limiting factor for entering between the graphene nanosheets. A more detailed comprehension of these mechanisms will be attained using *ac*-electrogravimetry measurements in section III-3.

A smaller cation, Li^+, was then used to investigate the effect of cation size on these interactions. Known for their use in Li-ion batteries, these cations have previously been used in combination with graphene nanosheet anodes [16]. In such cases, Li^+ cations are inserted within

the graphene layers, whereas for this study of VOGNs as EDLCs Li^+ cations will only be adsorbed on the surface of the nanosheets. **Fig. III-2c** depicts the EQCM results with PC+0.5M $LiClO_4$ as electrolyte. A reversible mass increase of around 150 ng was observed from -0.6 V to 1 V vs Ag/Ag^+, showing that anions still have a strong contribution in this potential region. However a reversible mass decrease of 80 ng is also observed from -1.5 V to -0.6 V vs Ag/Ag^+, indicating that the newly introduced Li^+ cations play a larger role in the energy storage mechanism than that of TBA^+ cations. The MPE calculations resulted in around 34 $g.mol^{-1}$ above -0.5 V and -31 $g.mol^{-1}$ below -0.75V (**Table III-3**). These values are respectively smaller than ClO_4 molar mass (99.4 $g{\cdot}mol^{-1}$) and higher than Li^+ molar mass (6.9 $g{\cdot}mol^{-1}$), indicating that anions and cations are not being exchanged exclusively on either side of the potential window. The solvation of Li^+ cations within the PC-based electrolyte is the main reason for such non-trivial exchange processes. Li^+-$(PC)_n$ solvation structures are observed in bulk PC with $1 \leq n \leq 4$ varying with salt concentration [17]. Upon Li^+ adsorption at the VOGN surface, partial desolvation of the cations may occur, but the remaining PC molecules may add weight on the VOGN structure and lead to a more complex interpretation of EQCM measurements [15]. The *ac*-electrogravimetry results will be analyzed in the next section to achieve a better understanding of the role of PC molecules in these exchange mechanisms.

An ionic liquid-based electrolyte, N_{1114}TFSI, was then used to characterize the exchange mechanisms with a similar VOGN electrode. After unsuccessful EQCM results with this particular ionic liquid due to it's significantly high viscosity (86 mPa.s at 303 K [18]) causing hydrodynamic damping of the resonance, the measurements were performed in a mixture of the studied ionic liquid with PC. This ionic liquid was selected for the mixture in this study due to the good results in terms of capacitance and stability obtained in VOGN and SiNW-based supercapacitor applications [10, 19].

Fig. III-2d presents the EQCM results with 50% PC+50% N_{1114}TFSI (w.t.) as electrolyte at 100 $mV{\cdot}s^{-1}$. This ionic liquid ratio was chosen according to its optimal properties in terms of conductivity and the capacitive properties obtained in chapter 3-II-2 [14]. A reversible mass increase of 430 ng is obtained over the whole potential window from -1.5 V to 1 V vs Ag/Ag^+, suggesting that anions contribute to the majority of the ionic exchanges. The slope of this mass increase varies from negative to positive potentials, leading to MPE values around 25 $g.mol^{-1}$

below -0.3 V and 90 g.mol^{-1} above 0 V vs Ag/Ag$^+$ (**Table III-3**). TFSI$^-$ anions have a molar mass of 280.09 g.mol^{-1}, which is much higher than the MPE. This tendency indicates that anions are not the only species exchanged with the electrode during cycling. N_{1114}^+ cations (106 g·mol^{-1}) are much lighter and smaller than TBA$^+$ cations and may have less difficulty to access to various adsorption sites on the graphene nanosheets. Once again *ac*-electrogravimetry will play a key role to determine the mutual role of cations, anions and free solvent molecules to the exchange mechanisms. **Table III-3** summarizes the results of the MPE calculations for all four electrolytes.

Electrolyte	$TBABF_4$	$TBAClO_4$	$LiClO_4$	$PC+N_{1114}TFSI$
MPE (g. mol^{-1})	65	70 above -1 V 30 below -1 V	34 above -0.75 V -31 below -0.75 V	90 above 0 V 25 below -0.3 V
Anion mass (g. mol^{-1})	86.8	99.4	99.4	280
Cation mass (g. mol^{-1})	242	242	6.9	106

Table III-3: Mass per mole of electrons (MPE) obtained with $TBABF_4$, $TBAClO_4$, $LiClO_4$ and $PC+N_{1114}TFSI$ and the corresponding anion and cation molar masses.

III-3. *Ac*-electrogravimetry on VOGNs

III.3.i. Initial data and fitting

Ac-electrogravimetry measurements were performed on the same VOGN electrodes with the same electrolytes to better understand the contribution and dynamics of each species in these exchanges. These measurements were performed at every 0.2 V from -1.5 V to 1 V vs Ag/Ag$^+$. Following each measurement, the theoretical models described in Chapter 2-III were adapted to the particular experimental cases in order to fit the impedance, charge/potential, mass/potential as well as partial mass/potential TFs with the same set of parameters. For each experimental data, three species were initially considered in the exchanges with the electrolyte: cations, anions and free solvent molecules. The species which does not participate in these exchanges was then removed from the model. The results are depicted at 1V and -1 V vs Ag/Ag$^+$ in the form of Nyquist plots of the experimental charge/potential TF $\frac{\Delta q}{\Delta E}(\omega)$ (**Fig. III-3a, c, e and g**) and mass/potential TF $\frac{\Delta m}{\Delta E}(\omega)$ (**Fig. III-3b, d, f and h**) together with the theoretical curves fitting the experimental data with **Eq. III-17&18** in Chapter 2-III-5.

For all electrolytes except PC+0.5M $LiClO_4$ and at all potentials a suppressed loop is observed in the first quadrant of the mass/potential TF $\frac{\Delta m}{\Delta E}(\omega)$, indicating a major anion contribution. This result is in good agreement with the EQCM measurements performed in the previous section. However, for each of those cases a model using only anion exchanges would result in a larger loop for $\frac{\Delta m}{\Delta E}(\omega)$ and would not fit the experimental data. With PC+0.5M $LiClO_4$ the same reasoning applies over -0.6 V vs Ag/Ag^+, but below this potential the loop shifts to the 3rd quadrant, indicating a major cation contribution. The width of these suppressed loops are proportional to the mass change involved in the exchange, explaining the fact that Li^+ exchanges observed at -1 V vs Ag/Ag^+ induce a much smaller loop than ClO_4^- exchanges at 1 V (**Fig.III-3f**). In PC+0.5M $TBABF_4$, BF_4^- anions were used in the model to fit the *ac*-electrogravimetry results at all potentials while TBA^+ cations were used only below -0.5 V vs Ag/Ag^+ and free PC molecules above -1 V vs Ag/Ag^+ (**Fig. III-3a-b** shows only the results obtained at 1 V and -1 V as examples). In the case of PC+0.5M $TBAClO_4$ however, the results were fitted with TBA^+ cations, ClO_4^- anions and free PC solvent molecules for all potentials except 0 V vs Ag/Ag^+, where cations were not included in the model (**Fig. III-3c-d**). During the search for a proper theoretical model to interpret the results obtained in PC+0.5M $LiClO_4$, multiple solvation numbers for Li^+ cations have been tested. Monosolvated Li^+ cations ($PC\text{-}Li^+$) and ClO_4^- anions were the only two species that resulted in a good agreement of the experimental and theoretical curves (**Fig. 3-3e-f**). Therefore, Li^+ cations are found to keep a solvation number of n=1 upon adsorption at the VOGN surface.

Below 0 V vs Ag/Ag^+ the results obtained with 50% PC+50%$N_{1114}TFSI$ were fitted with the participation of N_{1114}^+ cations and $TFSI^-$ anions only, with an addition of PC molecules to the model above 0 V (**Fig. III-3g-h** shows only the results obtained at 1 V and -1 V as examples).

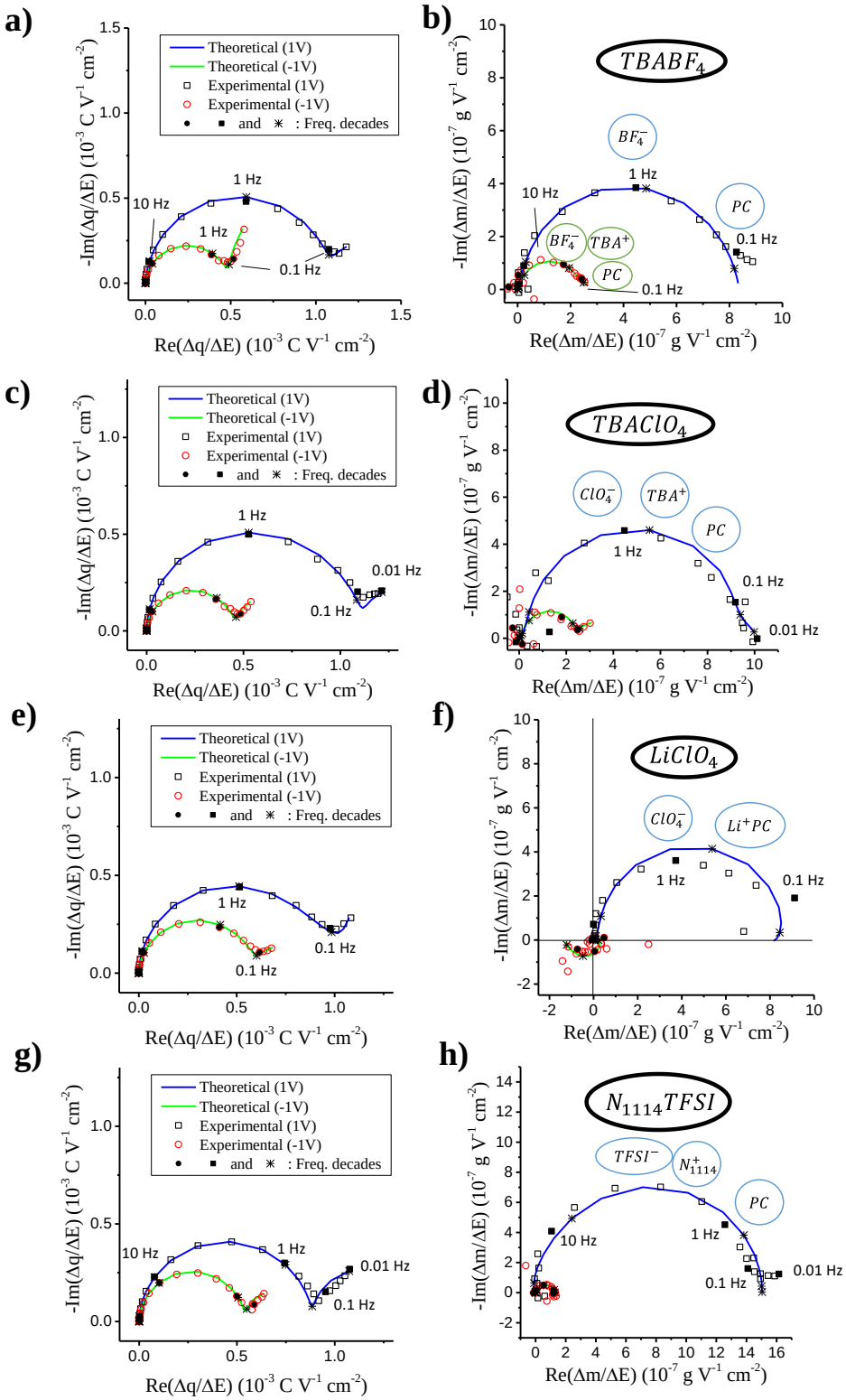

Figure III-3: Experimental results of *ac*-electrogravimetry on VOGN electrodes at 1V and -1V (squares) and their corresponding fits (lines) in Nyquist plots of the charge/potential TFs $\Delta q/\Delta E(\omega)$ (left), and the mass/potential TFs $\Delta m/\Delta E(\omega)$ (right) in **a-b)** PC+0.5M $TBABF_4$, **c-d)** PC+0.5M $TBAClO_4$, **e-f)** PC+0.5M $LiClO_4$, **g-h)** PC+$N_{1114}TFSI$.

III.3.ii.Partial mass/potential TFs - separating each species contribution

In the majority of these experiments, anions and cations are exchanged simultaneously and their contributions are observed at around the same frequencies, leading to only one loop with a reduced width due to the combination of both exchange mechanisms. However, the theoretical expressions in the *ac*-electrogravimetry model can be used to separate these contributions mathematically and clearly show the contribution of each species in partial TF graphs. **Fig. III-4a, c, e and g** depict the Nyquist plots of the cation-solvent partial mass/potential TFs at 1 V and -1 V vs Ag/Ag^+ for all electrolytes, calculated with the removal of the anion contribution from $\frac{\Delta m}{\Delta E}(\omega)$ using **Eq. III-20&22** from chapter 2-III-5.

Almost all the resulting plots only show a suppressed loop in the 3rd quadrant, characteristic for cation contribution. An exception is observed with PC+0.5M $TBABF_4$ at positive potentials, where this loop continues towards the upper quadrants as a result of free solvent molecules being exchanged with the same flux direction as the anions (**Fig. III-4a**), dominating over the contribution of the cations. Similarly, **Fig. III-4b, d, f and h** display the Nyquist plots for the anion-solvent partial mass/potential TFs calculated using **Eq. III-19&21** from chapter 2-III-5. Suppressed loops in the 1st quadrant are always observed, characteristic of the contribution of anions and solvent molecules exchanged in the same direction and magnified due to the removal of the contribution of the cations.

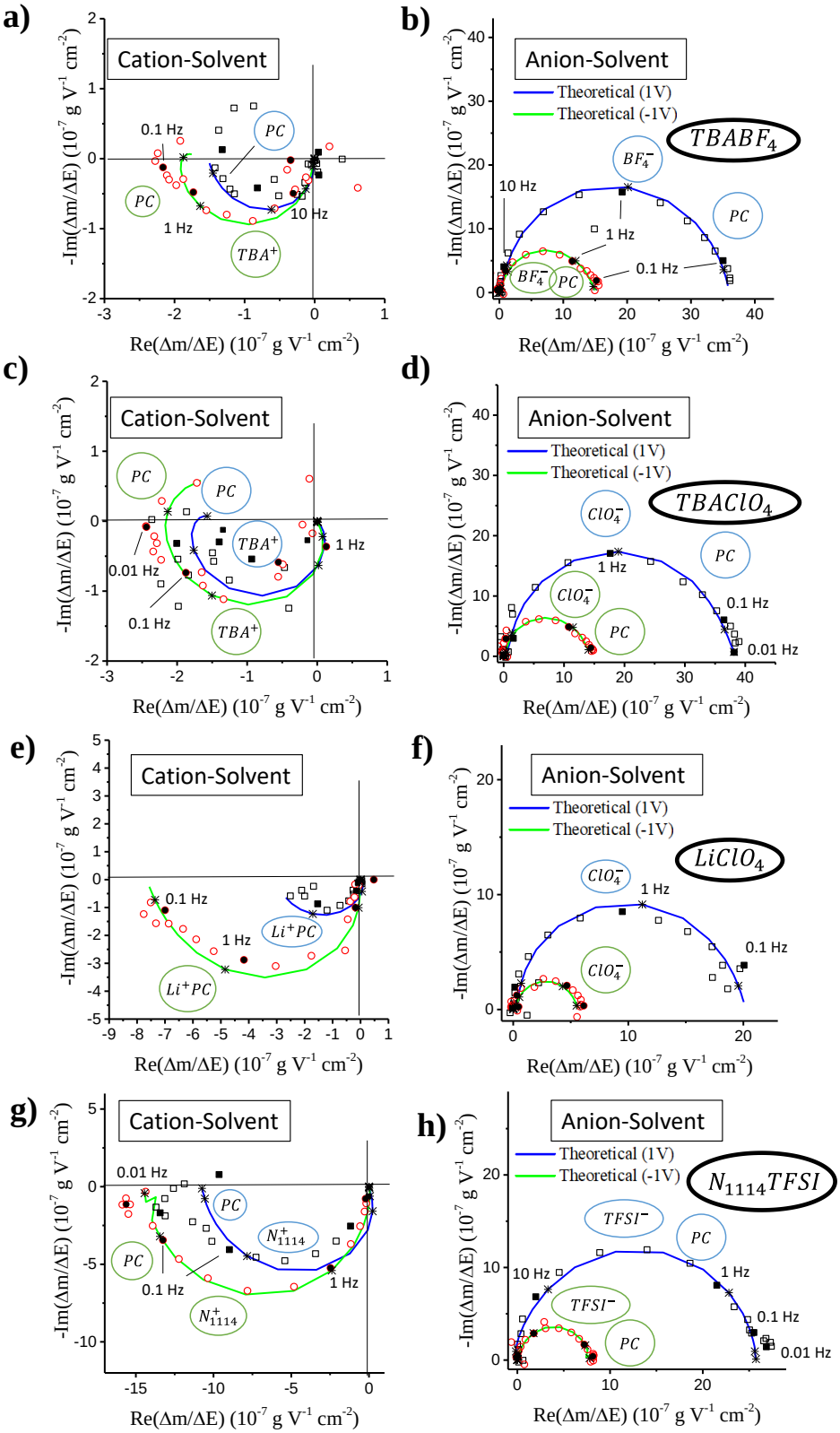

Figure III-4: Nyquist plots of the cation-solvent (left) and anion-solvent partial mass/potential TFs (right) in **a) b)** PC+0.5M $TBABF_4$, **c) d)** PC+0.5M $TBAClO_4$, **e) f)** PC+0.5M $LiClO_4$, **g) h)** PC+$N_{1114}TFSI$.

III.3.iii. Analysis of the kinetic parameters and the transfer resistance

For each studied electrolyte and at each measured potential, the fitted *ac*-electrogravimetry data allowed the derivation of the kinetic and conductance parameters K_i and G_i of each species in the model. **Fig. III-5a, c, e and g** depict the evolution of the kinetic parameters K_i obtained for each electrolyte. With $TBABF_4$, anions and cations have equivalent values of kinetic parameters around 10^{-3} cm.s^{-1}, showing that BF_4^- anions are exchanged as fast as the heavier TBA^+ (M_{TBA+} = 242.46 g.mol^{-1}) (**Fig. III-5a**). The same observation is made for $TBAClO_4$ below 0 V vs Ag/Ag^+ (**Fig. III-5c**). This is not the case for $LiClO_4$, where ClO_4^- anions exchanged faster than monosolvated Li^+ cations (**Fig. III-5e**). Above 0 V with $TBAClO_4$ anions are also exchanged faster with $K_a = 10^{-3}$ cm.s^{-1} and $K_c = 10^{-4}$ cm.s^{-1}. In the case of the diluted N_{1114}TFSI ionic liquid, both cations and anions have their kinetic parameters around $3{\cdot}10^{-3}$ cm.s^{-1}, showing that massive anions such as $TFSI^-$ (M_{TFSI-} = 280 g.mol^{-1}) can be exchanged as rapidly as the lighter BF_4^- anions (**Fig. III-5g**). For all electrolytes with free solvent molecules exchanges in the model, these take place at very slow rates of transfer ($K_s = 2{\times}10^{-6}$ to $5{\times}10^{-6}$ cm·s^{-1}). From these results, it appears that the ion size has no major effect on the exchange kinetics.

The transfer resistance $Rt_i = \frac{1}{FG_i}$ is depicted for each electrolyte in **Fig. III-5b, d, f and h** at all the studied potentials. Free solvent molecules always have the highest transfer resistance (Rt_s = 13 to 120 kΩ.cm^2), followed by cations (Rt_{TBA}^+ = 0.4 to 15 kΩ.cm^2, Rt_{Li^+PC} = 0.2 to 0.5 kΩ.cm^2, Rt_{N1114}^+ = 40 to 250 Ω.cm^2) and anions (Rt_{BF4}^-= 100 to 150 Ω.cm^2, Rt_{ClO4}^- = 10 to 100 Ω.cm^2, Rt_{TFSI}^- = 10 to 60 Ω.cm^2).

The combination of K_i and Rt_i collected for each species at various potentials reveals the dynamics of the charge transfer mechanism, showing that in many cases anions have a major contribution to the energy stored in VOGN electrodes.

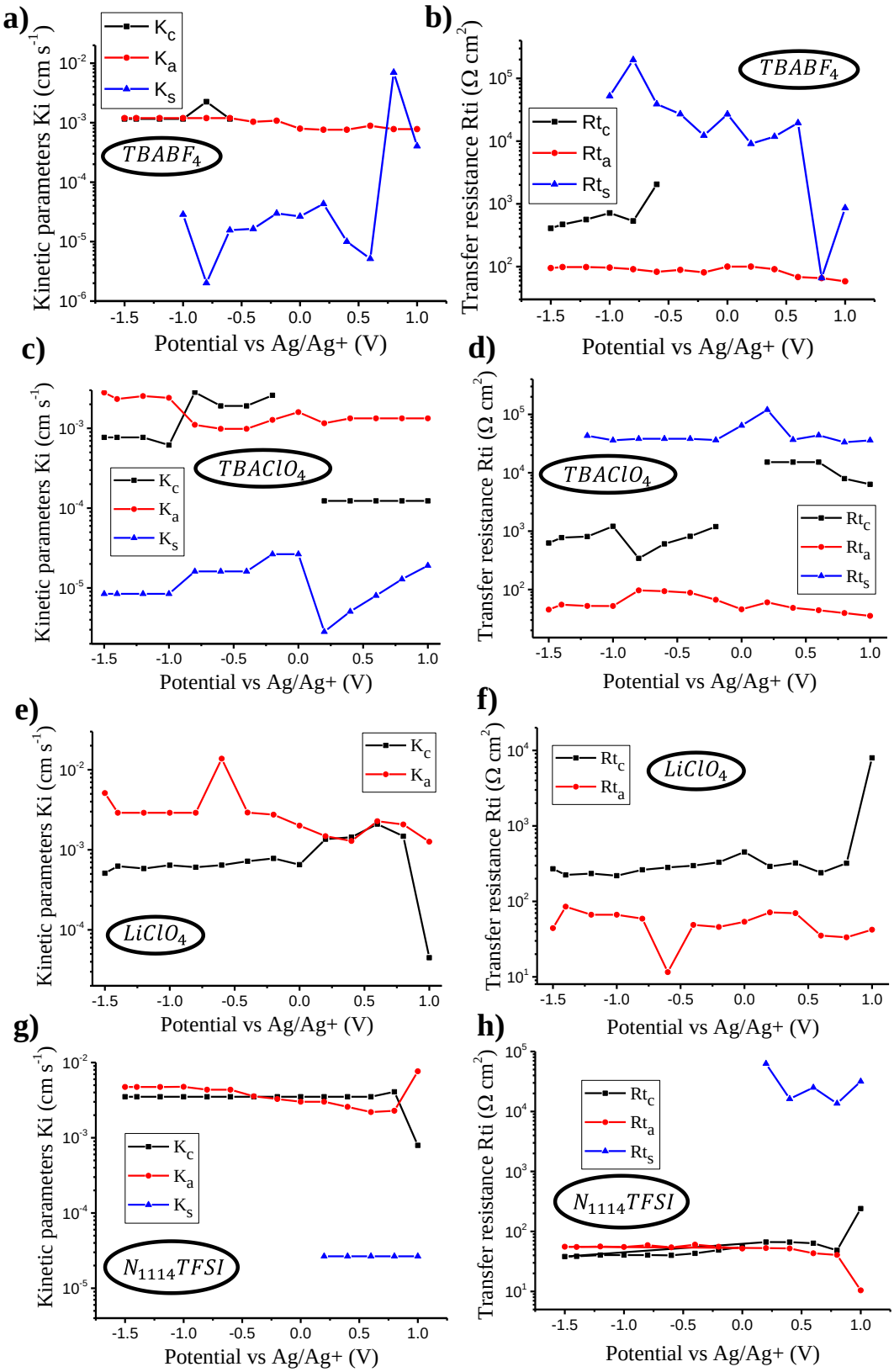

Figure III-5: Evolution of the kinetic parameters K_i (cm s-1) (left) and the transfer resistance values Rt_i (Ω cm2) (right) in **a) b)** PC+0.5M $TBABF_4$, **c) d)** PC+0.5M $TBAClO_4$, **e) f)** PC+0.5M $LiClO_4$, **g) h)** PC+$N_{1114}TFSI$.

III.3.iv. Concentration and mass variations for each species

The values of K_i and Rt_i also allow the calculation of the relative concentration changes of individual species C_i-C_0 with the integration of $\left.\frac{\Delta C_i}{\Delta E}\right|_{\omega \to 0} = -\frac{G_i}{K_i}$ [20]. **Fig. III-6a, c, e and g** depicts C_i-C_0 calculated for each electrolyte and for each species identified in the corresponding theoretical model to fit the *ac*-electrogravimetry data. In both PC+0.5M $TBABF_4$ and PC+0.5M $TBAClO_4$ anions have the highest concentration variations which increases linearly from -1.5 V to 1 V vs Ag/Ag^+ while the concentration of TBA^+ cations rises very slightly at negative potentials (-0.75 V to -1.5 V vs Ag/Ag^+) (**Fig. III-6a, c**). These results show that BF_4^- and ClO_4^- anions behave almost in the same way as the VOGN electrode is charged and discharged: We have a permselectivity of anions in both cases due to the larger size of TBA^+ cations.

In the case of $LiClO_4$, both ClO_4^- anions and monosolvated Li^+ cations present high concentration variations with around 25 $mmol.cm^{-3}$ for anions and 13 $mmol.cm^{-3}$ for cations over the whole potential window (**Fig. III-6e**). This clearly shows that reducing the cation size can change the overall exchange mechanisms and have both cations and anions exchanged at the same time. For the mixture of PC and N_{1114}TFSI, both cations and anions have the same magnitude of concentration variations in opposite directions (**Fig. III-6g**). This demonstrates that both species are exchanged symmetrically in the studied potential window, even though the anion's larger mass (M_{TFSI^-} = 280 $g.mol^{-1}$) compared to cations (M_{N1114+} = 116 $g.mol^{-1}$) dominated the responses gravimetrically and gave the impression that $TFSI^-$ carried the majority of the ion exchanges in EQCM and raw *ac*-electrogravimetry results. Actually, for these two electrolytes, a failure of the electrode's permselectivity was observed which was revealed by the analysis of the *ac*-electrogravimetry data.

The potential-induced mass variations m_i for each species in the volume of the porous VOGN electrode $V_{electrode}$ can then be calculated ($m_i = M_i \cdot V_{electrode} \cdot (C_i - C_0)$, with M_i the molar mass of species *i*). **Fig. III-6b, d, f and h** depicts the total mass variations measured in CV and calculated with $m = \sum m_i$ for each electrolyte, with the individual calculated mass variations m_i depicted in the inset. In each case, Δm_{total} calculated from *ac*-electrogravimetry is in good agreement with the global Δm given by our classical EQCM, further validating the models used to fit the *ac*-electrogravimetry data.

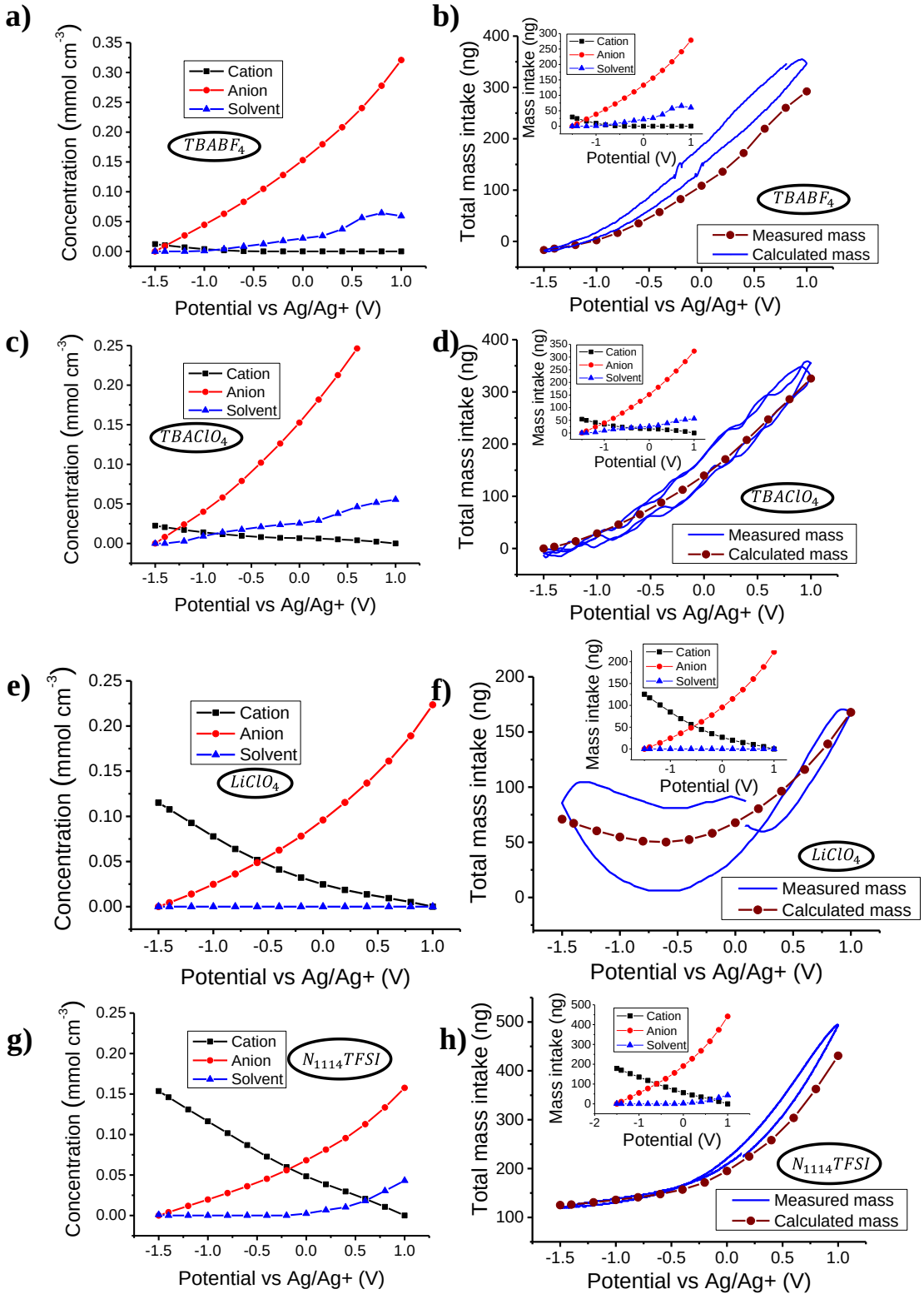

Figure III-6: Evolution of the relative concentrations, $C_i - C_0$, of each species exchanged, derived from *ac*-electrogravimetric measurements (left) and the resulting total mass variations calculated from *ac*-electrogravimetry and measured with EQCM at 10 mV.s^{-1} (results for individual species as inset) (right) in **a-b)** PC+0.5M $TBABF_4$, **c-d)** PC+0.5M $TBAClO_4$, **e-f)** PC+0.5M $LiClO_4$, **g-h)** PC+$N_{1114}TFSI$.

III-4. The effect of N-doping on the ion exchange behavior of VOGNs

Once the VOGN growth process is complete within ECR-CVD chamber, it is possible to strike the sample with highly energetic nitrogen atoms with exposure to nitrogen plasma. This will reduce the deposited mass of VOGNs by shredding the top of the nanosheets and dope the graphene with nitrogen. The nitrogen sites created within the graphene matrix have been shown to enhance the carrier mobility and bring variations in density [21]. Previous work by our team has shown that this process can lead to an increase of capacitance by a factor of two in VOGN supercapacitors using ionic liquids [10]. N-doped VOGNs have therefore been prepared on $GaPO_4$ resonators to perform EQCM measurements on these systems and monitor possible changes in ionic exchange mechanisms compared to usual VOGN electrodes. In order to maintain an equivalent thickness to that of the samples used for the previous EQCM studies, the growth time prior to the nitrogen doping was doubled (160 min instead of 80 min). **Fig. III-7a** depicts a SEM image of VOGNs grown on a gold patterned $GaPO_4$ resonator and doped with nitrogen plasma for 3 min. The morphology observed for this electrode shows the same features as undoped electrodes: The nanosheets maintained a vertical alignment along with a good coverage of the gold electrode despite the rough conditions in N_2 plasma. The thickness was measured around the same value (1 µm) despite a doubled growth time, showing that N_2 plasma etched around half of the VOGN electrode.

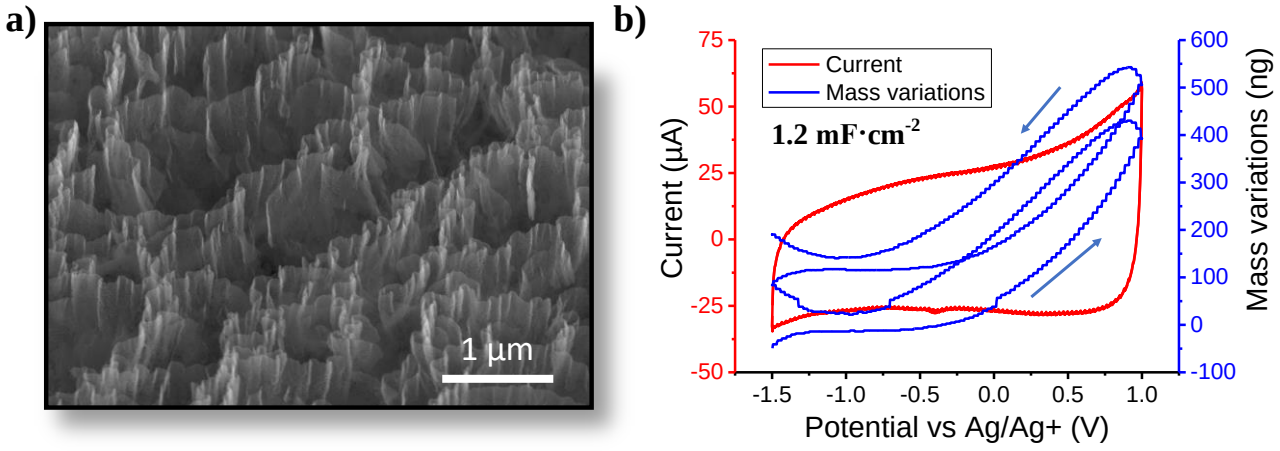

Figure III-7: a) SEM image of N-doped VOGNs grown on a $GaPO_4$ resonator. **b)** Cyclic voltammetry (red) coupled with mass variation measurements (blue) at 100 $mV \cdot s^{-1}$ in PC+0.5M $TBABF_4$.

EQCM measurements were performed in PC+0.5M $TBABF_4$, an electrolyte used in the beginning of the previous section that is stable from -1.5 V to 1 V vs Ag/Ag^+. The resulting specific capacitance and mass variations are both comparable to those obtained without N-doping: 1.2 $mF.cm^{-2}$ instead of 1.3 $mF.cm^{-2}$ and 400 ng instead of 365 ng (**Fig. III-7b**). Similarly to undoped VOGNs, the reversible mass increase above -0.5 V vs Ag/Ag^+ is associated to mainly anions being adsorbed at the surface of the electrode. The MPE value around 95 $g.mol^{-1}$ in this region is slightly bigger than the anion molar mass ($M_{BF_4^-} = 86.8\ g.mol^{-1}$), meaning that some solvent molecules are probably absorbed at the same time. Below -0.5V vs Ag/Ag^+ the slope of the mass variations and therefore the MPE decreases rapidly, meaning that cations also take part in the ionic exchanges in this region.

Ac-electrogravimetry measurements were performed in the same potential window and were fitted using only BF_4^- anions and free PC molecules in the model above -0.5 V vs Ag/Ag^+ and only BF_4^- anions and TBA^+ cations below -0.5 V (**Fig. III-8a-b**). Applying an identical procedure as in the section III-3, the anion and cation contributions were separated mathematically and shown in the anion-solvent and cation-solvent partial TFs (**Fig. III-8c-d**). These graphs reveal that the nature of ionic exchanges is very similar with N-doped VOGNs and standard VOGNs. The main difference lies in the concentration variations C_i-C_0 calculated for free solvent molecules (**Fig. III-8e**), with total variations around 0.21 $mmol.cm^{-3}$ instead of 0.05 $mmol.cm^{-3}$ for undoped VOGNs. This larger contribution of solvent molecules, which may be related to the fact that surface becomes more hydrophilic with N-doping, explains the increase in mass variations for N-doped VOGNs. A reconstruction of the mass variations from EQCM was performed using the results obtained with *ac*-electrogravimetry, and both curves were found in very good agreement (**Fig. III-8f**).

As the specific capacitance increase previously observed on N-doped VOGNs in ionic liquids could not be reproduced, the same measurements were performed in pure $N_{1114}TFSI$. Although microbalance measurements were unstable due to the high viscosity of $N_{1114}TFSI$, a specific capacitance of 0.9 $mF{\cdot}cm^{-2}$ was obtained, showing that the electrolyte is not the limiting parameter. The highly capacitive N-doped VOGNs obtained by our team were synthetized on silicon wafers [10], thus the same growth substrate could not be obtained with the microbalance. Although it remains unclear why N-doped VOGNs did not bring a significant capacitance change

on the microbalance, the change in morphology due to the gold used as growth substrate is a plausible explanation.

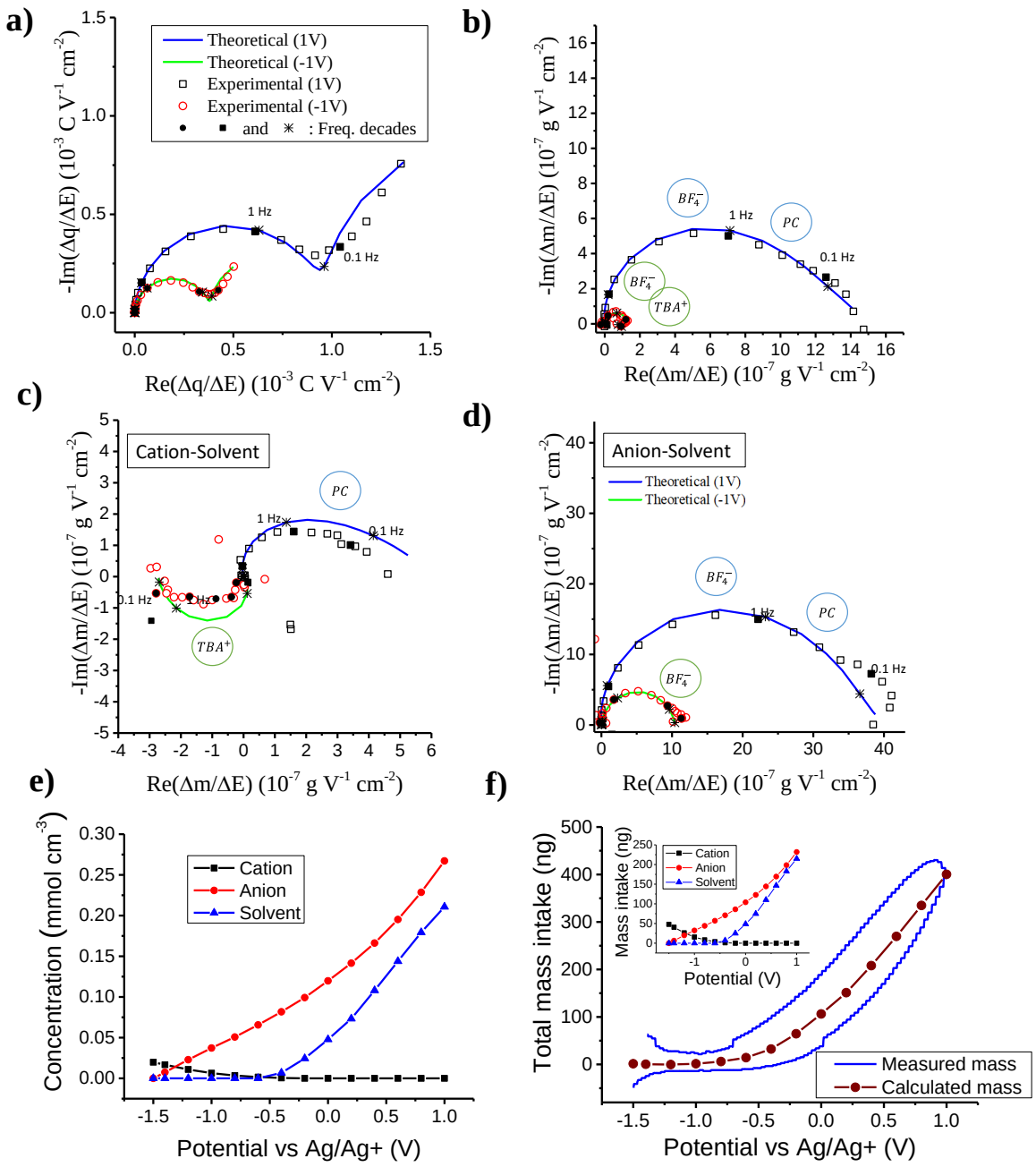

Figure 3-8: a-d) Nyquist plots of the experimental *ac*-electrogravimetry results on N-doped VOGN electrodes at 1V and -1V (squares) and their corresponding fits (lines) in PC+0.5M $TBABF_4$, with **a)** the charge/potential TFs $\Delta q/\Delta E(\omega)$, **b)** the mass/potential TFs $\Delta m/\Delta E(\omega)$, **c)** the cation-solvent partial TFs and **d)** the anion-solvent partial TFs. **e)** The calculated concentration variations for each species. **f)** The total mass variations calculated from *ac*-electrogravimetry and measured with EQCM (results for individual species as inset).

Conclusions

Electroacoustic measurements were performed on VOGN electrodes before and after growth on $GaPO_4$ resonators, with and without electrolyte. The good quality factors obtained with these measurements confirmed the possibility of using EQCM to study such nanostructured materials. EQCM and *ac*-electrogravimetry measurements were performed with a comparison between various salts in an organic electrolyte. The analysis of the EQCM results brought significant insights on the overall mechanisms of ionic exchanges at the VOGN surface. In particular, a major contribution of anions for both $TBABF_4$ and $TBAClO_4$ has been revealed, showing the permselectivity of the electrode for these electrolytes.

A deeper understanding of these mechanisms along with a better comprehension of the exchange dynamics of individual species was obtained with *ac*-electrogravimetry. The mutual contribution of anions, cations and free solvent molecules were differentiated, as for example the non-obvious case of permselectivity failure with symmetrical exchanges of anions and cations in $PC+N_{1114}TFSI$. A solvation number upon adsorption of zero for most ions and one for Li^+ cations was derived from *ac*-electrogravimetry analysis. N-doped VOGNs were synthetized on $GaPO_4$ resonators and were found to have similar ionic exchanges as the undoped counterparts. For each system studied in this chapter, the global mass variations derived from *ac*-electrogravimetry were found in good agreement with classical EQCM results and the individual dynamic parameters found for each species provided further valuable information about the electrochemical system.

References

[1] A. Tyagi, K.M. Tripathi, R.K. Gupta, Recent progress in micro-scale energy storage devices and future aspects, J. Mater. Chem. A. 3 (2015) 22507–22541.

[2] Z. Bo, S. Mao, Z.J. Han, K. Cen, J. Chen, K.K. Ostrikov, Emerging energy and environmental applications of vertically-oriented graphenes, Chem. Soc. Rev. 44 (2015) 2108–2121.

[3] G. Xiong, C. Meng, R. G. Reifenberger, P. P. Irazoqui, T. S. Fisher, A review of graphene-based electrochemical microsupercapacitors, Electroanalysis. 26 (2014) 30 - 51.

[4] C. Junhong, Z. Bo, L. Ganhua, Vertically-oriented Graphene: PECVD Synthesis and Applications, Chapter 7: Vertically-oriented graphene supercapacitors, Ed. Springer, 2015, pp. 79-94.

[5] T. Lé, D. Aradilla, G. Bidan, F. Billon, M. Delaunay, J.M. Gérard, H. Perrot, O. Sel, Unveiling the ionic exchange mechanisms in vertically-oriented graphene nanosheet supercapacitor electrodes with electrochemical quartz crystal microbalance and ac-electrogravimetry, Electrochemistry Communications. 93 (2018) 5–9.

[6] M. Delaunay, Permanent magnet linear microwave plasma source. US6319372 B1 (1987).

[7] M. Delaunay, E. Touchais, Electron cyclotron resonance plasma ion source for material depositions, Rev. Sci. Instrum. 69 (1998) 2320.

[8] S. Jakab, S. Picart, B. Tribollet, P. Rousseau, H. Perrot, C. Gabrielli, Study of the dissolution of thin films of cerium oxide by using a GaPO4 crystal microbalance, Anal. Chem. 81 (2009), 5139-5145.

[9] D. Aradilla, M. Delaunay, S. Sadki, J.M. Gérard, G. Bidan, Vertically aligned graphene nanosheets on silicon using an ionic liquid electrolyte: towards high performance on-chip micro-supercapacitors, J. Mater. Chem. A. 3 (2015) 19254–19262.

[10] D. Aradilla, M. Delaunay, M. Buhagiar, D. Aldakov, J. Faure-Vincent, H. Okuno, J.M. Gérard, G. Bidan, Plasma Heavily Nitrogen-Doped Vertically Oriented Graphene Nanosheets (N-VOGNs) for High Volumetric Performance On-Chip Supercapacitors in Ionic Liquid, Curr. Smart Mater. 2 (2017) 1–8.

[11] H. Goubaa, F. Escobar-Teran, I. Ressam, W. Gao, A.E. Kadib, I.T. Lucas, M. Raihane, M. Lahcini, H. Perrot, O. Sel, Dynamic Resolution of Ion Transfer in Electrochemically Reduced Graphene Oxides Revealed by Electrogravimetric Impedance, The Journal of Physical Chemistry C. 121 (2017) 9370–9380.

[12] H.D.B. Jenkins, K.P. Thakur, Reappraisal of thermochemical radii for complex ions, J. Chem. Educ., 56, 576 (1979).

[13] A.F. Wells, "Structural Inorganic Chemistry," 5th ed., Clarendon Press, Oxford, 1984, p. 1288.

[14] T. Lé, P. Gentile, G. Bidan, D. Aradilla, New electrolyte mixture of propylene carbonate

and butyltrimethylammonium bis(trifluoromethylsulfonyl)imide (N 1114 TFSI) for high performance silicon nanowire (SiNW)-based supercapacitor applications, Electrochimica Acta. 254 (2017) 368–374.

[15] C. R. Arias, C. Debiemme-Chouvy, C. Gabrielli, C. Laberty-Robert, A. Pailleret, H. Perrot, O. Sel, New Insights into Pseudocapacitive Charge-Storage Mechanisms in Li-Birnessite Type MnO_2 Monitored by Fast Quartz Crystal Microbalance Methods, J. Phys. Chem. C 118 (2014), 26551-26559.

[16] H. Kim, Z. Wen, K. Yu, O. Mao, J. Chen, Straightforward fabrication of a highly branched graphene nanosheet array for a Li-ion battery anode, Journal of Materials Chemistry. 22 (2012) 15514.

[17] P. Shi, M. Lin, H. Zheng, X. He, Z. Xue, H. Xiang, C. Chen, Effect of propylene carbonate-Li solvation structures on graphite exfoliation and its application in Li-ion batteries, Electrochimica Acta 247 (2017), 12-18.

[18] J. Jacquemin, P. Husson, A.A.H. Padua, V. Majer, Density and viscosity of several pure and water-saturated ionic liquids, Green Chem. 8 (2006) 172–180.

[19] V. Chakrapani, F. Rusli, M.A. Filler, P.A. Kohl, Quaternary ammonium ionic liquid electrolyte for a silicon nanowire-based lithium ion battery, J. Phys. Chem. C 115 (2011) 22048–22053.

[20] C. Gabrielli, J.J. García-Jareño, M. Keddam, H. Perrot, F. Vicente, Ac-Electrogravimetry Study of Electroactive Thin Films. I. Application to Prussian Blue, J. Phys. Chem. B. 106 (2002) 3182–3191.

[21] S. Ghosh, S.R. Polaki, N.G. Krishna, M. Kamruddin, Influence of nitrogen on the growth of vertical graphene nanosheets under plasma, Journal of Materials Science. 53 (2018) 7316–7325.

Chapter 5:
Conclusion and perspectives

The study presented in this thesis is a first glance at the possibilities offered by electrogravimetric techniques to investigate ionic exchanges in vertically-oriented nanostructures, and the limitations inherent with such morphologies. These limitations appear at two different levels:

- During the synthesis of the nanostructures on the QCM electrode, growth conditions requiring high temperatures and/or a harsh chemical treatment hinder the use of a standard quartz microbalance.
- With the introduction of the electrolyte, the shear wave of the QCM can experience serious damping due to hydrodynamic drag forces and/or inertia of trapped fluid.

To circumvent these limitations various strategies have been presented. With the use of $GaPO_4$ piezoelectric crystals as resonators, the high temperature growth of SiNWs and VOGNs at 600°C and 450°C respectively has been achieved while maintaining good QCM quality factors. The adaptation of the electrode configuration, with a thin Ti adhesion layer and a thicker Pt layer, was essential to maintain conductive electrodes firmly attached to the surface of $GaPO_4$ resonators after the harsh conditions experienced during the CVD growth of SiNWs. When the electrochemical growth of the vertically-oriented nanostructure is possible, without using harsh post-treatment conditions, then a standard QCM can be used. In this thesis, PEDOT NWs were grown with a one-step electropolymerization technique that caused no damages to the resonator.

To reduce the extent of resonance damping due to hydrodynamic drag forces on the nanostructures, we have shown that a crucial parameter is limiting the height of the vertical nanostructures to 1-2 µm. Using 10 µm SiNW arrays, drag forces on the nanostructures have been shown to create a distortion of the force experienced by the resonator that hinder their use for EQCM and *ac*-electrogravimetry. Another crucial parameter is the viscosity of the electrolyte: Using a very low viscosity medium such as ACN the hydrodynamic damping can be significantly

reduced. In this solvent, electrogravimetric measurements were successfully performed on PEDOT NWs with limited perturbations from drag forces. In the case of SiNWs these perturbations could not be sufficiently reduced due to the length of the nanowires. For bare SiNWs this length cannot be reduced without reducing the current significantly and thus also hinder electrogravimetric measurements. This reflects the fine balance which needs to be respected to keep enough mass change without inducing resonance damping. Nevertheless, the electrochemical characterization of SiNW electrodes allowed the derivation of an ideal ratio for the mixture of PC+N_{1114}TFSI. Furthermore, PEDOT-covered SiNWs were developed as hybrid supercapacitor electrodes with much higher capacitance than SiNWs for the same length. These performances triggered very large mass variations in EQCM measurements that could be successfully measured in spite of the low QCM stability.

Among both PEDOT NWs and VOGN electrodes, very interesting ionic exchange mechanisms were unveiled using EQCM and *ac*-electrogravimetry. The pseudo-capacitive ionic exchanges involved in PEDOT NWs were first investigated with EQCM, allowing the identification of a major cation contribution in ACN+0.5M $TBABF_4$. *Ac*-electrogravimetry was then used to perform the deconvolution of the EQCM response, revealing that Li^+ cations from the initial doping of PEDOT had dissolved in the electrolyte and contributed equally with TBA^+ cations to the ionic exchanges.

The dynamic exchange mechanisms at the interface of VOGN electrodes were investigated using various ionic compositions. In both PC+0.5M $TBABF_4$ and PC+0.5M $TBAClO_4$, the permselectivity of the electrode to anions was evidenced using EQCM. A deconvolution of the EQCM results for four different electrolytes using *ac*-electrogravimetry revealed the dynamics and proportions of the exchanges for each species involved, along with the respective solvation numbers. In a mixture of PC+N_{1114}TFSI, the large $TFSI^-$ anions and the smaller N_{1114}^+ cations were found to exchange symmetrically with equal proportions, although $TFSI^-$ anions contributed the most to the mass variations.

The present study aims at paving the way to the electrogravimetric characterization of many other nanostructured supercapacitor materials. In the continuation of the results obtained with 10 µm-long PEDOT-covered SiNWs, shorter nanowires could be used to reduce the hydrodynamic drag forces, facilitating the use of *ac*-electrogravimetry for their characterization.

Another hybrid architecture consisting of SiNWs covered with MnO_2 nanoflakes has recently been reported to offer great performance improvements as pseudo-capacitor electrode (**Fig. 1a-b**) [1]. From a structural point of view such electrodes are similar to PEDOT-covered SiNWs and if the nanowires are not too long they should be suitable for electrogravimetric investigations. VOGN electrodes covered with Co_3O_4 nanoparticles have also been demonstrated as pseudo-capacitive materials with a specific capacitance of 3480 $F.g^{-1}$, near the maximal theoretical value (**Fig. 1d**) [2].

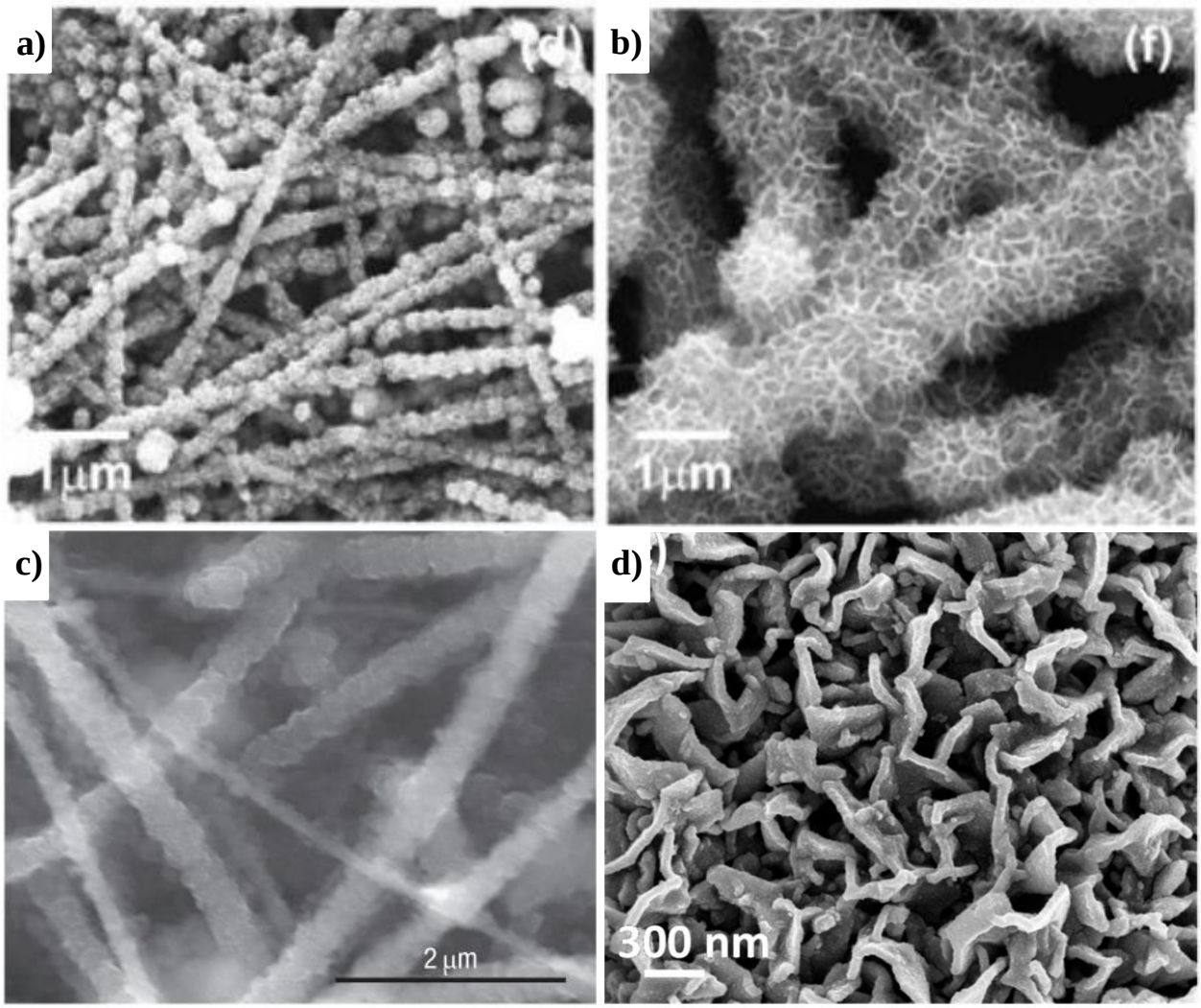

Figure 1: SEM images of **a-b)** SINWs covered with MnO_2 nanoflakes [1], **c)** SiNWs after cycling as Li-ion battery anodes [6] and **d)** VOGNs covered with Co_3O_4 nanoparticles [2].

EQCM and *ac*-electrogravimetry are not limited to supercapacitor electrodes and can be used to characterize the ionic exchanges in other energy storage devices such as Li-ion batteries [3], [4]. Nanostructuration of the electrodes is also a key development path for batteries as it can

increase the accessibility to the electrode material, increase the power density, and increase the lifetime of battery electrodes [5]–[7]. The reflections and methods developed in this study could be of use to apply electrogravimetric characterization to nanostructured battery materials. In fact, the vertically-oriented nanostructures studied in this thesis could be used as well as battery electrodes. Both SiNWs and VOGNs have shown a great potential as Li-ion battery anodes, with in particular the case of the volume change in Si anodes that the nanowire structures can accept more durably (**Fig. 1c**) [6], [8], [9].

Electrogravimetric techniques could be used to characterize Li-ion batteries with Si-based anodes if short nanowire length (1-2 µm) or silicon nanoparticles are used along with a low viscosity electrolyte. Such measurements would allow the investigation of the Li-Si alloying process as well as the formation of the solid electrolyte interface (SEI).

Many aspects of the information that can be collected with EQCM and *ac*-electrogravimetry have been presented throughout this work, showing that these techniques are well adapted to bring valuable insights on the ionic exchange mechanisms in thin nanostructured supercapacitor electrodes. Further developments of these techniques could be investigated to have an even greater adaptation with nanostructured materials, such as a more complex *ac*-electrogravimetry model that would take into account the morphology of the electrode. Modelling could also be used to better understand the effect of drag forces and the inertia of trapped fluids on the resonance frequency and damping of the shear waves.

References

[1] D. P. Dubal, D. Aradilla, G. Bidan, P. Gentile, T. J. S. Schubert, J. Wimberg, S. Sadki, and P. Gomez-Romero, '3D hierarchical assembly of ultrathin MnO_2 nanoflakes on silicon nanowires for high performance micro-supercapacitors in Li- doped ionic liquid', *Sci. Rep.*, 5, p. 9771, May 2015.

[2] Q. Liao, N. Li, S. Jin, G. Yang, and C. Wang, 'All-Solid-State Symmetric Supercapacitor Based on Co3O4 Nanoparticles on Vertically Aligned Graphene', ACS Nano. 9 (2015) 5310–5317.

[3] M. Moshkovich, M. Cojocaru, H. E. Gottlieb, and D. Aurbach, 'The study of the anodic stability of alkyl carbonate solutions by in situ FTIR spectroscopy, EQCM, NMR and MS', *J. Electroanal. Chem.*, 497, no. 1, pp. 84–96, Feb. 2001.

[4] D. Aurbach and M. Moshkovich, 'A Study of Lithium Deposition-Dissolution Processes in a Few Selected Electrolyte Solutions by Electrochemical Quartz Crystal Microbalance', *J. Electrochem. Soc.*, 145, no. 8, pp. 2629–2639, Jan. 1998.

[5] J. Hassoun, S. Panero, P. Simon, P. L. Taberna, and B. Scrosati, 'High-Rate, Long-Life Ni–Sn Nanostructured Electrodes for Lithium-Ion Batteries', *Adv. Mater.*, 19, no. 12, pp. 1632–1635, Jun. 2007.

[6] C. K. Chan, H. Peng, G. Liu, K. McILWRATH, X. F. Zhang, R. A. Huggins, and Y. Cui, 'High-performance lithium battery anodes using silicon nanowires', in *Materials for Sustainable Energy*, 0 vols, Co-Published with Macmillan Publishers Ltd, UK, 2010, pp. 187–191.

[7] M.-K. Song, S. Park, F. M. Alamgir, J. Cho, and M. Liu, 'Nanostructured electrodes for lithium-ion and lithium-air batteries: the latest developments, challenges, and perspectives', *Mater. Sci. Eng. R Rep.*, 72, no. 11, pp. 203–252, Nov. 2011.

[8] X. Xiao, P. Liu, J. S. Wang, M. W. Verbrugge, and M. P. Balogh, 'Vertically aligned graphene electrode for lithium ion battery with high rate capability', *Electrochem. Commun.*, 13, no. 2, pp. 209–212, Feb. 2011.

[9] Y. Wang, B. Chen, D. H. Seo, Z. J. Han, J. I. Wong, K. (Ken) Ostrikov, H. Zhang, and H. Y. Yang, 'MoS_2-coated vertical graphene nanosheet for high-performance rechargeable lithium-ion batteries and hydrogen production', *NPG Asia Mater.*, 8, no. 5, p. e268, May 2016.

Études fondamentales des échanges ioniques au sein d'électrodes nanostructurées verticalement par microbalance à quartz en mode dynamique: Application au stockage électrochimique de l'énergie.

Table des matières

Chapitre 1 : Etat de l'art

1. Stockage de l'énergie électrique

Les méthodes permettant de stocker de l'énergie provenant d'une source électrique et de la restituer de manière réversible sont d'une importance grandissante à toutes les échelles. Aux grandes échelles les méthodes de stockages sont essentielles à la mise en place d'une transition énergétique vers les énergies renouvelables, notamment pour stocker l'énergie provenant de sources d'énergie intermittentes comme le solaire ou l'éolien [1]. Aux échelles intermédiaires le stockage d'énergie électrique permettra le déploiement de solutions de transport plus efficaces en énergie n'émettant ni gaz ni de particules. A plus petite échelle, le développement de plus en plus accru des technologies portatives à haute puissance de calcul (ordinateurs portables, tablettes, « smartphones », etc.) nécessite des moyens de stockage d'énergie de plus en plus denses et durables. A l'échelle micrométrique, de nouvelles technologies à base de microcomposants indépendants (Dispositifs bio-implantables, réseaux de capteurs, etc.) voient peu à peu le jour et nécessiteront des moyens de stocker de l'énergie de manière miniaturisée (**Fig. 1-1**).

Figure 1-1: Différentes échelles des besoins de stockage d'énergie électrique: **a)** Réseau de distribution électrique et transition énergétique. **b)** Véhicules électriques. **c)** Electronique portable. **d)** Micro-composants et capteurs bio-implantables. Images tirées de [2]-[10].

Pour répondre à cette demande multi-échelle, des solutions de stockage très variées sont utilisées. A grande échelle les barrages hydrauliques sont le plus couramment utilisés du fait de leur faible coût au kWh stocké. En revanche l'impossibilité d'en implanter dans une majorité des régions du monde ont fait apparaître des solutions alternatives comme le stockage de l'énergie via de l'air comprimé (CAES), la liquéfaction de l'air (LAES), des batteries à flux ou des réseaux de batteries Li-ion. Aux échelles intermédiaires et pour l'électronique portative les batteries Li-ion ont largement conquis le marché, a l'exception d'une partie des véhicules électriques s'orientant plutôt vers les piles à combustible. La **figure**

1-2 montre différents moyen de stocker et de restituer l'énergie électrique en fonction de leur densité moyenne d'énergie et de leur efficacité.

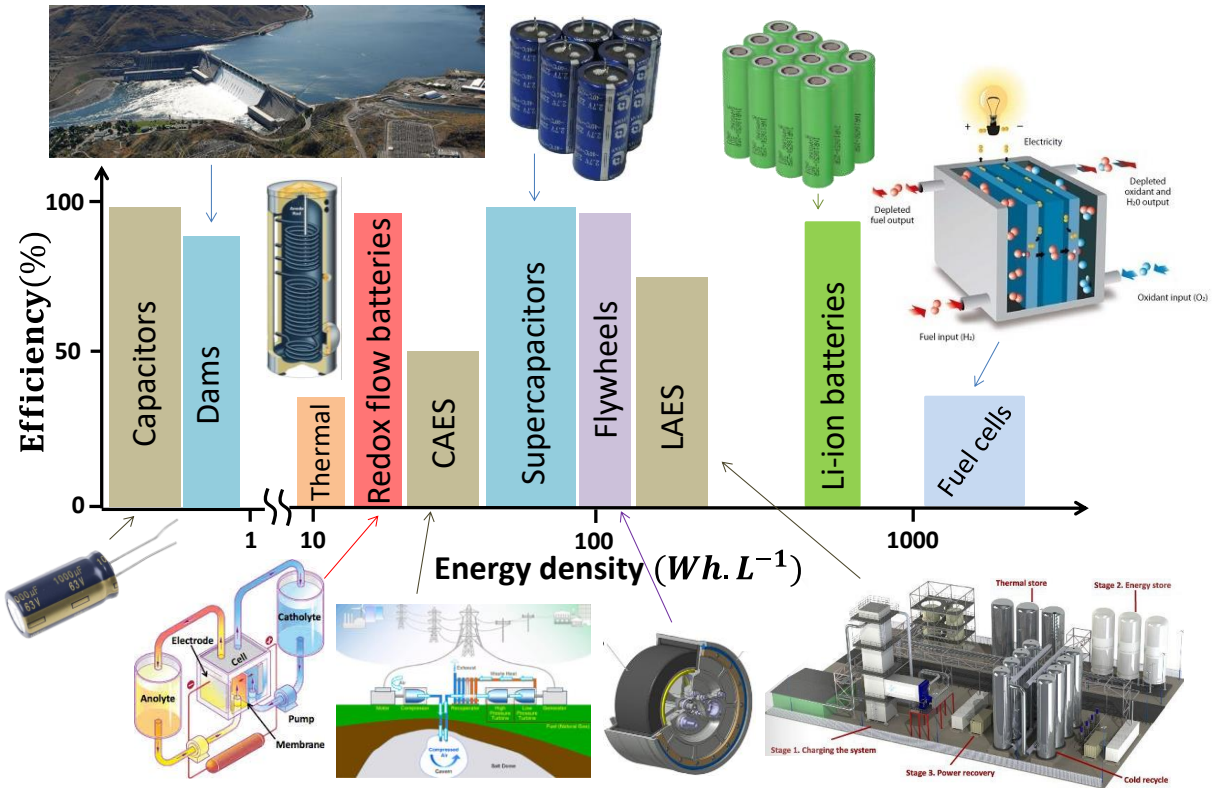

Figure 1-2: Différentes solutions utilisées pour stocker de l'énergie électrique de manière réversible triées en fonction de leur densité d'énergie et de leur efficacité. Images tirées de [11]-[19].

Les batteries Li-ion sont de plus en plus répandues mais présentent l'inconvénient de délivrer une densité de puissance relativement basse (environ 500 $W.kg^{-1}$) comparé aux condensateurs électrolytiques (>10 000 $W.kg^{-1}$) et de perdre une bonne partie de leur capacité après 1000 cycles [20]. Les supercondensateurs sont des dispositifs de stockage se plaçant entre les batteries et les condensateurs en termes de densité d'énergie et de puissance et pouvant soutenir des millions de cycles de charge-décharge avec une très faible dégradation [21]. Découverts en 1957 par H. Becker, ces dispositifs sont aujourd'hui en plein essor et sont déjà utilisés dans plusieurs domaines (**Fig. 1-3**). La possibilité de les charger/décharger rapidement et leur durabilité sont mis à profit dans des systèmes de récupération de l'énergie de freinage et de « Start and stop » de certaines voitures ainsi que dans certains tramways et bus électriques pour pouvoir les déplacer dans des zones sans caténaires. Des grues hybrides s'en servent également pour fournir les pics de puissance nécessaires à soulever de lourdes charges. Enfin du fait de leur durabilité les supercondensateurs sont très prometteurs pour les

applications de stockage d'énergie miniaturisées où ils pourront être couplés à des microsystèmes électromécaniques (MEMS) ou encore des bio-capteurs intégrés.

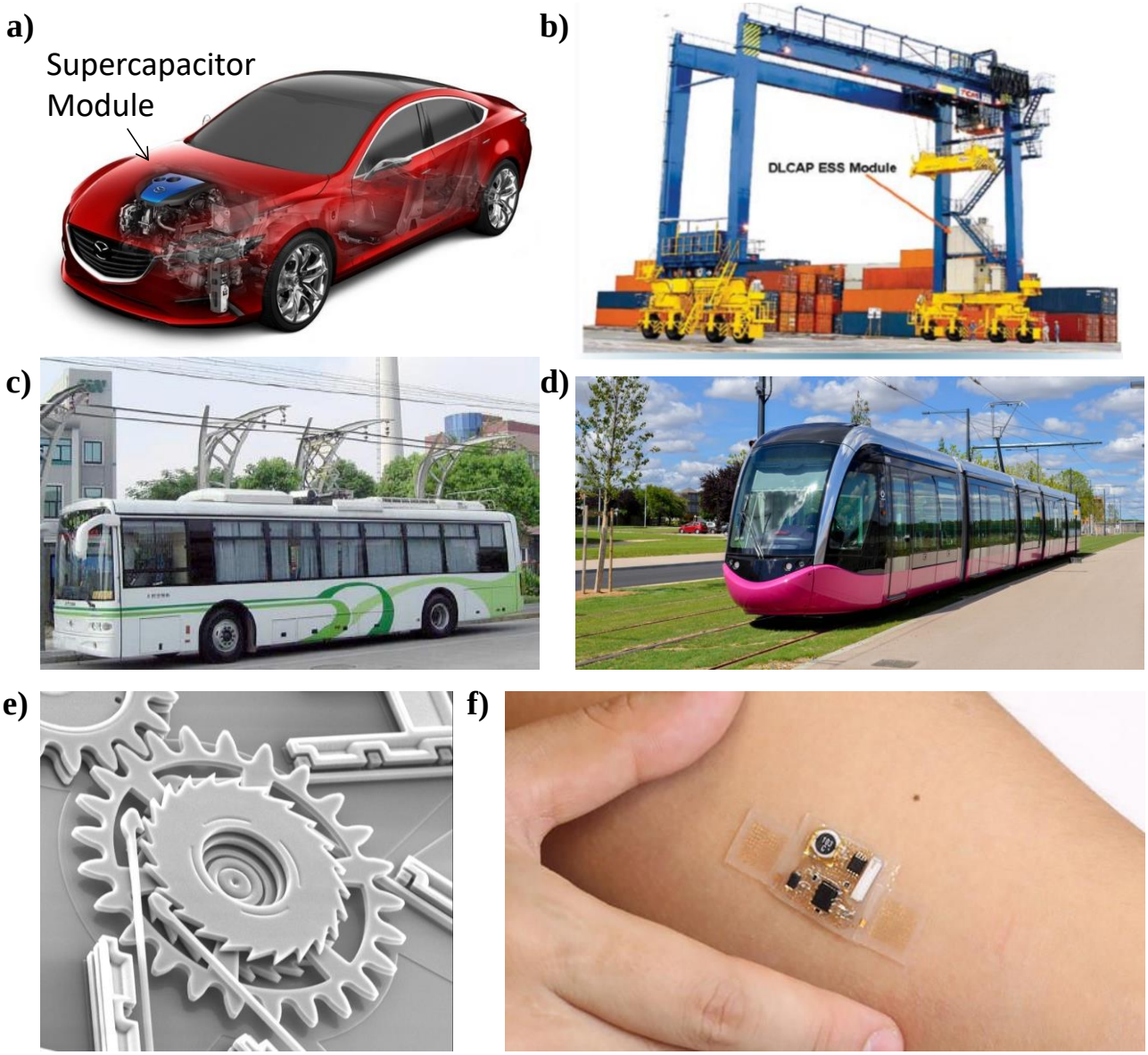

Figure 1-3: Diverses applications des supercondensateurs: **a)** Récupération de l'énergie au freinage par Mazda. **b)** Grue hybride thermique-électrique. **c)** Bus électrique n'utilisant que des supercondensateurs pour stocker l'énergie à Shanghai. **d)** Tramway. **e)** MEMS **f)** Bio-capteurs. Images tirées de [22]-[27].

2. Fonctionnement d'un supercondensateur

Les supercondensateurs sont classés en trois catégories principales montrées **figure 1-4**.

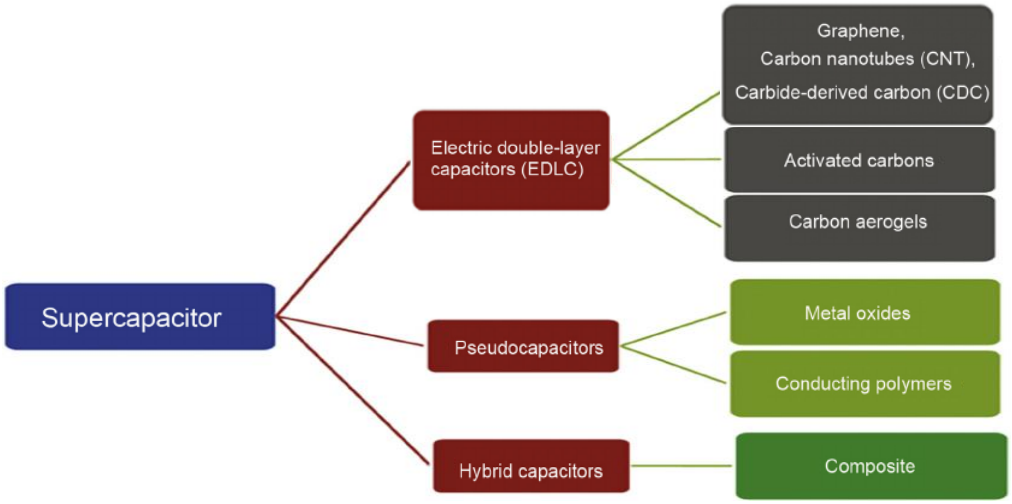

Figure 1-4: Familles de condensateurs : Les condensateurs à double couche électrochimique (EDLC), les pseudo-condensateurs et les condensateurs hybrides. Adapté de [28].

Dans ces catégories, les supercondensateurs à double-couche électrochimique (EDLC) sont les plus simples en termes de fonctionnement car ils ne requièrent pas de réactions d'oxydoréduction aux électrodes. Leur énergie est stockée de manière électrostatique par l'attraction des ions à la surface des électrodes [29]–[32]. Hermann von Helmholtz fut le premier à décrire ce phénomène en 1853 dans un modèle appelé « double couche électrique » qui fut plus tard amélioré par Gouy, Chapman, Stern et Grahame (**figure 1-5**).

Cette simplicité de fonctionnement permet aux EDLCs de bénéficier de plusieurs avantages par rapport aux autres familles de supercondensateurs :

- Ils permettent de délivrer plus de densité de puissance du fait de de l'absence de réactions chimiques impliquant des limitations cinétiques.
- Ils sont extrêmement durables du fait qu'il n'y a pas de mécanismes irréversibles dans ce procédé de stockage.

En assemblant symétriquement deux électrodes à double couche électrochimique avec un électrolyte entre les deux on forme un EDLC dans lequel les ions se déplacent d'une électrode à l'autre au cours des cycles de charge/décharge.

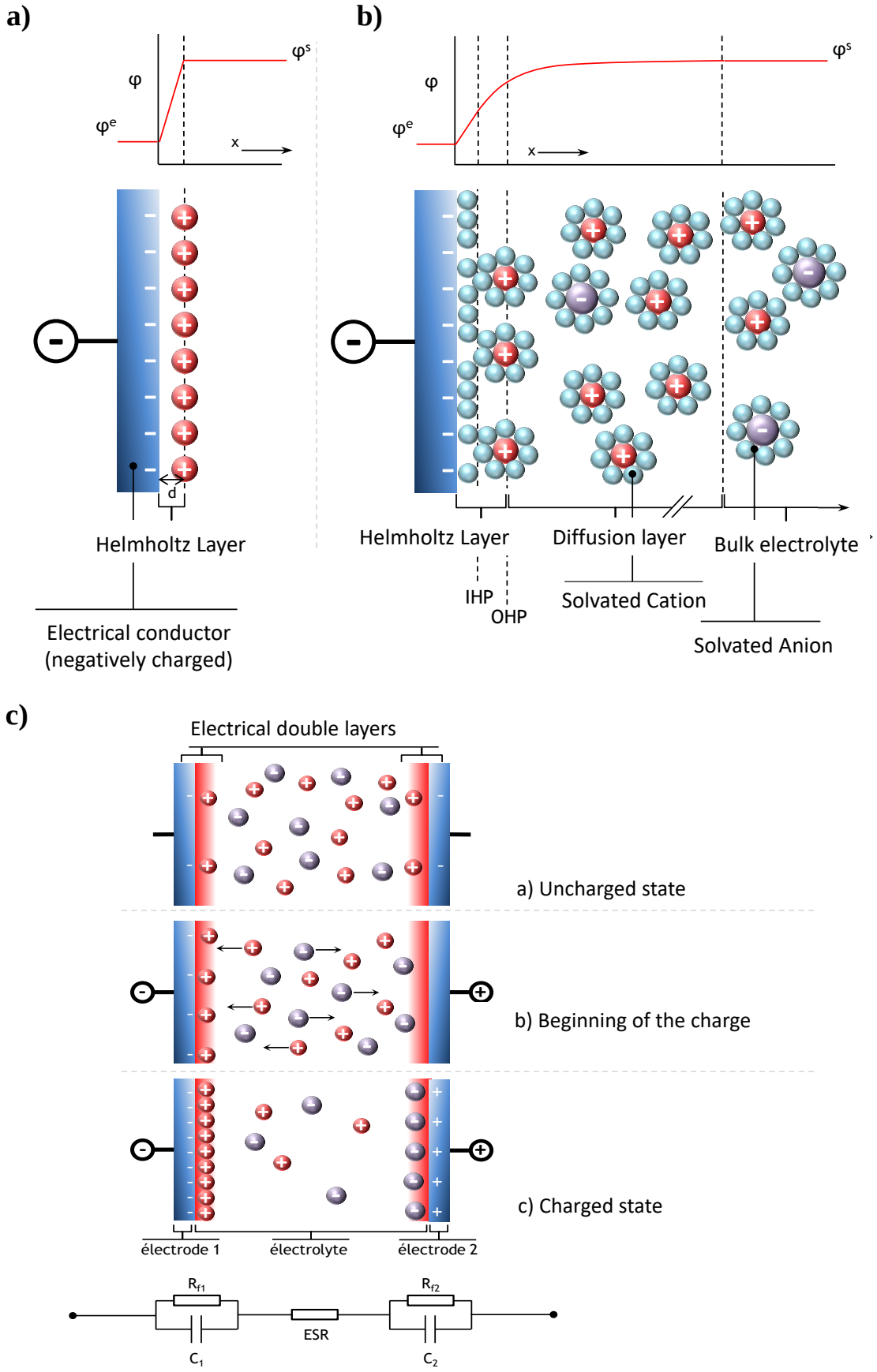

Figure 1-5: a) Représentation schématique du modèle de double-couche électrique de Helmholtz. **b)** Modèle plus complexe développé par Gouy, Chapman, Stern et Grahame **c)** Représentation du fonctionnement global d'un EDLC et circuit électrique équivalent. Adapté de [30],[31].

Les pseudo-condensateurs, contrairement aux EDLCs, utilisent pour stocker de l'énergie des processus faradiques réversibles à cinétique rapide. Ces réactions d'oxydoréduction, ayant à la surface des électrodes, permettent aux pseudo-condensateurs d'avoir une capacité bien plus élevée que les EDLCs, avec cependant une densité de puissance et une durabilité plus réduites. Les matériaux d'électrode utilisés pour ces condensateurs sont généralement des oxydes métalliques (RuO_2, MnO_2, etc.) ou des polymères conducteurs (PEDOT, PPy, PANi, etc.) sous forme de couches minces ou sous forme de structures nanométriques. Le principe de fonctionnement de ces condensateurs en fait des dispositifs proches des batteries. Il est cependant possible de les différentier par leur comportement électrochimique (**figure 1-6**).

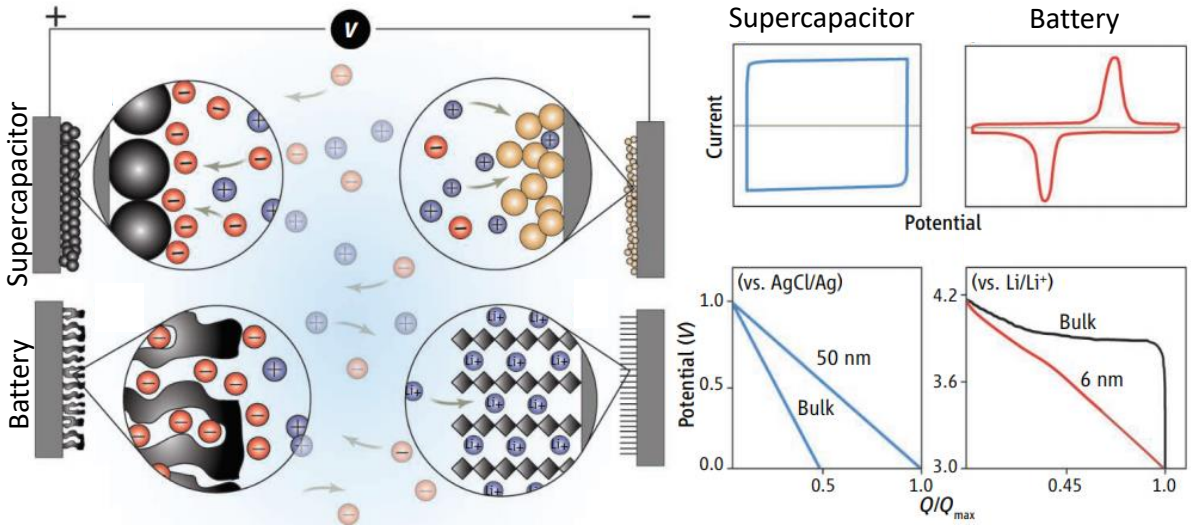

Figure 1-6: Illustration présentant la différence de fonctionnement entre les batteries et les pseudo-condensateurs. [33]-[34]

Enfin, les condensateurs hybrides s'éloignent des condensateurs symétriques par l'utilisation de deux électrodes de nature différentes afin de combiner les avantages des deux : Une électrode à double-couche électrique et une électrode de batterie.

3. Electrodes nanostructurées pour supercondensateurs

La nanostructuration des électrodes de supercondensateurs a été introduite récemment pour augmenter leur surface spécifique en contact avec l'électrolyte et ainsi augmenter leur capacité. Dans le domaine des EDLCs le carbone est l'un des matériaux les plus avantageux du fait de sa haute conductivité et de son faible coût. Le charbon actif et les autres formes de carbone poreux sont les plus répandus comme matériaux d'électrode de supercondensateurs

du commerce. Ainsi, de nombreuses formes de carbone nanostructuré ont commencé à être utilisées comme matériaux d'électrode d'EDLCs (**figure 1-7**).

Material	Carbon onions	Carbon nanotubes	Graphene	Activated carbon	Carbide derived carbon	Templated carbon
Dimensionality	0-D	1-D	2-D	3-D	3-D	3-D
Conductivity	High	High	High	Low	Moderate	Low
Volumetric Capacitance	Low	Low	Moderate	High	High	Low
Cost	High	High	Moderate	Low	Moderate	High
Structure	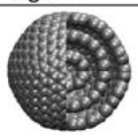	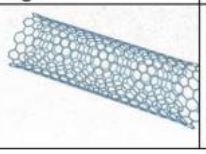	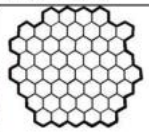	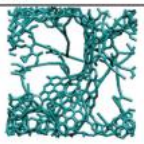	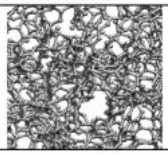	

Figure 1-7: Comparaison de différentes formes de carbone nanostructuré utilisées pour les EDLCs. Adapté de [35].

Parmi ces électrodes nanostructurées, les nanostructures verticales comme les voiles de graphène orientés verticalement (VOGNs) ont montré de grands avantages par rapport aux autres formes de nanostructuration pour l'accessibilité des ions (**figure 1-8**).

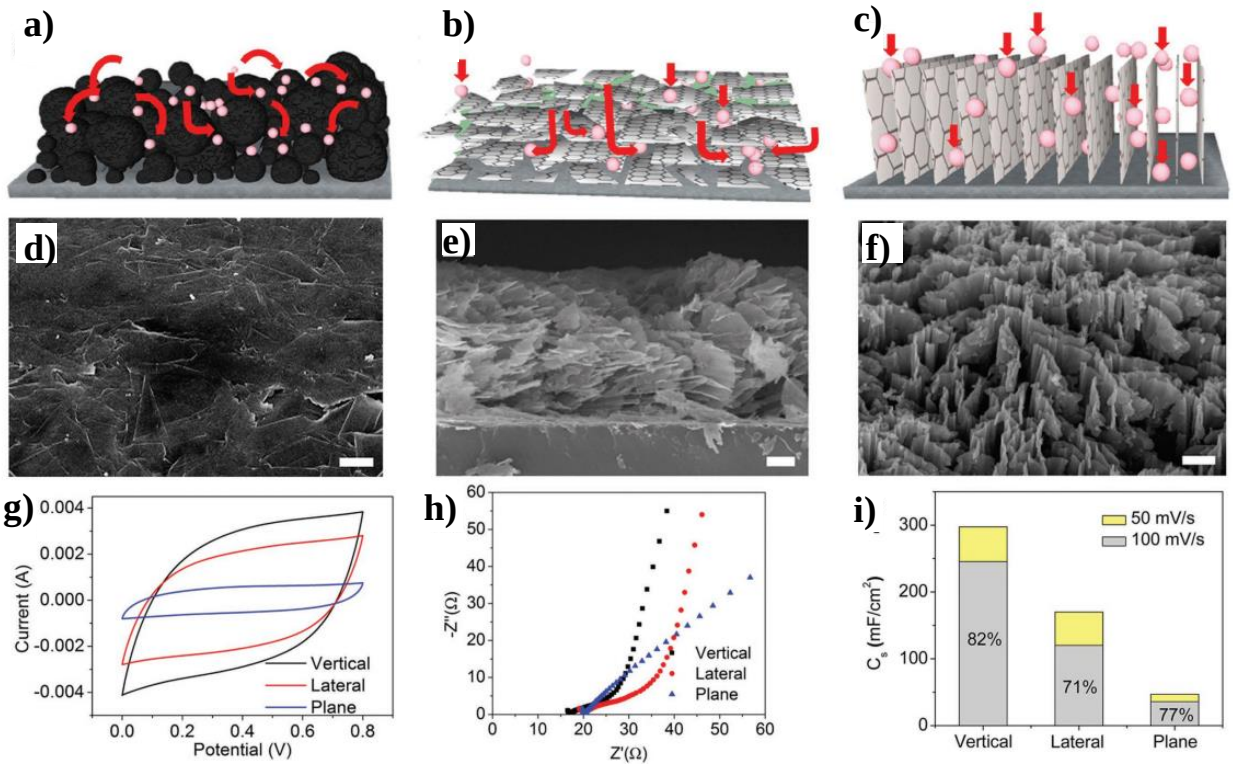

Figure 1-8: Illustrations and images de différentes architectures de graphene orientées **a,d)** dans le plan, **b,e)** latéralement et **c,f)** verticalement. **g)** Voltamogrammes correspondants. **h)** Résultats de spectroscopie d'impédance électrochimique (EIS). **i)** Capacités surfaciques. [36]

Les nanofils et nano-arbres de silicium sont une autre forme d'électrodes nanostructurées qui ont été utilisées pour les EDLCs, avec l'avantage de pouvoir être plus facilement intégrés dans la micro-électronique actuelle qui est à base de silicium.

La conception de ces nanofils et nanoarbres se fait généralement par dépôt chimique en phase vapeur (CVD), avec un mécanisme de croissance vapeur-liquide-solide (VLS) décrit dans la **figure 1-9**.

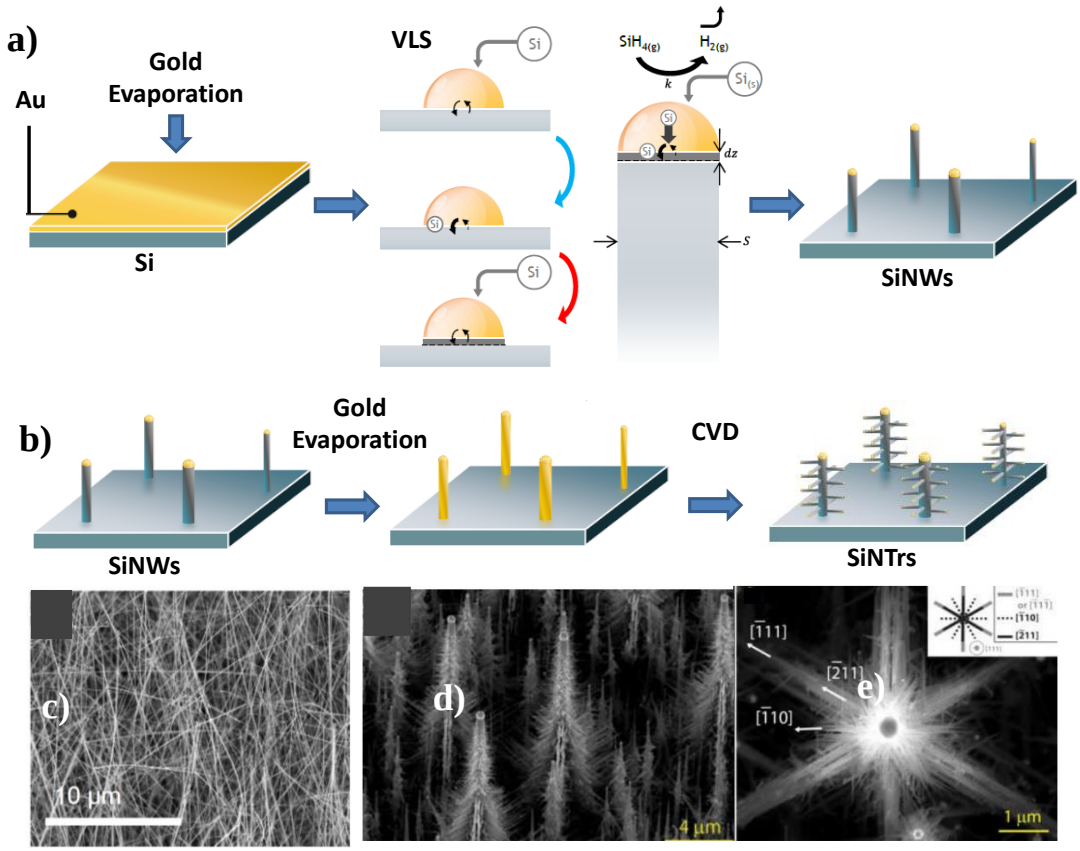

Figure 1-9: a) Illustration de la croissance de nanofils de silicium par CVD. **b)** Procédé utilize pour faire pousser des branches sur les nanofils pour former des nano-arbres. **c)** Nanofils de silicium. **d-e)** Nano-arbres de silicium. Adapté de [37], [38].

Du côté des pseudo-condensateurs, des nanofils de polymère conducteur ont aussi été développés en tant qu'électrodes performantes pour supercondensateurs (**figure 1-10**). [39]

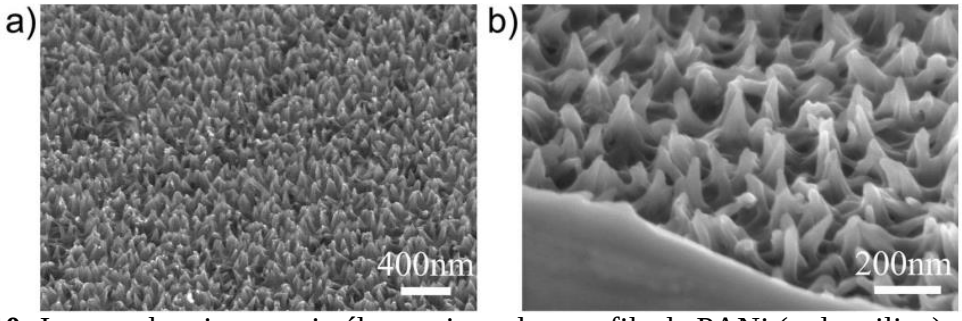

Figure 1-10: Images de microscopie électronique de nanofils de PANi (polyaniline) utilisés comme électrode de pseudo-condensateur. [39]

4. Méthodes de caractérisation par microbalance à quartz électrochimique

La microbalance à quartz électrochimique (EQCM) est une technique de caractérisation de systèmes électrochimiques couplant les mesures classiques de l'électrochimie avec une mesure très précise (à quelques ng près) de la masse de l'électrode. Cette mesure de la masse est faite en utilisant une microbalance à quartz, un dispositif piézoélectrique qui résonne à une fréquence qui est directement proportionnelle à la masse de l'électrode. Le couplage de la mesure de la masse avec les mesures électrochimiques permet d'identifier les espèces ioniques échangées par l'électrode avec l'électrolyte. Cet outil est donc un atout majeur pour la caractérisation d'électrodes de supercondensateurs.

La technique d'« *ac*-electrogravimetry » couple la mesure des variations de masse avec la spectroscopie d'impédance électrochimique et permet de discriminer en fréquence les espèces ioniques observées. Cette technique plus avancée permet d'effectuer une déconvolution des mesures obtenues par EQCM afin de déterminer la contribution individuelle des espèces échangées ainsi que la cinétique de ces échanges.

Cependant des facteurs limitants comme l'amortissement des ondes de la microbalance en milieu liquide restreignent la plupart du temps l'utilisation de ces méthodes de caractérisation à des films fins et rigidement attachés au substrat (**figure 1-11**).

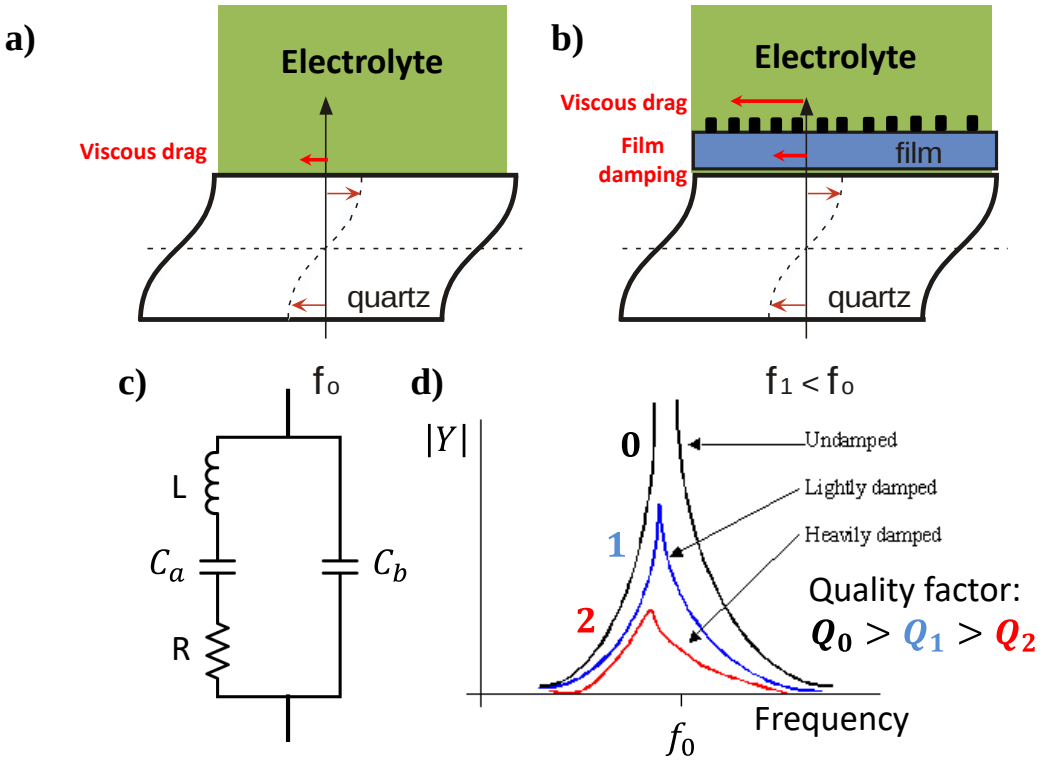

Figure 1-11: a-b) Représentation schématique de la microbalance à quartz en milieu liquide. **c)** Circuit équivalent. **d)** Amortissement du signal de résonnance.

5. Objectif de la thèse

L'objectif de cette thèse est d'appliquer les méthodes de caractérisation par microbalance à quartz électrochimique à des électrodes de supercondensateurs nanostructurées verticalement, ce qui n'a encore jamais été fait précédemment. La croissance de ces nanostructures directement sur la surface de la microbalance sans endommager les propriétés de cette dernière sera un premier défi conséquent pour certains matériaux. L'effet de l'amortissement de la résonance sur ces nanostructures sera ensuite étudié et si possible contourné pour pouvoir les caractériser via des mesures d'EQCM et d'*ac*-electrogravimetry. Les nanostructures étudiées au cours de cette thèse seront des nanofils de silicium, des nanofils de PEDOT, des nanofils hybrides silicium/PEDOT ainsi que des voiles de graphène orientés verticalement.

Chapitre 2 : Méthodes

1. Caractérisation de la morphologie et des propriétés électrochimiques

La morphologie des nanostructures étudiées a été examinée par le biais d'un microscope électronique à balayage (MEB), un instrument utilisant un faisceau d'électrons canalisés sur l'échantillon et un détecteur d'électrons secondaires ré-émis par ce dernier pour former une image en relief des nanostructures. Des techniques standard d'électrochimie ont ensuite été utilisées pour effectuer une première caractérisation des électrodes. Parmi ces techniques, la cyclo-voltamétrie et les cycles de charge/décharge galvanostatiques permettent de déterminer la capacité, la densité d'énergie et de puissance ainsi que la durabilité des électrodes. La **figure 2-1** montre une cellule électrochimique et un dispositif à deux électrodes qui sont utilisés pour ces charactérisations.

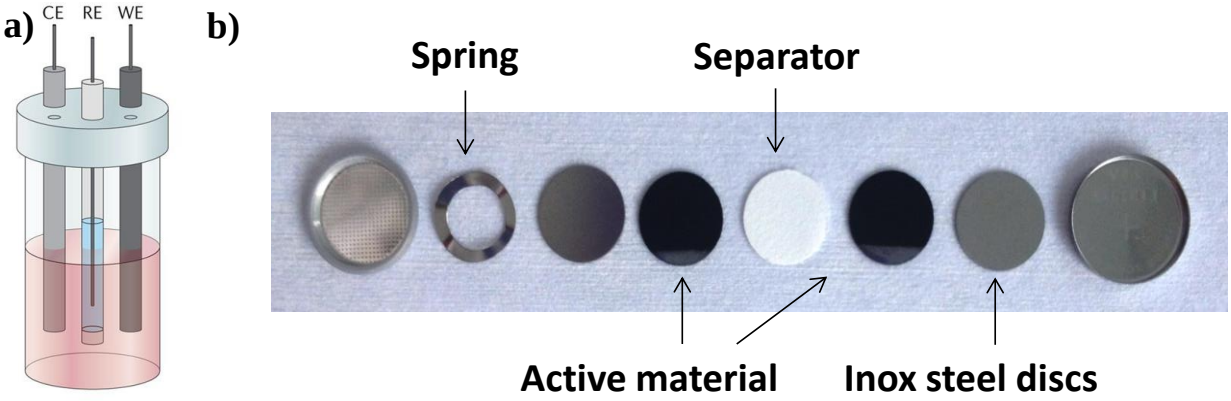

Figure 2-1: a) Cellule électrochimique à trois électrodes. **b)** Composants permettant de concevoir une pile-bouton.

2. Expériences de microbalance à quartz électrochimique

Les mesures par microbalance à quartz électrochimique se font en utilisant la cellule électrochimique modifiée et le montage décrits dans la **figure 2-2**.

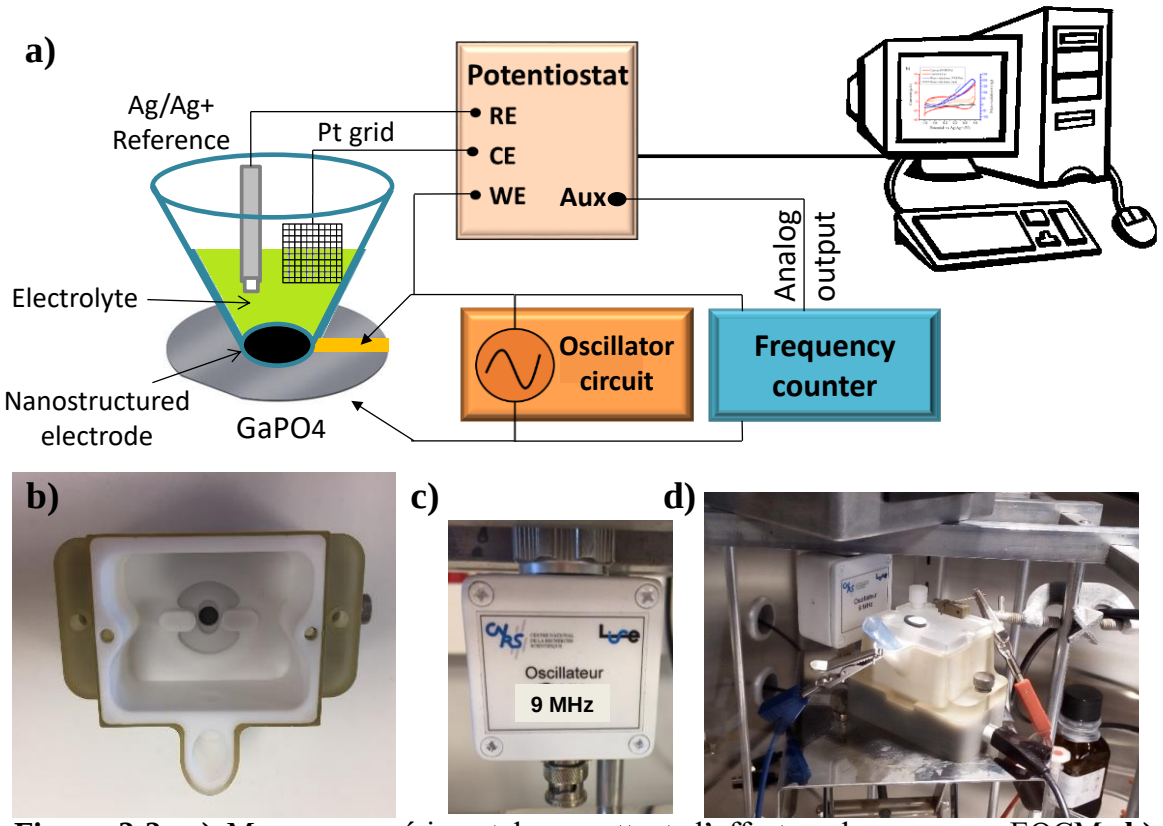

Figure 2-2: a) Montage expérimental permettant d'effectuer les mesures EQCM. **b)** Cellule électrochimique adaptée à la microbalance. **c)** Circuit d'alimentation de l'oscillateur. **d)** Montage complet en boîte à gants.

Un circuit électronique alimente les oscillations de la microbalance tandis qu'un fréquencemètre mesure sa fréquence de résonnance et la transmet au potentiostat via un signal analogique. En appliquant l'équation de Sauerbrey, les variations de fréquence mesurées pendant la mesure électrochimique sont transformées en variations de masse.

Le montage permettant de faire les mesures d'*ac*-electrogravimetry est plus complexe, avec notamment l'ajout d'un analyseur de réponse fréquencielle (FRA), d'un synthétiseur de fréquences et d'un circuit de conversion du signal (**figure 2-3**). Les fonctions de transfert obtenues après la mesure nécessitent plusieurs étapes de traitement avant d'être exploitables.

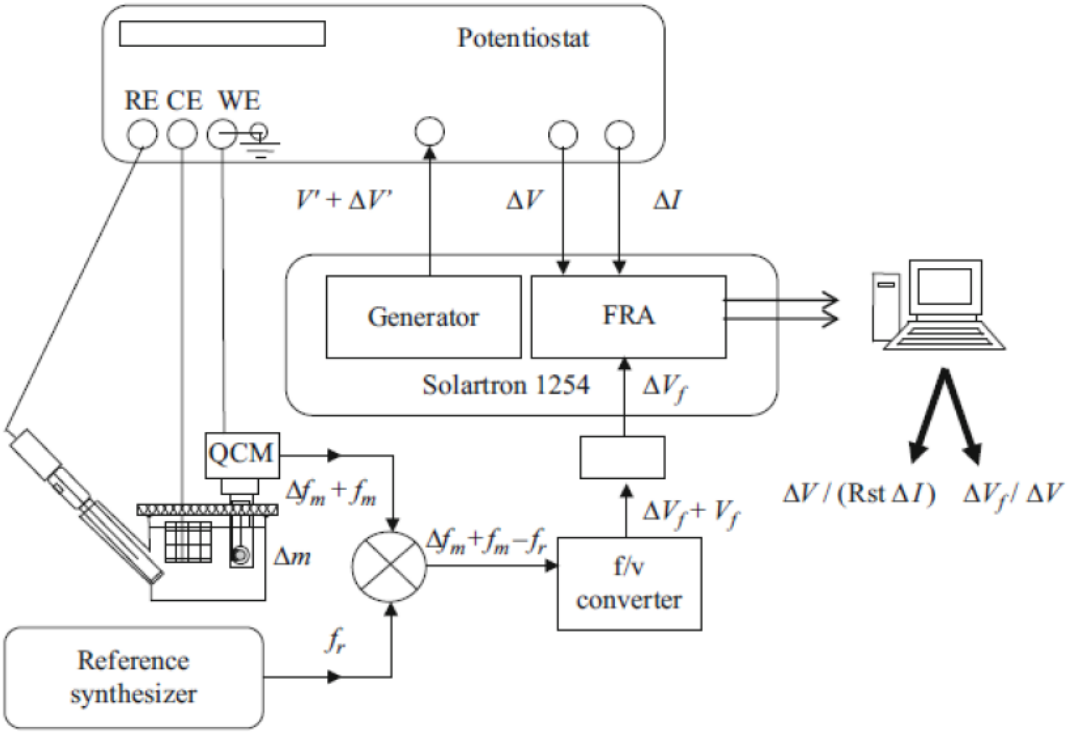

Figure 2-3: Montage expérimental permettant d'effectuer des mesures d'*ac*-electrogravimetry.

3. Modélisation et ajustement des données d'*ac*-electrogravimetry

Le résultat des mesures d'*ac*-electrogravimetry permet d'obtenir deux fonctions de transfert correspondant à l'impédance électrochimique $\left(\frac{\Delta E}{\Delta I}\right)$ et aux variations de masse $\left(\frac{\Delta m}{\Delta E}\right)$ que l'on peut représenter dans des diagrammes de Nyquist (**figure 2-4**). L'interprétation de ces données passe par l'utilisation d'un modèle approprié dont l'ajustement des paramètres permet d'ajuster les données expérimentales. Un programme spécifiquement destiné à effectuer ces ajustements a été développé au cours de la thèse pour extraire les informations voulues des résultats d'*ac*-electrogravimetry.

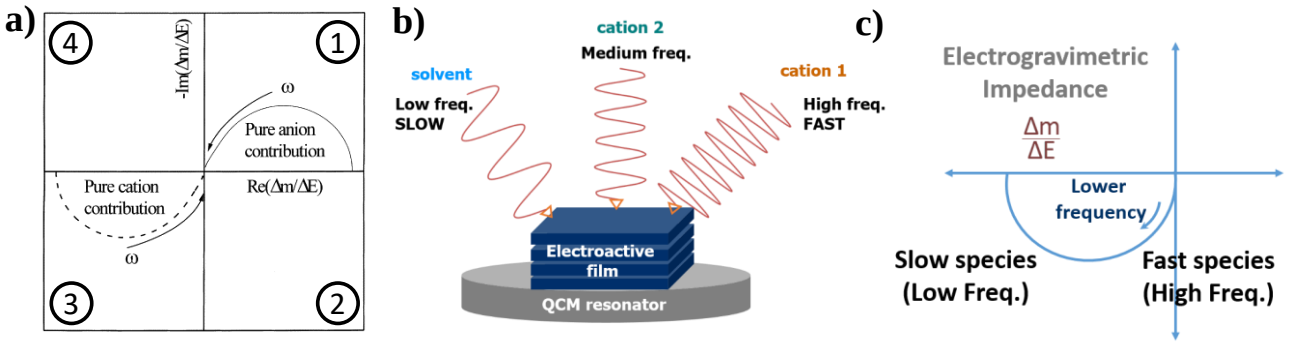

Figure III-7: a) Diagramme Nyquist de $\frac{\Delta m}{\Delta E}(\omega)$ pour des contributions purement anionique ou cationique. **b)** Schéma représentant trois espèces échangées, dont deux cations, avec des cinétiques différentes et **c)** diagramme Nyquist de $\frac{\Delta m}{\Delta E}(\omega)$ correspondant. Adapté de [40].

Chapitre 3 : Electrodes de supercondensateur à base de nanofils

1. Nanofils de silicium

La croissance de nanofils de silicium par CVD sur des microbalances à quartz a été rendue difficile par les relativement basses températures supportées par le quartz (autour de 380°C). Différentes stratégies ont été employées sur les conditions de croissance et des nanofils d'alliage silicium-germanium ont pu être obtenus, mais aucun des quartz utilisés n'a été en mesure de résonner après les croissances (**figure 3-1a-c**).

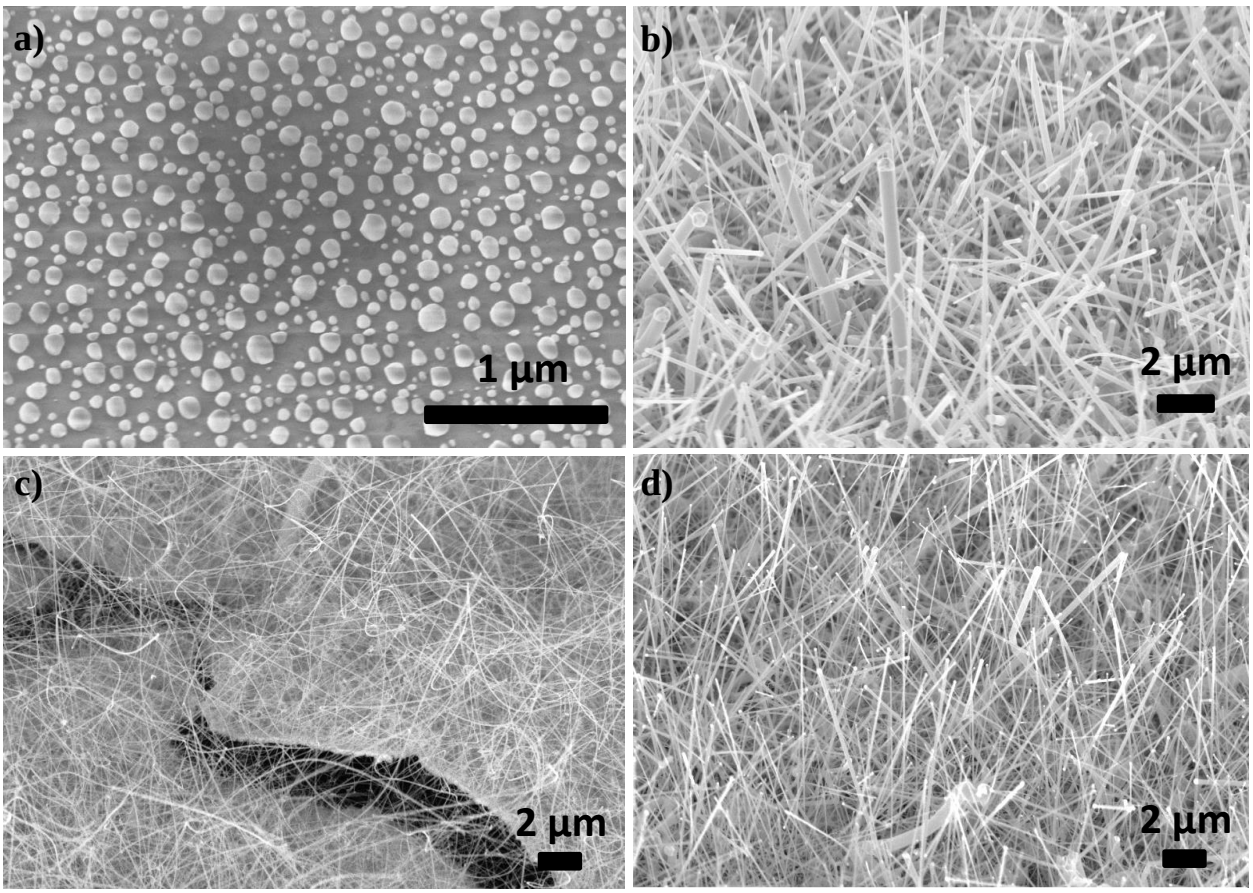

Figure 3-1: Images MEB de différentes configurations testées: **a)** Tentative de croissance de nanofils de silicium sur microbalance à quartz à 380°C. **b)** Nanofils d'alliage silicium-germanium sur microbalance, mais sans résonnance possible. **c)** Nanofils Si-Ge sur microbalance avec des électrodes en platine se décollant après la croissance. **d)** Nanofils de silicium sur microbalance en $GaPO_4$ fonctionnelle après la croissance à 600°C.

Une stratégie différente a dû être adoptée, et le $GaPO_4$ a été choisi comme matériau piezoélectrique pour les microbalances du fait de sa plus forte résistance aux hautes températures. La croissance de nanofils de silicium à 600°C a pu être réalisée avec succès sur une microbalance fonctionnelle avec des électrodes en Pt (**figure 3-1d**). Les nanofils obtenus ont un diamètre entre 100 et 500 nm, une longueur de 10 µm et un poids total de 220 $\mu g.cm^{-2}$.

Le facteur de qualité de 4610 obtenu pour la microbalance couverte de nanofils dans l'air a été réduit d'un facteur 20 dans de l'acétonitrile (ACN), et d'un facteur 40 dans du propylène carbonate (PC). Cette grande perte de sensibilité due à l'amortissement des ondes transverses de la microbalance ainsi que les faibles courants générés par les nanofils de 10 µm n'ont pas permis d'obtenir des résultats en EQCM et *ac*-electrogravimetry. La caractérisation électrochimique de ce type électrodes a cependant permis de trouver un ratio idéal de 50% pour les mélanges PC+N_{1114}TFSI, alliant les bonnes propriétés de conduction ionique du PC et les larges fenêtres de potentiel du liquide ionique (**figure 3-2**).

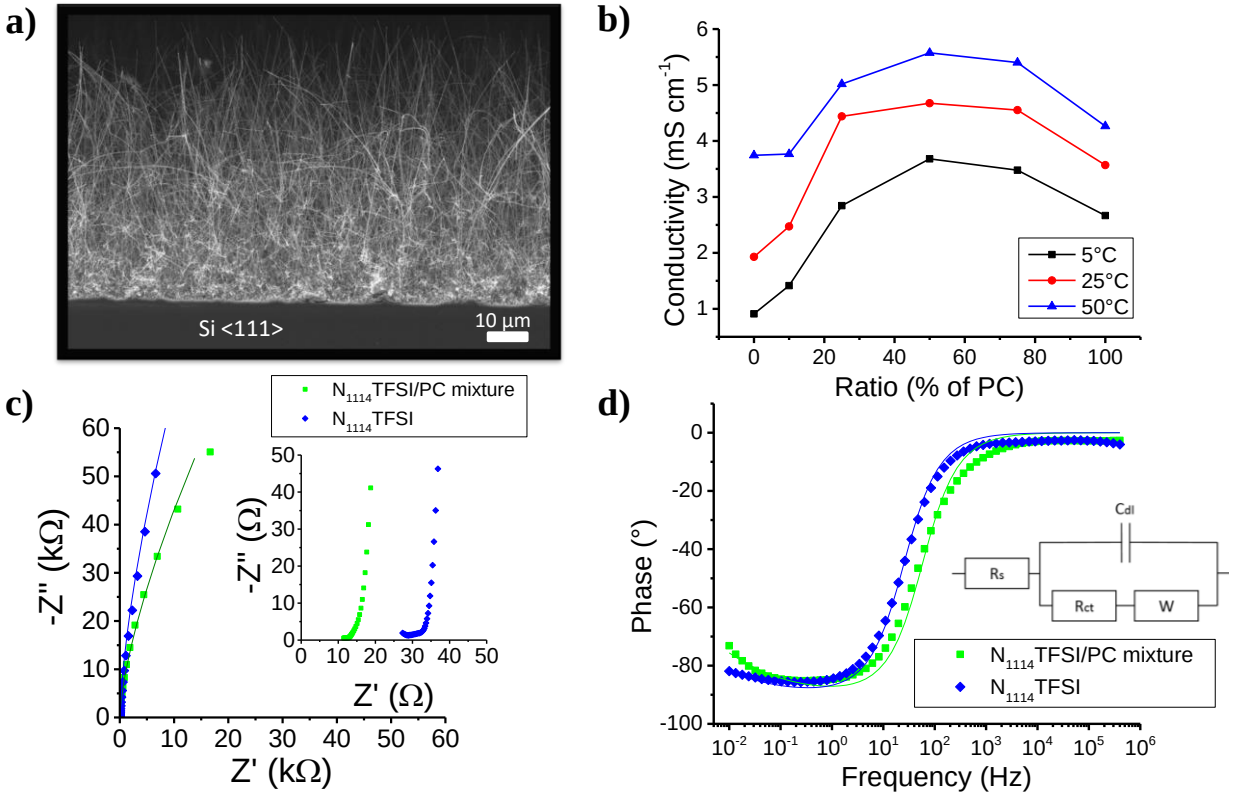

Figure 3-2: a) Images MEB de nanofils de silicium utilisés pour cette étude. **b)** Conductivité ionique de différents mélanges PC+N_{1114} TFSI. **c)** Diagramme Nyquist de la spectroscopie d'impédance électrochimique effectuée avec le liquide ionique pur et le mélange à 50% avec du PC. **d)** Phase du diagramme de Bode correspondant.

2. Nanofils de PEDOT

Des nanofils de PEDOT ont été synthetisés par électropolymérisation sur des électrodes de microbalance à quartz (**figure 3-3a**). Ces nanofils de 1-2 µm de longueur sont plus courts mais produisent plus de courant que les nanofils de silicium étudiés précédemment du fait des mécanismes pseudo-capacitifs ayant lieu dans le polymère conducteur. Ainsi, des mesures d'EQCM et d'*ac*-electrogravimetry ont pu être menées à bien pour ces électrodes

(**figure 3-3b-e**). Les résultats obtenus ont permis d'identifier les espèces échangées avec l'électrolyte au cours des cycles de charge/décharge comme étant les cations TBA^+ et Li^+.

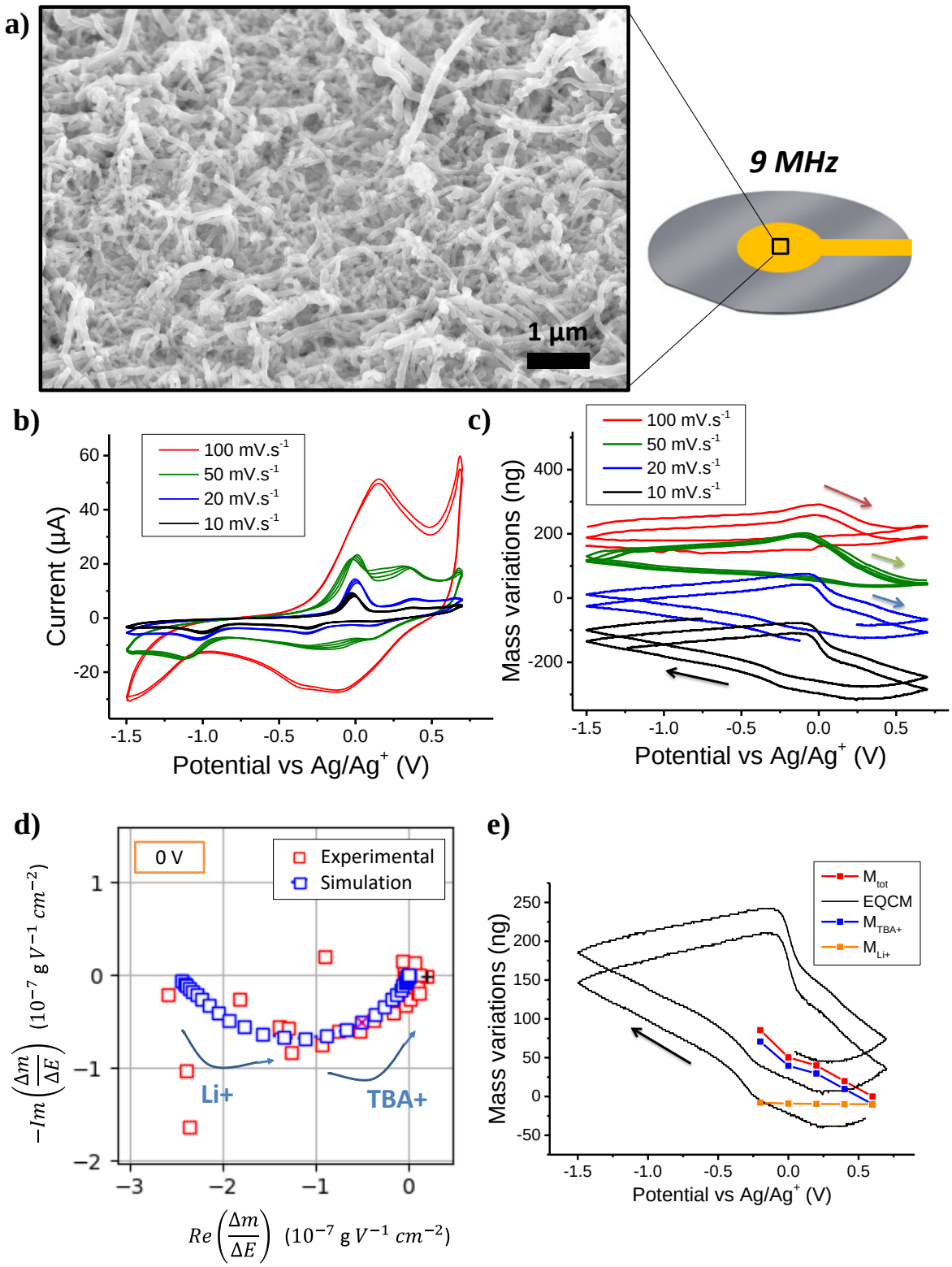

Figure 3-3: a) Image MEB de nanofils de PEDOT à la surface d'une microbalance à quartz. **b)** Cyclo-voltammétrie effectuée à différentes vitesses de balayage sur les nanofils de PEDOT en milieu ACN+0.5M $TBABF_4$ et **c)** les variations de masse correspondantes. **d)** Diagramme Nyquist de la fonction de transfert $\frac{\Delta m}{\Delta E}$ obtenue par *ac*-electrogravimetry. **e)** Reconstruction des variations de masse mesurées par EQCM avec les données d'*ac*-electrogravimetry.

3. Nanofils hybrides silicium/PEDOT

Des nanofils de silicium synthétisés sur les microbalances en $GaPO_4$ ont été recouverts de PEDOT pour transformer ces électrodes d'EDLC en pseudo-condensateurs et ainsi augmenter le courant mesuré (**figure 3-4a**). Les nanofils obtenus ont permis de mesurer de larges variations de masse pendant les cycles de charge/décharge des électrodes malgré la faible sensibilité de la microbalance causée par la hauteur de ces nanostructures plongées dans l'acétonitrile. Ces résultats d'EQCM ont permis de dévoiler un échange majoritairement anionique entre le PEDOT et l'électrolyte (**figure 3-4b**). En revanche la sensibilité de la microbalance n'a pas permis d'obtenir des résultats en *ac*-electrogravimetry.

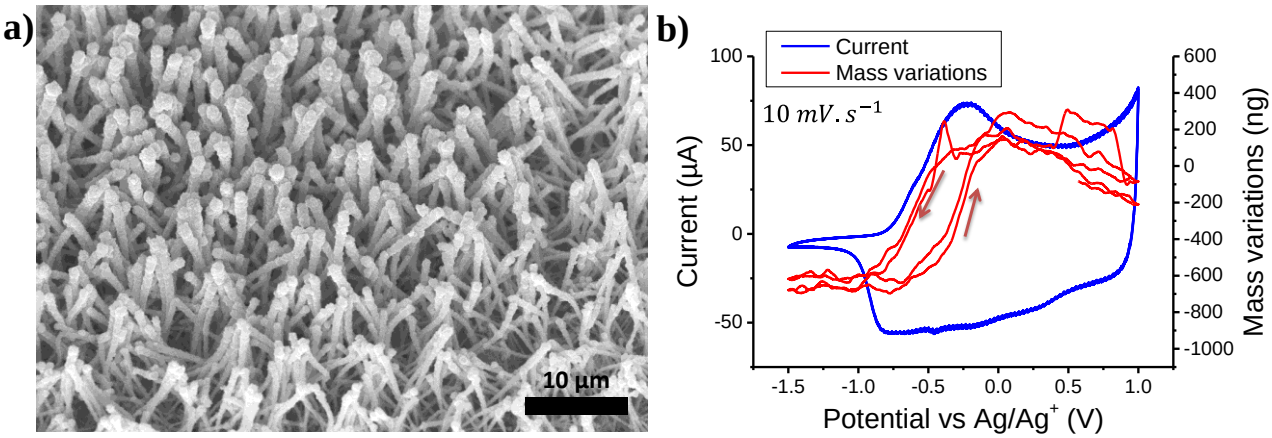

Figure 3-4: a) Image MEB de nanofils de silicium recouverts de PEDOT à la surface de résonateurs en $GaPO_4$. **b)** Résultats des mesures d'EQCM à 10 $mV.s^{-1}$ en milieu ACN+0.5M $TBABF_4$.

Chapitre 4 : Voiles de graphène orientés verticalement sur une microbalance

1. Mesures EQCM

Des voiles de graphène orientés verticalement (VOGNs) ont été synthétisés à la surface de microbalances à base de $GaPO_4$ (**figure 4-1a-b**). D'une épaisseur d'environ 1 µm, cette couverture de voiles de graphène ne présente pas autant de frottements hydrodynamiques que les nanofils de silicium, ce qui a permis leur caractérisation par EQCM dans différents électrolytes organiques ainsi que dans le mélange de liquide ionique et de PC étudié précédemment. Ces mesures ont révélé le comportement dominant des ions dans chacun des milieux, avec par exemple une contribution purement anionique dans les solutions de PC+0.5M $TBABF_4$ et PC+0.5M $TBAClO_4$.

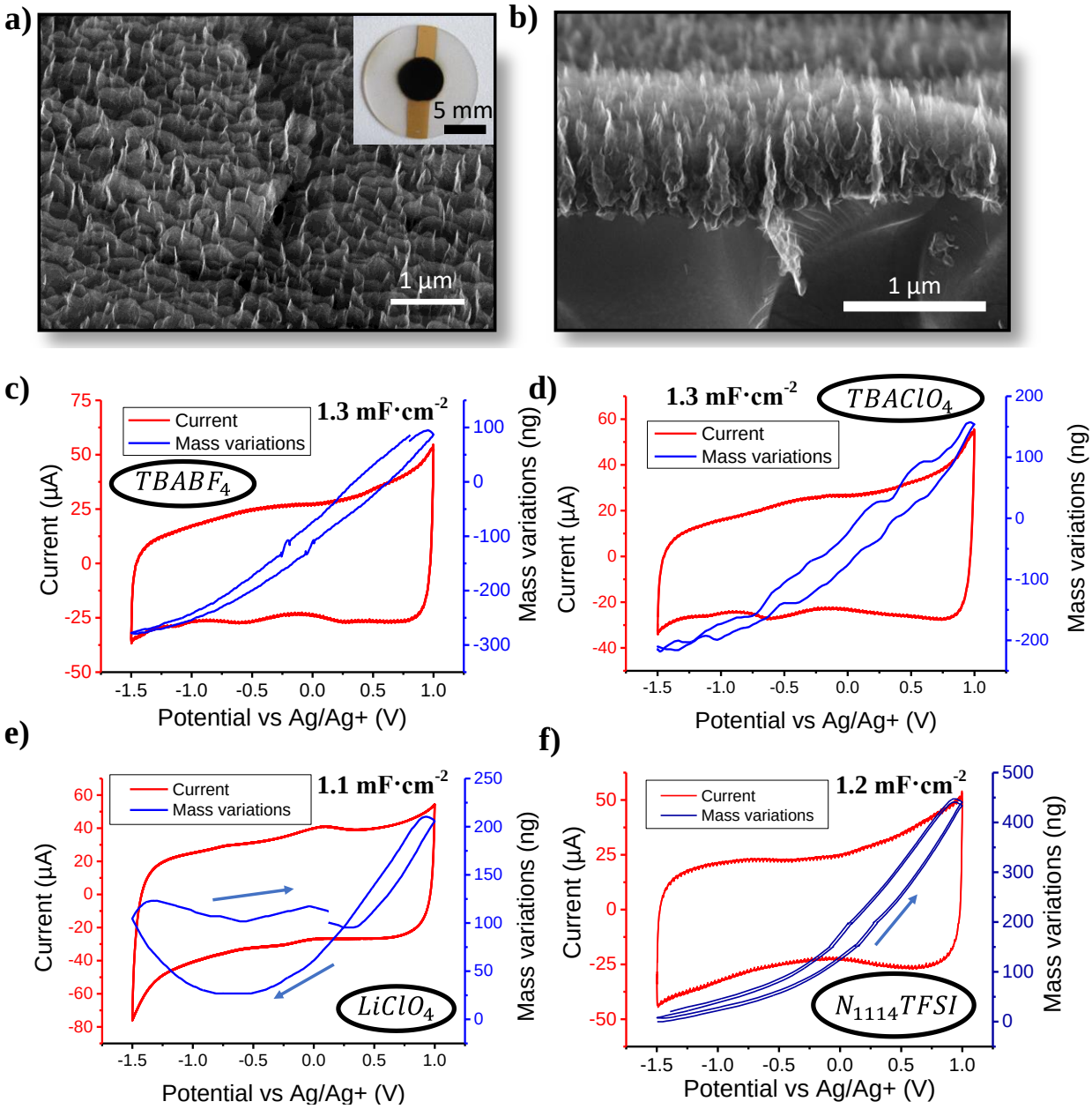

Figure 4-1: a-b) Images MEB de VOGNs synthétisés sur des microbalances à base de GaPO4. **c-f)** Mesures EQCM effectuées sur les VOGNs dans différents milieux: **c)** PC+0.5M $TBABF_4$, **d)** PC+0.5M $TBAClO_4$, **e)** PC+0.5M $LiClO_4$, **f)** 50% PC + 50% $N_{1114}TFSI$.

2. Mesures d'*ac*-electrogravimetry

Au moyen de mesures d'*ac*-electrogravimetry, les résultats obtenus par EQCM ont été déconvolués pour révéler la dynamique dans les mécanismes d'échanges ioniques ainsi que la contribution individuelle de chaque espèce échangée (**figure 4-2**). Ainsi, les variations de concentrations de chaque espèce au sein des voiles de graphène ont pu être calculées et les variations de masses obtenues par EQCM ont pu être reconstruites en utilisant les données

d'*ac*-electrogravimetry. Dans le cas du mélange de PC et de liquide ionique, une contribution égale de l'anion et du cation a été dévoilée.

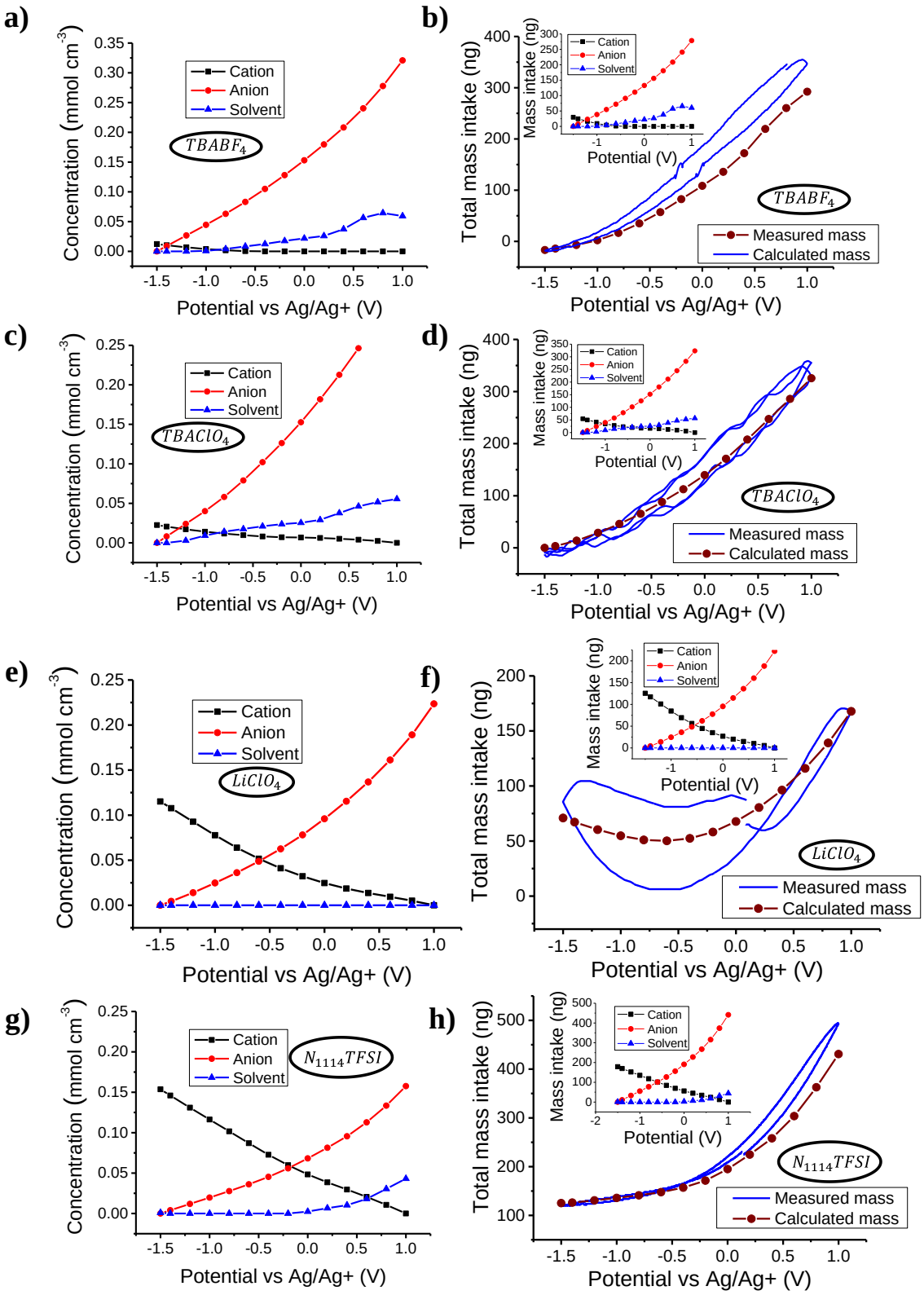

Figure 4-2: Variations de concentrations, $C_i - C_0$, obtenues par *ac*-electrogravimetry pour chaque espèce échangée (gauche) et reconstruction des variations de masse mesurées par EQCM avec les données d'*ac*-electrogravimetry pour chaque espèce échangée (droite) dans quatre milieu différents: **a) b)** PC+0.5M $TBABF_4$, **c) d)** PC+0.5M $TBAClO_4$, **e) f)** PC+0.5M $LiClO_4$, **g) h)** PC+N_{1114}TFSI.

Chapitre 5 : Conclusion et perspectives

Les échanges ioniques dynamiques ayant lieu au sein d'électrodes à base de VOGNs et de nanofils de PEDOT ont pu être dévoilés au moyens des techniques de microbalance à quartz électrochimique. Ces premières avancées dans l'application des mesures électrogravimétriques à des nanostructures verticales ont montré l'étendue des possibilités pour la caractérisation de supercondensateurs à électrodes nanostructurées. Les limites de ces techniques dues aux amortissements hydrodynamiques ont également été montrées pour les architectures plus hautes avec des nanofils de silicium.

Les perspectives d'application de ces techniques sont ouvertes à de nombreuses architectures d'électrodes nanostructurées, non seulement pour les supercondensateurs mais aussi pour les batteries. La **figure 5-1** présente quelques-unes de ces architectures telles qu'elles pourraient être étudiées par microbalance à quartz électrochimique. [41], [42], [43]

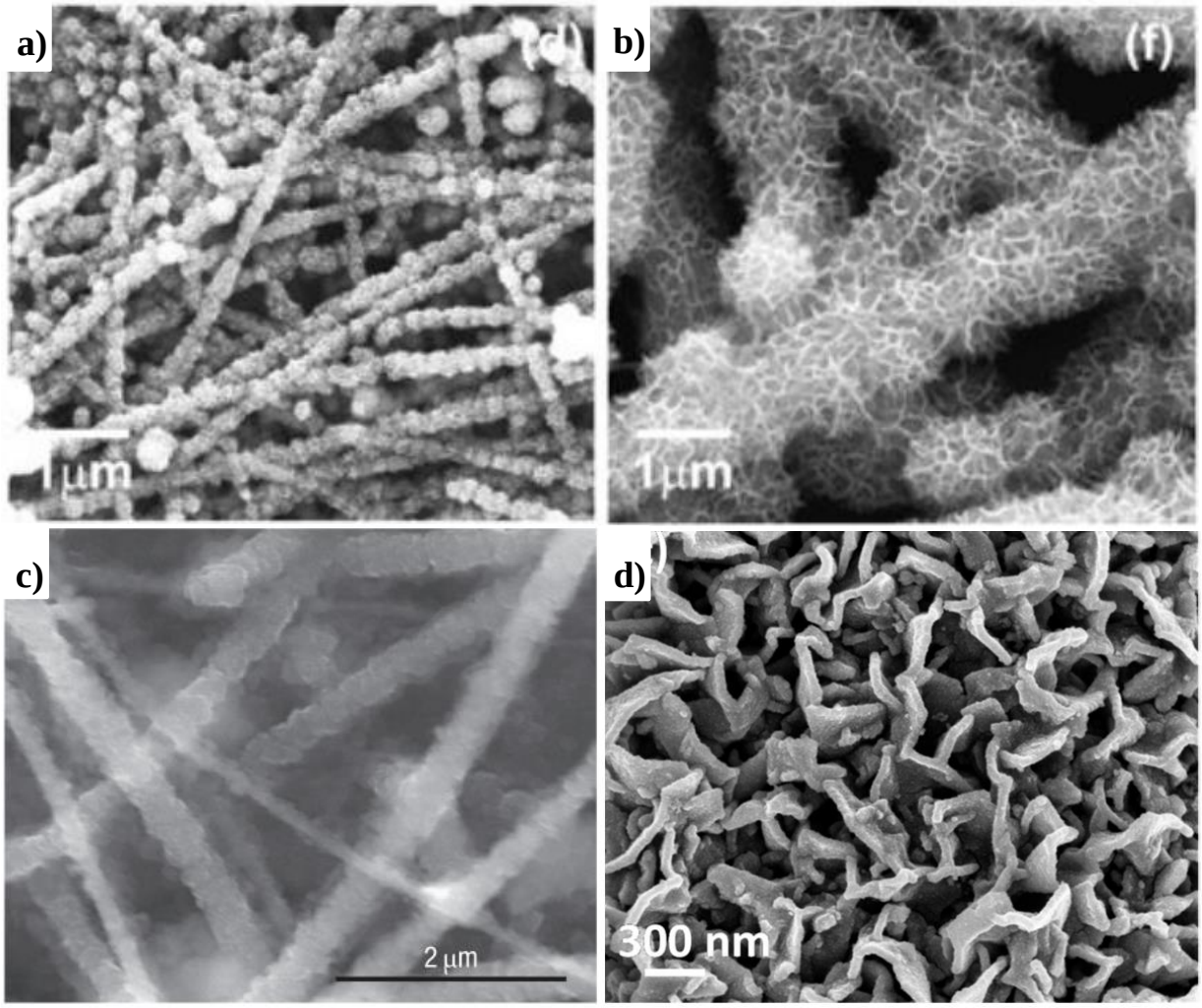

Figure 5-1: Images MEB de quelques nanostructures qui pourraient être étudiées par EQCM : **a-b)** Nanofils de silicium recouverts de MnO_2 [41], **c)** Nanofils de silicium après quelques cycles d'utilisation en tant qu'anodes de batteries [43] et **d)** VOGNs couverts de nanoparticules pseudo-capacitives de Co_3O_4 [42].

Références

[1] I. Dincer, 'Renewable energy and sustainable development: a crucial review', *Renew. Sustain. Energy Rev.*, vol. 4, no. 2, pp. 157–175, Jun. 2000.

[2] 'Tesla Model 3 specs: 220-mile standard with 310-mile option for $9k', *TESLARATI.com*, 29-Jul-2017. .

[3] 'Renewable Energy Sources', *CleanTechnica*. https://cleantechnica.com/renewable-energy-sources/. 27-Aug-2018.

[4] '10 best electric bikes', *The Independent*, 05-Jul-2016. http://www.independent.co.uk/extras/indybest/outdoor-activity/cycling/best-electric-bike-rated-under-500-halfords-brompton-brands-reviews-a7120306.html. 27-Aug-2018.

[5] 'Top 10 Best Smartwatches Under $300', *TechCinema*. .

[6] 'HP Windows 10 14" Laptop - Jet Black (14-BW012NR)'. /p/hp-windows-10-14-laptop-jet-black-14-bw012nr/-/A-52948509. 27-Aug-2018.

[7] CSols-Admin, 'RFID labelling for laboratories', 19-Dec-2011. .

[8] 'Smartphone hire - Roma - Snap Phone'. /en-gb/cellphone-and-smartphone-hire. 27-Aug-2018.

[9] A. Kiourti and R. Shubair, 'Implantable and Ingestible Sensors for Wireless Physiological Monitoring: A Review', 2017.

[10] 'Different Types of Sensors Based Engineering Projects And Applications', *Edgefxkits International*, 15-Jun-2017. .

[11] 'From hydrogen and oxygen to fuel cell', *Mass Flow ONLINE*, 08-Aug-2017. https://www.massflow-online.com/markets_applications/hydrogen-oxygen-fuel-cell/. 27-Aug-2018.

[12] B. R. Chalamala, T. Soundappan, G. Fisher, M. R. Anstey, V. Viswanathan, and M. Perry, 'Redox Flow Batteries: An Engineering Perspective', *Proc. IEEE*, vol. 102, pp. 976–999, Jun. 2014.

[13] 'Compressed Air Energy Storage: Renewable Energy'. https://phys.org/news/2010-03-compressed-air-energy-storage-renewable.html. 27-Aug-2018.

[14] admin, 'Highview Power Storage using Liquid Air', *Revolution-Green*, 04-Apr-2017. .

[15] 'About Grand Coulee Dam | Bureau of Reclamation'. https://www.usbr.gov/pn/grandcoulee/about/index.html. 27-Aug-2018.

[16] 'Demand For Lithium-Ion Batteries Outpacing Supply | Sensors Magazine'. https://www.sensorsmag.com/components/demand-for-lithium-ion-batteries-outpacing-supply. 27-Aug-2018.

[17] '200F Super Capacitor | Global Sources'. http://www.globalsources.com/si/AS/Green-Tech/6008848812833/pdtl/200F-Super-Capacitor/1111668057.htm. 27-Aug-2018.

[18] 'EEUFC1J102U | Panasonic Aluminium Electrolytic Capacitor FC Radial Series 63V dc 1000µF, Through Hole Electrolytic, ±20% +105°C | RS Components'. https://au.rs-online.com/web/p/aluminium-capacitors/0572215/. 27-Aug-2018.

[19] 'Volvo hybrid drive: 60,000 rpm flywheel, 25% boost to mpg - ExtremeTech'. http://www.extremetech.com/extreme/154405-volvo-hybrid-drive-60000-rpm-flywheel-25-boost-to-mpg. 27-Aug-2018.

[20] 'Specifications for NCR18650GA'. Panasonic, 02-Jul-2017.

[21] M. Beidaghi and Y. Gogotsi, 'Capacitive energy storage in micro-scale devices: recent advances in design and fabrication of micro-supercapacitors', *Energy Environ. Sci.*, vol. 7, no. 3, pp. 867–884, Feb. 2014.

[22] 'The supercapacitor electric bus is adopted in China - SupercapTech.com'. https://www.supercaptech.com/the-supercapacitor-electric-bus-is-adopted-in-china. 16-Aug-2018.

[23] B. Halvorson, 'Ultracapacitor Resistance Breaking Down Among Automakers?', *Green Car Reports*. https://www.greencarreports.com/news/1098550_ultracapacitor-resistance-breaking-down-among-automakers. 27-Aug-2018.
[24] 'Biosensors History|Scientific India Magazine'. http://www.scind.org/517/Science/biosensors-history.html. 27-Aug-2018.
[25] 'Le tramway à Toulon', *Collectif Tramway Toulon*. http://www.tramwaytoulon.com/. 27-Aug-2018.
[26] 'MEMS Waveguide Switch Controls 500 to 750 GHz', *Microwaves & Radio Frequency*, 02-Aug-2017. https://www.mwrf.com/components/mems-waveguide-switch-controls-500-750-ghz. 27-Aug-2018.
[27] J. R. Miller and P. Simon, 'Electrochemical Capacitors for Energy Management', *Science*, vol. 321, no. 5889, pp. 651–652, Aug. 2008.
[28] A. Anwar, A. Majeed, N. Iqbal, W. Ullah, A. Shuaib, U. Ilyas, F. Bibi, and H. M. Rafique, 'Specific Capacitance and Cyclic Stability of Graphene Based Metal/Metal Oxide Nanocomposites: A Review', Aug. 2015.
[29] A. J. Bard and L. R. Faulkner, 'Electrochemical Methods: Fundamentals and Applications, 2nd Edition', *Wiley.com*. https://www.wiley.com/en-fr/Electrochemical+Methods%3A+Fundamentals+and+Applications%2C+2nd+Edition-p-9780471043720. 16-Aug-2018.
[30] F. Béguin, V. Presser, A. Balducci, and E. Frackowiak, 'Carbons and Electrolytes for Advanced Supercapacitors', *Adv. Mater.*, vol. 26, no. 14, pp. 2219–2251, Apr. 2014.
[31] J.-C. LASSÈGUES, 'Supercondensateurs', *Ref : TIP301WEB - 'Conversion de l'énergie électrique'*, 10-May-2001. /base-documentaire/energies-th4/accumulateurs-d-energie-42243210/supercondensateurs-d3334/. 16-Aug-2018.
[32] F. Miomandre, S. Sadki, P. Audebert, and R. Méallet-Renault, *Électrochimie*. 2018.
[33] T. Brousse, D. Belanger, and J. W. Long, 'To Be or Not To Be Pseudocapacitive?', *J Electrochem. Soc*, vol. 162, no. 5, pp. A5185–A5189, 2015.
[34] P. Simon, Y. Gogotsi, and B. Dunn, 'Materials science. Where do batteries end and supercapacitors begin?', *Science*, vol. 343, no. 6176, pp. 1210–1211, Mar. 2014.
[35] P. Simon and Y. Gogotsi, 'Capacitive Energy Storage in Nanostructured Carbon–Electrolyte Systems', *Acc. Chem. Res.*, vol. 46, no. 5, pp. 1094–1103, May 2013.
[36] Z. Zhang, C.-S. Lee, and W. Zhang, 'Vertically Aligned Graphene Nanosheet Arrays: Synthesis, Properties and Applications in Electrochemical Energy Conversion and Storage', *Adv. Energy Mater.*, vol. 7, no. 23, p. 1700678, Dec. 2017.
[37] D. Gaboriau, *Nanostructures de silicium par croissance chimique catalysée : une plate-forme pour des applications micro-supercondensateurs*. Grenoble Alpes, 2016.
[38] F. Oehler, P. Gentile, T. Baron, M. D. Hertog, J. Rouvière, and P. Ferret, 'The morphology of silicon nanowires grown in the presence of trimethylaluminium', *Nanotechnology*, vol. 20, no. 24, p. 245602, 2009.
[39] K. Wang, J. Huang, and Z. Wei, 'Conducting Polyaniline Nanowire Arrays for High Performance Supercapacitors', *J. Phys. Chem. C*, vol. 114, no. 17, pp. 8062–8067, May 2010.
[40] H. Goubaa, F. Escobar-Teran, I. Ressam, W. Gao, A. El Kadib, I. T. Lucas, M. Raihane, M. Lahcini, H. Perrot, and O. Sel, 'Dynamic Resolution of Ion Transfer in Electrochemically Reduced Graphene Oxides Revealed by Electrogravimetric Impedance', *J. Phys. Chem. C*, vol. 121, no. 17, pp. 9370–9380, May 2017.
[41] D. P. Dubal, D. Aradilla, G. Bidan, P. Gentile, T. J. S. Schubert, J. Wimberg, S. Sadki, and P. Gomez-Romero, '3D hierarchical assembly of ultrathin MnO_2 nanoflakes on silicon nanowires for high performance micro-supercapacitors in Li- doped ionic liquid', *Sci. Rep.*, vol. 5, p. 9771, May 2015.

[42] Q. Liao, N. Li, S. Jin, G. Yang, and C. Wang, 'All-Solid-State Symmetric Supercapacitor Based on Co3O4 Nanoparticles on Vertically Aligned Graphene', *ACS Nano*. 9 (2015) 5310–5317.
[43] C. K. Chan, H. Peng, G. Liu, K. McILWRATH, X. F. Zhang, R. A. Huggins, and Y. Cui, 'High-performance lithium battery anodes using silicon nanowires', in *Materials for Sustainable Energy*, 0 vols, Co-Published with Macmillan Publishers Ltd, UK, 2010, pp. 187–191.